DOCTORAL SCHOOL
UNIVERSITY OF MILANO-BICOCCA

Department of
PHYSICS "G. Occhialini"
PhD program in Physics and Astronomy - XXXV Cycle

---

# Development of innovative techniques for ultra-trace elements analysis

Andrea Barresi
Registration number 775677

Tutor: Prof. Ezio Previtali

Coordinator: Prof. Stefano Ragazzi

Academic year 2021/2022

# Contents

# Introduction

The JUNO experiment (Jiangmen Underground Neutrino Observatory) was proposed with the main aim of solving the problem related to the neutrino mass ordering through accurate measurements of the antineutrinos flow produced by the nuclear reactors of two power plants located about 53 km away from the experiment site. The excellent characteristics of the JUNO detector will allow providing important contributions to neutrino physics, obtaining a better estimate of the parameters that describe the neutrino flavor oscillation, measuring the flux of neutrinos of solar and terrestrial origin, and studying neutrinos of atmospheric origin. The JUNO detector consists of an acrylic sphere with an internal diameter of 35.4 m containing 20 000 t of liquid scintillator and surrounded by 17612 photomultiplier tubes to detect the energy depositions in the liquid scintillator volume. Reactor antineutrinos will interact in the JUNO detector via inverse beta decay reaction that occurs between the neutrinos and the protons of the atomic nuclei of the liquid scintillator. Due to the extremely small cross-section of neutrinos, the number of expected signal events is very small, about 60 IBD events per day, and it is therefore essential to keep under control the rate of background events that could greatly reduce the measurement sensitivity of the experiment, masking the presence of signal events. This can be achieved by minimizing all the sources that contribute to the generation of spurious events, those that are indistinguishable from signal events, and in the first place those generated by the radioactive background. One of the sources that contribute most to the background of rare event physics experiments, such as JUNO, is the natural radioactivity present in the environment where the detector will be installed and, in the materials, used to build the detector itself. By using Monte Carlo simulations of the detector response, a limit on the total rate of events for the different background sources was set to guarantee the final sensitivity of the JUNO experiment. Considering this, it is evident how essential it is to carry out an accurate selection of the materials that will be used in the construction of the various parts of the detector in order to reduce the intrinsic background generated. The natural sources of radioactivity are mainly constituted by the nuclides of the radioactive chains of $^{238}$U and $^{232}$Th and from $^{40}$K. For each progenitor of the natural chains, for the $^{40}$K, and for some key artificial and natural nuclides, such as $^{60}$Co and $^{210}$Pb, it is necessary to impose strong limits on the concentration that may be present within the various materials that will make up the detector. Given the structure of the JUNO detector, the most critical material is the liquid scintillator because any decay event that occurs within it will produce a signal that will be detected. For this material, uranium and thorium concentrations below $1{\cdot}10^{-15}$ g/g and potassium below $1{\cdot}10^{-16}$ g/g are required. An extremely sensitive trace element analysis technique is neutron activation analysis (NAA). It is based on the exposition of the sample to be analysed to an intense flux of neutrons and the determination of the concentration of the nuclides produced by neutron capture by measuring the induced radioactivity. Using this technique with standard low background High purity germanium (HPGe) detectors it is possible to achieve sensitivity in the order of ppt. In the context of the JUNO experiment, this technique can be widely used to carry out analyses on the materials proposed for the construction of the experiment, for which the sensitivity obtainable with neutron activation is sufficient to satisfy the imposed requirements. However, this sensitivity is not sufficient for the radio purity requirements of the liquid scintillator. For this reason, it is necessary to implement an innovative technique that allows reaching the required sensitivity.

In this thesis, I present the work I did in this context during my Ph.D. with two main purposes. The first one is the validation of the Monte Carlo software of the JUNO experiment applied to the background simulations with the aim of verifying the radiopurity limits imposed for the materials and determining the background budget of the experiment. The second one is the implementation of a measurement technique that allows reaching the sensitivities required for the measurement of the content of uranium, thorium, and potassium in the liquid scintillator.

The validation of the Monte Carlo software of the JUNO experiment (SNiPER) was performed by comparing its results with those of two other simulation codes, in particular with the software Arby, developed at the University of Milano-Bicocca. I was able to study different aspects and many critical issues of the simulation of the background and the results reported by the official tool, such as the application of the quenching factor and the shape of the radioactive $\beta$-decay spectra. Due to its complexity, the implementation in Arby of the geometry of the JUNO detector was not trivial and it required the implementation of techniques to reduce its complexity in order to cut down the computation time. Once the most suitable geometry was implemented, the spectra of the deposited energy produced by the contaminations in the main components of the JUNO detector were computed with the Monte Carlo codes. The spectra associated with the liquid scintillator and the acrylic sphere contaminations are compared bin-to-bin, while for the other external components only the total number of events was compared (integral of the spectrum). For each of the main components that are expected to contribute to the background of the experiment, the rate of events induced in the detector was assessed based on the imposed radiopurity limits, obtaining the expected total background event rate. The value obtained is lower than the limit set to ensure the final sensitivity of the experiment. This allowed correcting and validating the answer of the official software of the JUNO experiment and verifying the actuality of the radiopurity limits initially defined for the components of the detector, thanks to the simulations carried out with Arby that, for some components, turned out to be essential as they have not yet been implemented in SNiPER and therefore cannot be simulated directly.

A very huge effort has been carried out by the JUNO collaboration in order to guarantee that the radiopurity requirements for the materials of each component are observed. Since these materials have very different matrices and requirements in terms of nuclides concentration, different techniques have been applied in order to certify each of them. The main critical one is the liquid scintillator because a radioactive background event associated with internal contaminations is detected with an efficiency almost unitary and its contribution cannot be reduced by reducing the fiducial volume, as can be done for external sources. Its radiopurity requirements on uranium, thorium, and potassium are at the ppq scale and a measurement technique able to perform this measurement is very important because it would allow the radiopurity of the liquid scintillator to be certified during each of the purification steps during mass production.

During my master's thesis, I started to develop a new measurement system, called GeSparK, that exploits the coincidence between a liquid scintillator and an HPGe detector to reduce the background of the single HPGe detector, obtaining a stronger marker of the decay of interest and therefore increase the measurement sensitivity on the activated samples. During my Ph.D. I completed its development, in particular by implementing a better veto system of cosmic muons, optimizing the data acquisition and analysis system, and the configuration of the detector itself. Since the use of the coincidence is not enough to reach the required sensitivities, I worked on the development of a new delayed coincidence technique that exploits the nuclear structure of $^{239}$Np, the activation product of $^{238}$U, which has a metastable level, in order to obtain an extremely strong marker of this particular decay and significantly increase the measurement sensitivity compared to the traditional approach. The development of this technique has also led to the measurement of the metastable level's lifetime itself with twenty times better accuracy than previous results. A measurement was carried out on a sample of liquid scintillator using these techniques obtaining very good results, especially for the uranium concentration.

Despite the use of the new GeSparK detector and the delayed coincidence technique for the measurement of $^{238}$U, the sensitivity obtained was still insufficient compared to the requests of JUNO and for this reason, it was decided to implement a series of radiochemical treatments on the sample to obtain the required increase in sensitivity. Different treatments have been proposed, tested, and implemented with the two aims of increasing the mass of the measurable sample and reducing the concentration of interfering nuclides, whose activation increases the measurement background, reducing the sensitivity of the detector. The technique developed for uranium and thorium involves a liquid-liquid extraction phase which allows the uranium and thorium to be transferred from the liquid scintillator to an acid aqueous solution, which can be treated by extraction chromatography with UTEVA and TEVA resins respectively before and after irradiation in order to concentrate the radionuclides of interest and remove the interfering ones. A crucial aspect of these treatments is that at the required radiopurity level, the risk of contamination of the sample by the used materials and reagents is extremely high so the control of the contamination sources was a crucial aspect of this activity, making it necessary to validate each reagent and develop a dedicated cleaning protocol. Two measurements conducted on "blank samples" by combining the GeSparK detector, the delayed coincidence technique, and the radiochemical treatments, in order to determine the final sensitivity obtained, allowed us to achieve a sensitivity that is compatible with the limits imposed by JUNO for the liquid scintillator at the ppq level.

The outline of the present thesis is as follows: in the first chapter, neutrino physics and the JUNO experiment will be discussed. In particular, the neutrino will be introduced from a theoretical point of view, with particular reference to its role within the Standard Model, describing the discovery of mass and the phenomenon of neutrino oscillations and the relative implications. The second part of the chapter will describe the JUNO experiment, its physics objectives, and the detector structure, as well as the type of signal produced by the detector. In chapter 2 a description of the JUNO background sources will be provided and subsequently, the work carried out on the validation of the Monte Carlo software and radiopurity requirements will be described. Chapter 3 is dedicated to the description of the development of the new GeSparK detector and, in the last part of the chapter, the measurement techniques used for uranium, thorium, and potassium will be described. To conclude it, the measurements carried out on a sample of liquid scintillator using these techniques will be presented. Chapter 4 describes the different radiochemical treatments proposed, tested, and implemented with the two aims of increasing the mass of the measurable sample and reducing the concentration of interfering nuclides. The general characteristics of these treatments and the specific implementation for the measurement of uranium and thorium in the liquid scintillator will be discussed. At the end of the chapter, will be presented the two measurements conducted on "blank samples" showing the performance of the developed technique.

# Chapter 1

# Neutrino physics and the JUNO experiment

## 1.1 Neutrino oscillations and mass ordering

### 1.1.1 Introduction to neutrino physics and Standard Model

The existence of neutrinos was proposed by Wolfgang Pauli in 1930 as a "desperate remedy" to save the law of energy conservation in beta decays because the apparent emission of only one electron in beta decays was in contradiction with its continuum energy spectrum, experimentally observed. The introduction of this new particle, emitted in the beta decay together with the electron, which is electrically neutral and with intrinsic angular momentum (spin) 1/2, made the beta decay a three-body-decay, perfectly consistent with a continuum energy spectrum for the electron. This new particle played a crucial role in Fermi's theory of beta decay and its existence was experimentally confirmed in 1956 when Clyde Cowan and Fred Reines detected antineutrinos emitted from a nuclear reactor.

Two years later, Goldhaber and co-workers measured the handedness of neutrinos, showing that neutrinos are always left-handed (LH). This important result implies that neutrinos must be massless, moving at the speed of light, because otherwise, it should be possible for an inertial observer to move faster and see the neutrino right-handed (RH). Since RH neutrinos have never been detected, physicists concluded that neutrinos had to be massless. In force of this experimental result, neutrinos were included in the Standard Model (SM) of particle physics with zero mass.

Nowadays we know that all the elementary particles, six quarks, and six leptons, are grouped into exactly three generations, a fact confirmed by precision experiments permed at the LEP at CERN. The first generation is formed by the up and down quarks, the electron, and the electron neutrino. The second and third generation comprises heavier versions of the first-generation particles with the same quantum numbers. All these particles and their antiparticles, together with those that carry the forces between them (photons, W and Z bosons, and gluons) and the Higgs particle, which is responsible for their mass, are at the basis of the Standard Model of particle physics.

The Standard Model of electroweak interaction is based on the symmetry group SU(2) x U(1), combining the quantum electrodynamics U(1) gauge group with the weak interaction SU(2) gauge group. In this model only the chiral LH fermions fields transform as doublets under SU(2):

$$\Psi_i = \begin{pmatrix} \nu_i \\ l_i^- \end{pmatrix} = \left\{ \begin{pmatrix} \nu_e \\ e^- \end{pmatrix}, \begin{pmatrix} \nu_\mu \\ \mu^- \end{pmatrix}, \begin{pmatrix} \nu_\tau \\ \tau^- \end{pmatrix} \right\} \tag{1.1}$$

and

$$\Psi_i = \begin{pmatrix} u_i \\ d_i' \end{pmatrix} = \left\{ \begin{pmatrix} u \\ d \end{pmatrix}, \begin{pmatrix} c \\ s \end{pmatrix}, \begin{pmatrix} t \\ b \end{pmatrix} \right\} \tag{1.2}$$

The RH fields are SU(2) singlets and therefore do not interact via electromagnetic or weak forces, but their presence is responsible for the different probability of interactions of massive particles based on the content of the RH component with respect to the LH one.

To explain the nature of the strong force responsible for the bound states of quarks inside the baryons, the SM is extended including the Quantum Chromodynamics (QCD) into the more general gauge theory based on the group SU(3) x SU(2) x SU(1). This general theory provides for example explanation for the CP violation in the quark sector because, since each family of quarks is an SU(2) doublet, the electroweak interactions should live in a single family and so conserve the CP symmetry. The violation of this symmetry was observed and explained by introducing the Cabibbo-Kobayashi-Maskawa (CKM) mixing matrix. This is a 3x3 unitary matrix that links the up-type quarks with the down-type quarks of the three families, based on the mass-to-flavors bases transformation. This is associated with the fact that the mass eigenstates of the quarks do not coincide with the flavor eigenstates, those that interact by weak force. The CKM matrix is fully defined by three angles and one complex phase, responsible for the CP violation in weak transitions of quarks because its presence produces different probabilities under CP transformation.

The effectiveness of this theory has been proved over the years by the huge amount of experimentally confirmed predictions for the phenomenology of the interaction of elementary particles. One important aspect of the weak interactions is that they are a powerful and sensitive tool to test the prediction of the Standard Model for unpredicted features and the neutrinos are the best probes for this because they are the only particles that interact only by weak interactions.

### 1.1.2 Neutrino mass discovery

As introduced before, the first formulation of the Standard Model included three neutrinos $\nu_e$, $\nu_\mu$, $\nu_\tau$ (and their anti-particle $\overline{\nu}_e$, $\overline{\nu}_\mu$, $\overline{\nu}_\tau$), all initially assumed to be massless. The incompleteness of this framework became clear when the solar neutrinos were observed by Davis et al [1] with a deficit of factor 3 in their flux as compared with the prediction of the Bahcall's standard solar model [2, 3]. The so-called "solar neutrino problem" was confirmed by other experiments [4, 5, 6] while other results also confirmed the solar standard model [7].

A milestone in this puzzle arrived from the SuperKamiokande experiment (SK), in Japan, thanks to the observation of the neutrinos produced in the atmosphere when cosmic rays interact with oxygen or nitrogen nuclei [8]. These atmospheric neutrinos are mostly muon neutrinos because they are produced in the decay of pions. The SK detector is composed of 50 000 tonnes of water in which the high-energy neutrinos interact via charged current interaction with atomic nuclei to produce the corresponding lepton (electrons, muons, or tau) that emitting Cerenkov radiation can be detected with photomultipliers. The signal provided by the SK detector also allowed determining the direction of the interacting neutrinos. The SK detector observed that about one-half of the atmospheric neutrinos from the opposite side of the Earth were lost, while those from above were not. The most likely explanation for this result is that muon neutrinos converted into tau neutrinos during the traveling across the Earth, which are not detectable by SK. This process, called "oscillation", is a spontaneous and periodic transition between the different flavor neutrinos and does not take place unless neutrinos have non-zero masses and lepton flavors are mixed.

The solar problem was finally solved by the SNO experiment [9] which found that the deficit in the solar neutrino flux was due to the neutrinos oscillation, confirming that the total number of neutrinos from the Sun agreed with theoretical calculations and providing further evidence for non-zero neutrino mass.

### 1.1.3 Neutrinos oscillation

The existence of the flavor oscillation implies that if a given flavor neutrino is produced in some weak interaction process with an energy E, the probability of observing a neutrino of a different flavor at a sufficiently large distance, L, is not zero. This is defined as "transition" or "oscillation probability" $P(\nu_i \to \nu_j; E, L)$. In this case, the quantity $P(\nu_i \to \nu_i; E, L)$ is called "survival probability" and describes the probability that a neutrino of a given flavor will not change into a neutrino of a different flavor. In the case of the solar neutrino problem, since the sun is a pure source of $\nu_e$ and the detectors were designed to detect only $\nu_e$, a fraction of the expected neutrino will be observed because the other oscillate into $\nu_\mu$, not detectable by the experiments.

As introduced in 1.1.2 the oscillation takes place only if neutrinos have non-zero masses and their flavors are mixed. The meaning of the flavor mixing is the following: neutrinos are created and interact as flavor eigenstates of the weak interaction but propagate in space as a superimposition of mass eigenstates with different velocities depending by the E/m ratio. Since the two bases are different, the neutrino of definite flavor entering a reaction is a linear combination of three neutrino mass eigenstates $\nu_j$ at the interaction point:

$$|\nu_l\rangle = \sum_{j=1}^{3} U^*_{lj} |\nu_j\rangle \qquad l = e, \mu, \tau \quad j = 1, 2, 3 \tag{1.3}$$

where the matrix U, known as Pontecorvo-Maki-Nakagawa-Sakata (PMNS) matrix, is a 3x3 complex unitary matrix, defined by 3 angles and 3 phases. Therefore, the PMNS matrix acts as a base transformation between the mass base and flavor base. Since during the propagation the relative content of each mass eigenstate is different, it is also different the relative content of the flavors at the interaction point. So, there is a defined probability that a neutrino, created with a defined flavor, interacts with a different flavor.

The standard parametrization for the PMNS matrix is the following:

$$\begin{aligned} U = &\begin{bmatrix} 1 & 0 & 0 \\ 0 & c_{23} & s_{23} \\ 0 & -s_{23} & c_{23} \end{bmatrix} \begin{bmatrix} c_{13} & 0 & s_{13}e^{-\mathrm{i}\delta} \\ 0 & 1 & 0 \\ -s_{13}e^{\mathrm{i}\delta} & 0 & c_{13} \end{bmatrix} \begin{bmatrix} c_{12} & s_{12} & 0 \\ -s_{12} & c_{12} & 0 \\ 0 & 0 & 1 \end{bmatrix} \begin{bmatrix} e^{i\eta_1} & 0 & 0 \\ 0 & e^{i\eta_2} & 0 \\ 0 & 0 & 1 \end{bmatrix} = \\ &\begin{bmatrix} c_{12}c_{13} & s_{12}c_{13} & s_{13}e^{-\mathrm{i}\delta} \\ -s_{12}c_{23} - c_{12}s_{13}s_{23}e^{\mathrm{i}\delta} & c_{12}c_{23} - s_{12}s_{13}s_{23}e^{\mathrm{i}\delta} & c_{13}s_{23} \\ s_{12}s_{23} - c_{12}s_{13}c_{23}e^{\mathrm{i}\delta} & -c_{12}s_{23} - s_{12}s_{13}c_{23}e^{\mathrm{i}\delta} & c_{13}c_{23} \end{bmatrix} \begin{bmatrix} e^{i\eta_1} & 0 & 0 \\ 0 & e^{i\eta_2} & 0 \\ 0 & 0 & 1 \end{bmatrix} \end{aligned} \tag{1.4}$$

where $c_{ij} = \cos(\theta_{ij})$, $s_{ij} = \sin(\theta_{ij})$, $\delta$ is the Dirac CP violation phase and $\eta_1, \eta_2$ are the Majorana CP violation phases. The PMNS matrix allow computing the transition probability from a flavor $\alpha$ to $\beta$ as $P_{\alpha\beta} = |\langle\nu_\beta|\nu_\alpha(t)\rangle|^2 = \left|\sum_{i=i}^{3}\sum_{j=1}^{3} U^*_{\alpha i}U_{\beta j}\langle\nu_j|\nu_i(t)\rangle\right|^2$, that for the specific case of reactor antineutrinos ($\overline{\nu}_e$) experiments it gives the following survival probability:

$$\begin{aligned} P_{\overline{\nu}_e\overline{\nu}_e} = 1 &- \cos^4(\theta_{13})\sin^2(2\theta_{12})\sin^2\left(\frac{\Delta \mathrm{m}^2_{12}L}{4E}\right) \\ &- \cos^2(\theta_{12})\sin^2(2\theta_{13})\sin^2\left(\frac{\Delta \mathrm{m}^2_{31}L}{4E}\right) \\ &- \sin^2(\theta_{12})\sin^2(2\theta_{13})\sin^2\left(\frac{\Delta \mathrm{m}^2_{32}L}{4E}\right) \end{aligned} \tag{1.5}$$

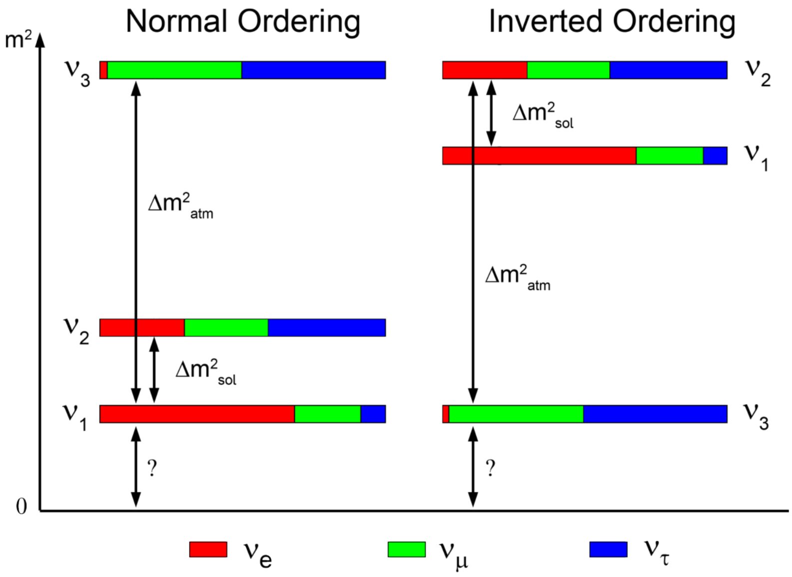

Figure 1.1: The two neutrino mass ordering possibilities: normal and inverted

This probability depends on the neutrino energy, E, on the source-detector distance, L, on the elements of the U matrix, $\theta_{ij}$, and on $\Delta m^2_{ij} = (m^2_i - m^2_j)$. In the case of three neutrinos mixing there are three $\Delta m^2$ but only two are independent, say $\Delta m^2_{21}$ and $\Delta m^2_{31}$. Since the numbering of the neutrino mass states is arbitrary it is possible to identify $\Delta m^2_{21}$ with the smaller of the two differences and to impose $m_1 < m_2$ so that $\Delta m^2_{21} > 0$. With this convention, there are two possibilities for the third neutrino: $m_1 < m_2 < m_3$ or $m_3 < m_1 < m_2$. These two possibilities are called Normal and Inverted mass Ordering (NO and IO). The Figure 1.1 shows a graphical representation of these two possibilities, showing also the different flavor composition of the mass eigenstates. The two independent squared-mass differences are often called "Solar" ($\Delta m^2_\odot = \Delta m^2_{21}$) and "Atmospheric" ($\Delta m^2_{atm} = \Delta m^2_{31}(NO)/\Delta m^2_{32}$ (IO)) because the values of these quantities were initially measured by studying the oscillation of that particular type of neutrinos. The equation 1.5 on the previous page can be rewritten in a way that clearly shows the dependence on the two independent squared-mass differences (solar and atmospheric) and on the mass ordering:

$$
\begin{aligned}
P_{\overline{\nu}_e\overline{\nu}_e} = 1 &- \frac{1}{2}\sin^2 2\theta_{13}\left(1-\cos\frac{\Delta \mathrm{m}^2_{atm}L}{2E}\right) \\
&-2\cos^4\theta_{13}X^2\left(1-X^2\right)\left(1-\cos\frac{\Delta \mathrm{m}^2_{\odot}L}{2E}\right) \\
&-\frac{1}{2}\sin^2 2\theta_{13}X^2\left(\cos\left(\frac{\Delta \mathrm{m}^2_{atm}L}{E}-\frac{\Delta \mathrm{m}^2_{\odot}L}{E}\right)-\cos\frac{\Delta \mathrm{m}^2_{atm}L}{E}\right)
\end{aligned}
\tag{1.6}
$$

where $\Delta m^2_\odot = \Delta m^2_{21}$, $\Delta m^2_{atm} = \Delta m^2_{31}$ and $X = \sin^2\theta_{12}$ in the NO case and $\Delta m^2_{atm} = -\Delta m^2_{32}$ and $X = \cos^2\theta_{12}$ in the IO case. The survival probability in equation 1.6 depends on the $X^2$ coefficient whose value is about a factor 2.3 larger for NO with respect to IO case, based on the best fit value for $\theta_{12}$. Since this is a quite large difference it can be used to discriminate between the two mass ordering by analyzing the distortion in the oscillated $\overline{\nu}_e$ spectrum. Although the relatively large value of $\theta_{23}$ provided the opportunity to solve the mass ordering with different neutrino oscillation experiments, with the medium baseline

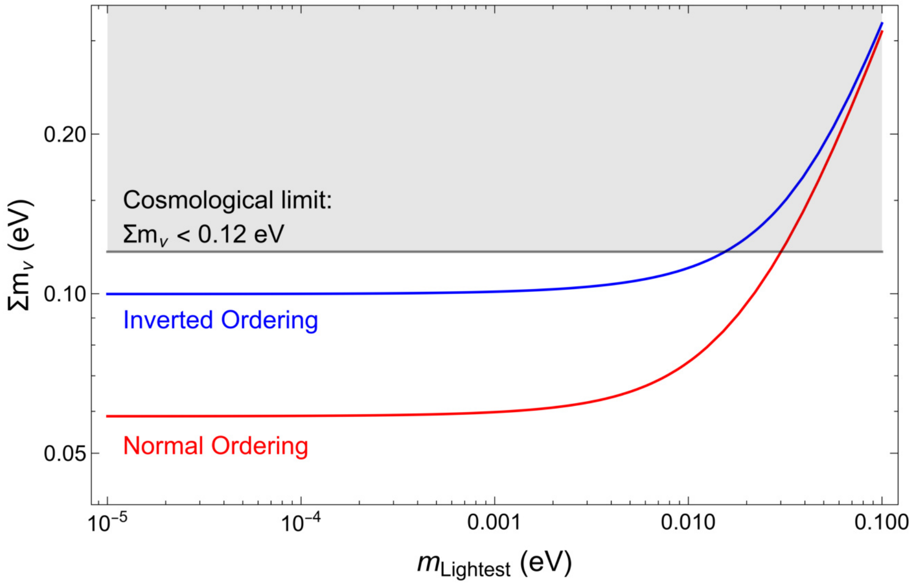

Figure 1.2: The sum of the neutrinos masses as a function of the mass of the lightest neutrino, $m_1$ or $m_3$ for the normal and inverted ordering, in red and blue respectively. The gray line represents the cosmological limit of the neutrino masses sum [10].

reactor antineutrino experiments it is not necessary to include the matter effect in the neutrino propagation.

### 1.1.4 Neutrino mass and its implications

Neutrino oscillation experiments have so far only been sensitive to the squared mass differences between neutrino masses, which are known with quite high accuracy. Given the two mass splittings it is possible to guarantee that two neutrinos have a mass larger than $\sqrt{\Delta m^2_{21}} \simeq 8\,\text{meV}$ and at least one of these two has a mass larger than $\sqrt{\Delta m^2_{31}} \simeq 50\,\text{meV}$. This estimation can be simply obtained by assuming that the mass of one neutrino is zero because in this case, the $\Delta m^2$ became $m^2$ since one therm is zero. By using the same consideration it is also possible to impose lower limits on the sum of the neutrinos masses:

$$\text{NO:} \sum m_\nu = m_1 + \sqrt{m_1^2 + \Delta m^2_{21}} + \sqrt{m_1^2 + \Delta m^2_{31}} \gtrsim 0.06\,\text{eV} \tag{1.7}$$

$$\text{IO:} \sum m_\nu = m_3 + \sqrt{m_3^2 + \Delta m^2_{31}} + \sqrt{m_3^2 + \Delta m^2_{31} + \Delta m^2_{21}} \gtrsim 0.1\,\text{eV} \tag{1.8}$$

Upper limits on the neutrinos masses sum can be instead provided by cosmological observations. The Cosmic Microwave Background (CMB) data of the WMAP and PLANCK satellites, combined with supernovae and other cosmological and astrophysical data can be used to obtain an upper limit on the sum of neutrinos masses. Assuming the existence of three light massive neutrinos and the validity of the ΛCDM cosmological model, the Plank Collaboration reported the updated upper limit on the sum of the neutrino masses: $\sum m_\nu < 0.12\,\text{eV}$ at 95% of CL [10].

The sum of the three neutrinos' masses as a function of the mass of the lightest one ($m_1$ or $m_3$) is shown in Figure 1.2 together with the current cosmological upper limit.

Once the neutrinos masses are discovered to be non-zero, a correct theoretical framework must be provided. The are two problems associated with the neutrinos masses: the first is to overcome the contradiction between left-handedness and non-zero mass, while the second is to understand why the neutrino masses are so small compared with the other particles in the SM. In fact, the lightest particle in SM is the electron which is at least 500 000 times more massive than neutrinos.

The first possible approach to extending the SM is to consider the neutrino as Dirac particle. In this case, the neutrinos get their mass from the Higgs mechanism and the resulting value is given by $m_\nu = \lambda_\nu v$, where $\lambda_\nu$ is the Yukawa coupling of $\nu$ to the Higgs field and $v$ is the vacuum expectation value for the Higgs field. Based on the current limit on neutrino masses ($m_e < 0.1\,\mathrm{eV}$) the coupling should be in the order of $10^{-12}$. This model requires to introduce a sterile right-handed neutrino and left-handed antineutrino that interact only via gravitational force. The biggest problem of this model is that it implies that the coupling constant $\lambda_\nu$ must be unreasonably small compared with respect to one of the other fermions and an unnatural by-hand introduction of another data-driven parameter and non-interacting particles.

The second approach is to consider the neutrino as a Majorana particle. One advantage of this approach is that it no longer requires including non-interacting right-handed neutrinos. In this model, the fundamental distinction between matter and antimatter must be given up because it assumes that neutrinos and antineutrinos are the same particle and what we call neutrino and antineutrino are instead only the left- and right-handed version of the same particle. In this case, a non-renormalizable therm is added to SM lagrangian that couples the leptonic doublet to the Higgs field: $\frac{(LH)^2}{2\Lambda_L}$, where L is the lepton doublet and $\Lambda_L$ is a new energy scale that automatically suppresses the effect of Higgs coupling. This operator gives a Majorana neutrino mass $m_\nu L \sim \frac{v^2}{\Lambda_L}$ for the LH neutrino and $m_\nu R \sim \Lambda_L$ for the RH neutrino. This results in a mass of $0.1\,\mathrm{eV}$ and $10^{15}\,\mathrm{GeV}$ respectively for the LH and RH neutrinos for $\Lambda_L \sim 10^{15}\mathrm{GeV}$ (see-saw model). In this case, neutrinos masses might be the first manifestation of a new length scale $\Lambda_L$ in nature [11]. Alongside this simple model, more complex and exotic mass theories and solutions have been developed.

A consequence of the Majorana model for the neutrino mass is the possibility to realize the so-called $0\nu\beta\beta$ decay, a double beta decay without the emission of neutrinos. This is possible only if the neutrino and antineutrino are the same particle and an experimental signal of the existence of this process would constitute evidence of the Majorana neutrino character. The non-observation of the process provides bounds on the so-called effective Majorana mass $m_{\beta\beta}$, which is a combination of the (Majorana) neutrino masses weighted by the leptonic flavor mixing: $m_{\beta\beta} = \sum_{j=1,2,3} |U_{ej}|^2 m_j e^{i\eta_j}$. In Figure 1.3 is shown the credible interval for the $m_{\beta\beta}$ as a function of the lightest neutrino mass [12]. From this plot, it is clear that $0\nu\beta\beta$ decay can discriminate between normal and inverted ordering only if the lightest neutrino mass is lower than about 40 meV. In this case, an experiment that can test the $m_{\beta\beta}$ region below 10 meV would be able to rule out the inverted scenario, while a positive detection of the $0\nu\beta\beta$ decay above the 10 meV region is not sufficient to determine the mass ordering without independent information on the mass of the lightest neutrino.

For these reasons the different experiments in neutrino physics, such as oscillation, $0\nu\beta\beta$, cosmological, and also the not discussed beta decay measurements, provide complementary information about neutrinos properties that can impose important constraints. In particular, the determination of mass ordering imposes a strong constraint on the sensitivity required by the next generation $0\nu\beta\beta$ experiments and also on the absolute scale of neutrino masses based on the cosmological and beta decay measurements and it is a crucial factor for the determination of the CP violation phase. From the theoretical point of view, mass ordering is one of the most important indicators for flavor models and mass origin.

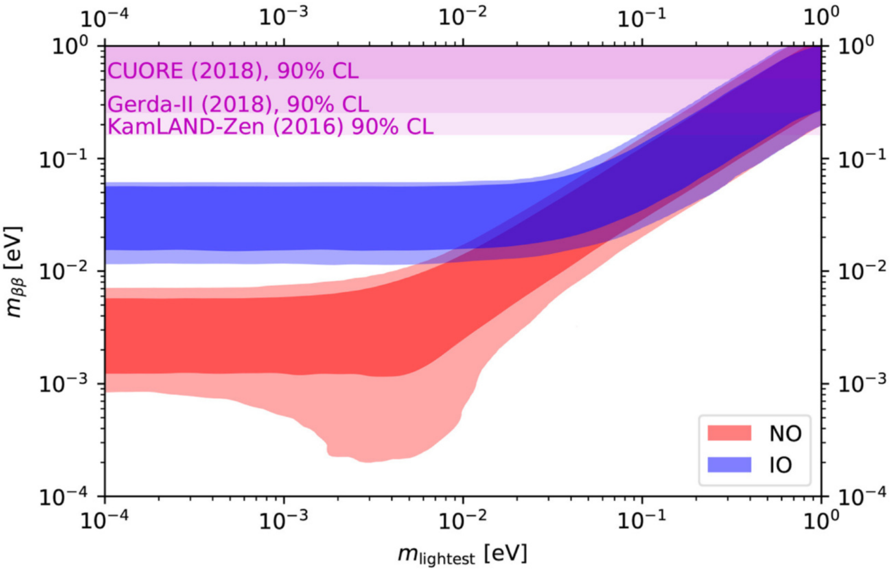

Figure 1.3: Bayesian credible intervals for the effective Majorana mass, $m_{\beta\beta}$, as a function of the lightest neutrino mass [12].

| Experiment | Dominant | Important |
|---|---|---|
| Solar | $\theta_{12}$ | $\Delta m^2_{12}$ , $\theta_{13}$ |
| Reactor LBL | $\Delta m^2_{12}$ | $\theta_{12}$ , $\theta_{13}$ |
| Reactor MBL | $\theta_{13}$ , $\Delta m^2_{atm}$ | |
| Atmospheric | | $\theta_{23}$ , $\Delta m^2_{atm}$ , $\theta_{13}$ , $\delta_{CP}$ |
| Accelerator $\nu_\mu, \overline{\nu}_\mu$ Disappearance | $\Delta m^2_{atm}$ , $\theta_{23}$ | |
| Accelerator $\nu_e, \overline{\nu}_e$ Appearance | $\delta_{CP}$ | $\theta_{13}$ , $\theta_{23}$ |

Table 1.1: Sensitivity of different experiment types on oscillation parameters.

### 1.1.5 Actual knowledge and missing information

The current knowledge about neutrino physics, in particular all the parameters associated with oscillations, has been obtained by numerous neutrino experiments that measured solar, atmospheric, accelerator, and reactor neutrinos or antineutrinos. All the experimental results are fully described assuming the existence of three different mass eigenstates that follow the normal or inverted mass ordering.

In Table 1.1 are summarized the different experiment types which dominantly contribute to the actual knowledge of the different oscillation parameters, and in Table 1.2 are reported the best-fit values from the global analysis of current experimental data from the nu-fit group [13].

Although the data provided by the oscillation experiments allowed the mixing parameters to be determined with more or less precision, there are some important missing information about them and in general in neutrino physics that are going to be studied by future experiments.

- The values of $\theta_{13}, \theta_{23}$, and $\delta_{CP}$ must be determined with higher precision, but they are sensitive to the mass ordering, so firstly it is crucial the determine the correct one.
- The value of $\delta_{CP}$ should be determined with higher precision in order to confirm the

|  | Normal ordering |  | Inverted ordering |  |
|---|---|---|---|---|
|  | bfp $\sim 1\sigma$ | $3\sigma$ range | bfp $\sim 1\sigma$ | $3\sigma$ range |
| $\sin^2\theta_{12}$ | $0.304^{+0.012}_{-0.012}$ | $0.269 \to 0.343$ | $0.304^{+0.013}_{-0.012}$ | $0.269 \to 0.343$ |
| $\theta_{12}(^\circ)$ | $33.45^{+0.77}_{-0.75}$ | $31.27 \to 35.87$ | $33.45^{+0.78}_{-0.75}$ | $31.27 \to 35.87$ |
| $\sin^2\theta_{23}$ | $0.450^{+0.019}_{-0.016}$ | $0.408 \to 0.603$ | $0.570^{+0.016}_{-0.022}$ | $0.410 \to 0.613$ |
| $\theta_{23}(^\circ)$ | $42.1^{+1.1}_{-0.9}$ | $39.7 \to 50.9$ | $49.0^{+0.9}_{-1.3}$ | $39.8 \to 51.6$ |
| $\sin^2\theta_{13}$ | $0.02246^{+0.00062}_{-0.00062}$ | $0.02060 \to 0.02435$ | $0.02241^{+0.00074}_{-0.00062}$ | $0.02055 \to 0.02457$ |
| $\theta_{13}(^\circ)$ | $8.62^{+0.12}_{-0.12}$ | $8.25 \to 8.98$ | $8.61^{+0.14}_{-0.12}$ | $8.24 \to 9.02$ |
| $\delta_{CP}$ | $230^{+36}_{-25}$ | $144 \to 350$ | $278^{+22}_{-30}$ | $194 \to 345$ |
| $\frac{\Delta m^2_{21}}{10^{-5}}(eV^2)$ | $7.42^{+0.21}_{-0.20}$ | $6.82 \to 8.04$ | $7.42^{+0.21}_{-0.20}$ | $6.82 \to 8.04$ |
| $\frac{\Delta m^2_{3l}}{10^{-3}}(eV^2)$ | $2.510^{+0.027}_{-0.027}$ | $2.430 \to 2.593$ | $-2.490^{+0.026}_{-0.028}$ | $-2.574 \to -2.410$ |

Table 1.2: Current best estimation for the values of the mixing parameters (best fit and $3\sigma$ range) obtained assuming normal and inverted mass ordering and using also the result obtained by Super-Kamiokande experiments.[13]

hint of $\delta_{CP} \neq 0$ with a high confidence level since it implies leptonic CP violation. This can be done only by appearance experiments because the value of $\delta$ affects only the appearance probability.

- The $\theta_{23} = 45^\circ$ cannot be excluded at $2\sigma$ level, thus is important to determine its value with higher precision in order to determine the strength of the $\mu - \tau$ symmetry breaking in the mixing matrix.

- Nature of neutrino: whether or not $\nu$ and $\overline{\nu}$ are the same particle (Dirac or Majorana particle) but, at the moment, only the neutrino-less double-beta ($0\nu\beta\beta$) decays experiments are able to probe the neutrino nature.

- Mass ordering: normal or inverted, as discussed in the previous section.

- Absolute neutrino mass scale. The oscillations of neutrinos allow measuring only the mass-squared differences, but the absolute mass scale is an important information that must be probed with other experiments such as ($0\nu\beta\beta$) decays and direct measurement from beta decay or cosmological measurements.

- Octant of $\theta_{23}$. Since the value of $\theta_{13}$ was already determined, the structure of the MNSP $U$ matrix can be fixed by the octant of $\theta_{23}$ and the value of $\delta$, which are both unknown. The current experimental data support an approximate symmetry for $\mu - \tau$ permutation. Since $\theta_{23} = 45^\circ$ is favored in many neutrino mass models as a consequence of the $\mu - \tau$ or other flavor symmetries, deviation from this value is a useful model discriminator.

- Existence of extra light or heavy sterile neutrinos. A fundamental question in neutrino physics is whether there exist extra species of neutrinos that do not participate in the standard weak interactions (sterile). Although there are no experimental proofs about the existence of these neutrinos, it is theoretically motivated and experimentally implied. The heavy sterile neutrino does not participate in flavor oscillations but may violate the unitary of the MNSP matrix, while the light sterile neutrino can contribute with extra oscillation terms to the oscillation probabilities. The unitary test of the MNSP matrix is an important probe in order to study these effects.

Figure 1.4: Location of the experimental site of JUNO and TAO.

## 1.2 The JUNO experiment

The Jiangmen Underground Neutrino Observatory (JUNO) [14] is a massive multipurpose underground neutrino observatory proposed in 2008 and currently under construction in the south of China. Its main physics goal is the determination of the neutrino mass ordering by measuring the spectrum of the oscillated antineutrinos originating from the Yangjiang and Taishan nuclear power plants located at a baseline of about 53 km, which was optimized for the best sensitivity to neutrino mass ordering measurement. As mentioned before, the knowledge of the reactor neutrinos spectrum shape is very important for the JUNO experiment, thus a dedicated small detector, TAO, is placed at about 30 m from one of the Taishan reactors to precisely measure it to constrain the spectra of the other cores. Figure 1.4 shows the location of the experimental site of JUNO and TAO. Thanks to its excellent expected performances JUNO has a rich scientific program that covers many crucial open issues of neutrino and astro-particle physics.

### 1.2.1 Physics goals of JUNO

As introduced before, the main physics goal of JUNO is the determination of neutrino mass ordering by measuring the energy spectrum of reactors antineutrinos. This has a deep impact on our understanding of neutrino physics, neutrino astronomy, and neutrino cosmology. Although the mass ordering can be determined also with long-baseline accelerator or atmospheric neutrino experiments, the JUNO sensitivity is based only on the vacuum oscillation effect, while the other experiments rely on the dependence of the matter effect, and it is not related to the CP-violating phase and the $\theta_{23}$ octant.

In order to extract the mass ordering information from the spectral distortions, an excellent energy resolution of $(3\%/\sqrt{E})$, a good understanding of the energy response (better than 1%), and a large statistics of signal events O(100k) are required.

The large detector volume of about 20 000 t of liquid scintillator (LS) and the unprecedented energy resolution, makes JUNO the largest LS-based, underground neutrino observatory capable of addressing many important topics in different field of neutrino physics. Therefore, besides the determination of the neutrino mass ordering, JUNO will also allow various aspects of neutrino oscillations to be studied, including high precision measurement of the mixing parameters $\theta_{12}, \Delta m^2_{21}, \Delta m^2_{32}$ at 0.5% level.

The extensive physics program of JUNO comprises solar neutrinos, atmospheric neutrinos, supernova neutrinos, and geo-neutrinos, as well as beyond Standard Model physics topics.

#### 1.2.1.1 Solar neutrinos

Solar neutrinos offer the possibility to investigate many aspects of neutrino physics, such as the consistency of the standard three neutrino framework, the existence of sterile neutrinos, and new physics beyond the Standard Model, but also to contribute to solar physics, especially the question of solar metallicity. The JUNO experiment has many advantages in performing solar neutrino measurements compared with previous detectors. It has the benefit of the high resolution and low energy threshold of the LS detector, like Borexino and KamLAND, but with a large mass that allows having large statistics comparable to Super-Kamiokande. The primary detection channel for solar neutrino in JUNO is electron elastic scattering. Since it is a single-event signal, the intrinsic, reactor, and cosmogenic backgrounds can have a deep impact on the sensitivity of solar neutrino measurements. For this reason, the background level must be kept extremely low. The background will be discussed in the dedicated section.

#### 1.2.1.2 Atmospheric neutrinos

Atmospheric neutrinos are a very important source to study neutrino oscillations. Since the Earth is almost transparent to neutrinos, a detector is able to observe neutrinos coming from all directions. The matter effect, acting on neutrinos passing through the Earth, plays a key role in determining the neutrino mass ordering. The JUNO mass ordering sensitivity from atmospheric neutrinos is complementary to that from reactor antineutrinos thus the combined sensitivity will exceed the purely statistical combination of the single sensitivities. Furthermore, atmospheric neutrinos allow JUNO to study the CP-violating phase, since the appearance probability ($P(\nu_e \to \nu_\mu)$) depends on the $\delta$ phase, and the $\theta_{23}$ octant. Finally, the atmospheric neutrinos studies with JUNO can also probe new physics beyond the standard model, such as the non-standard neutrino interactions and sterile neutrinos.

#### 1.2.1.3 Supernova neutrino

The detection of a neutrino burst from the next supernova event is a primary target of low-energy neutrinos physics and astrophysics because they are crucial players during all stages of stellar collapse and explosion. Very massive stars ($M > 8M_{.}$) can undergo core collapse when nuclear fusion reactions become unable to sustain the core against its gravity, which is the cause of all types of supernovae (except Ia). The collapse may cause violent expulsion of the outer layers of the star resulting in a supernova. About 99% of the energy liberated in the core collapse is emitted in the form of neutrinos. Every second a few core-collapse events happen in the visible universe, but JUNO (and similar experiments) cover only our galaxy and its satellites. The first and only observed SN neutrino signal was produced by the SN1987A in the Large Magellanic Cloud (LMC) at a distance of 50 kpc and was detected by the Kamiokande experiment with two dozen events [15]. The expected number of events in JUNO is about 200 events for a SN in the LMC and about 5000 events considering a SN at the average possible distances of 10 kpc. For comparison, only one event is expected for a SN in the Andromeda galaxy, our nearest-neighbor big galaxy at 750 kpc. The observation of these neutrino bursts allows a deeper understating of the explosion mechanism to be obtained and the intrinsic properties of the neutrinos themselves to be probed, for example constraining the absolute scale of neutrinos masses. JUNO is also expected to play a central role in the next generation of multi-messenger astronomy. Finally, JUNO will be able to detect some events from the diffuse SN neutrino background, a low energy neutrinos flux produced by all past stellar core-collapse SN, improving the understanding of the average SN neutrinos signal and the underlying cosmology.

#### 1.2.1.4 Geoneutrinos

The surface heat flow of the Earth was established as (46±3) TW but the fraction that comes from primordial versus radioactive sources is not established yet. Over the last decade, the $\overline{\nu}_e$ flux produced by naturally occurring radioactive beta decay inside the Earth was detected. Since the matter is mostly transparent to neutrinos, by studying the geoneutrinos flux it is possible to study the amount of radiogenic power produced in the depths of the Earth and have information about the relative abundance of uranium, thorium ad potassium, the naturally occurring radioactive nuclides. This information is also important for understanding the formation and evolution of the Earth. Within the first year of running, JUNO is expected to detect more geoneutrinos events than all other detectors will have accumulated to that time, about 400 events per year [16, 17]. The 500 km range of the crust around JUNO contributes more than 50% to the total signal. Thus, local refined geological models are needed for a precise estimation of the crustal signal to disentangle the mantle one, because the latter is related to radiogenic heating. The main challenge for the JUNO geoneutrinos measurement is the large reactor antineutrinos background because the geoneutrinos are detected using the same reaction (IBD).

### 1.2.2 Detector structure

The JUNO detector consists of a Central Detector (CD), a water Cherenkov detector (WCD), in which the CD is submerged, and a muon tracker placed on top of them, as shown in Figure 1.5 on the next page. The 20 000 t of liquid scintillator are contained in a spherical acrylic vessel with an inner diameter of 35.4 m and a thickness of 12 cm. The acrylic vessel is supported by a spherical stainless steel (SS) structure with an inner diameter of 40.1 m, sitting on 30 pairs of stainless steel (SS) legs safely rooted to the concrete floor. The anchoring of the acrylic vessel to the SS truss is ensured by 590 stainless steel rods (SS bars), which end at the vessel side with hinged connections within acrylic nodes to ensure the required stress relief. The scintillation light emitted by the LS is read by 17612 20-inch photomultiplier tubes (LPMTs, for large PMTs) and 25600 3-inch photomultiplier tubes (SPMTs, for small PMTs), which are installed on the inner side of the SS truss. All LPMTs feature a special protection in case of implosion: 10 mm thick acrylic semi-sphere on the front, supported by a 2 mm thick stainless steel semi-sphere on the back.

The entire CD is submerged in a cylindrical water pool with a diameter of 43.5 m and a height of 44 m, providing sufficient water thickness in all directions (at least 3.9 m) to shield the detector from the radioactivity of the surrounding rock. The 2.3 m thick water shell between the SS structure and the acrylic sphere shields the LS from the radioactivity of the PMTs with a 1.4 m distance between the acrylic vessel and the front face of the PMT glass bulb. The water pool is equipped with about 2400 LPMTs to act as a WCD to veto cosmic muons. The CD and the WCD are optically separated with Tyvek. The WCD LPMTs are installed on the outside of the SS truss. Tyvek reflective foils provide a coating for the pool walls and the SS structure to increase light collection efficiency. Finally, on the top of the water pool, a top tracker (TT) is installed to precisely measure the muon directions and support the veto strategies.

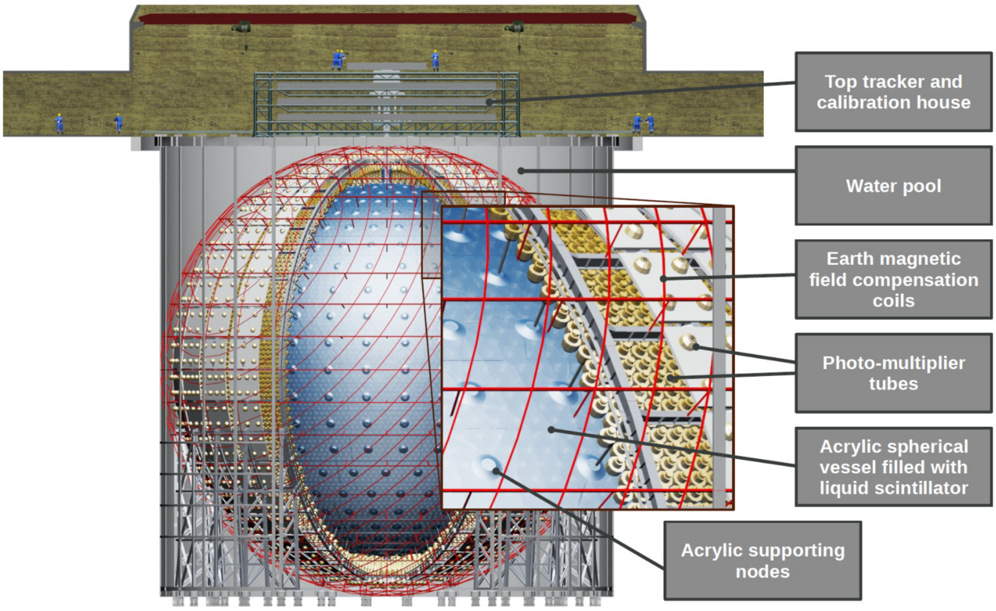

Figure 1.5: Schematic representation of the JUNO detector and its main components

In the next sections, a more detailed description of the main components will be provided.

#### 1.2.2.1 CD structure and liquid scintillator

The Central Detector is one of the most challenging parts of JUNO, especially for mechanics and radiopurity. The acrylic vessel is made by bulk polymerization of 265 pieces of spherical acrylic panels. The composition of the acrylic is carefully tuned in order to maximize the transparency and improve the anti-aging and creep resistance and a dedicated acrylic panel production line is established also in order to reduce the radioactive background. The acrylic vessel is supported by connection structures linked to the stainless steel main structure with a total of 590 connecting bars. The SS main structure is composed of 30 longitudinal H-beams and 23 latitudinal H-beams supported by 30 pairs of supporting legs and 60 base plates, rooted on the concrete floor of the water pool.

The liquid scintillator of JUNO has a similar recipe as the Daya Bay LS but without Gadolinium loading [18, 19]. It consists of linear alkylbenzene (LAB), a straight alkyl chain of 10-13 carbon atoms attached to a benzene ring, used as detection medium due to excellent transparency, high flash point, low chemical reactivity, and good light yield. The JUNO LS contain also 2.5 g/L of PPO (2,5-dyphenyloxazole) as fluor and 3 mg/L of bis-MSB (1,4-bis(2-methylstyryl) benzene) as a wavelength shifter. The density is 0.86 g/cm$^3$ at room temperature. The LS scintillator is subjected to multiple steps of purification in order to improve the radiopurity and transparency which are critical aspects for such a big detector. The radiopurity requirement on U/Th of the LS is $1{\cdot}10^{-15}$ g/g for the reactor neutrinos studies and $1{\cdot}10^{-17}$ g/g for the solar neutrinos studies. Since it is difficult to quantitatively demonstrate that the LS could be purified to such a low level without the data of the JUNO detector itself, the minimum requirement is determined to be $1{\cdot}10^{-15}$ g/g upon filling. The LS will be further purified online, with the water extraction and gas stripping systems, to reach the goal of $1{\cdot}10^{-17}$ g/g. The purification system is composed of four steps [20]: alumina column treatment, distillation, water extraction, and stripping. The first step is

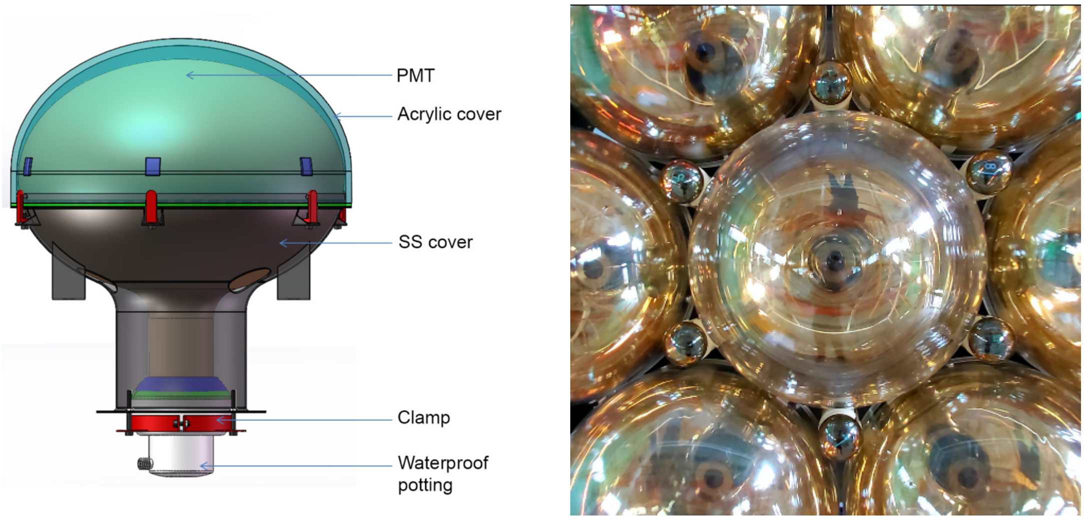

(a) Schematic drawing of the LPMTs with the acrylic and stainless steel covers

(b) Photograph of the LPMTs and SPMTs in the pattern used to cover the CD sphere

Figure 1.6: Large and small PMTs of the JUNO detector

the alumina column purification used to improve the transparency of LAB. This is followed by distillation in partial vacuum (5 mbar) to remove the heaviest radio-impurities ($^{238}$U, $^{232}$Th, and $^{40}$K) and to further improve the optical properties in terms of absorbance and attenuation length. At this point, the PPO and bis-MSB are dissolved into the LAB. The complete LS mixture is then subjected to water extraction to further remove $^{238}$U and $^{232}$Th, potentially introduced by PPO and bis-MSB. The final step is the stripping, whose main purpose is the removal of radioactive gases and gaseous impurities from the liquid scintillator, using gaseous steam of nitrogen and/or superheated steam in counter-current flow mode, all performed in partial vacuum at about 250 mbar.

#### 1.2.2.2 PMTs

In order to determine the neutrino mass ordering, JUNO requires an excellent energy resolution of $3\%/\sqrt{E}$. From the PMTs point of view, this requires a large photodetection area coverage, high photon detection efficiency, low dark noise, and stable operation of the whole PMT system. As introduced in 1.2.2, the whole PMTs system is composed of 17612 LPMTs and 25600 SPMTs instrumented with high voltage dividers, waterproof sealings, and protection covers, and they are connected to dedicated electronics to process the signals. The structure of the LPMTs is shown in Figure 1.6a. The PMTs electronics is composed of two parts: the "wet" electronics is located a few meters from the PMTs inside the custom-made stainless steel underwater boxes (UWBs), while the "dry" electronics is placed in a dedicated room above the pool. Each UWB contains the customized high voltage (HV) module, front-end board, and readout card for 3 LPMTs or 128 SPMTs. The HV divider circuit to provide the working voltage to the PMTs is placed at the back of each phototube inside a customized experimental volume with waterproof potting. The cables connecting the PMTs to the UWBs and the UWBs to the "dry" electronics are kept inside waterproof SS bellows. In the space between the LPMTs will be installed the SPMTs (Figure 1.6b. The primary goal of these PMTs is to provide a complementary set of sensors looking at the same events in the LS. This allows providing them a calibration reference, reducing the impact of any systematic uncertainties in the energy response of the LPMTs

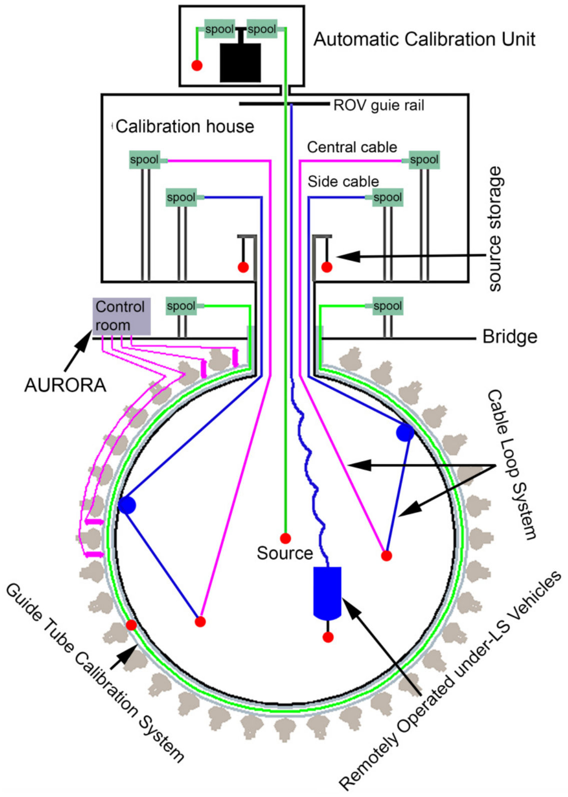

Figure 1.7: Overview of the calibration system

and improving the energy resolution, but also to perform some physics measurements in a semi-independent way, allowing independently cross-checking of the systematic uncertainties to be performed. Furthermore, they allow extending the dynamic range of the detector and mitigating the saturation effect of the LPMTs at high energy.

#### 1.2.2.3 Water pool and Cherenkov detector

The JUNO detector is installed in a cylindrical water pool with a diameter of 43.5 m and a height of 44 m, filled with 35 kt of ultrapure water. To prevent $^{232}$Rn diffusion from the external rocks from dissolving into the water, 5 mm thick HDPE panels (liner) are sealing the pool walls and are sustained by a concrete barrier with a minimum thickness of 70 cm placed in front of the cavity rock. The Cherenkov light produced by muons passing through the volume is detected by about 2400 LPMTs installed on the outer surface of the SS structure of the CD.

In order to guarantee stable performances of the WCD, a water system will provide and monitor the ultra-high purity of the water and ensure temperature uniformity over the whole volume. The temperature of the water must be stabilized at (21±1)° to maintain the mechanical stability of the detector and the water circulation is necessary to remove the heat from the electronics of PMTs.

#### 1.2.2.4 Calibration system

The neutrino mass ordering requires stringent detector response knowledge and in particular, the non-linearity must be below 1%. To reach this goal multiple calibrations sources and multiple dimensional scan systems are developed to correct the energy non-linearity and spatial non-uniformity of the detector response. The calibration system consists of 4 main different bus-system, which are shown in Figure 1.7 on the facing page. For a one-dimensional scan, the Automatic Calibration Unit (ACU) can deploy multiple radioactive sources or a pulsed laser diffuser ball along the central axis of the CD. Off-axis calibration, necessary for studying the non-uniformity response, is performed by the two Cable Loop Systems (CLS), each consisting in a radioactive source that can be moved on a vertical half-plane by adjusting the lengths of two connection cables. The Guide Tube (GT) surrounds the outside of the CD running in a longitudinal loop containing a movable radioactive source that allows the calibration of the non-uniformity at the CD boundary. For a full-volume scan, a source attached to a Remotely Operated under-LS vehicle (ROV) can be used to study specific locations inside the CD.

Other auxiliary systems allow monitoring the detector to determine the position of the calibration sources and to measure the optical properties of the LS. These systems are the Ultrasonic Sensor System (USS), used to reconstruct the source positions, and the AURORA laser device used to measure the attenuation length and Rayleigh scattering length of the LS.

### 1.2.3 Antineutrino signals and radioactive background

The main goal of JUNO will be reached by measuring the energy spectrum of antineutrinos produced in nuclear power plants. These neutrinos are produced in electron flavor as a consequence of the $\beta^-$ decay of the fission products. In pressurized water reactors (PWR) the fuel is enriched Uranium so more than 99.7 % of the thermal power and antineutrinos are generated by the fission of four isotopes: $^{235}$U, $^{238}$U, $^{239}$Pu, and $^{241}$Pu. On average, every fission reaction is followed by six $\beta$-decays that emit six electron-type antineutrinos. The thermal power output of a typical nuclear power reactor is in the order of some GW. Considering that every fission release is about 200 MeV, the antineutrino emission rate is about $2{\cdot}10^{20}$ per second, emitted isotropically. The total flux is given by the sum of the contributions of the four fissioning isotopes. To estimate the total flux, which is a crucial parameter for neutrinos oscillation experiments, a direct calculation based on the beta spectra of all the isotopes involved in fission reactions could be done, but the final result is affected by an uncertainty of about 10 %. More accurate evaluations are obtained by inverting the measured beta spectra of the thermal fissile isotopes $^{235}$U, $^{239}$Pu, and $^{241}$Pu and by theoretically computing the contribution of the fast neutron fissile isotope $^{238}$U.

Electron antineutrinos are detected via the inverse beta decay (IBD) reaction:

$$\overline{\nu}_e + p \rightarrow e^+ + n \tag{1.9}$$

where the antineutrino interacts with a proton creating a positron and a neutron. Since this reaction has a threshold of 1.8 MeV, only the flux above this energy can be detected. The different component of the neutrino flux and their typical measured spectrum is shown in Figure 1.8 on the next page. In this plot is also shown the total cross-section of the antineutrino via IDB reaction.

Since the energy of reactor neutrinos is lower than 10 MeV, the $\overline{\nu}_e$ disappearance is the only oscillation channel that can be studied using reactors and liquid scintillator detectors, like JUNO.

In the inverse beta decay reaction (eq. 1.9), when the neutrino interacts with a proton of the LS creating a positron and a neutron, the positron quickly deposits its kinetic energy and annihilates intro two 511 keV $\gamma$-rays, which provides a prompt signal. The neutron scatters in the LS until being thermalized and then it is captured by a proton about 200 µs

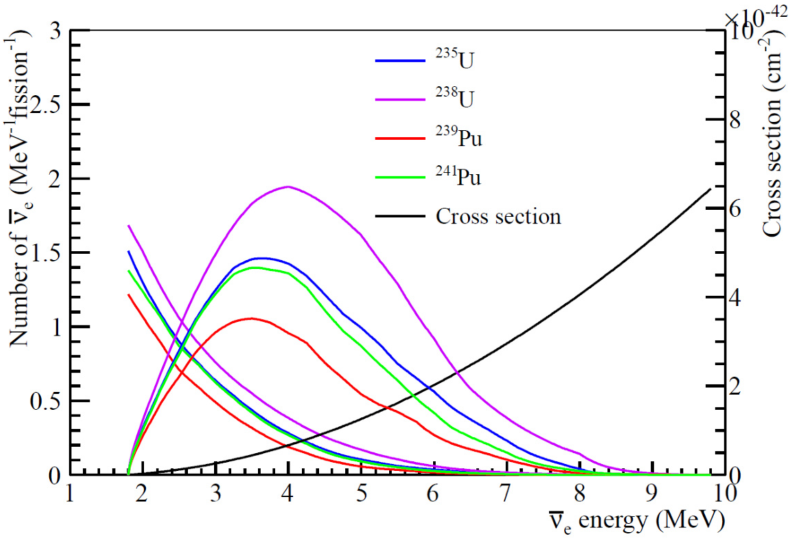

Figure 1.8: Observable $\overline{\nu}_e$ spectra given by the product of the reactor antineutrino fluxes and the cross-section of IDB (black line). The contributions of the four fission isotopes of a PWR reactor to the antineutrino flux are shown.

later and emits a 2.2 MeV $\gamma$-ray. This is the delayed signal. Since the positron carries almost all energy of the neutrino, the neutrino spectrum can be obtained from the prompt signal spectrum with a shift of about 0.8 MeV given by the following energy conservation balance (eq. 1.10):

$$\begin{aligned} E_{lost} &= m_n + m_{e^+} - m_p - m_{\overline{\nu}_e} - 2 \cdot E_\gamma \\ &= 939.565\,\text{MeV} + 0.511\,\text{MeV} - 938.272\,\text{MeV} - 2 \cdot 0.511\,\text{MeV} = 0.782\,\text{MeV} \end{aligned} \tag{1.10}$$

The expected $\overline{\nu}_e$ spectrum acquired by the JUNO experiment is shown in Figure 1.9 on the facing page. Here are visible the two modulations produced by the solar squared-mass difference, associated with the low-frequency modulation, and the atmospheric squared-mass difference, associated with the high-frequency modulation. In the spectrum are also highlighted the two different shapes expected in the case of normal and inverted mass ordering.

Taking into account the low cross-section of the IBD reaction, the expected signal rate is about 60 IBD events per day. Since the signal rate is very low, many background sources can interfere with the signal. The accidental, $^8$He/$^9$Li, fast neutron, and $(\alpha, n)$ backgrounds are the major sources for the reactor neutrino oscillation analysis. Fiducial volume cut can significantly reduce the accidental and the $(\alpha, n)$ background. The application of energy selection, time coincidence, and vertex correlation of the prompt and delayed signals allow further suppression of the accidental background. The cosmogenic background, such as $^8$He/$^9$Li and fast neutron, can be instead reduced with muon veto cuts.

The preliminary selection criteria for IBD events in the JUNO experiment are the following:

- Fiducial volume cut r $<$ 17.2 m;
- Prompt energy cut 0.7 MeV $< E_p <$ 12 MeV;
- Delayed energy cut 1.9 MeV $< E_d <$ 2.5 MeV;
- Time interval between prompt and delayed signals $\Delta t_{p-d} < 1\,\text{ms}$;

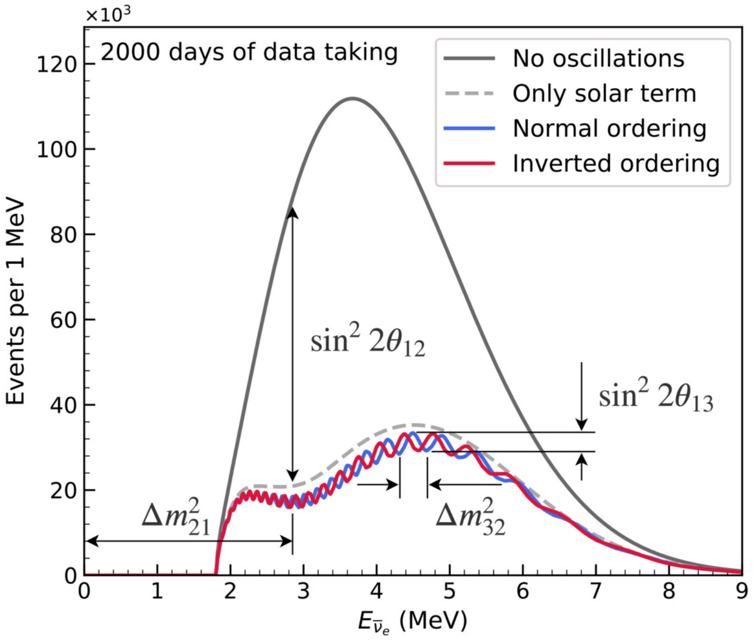

Figure 1.9: Expected $\overline{\nu}_e$ spectrum acquired by the JUNO experiment

- Prompt-delayed distance cut $R_{p-d} < 1.5\,\mathrm{m}$;
- Muon veto criteria:
  - For muons tagged by Water Pool, veto the whole LS volume for 1.5 ms
  - For well-tracked muons in the central detector and water Cerenkov detector, veto the detector volume within Rd2mu $< 3\,\mathrm{m}$ and Td2mu $< 1.2\,\mathrm{s}$
  - For the tagged, non-trackable muons in the central detector, veto the whole LS volume for 1.2 s

The events produced by natural radioactivity that satisfy these criteria cannot be distinguished from a true IBD event. Therefore it is mandatory to keep the radioactive background at extremely low levels with a careful design of the detector structure and an accurate material selection.

In other physics channels, such as the measurement of solar neutrinos, it is not possible to apply these selection criteria because the electron neutrinos interact with the electrons of the LS via elastic scattering and therefore only a fraction of their initial energy is transferred to the electrons and the resulting spectrum is continuous. For these studies, the demand for a low background level is even more stringent. In the next chapter, the background control strategy adopted for the JUNO experiment will be discussed.

## Chapter 2

# JUNO background control strategy

In this chapter, I'll give a brief introduction to the components of the radioactive background, and then I'll discuss the strategy applied to the JUNO experiment in order to keep under control its radioactive background. In particular, I'm going to focus on the work I have done in the validation of the Monte Carlo simulations of the different background components of the JUNO detector and the estimation of the expected background events rate based on the detector geometry and radionuclides concentration measured in each material.

## 2.1 Components of radioactive background

All the radioactive nuclides can be classified based on their origin. They can be naturally occurring or artificially produced. Regarding the first type, considering the age of the earth, which is $4.5 \cdot 10^9$ years, a naturally occurring radioactive nuclide must meet one of the three following conditions:

- The nuclide is a very long-lived one, with a half-life at least in the same order of magnitude as the age of the earth.
- The nuclide is a short-lived one but it is a daughter of a long-lived radionuclide.
- The nuclide is a short-lived one but is continuously produced on earth or its atmosphere by natural phenomena.

Every naturally occurring radionuclide can be classified into one of these three categories, which will be briefly discussed in the following sections together with the artificially produced radionuclides before introducing the problem of background reduction and material selection of rare physics experiments and in particular for JUNO.

### 2.1.1 Long-lived radionuclides and their chains

The most diffuse component of the natural radioactive background is associated with the long-lived nuclides and their chains, called fossil nuclides. Based on the age of the earth we can expect that all nuclides with a half-life lower than about $10^8$ year and produced during the formation of the solar system and that are not a daughter of other long-lived nuclides, would have decayed to an undetectable level. Among these nuclides, the most relevant for the radioactive background are $^{40}$K, $^{238}$U, $^{235}$U and $^{232}$Th. The first one is a very common nuclide with an isotopic abundance of 0.0117% and a half-life of $1.26 \cdot 10^9$ years which decays on stable nuclides. It decays by $\beta$ emission to $^{40}$Ca with a branching ratio of 89.3% or by EC with K-shell capture to an excited state of $^{40}$Ar with a branching ratio of 10.7% followed by a deexcitation with the emission of a 1460 keV gamma ray. The last three nuclides are instead the parents of three decay chains.

| Name | Type | Parent nuclide | Stable nuclide | $T_{1/2}(years)$ |
|---|---|---|---|---|
| Thorium | 4n | $^{232}$Th | $^{208}$Pb | $1.41 \cdot 10^{10}$ |
| Neptunium | 4n+1 | $^{237}$Np | $^{209}$Bi | $2.14 \cdot 10^{6}$ |
| Uranium | 4n+2 | $^{238}$U | $^{206}$Pb | $4.47 \cdot 10^{9}$ |
| Actinium | 4n+3 | $^{235}$U | $^{207}$Pb | $7.04 \cdot 10^{8}$ |

Table 2.1: Characteristics of the four independent decay chains. Only the first three exists nowadays.

The principal decay modes of a radionuclide are alpha, beta, and gamma decay. The alpha decay involves the emission of a monochromatic alpha particle, consisting of two neutrons and two protons, and so results in a mass reduction of the daughter nuclide of 4. On the contrary, the mass number does not changes in beta decays and gamma transitions because beta decays involve the transformation of a neutron into a proton or vice versa and for this reason, the total mass number is conserved, while the gamma transition involves only the emission of photons as a consequence of the deexcitation of excited states of the nucleus. As a consequence of the properties of the decay, the mass number for all radionuclides in a given decay chain can differ only for a multiple of 4 and, for this reason, only 4 independent decay chains can exist in nature. Three of them have as parent nuclide the $^{238}$U (4n+2), the $^{235}$U (4n+3), and the $^{232}$Th (4n), while the fourth (4n+1) is extinguished because the most long-lived nuclide of the chain ($^{237}$Np) has a half-life much lower than the age of the earth. In Table 2.1 are reported the four independent decay chains.

The three decay chains' parents nuclides decay on isotopes with a much shorter half-life, ranging from 300 ns up to $2.46 \cdot 10^{5}$ years, so they have survived since the formation of the earth due to a continuous production by the decay of the parent one. In absence of mechanical or chemical/physical effects that remove the nuclides from the matrix where they are produced, the secular equilibrium is established, that is a steady state condition of equal activities between a long-lived parent radionuclide and its short-lived daughters. The Figures 2.1, 2.2 and 2.3 shows respectively the radioactive chain of $^{238}U$, $^{235}U$ and $^{232}Th$.

The uranium series is characterized by a sequence of decays that stops on $^{206}$Pb. In the first part of the chain, from $^{238}$U to $^{230}$Th, the chemical properties of the daughter nuclides are quite similar to uranium and for this reason, the secular equilibrium can be easily reached because it is difficult that a process breaks it, although the half-life of these nuclides can be quite long, up to $2.46 \cdot 10^{5}$ y. In the second part of the chain, from $^{226}$Ra to $^{214}$Po, are present only very short-life nuclides but the presence of $^{226}$Ra and $^{222}$Rn makes this sub-chain easily to be found out of equilibrium with the progenitor $^{238}$U. Radium is an alkaline earth metal and, for this reason, is quite soluble in water and can be easily removed from the original matrix. The $^{222}$Rn is instead a noble gas with a quite long half-life (3.8 d) and can diffuse in materials and escape from the original matrix into the atmosphere or dissolve in water. Finally, the final part of the chain starts from $^{210}$Pb, which having a quite long half-life (22 y) can easily establish its sub-chain and is characterized by two daughters that decay via high energy beta and alpha decays. As a consequence of its long life, the $^{210}$Pb can accumulate from the decay of $^{222}$Rn and the rapid decays of its daughters, for example in the atmosphere particulate before it precipitates to earth's surface with the rain.

The $^{232}$Th and $^{235}$U chains have different characteristics from those of the $^{238}$U. The main reason is the very different half-life of the daughter because both $^{232}$Th and $^{235}$U

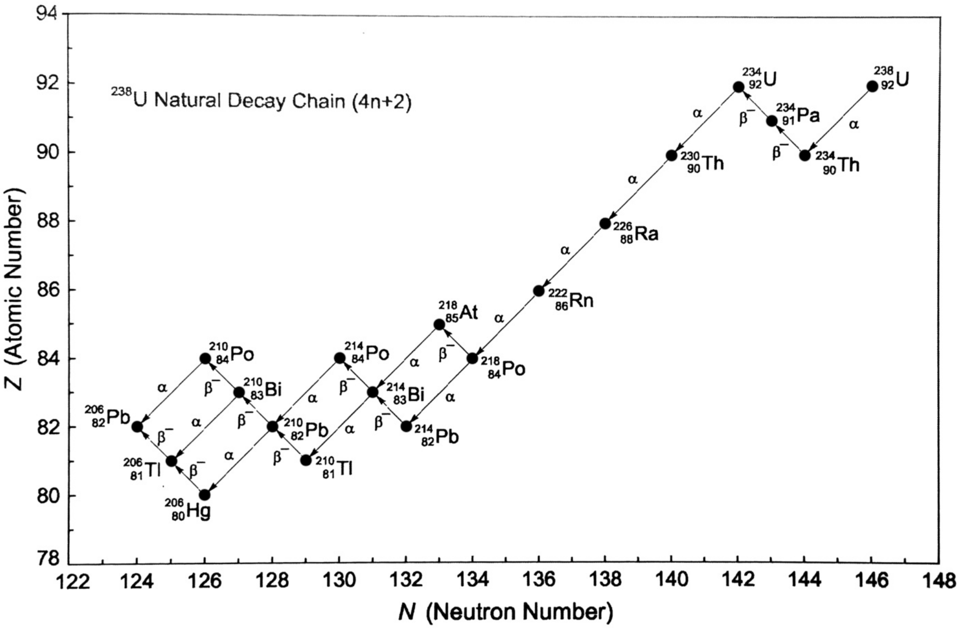

Figure 2.1: Decay chain of $^{238}$U

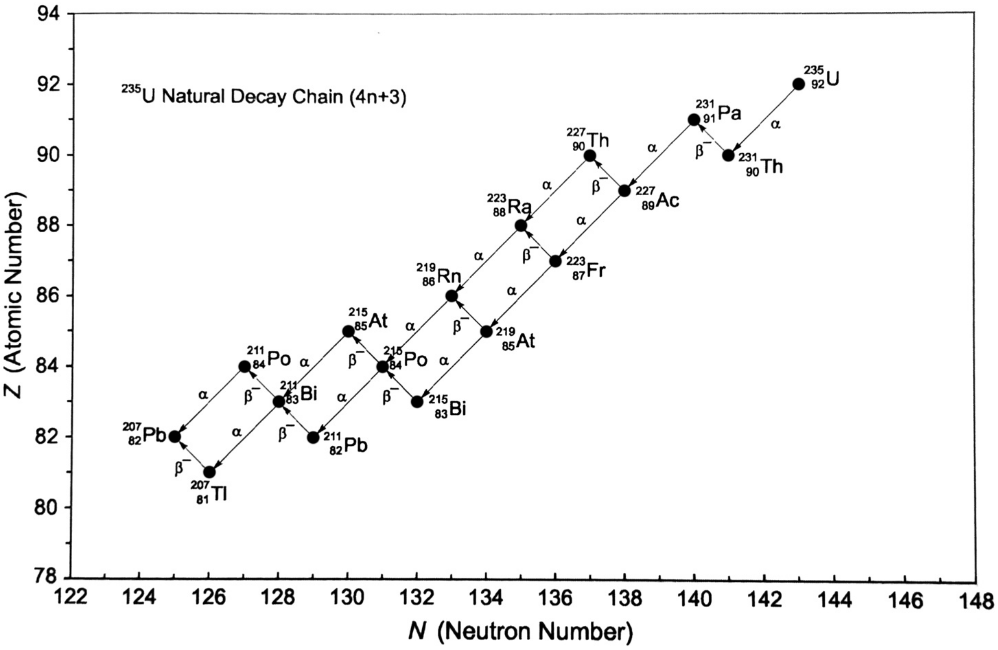

Figure 2.2: Decay chain of $^{235}$U

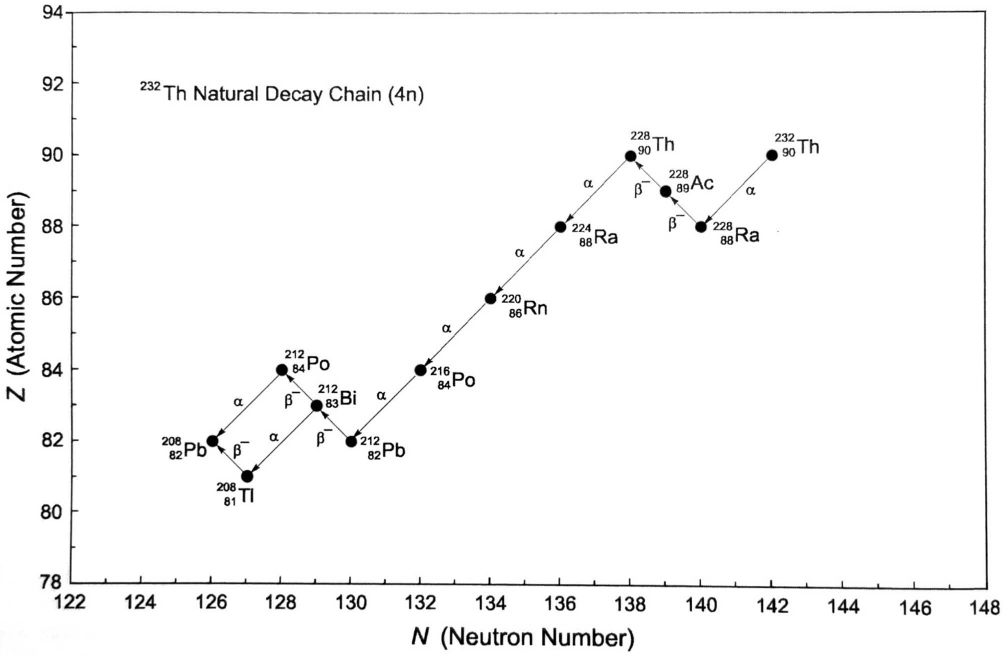

Figure 2.3: Decay chain of $^{232}$Th

chain nuclides have a very short half-life that makes the equilibrium hard to break. In particular the $^{232}$Th pass through the $^{220}$Rn that has chemical properties similar to $^{222}$Rn but having a half-life of only 56 s it has less opportunities to diffuse from the matrix in which it is created.

The fossil nuclides are present in the environment and all materials with different levels of concentration. As a consequence, a radioactive background produced by these nuclides is always present in every detector, but their contribution can be reduced, for example, by selecting or purifying the materials.

### 2.1.2 Cosmic muons and cosmogenic radionuclides

Another naturally occurring radioactive background source consists of cosmic particles and cosmogenic radionuclides. Charged particles originating from space that strike the top of the atmosphere form what is known as cosmic radiation. This radiation is classified into primary or secondary. The former are charged particles and nuclides accelerated by astrophysical sources, while the latter are particles produced in the interactions of the primaries with atmospheric gas. Free protons account for about 80% of the primary nucleons and alpha particles for 15%. Electrons and positrons contribute at a level of 2% and the remaining part is composed of heavier nuclides. The energy distribution of the cosmic radiation is shown in Figure 2.4a on the next page.

When the particles of cosmic radiation collide with atoms of the air on the top of the atmosphere, they produce a cascade of secondary subatomic particles and electromagnetic radiation, called showers of cosmic radiation. The shower can be split into two components: hadronic and electromagnetic. The hadronic component is mainly composed of mesons (kaons and pions), nucleons of various masses, and neutrons. The electromagnetic part is composed of the decay product of mesons, thus muons, neutrinos, electrons, positrons, and gamma photons. A schematic representation of the production of the cosmic radiation

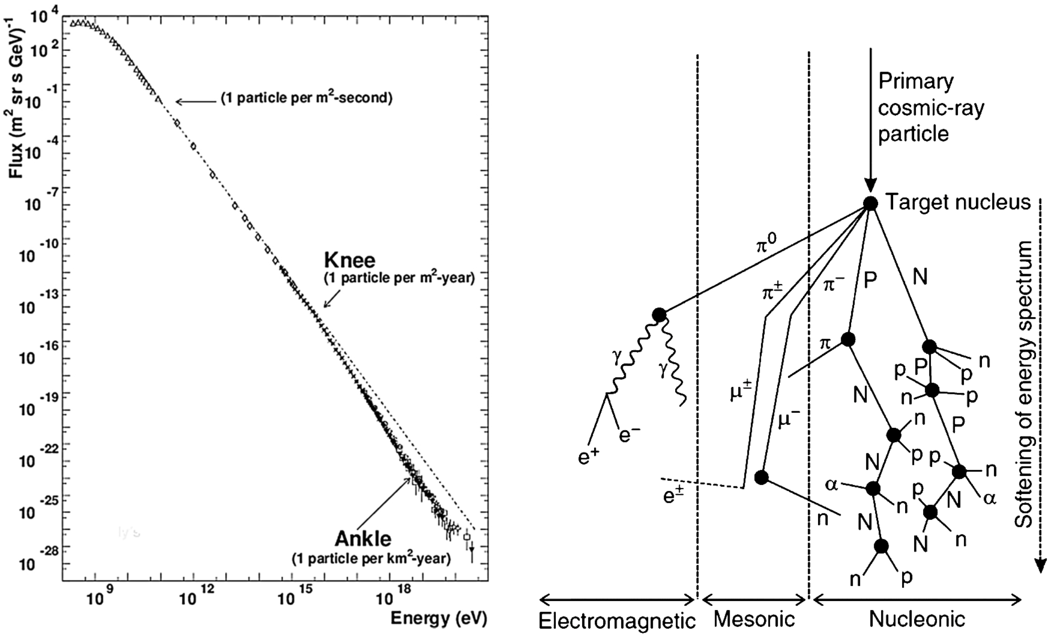

(a) Cosmic rays spectrum at sea level with energy greater than 100 MeV

(b) Graphical representation of the secondary cosmic rays shower produced by the interaction of one primary cosmic ay in the atmosphere [21] (Compilation by S. P. Swordy)

Figure 2.4: Energetic spectrum and shower representation of cosmic rays [22]

shower is shown in Figure 2.4b. The muons produced in the showers are relativistic and since they have a half-life of $2.2 \cdot 10^{-6}$ s, they can reach the earth's surface and penetrate the crust up to several kilometers depending on the initial kinetic energy. The muons are almost the only particles produced in the showers that can reach the earth's surface, while the others are mainly stopped by the atmosphere.

This muon flux contributes to the environmental background because the muons can themselves release energy by ionization, generating signals in detectors, emitting Cerenkov light during the passage through matter, and interacting with stable nuclei releasing neutrons that can activate other stable nuclides. When the primary and secondary cosmic rays interact with nuclei in the earth's atmosphere several radionuclides are produced. These isotopes are called cosmogenic isotopes and are continuously produced, thus it is possible to have nuclide with any half-life. The cosmogenic isotopes with the highest production rate are $^{14}$C, $^{3}$H, $^{3}$He, $^{7}$Be, $^{10}$Be and $^{36}$Cl, but the most important for the JUNO experiment are the $^{9}$Li and $^{8}$He that are produced in the interaction of muons and can mimic the IBD signal.

### 2.1.3 Artificially produced radionuclides

The last source of radioactive nuclides is those produced artificially. There are over 1300 of these nuclides, produced by nuclear reactions in accelerators, nuclear reactors, or nuclear weapons. Many of them have important applications in medicine, industry, and scientific research, but over time some of these nuclides have been spread into the environment and now we can find them for example in the soil, like $^{137}$Cs, or in the steel, like $^{60}$Co.

## 2.2 Background sources of the JUNO experiment

Not all the sources described in the previous section can be relevant for a given experiment or detector and the importance of each component depends on the characteristics of the signal to study and the structure of the detector itself. In the case of the JUNO experiment, the impact of a background source depends on the specific measurement performed because based on that, different selection criteria are applied and as a consequence, different background sources can be involved.

The main analysis channel is the IBD signal produced by reactor antineutrino, which will be used for the mass ordering determination. In this case, the selection criteria are very strong because it involves a coincidence between a prompt and a delayed signal with specific energy and timing properties, so this allows obtaining a strong reduction of the background associated with random events. For this analysis channel the most important residual background sources are the accidental coincidences between radioactivity events, the cosmogenic nuclides $^{9}$Li and $^{8}$He, the cosmogenic fast neutrons and the $(\alpha, n)$ reaction on $^{13}$C. Their expected distributions are showed in Figure 2.5 on the next page.

The accidental background is caused by the random coincidence of events within the time window of IBD signals that also respect the energy and distance cuts. The rate of these events can be computed as the product of the rates of the prompt-like and delayed-like events ($R_p$ and $R_d$), multiplied by the time coincidence window ($\Delta t$): $R_{acc} = R_p \cdot R_d \cdot \Delta t$. The sources of prompt- and delayed-like signals can be the radioactivity for both types, but also the cosmogenic isotopes and cosmogenic neutrons. Based on the production rate the last two contributions are negligible with respect to the radioactivity-radioactivity coincidence rate, which is estimated in 0.9 events per day.

The background produced by the decay of the cosmogenic nuclides $^{9}$Li and $^{8}$He represent one of the most significant components because their decay mode can mimic the IBD reaction, having a high probability to decay $\beta - n$. The production of these nuclides is due to the interaction of muons in the detector with a strong dependence on the muon energy. These events cannot be discriminated by using the signal produced in the detector, but by having a strong space and time correlation with the incident muon, their contribution can be reduced by exploiting the muon tracking system to veto the region of the detector associated with the transit of the muon. Based on the estimated production rate and muon veto efficiency, the expected rate is 0.8 events per day.

Another cosmogenic background is the production of fast neutrons as a consequence of the passage of muons in the surrounding material of the experiment, mainly the rock around the water pool. In this case, the muon veto system cannot track the muons and the emitted neutron can scatter and reach the LS where is captured. Their expected rate is 0.1 events per day.

Finally, the last source of background is the reaction $^{13}\mathrm{C}(\alpha, n)^{16}\mathrm{O}$ induced by the alpha particles emitted in the radioactive decays of the uranium and thorium and their daughters present in the liquid scintillator. Thanks to the high purity requirements of the LS, the expected rate of these background events is 0.05 events per day.

For other analysis channels of the JUNO experiment, the impact of the radioactivity background can be much more significant and one of the most important cases is the measurement of the solar neutrinos. As discussed before, the solar neutrinos will be detected by JUNO by using elastic scattering on electrons. In contrast to the IBD reaction, the detection of solar neutrinos appears as a single flash of light with a continuum energy spectrum for both continuum and monochromatic neutrinos sources because only a fraction of the neutrino energy is transferred to the electron. As a consequence, these events are not

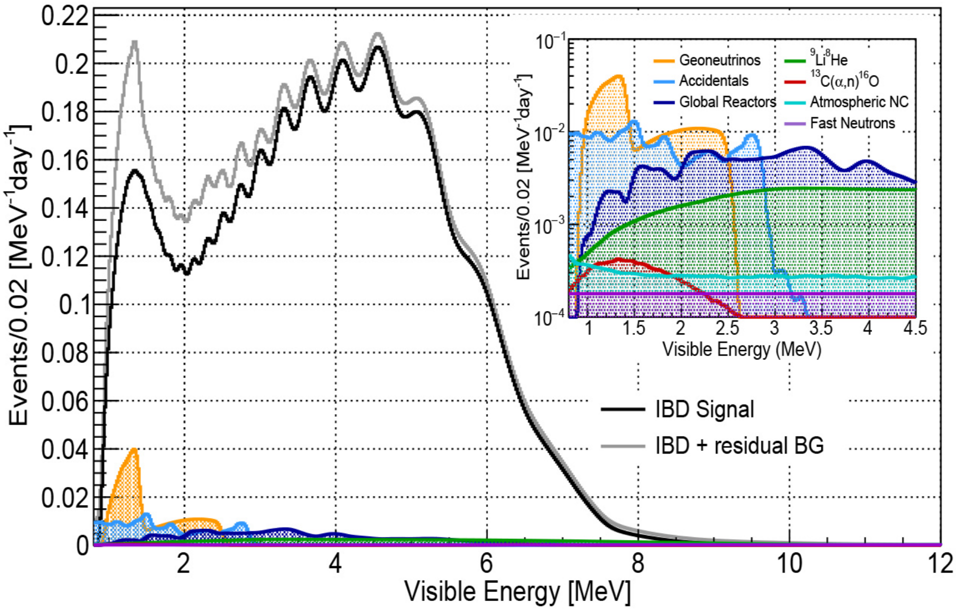

Figure 2.5: Expected energy spectrum of the reactor antineutrinos IBD events with the corresponding background spectra.

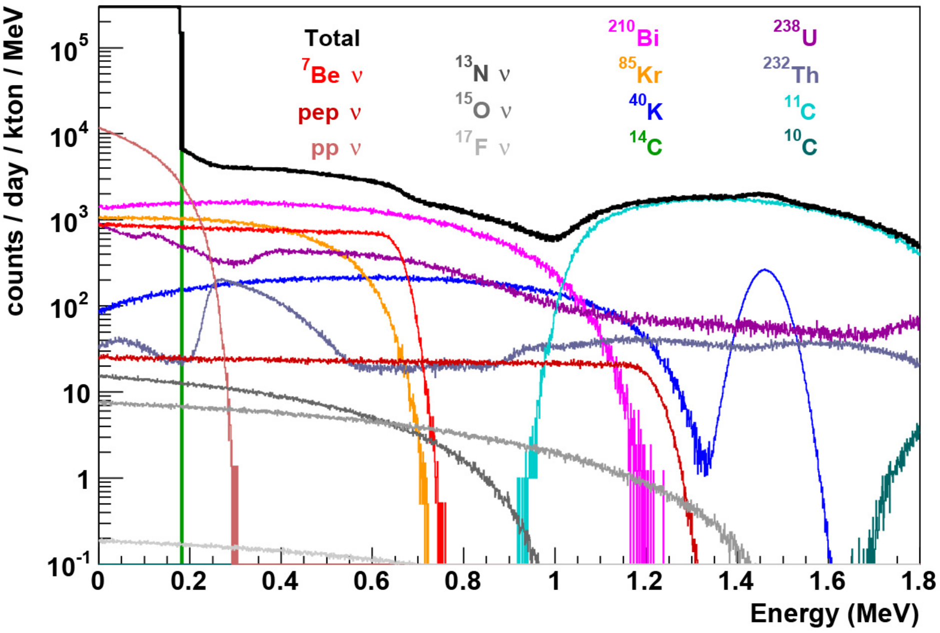

Figure 2.6: Expected spectrum of solar neutrinos and backgrounds signals with the radiopurity requirements reported in Table 2.2

distinguishable from the beta or gamma interaction events. For this reason, the intrinsic background of the detector is a primary requirement to allow this measurement to be performed with high sensitivity. The fiducial volume cut is a powerful tool to suppress the external sources of background by exploiting the auto-shielding at the expense of the sensitive volume, therefore the internal radioactivity in the LS is expected to be the dominant source of background events. As can be seen in Figure 2.6 on the preceding page, all the naturally occurring radionuclides contribute to the background for solar neutrinos, because their $\beta^-$ and $\gamma$ decays produce signals that overlap the regions of interest. Among all, one of the most important background sources is the $^{210}$Bi, whose beta decay has an energy similar to those of $^{7}$Be solar neutrinos. $^{210}$Bi is produced in the decay of $^{210}$Pb in the third $^{238}$U sub-chain. As introduced in the previous section, the $^{222}$Rn is a radioactive noble gas that can easily diffuse from the production matrix to air or water. In order to limit the diffusion of the radon contained in the rock at the JUNO's site, the entire water pool is coated with a polyethylene film, but a low quantity of radon can be dissolved in the water and in the LS itself due to contact with air. The background is not caused by the radon itself, because having a half-life of 3.8 d it decays completely in a couple of weeks if it is not restored, but its daughter $^{210}$Pb have a half-life of 22 years and then accumulates in the material, giving rise to its sub-chain. For this reason, a specific requirement of the $^{210}$Pb concentration is imposed for the JUNO liquid scintillator.

## 2.3 Radio-purity requirements and material selection for JUNO

### 2.3.1 Radioactive contaminants and radio-purity requirements

As introduced in 1.2.3 the radioactive background can have a deep impact on the sensitivity of the JUNO experiment. Due to the small cross-section of antineutrinos, the expected rate of IDB signals will be only 60 events per day, so it is mandatory to maintain the background at extremely low levels. The accidental background, produced by random coincidence between decays from natural radioactivity, can be kept under control with a strict reduction strategy during the detector design and construction. Natural radioactivity is present in all materials (see section 2.1.1) and can only be reduced by selecting the material with the highest radiopurity, purifying the materials that do not satisfy the requirements, and with accurate environmental control. These three approaches were applied to all materials used for the JUNO experiment.

The most critical contaminants are the following:

- Natural decay chains and long-lived nuclides: $^{238}$U, $^{235}$U, $^{232}$Th and $^{40}$K.
- Natural gaseous radionuclide: $^{222}$Rn
- Anthropocentric radionuclides: $^{60}$Co and $^{85}$Kr

All of these radionuclides can be present in the materials of the JUNO detector and may contribute to the rate of background events measured in the CD. The materials contaminations can be classified as *internal* or *external*. Internal are those contained in the liquid scintillator so that their contribution cannot be reduced by fiducial volume (FV) cut and all the radionuclides contribute to the deposited energy because it is released in the sensitive volume. On the other side, the external contamination contribution can be reduced with FV cuts because the external shell of LS can act as a shield for the inner region and only high energetic gamma rays can contribute to the background because low energy photons, alpha, and beta particles are stopped before reaching the LS. There are mainly four radionuclides that emit such high-energy gammas: $^{214}$Bi (from $^{238}$U chain), $^{208}$Tl (from $^{232}$Th chain), $^{40}$K and $^{60}$Co. All the others emit low-energy gammas that are almost completely absorbed before reaching the liquid scintillator.

Based on the auto-shielding and FV cuts consideration, the radiopurity requirements for the materials are less stringent as you move away from LS, from the acrylic sphere up to the water pool and the surrounding rock. In Table 2.2 on the next page are reported the minimal requirements for the radiopurity of the materials to be employed in the JUNO experimental setup. These values are expressed in Bq/kg or in mass concentration units (g/g, i.e. grams of contaminant per gram of material, and its sub-multiples ppm = $1{\cdot}10^{-6}$ g/g, ppb = $1{\cdot}10^{-9}$ g/g, and ppt = $1{\cdot}10^{-12}$ g/g).

Very often in low background experiments, the sensitivity needed to validate raw materials is at the limit of available screening techniques, and sometimes lower. This difficulty implies that the approval of certain materials or particular production and cleaning protocols requires itself to conceive non-trivial dedicated test facilities and develop new measurement techniques. JUNO surely benefits from the experience of past and running neutrino and dark matter experiments using the same type of detector to select the proper materials and related cleaning procedures to achieve its goals: the challenge comes from pushing of ultra-low background techniques to the largest experimental scale. In the next section, I'm going to briefly discuss the main techniques applied in material screening for the JUNO experiment, while in Chapter 4 I'm going to describe the dedicated experimental approach and measurement techniques we developed to validate the radiopurity of the liquid scintillator of JUNO.

### 2.3.2 Measurement techniques for materials screening

The most suitable techniques for measuring the radioactive contamination of materials depend on different factors, such as the lifetime of the radionuclides, the nature, and phase of the sample matrix, the distribution of the contamination (bulk or surface), etc. The most common techniques are gamma spectroscopy with High Purity Germanium Detectors (HPGe), Inductively Coupled Plasma Mass Spectrometry (ICP-MS), and, less common, Neutron Activation Analysis.

Gamma spectroscopy is the only technique suitable for short-lived nuclides that emit gamma rays in the decay sequence. This is a common technique for screening materials because it allows a multi-radionuclide analysis of a sample in one measurement, giving access to its bulk activity for natural radioactivity (U and Th chains and $^{40}$K), and for cosmogenic or artificial gamma emitters ($^{60}$Co, $^{137}$Cs, etc). The main advantage of this technique consists in measuring independently the activities of several radionuclides in the U/Th chains to check whether secular equilibrium is achieved. It is of great importance e.g. for the uranium chain since gamma spectroscopy can quantify $^{226}$Ra and $^{210}$Pb activities. Low background gamma spectroscopy with HPGe has typical sensitivities in the 10 ppt – 10 ppb range or more ($100\,\mu$Bq/kg – 100 mBq/kg). More technical detail about the HPGe detector and gamma ray spectroscopy will be provided in the dedicated section of Chapter 4.

The ICP-MS is most suitable for long-lived nuclides and it can be performed without any requirements on the nuclides decay type. It is widely used for screening materials of low background detectors due to its high sensitivity to trace $^{238}$U and $^{232}$Th. High sensitivity ICP-MS can reach detection limits lower than 0.01 ppt for pure water. Since this technique allows measuring only aqueous solutions of the materials, the material must be dissolved with a chemical treatment that should be critical for ultra-pure materials and does not apply to all materials, such as organic compounds. For example, for JUNO acrylic

| Material | Mass (t) | Radius (m) | $^{238}$U (ppb) | $^{232}$Th (ppb) | $^{40}$K (ppb) | $^{210}$Pb/$^{222}$Rn | $^{60}$Co (mBq/kg) |
|---|---|---|---|---|---|---|---|
| Liquid scintillator | | | | | | | |
| LS reactor | 2000 | 0-17.7 | $10^{-6}$ | $10^{-6}$ | $10^{-7}$ | $10^{-13}$ppb | |
| LS solar | | | $10^{-8}$ | $10^{-8}$ | $10^{-9}$ | $10^{-15}$ppb | |
| Acrylic vessel | 580 | 17.7-17.8 | 0.001 | 0.001 | 0.001 | | |
| Acrylic nodes | 28.5 | 17.8-17.9 | 0.001 | 0.001 | 0.001 | | |
| Calibration parts | 0.04 | | 1.5 | 4.5 | 0.02 | | |
| SS structure | | | | | | | |
| truss | 1000 | 20.0-20.05 | 1 | 3 | 0.2 | | 20 |
| bars | 65 | 17.9-20.0 | 0.2 | 0.6 | 0.02 | | 1.5 |
| LPMT glass | | | | | | | |
| NNTV | 84.5 | 19.2-19.8 | 200 | 120 | 4 | | |
| Hamamatsu | 33.5 | 19.2-19.8 | 400 | 400 | 40 | | |
| veto (NNTV) | 16.0 | 20.2-20.8 | 200 | 120 | 4 | | |
| LPMT cover | | | | | | | |
| acrylic | 110 | 19.2-19.4 | 0.003 | 0.01 | 0.01 | | |
| SS | 150 | 19.4-19.8 | 0.4 | 2.5 | 0.12 | | |
| LPMT readout | | | | | | | |
| divider | 0.6 | 19.8-19.9 | 3000 | 5000 | 100 | | |
| potting | 24.5 | 19.7-19.9 | 70 | 50 | 4 | | |
| UWB | 100 | 20.1-20.4 | 50 | 200 | 5 | | 20 |
| SPMT glass | 2.6 | 19.3-19.4 | 400 | 400 | 200 | | |
| SPMT readout | | | | | | | |
| divider | 0.15 | 19.4 | 3000 | 10000 | 200 | | |
| potting | 5.1 | 19.4-19.5 | 100 | 50 | 20 | | |
| UWB | 11 | 20.1-20.4 | 50 | 200 | 5 | | 20 |
| Water | 35000 | 17.8-21.8 | | | | 10 mBq/m$^3$ | |
| Rock | | | 10000 | 30000 | 5000 | | |

Table 2.2: Target values for the impurity concentrations in the different materials of the JUNO detector. For each detector component, the mass and its geometrical position, i.e. the radius quoted from the center of the LS volume, are reported [23].

screening, a vaporization setup for acrylic pretreatment is built in a Class 100 environment and with mature procedures for contamination control, the acrylic samples can be easily measured by ICP-MS to sub-ppt level in two days. Besides that, this technique will play an important role in the quality control of the cleaning procedures and the purified water [23]. Laser Ablation ICP-MS is a complementary technique to ICP-MS to measure U/Th contaminations. The chemical preparation of the sample is replaced by a UV femtosecond laser used in an ablation mode. This promising technique has preliminarily achieved a surface or bulk sensitivity better than $10^{-12}$ g/g level for U/Th in a few minutes with only a few tens of $\mu$g sample and is also well-suited to screen the surface treatment of the acrylic panels and other critical materials for JUNO [23].

NAA is a very sensitive method for the qualitative and quantitative determination of trace elements based on the measurement of characteristic radiation from activated radionuclides formed by neutron irradiation of the material. The principle is the following: the capture of a neutron by the nuclide under investigation produces a radioactive nuclide which is usually unstable and decays $\beta^-$ to excited states of the corresponding daughter nucleus, thus emitting characteristics $\gamma$-rays that can be measured by an HPGe spectrometer. NAA can achieve substantially greater sensitivity than direct gamma ray counting on long-lived nuclides: it can be applied to quantify the concentration of natural contaminants ($^{238}$U, $^{232}$Th, and $^{40}$K) in matrices that show no long-lived neutron activation products emitting lines which could interfere with the measurement. The Milano-Bicocca group has been applying the NAA technique on many materials for several years, using the TRIGA Mark II research reactor of the University of Pavia (Italy) as the neutron source and the various HPGe detectors at the Radioactivity Laboratory of Milano-Bicocca University. Typical sensitivities are at ppt and sub-ppt levels. For JUNO, NAA was used for the screening and quality control of acrylic, LAB, Teflon, and PPO. Also, this technique will be discussed in detail in the dedicated section of Chapter 4.

## 2.4 Monte Carlo codes for JUNO background

The Monte Carlo simulation software is a powerful tool that allows for investigating complex problems with a statistical approach instead of analytical calculation that are often impossible. For the JUNO background estimation, it is necessary to understand what is the contribution of a specific material and contaminant to determine a reasonable requirement on its radiopurity and eventually to understand how to modify the detector geometry if its contribution cannot be reduced. This is a very complex task that cannot be done analytically because there are many variables to take into account, in particular, the geometry and the material composition of the source and all the detector parts, which in such huge and complex detectors like JUNO are countless. The Monte Carlo software allows simulating the propagation of the particles emitted in the decay of radioactive nuclides into the whole geometry of the detector and, taking into account all the possible interaction processes, to simulate their effects.

One of the most powerful Monte Carlo tools that can be used to simulate the propagation of particles through matter is Geant4, developed by CERN [24] in C++ programming language. Geant4 is a simulation toolkit because it provides a very rich and complete set of classes that allow the user to write his application. The user must pay attention to accurately describe the geometry of the experimental setup and include the correct physics processes with the correct parameters. One might ask why it is necessary to include physics processes and parameters and the answer is that in a simulation there is a trade-off between the accuracy of the simulation and the adopted models and the speed. The user is free to decide how much detail to use in the physics modeling, weighing precision against the CPU time required by the simulation. In Geant4 this is done by choosing one of the available physics lists that are already implemented in the toolkit or building a new one, based on the simulation requirements. Since the native classes of the toolkit take care of propagating the particles through the geometry by selecting the correct process, another task that the user must perform is the implementation of the codes that generate the primary particles and that allows collecting all the required information during the propagation of the particles.

In the context of the work of the low background group of the JUNO collaboration, three different and independent codes, based on Geant4, have been used to cross-check the results and obtain some kind of validation while waiting for the experimental data. The three codes are described in the following sections and the comparison of the results is described in Section 2.7.2.

### 2.4.1 SNiPER simulation framework

The official simulation software of the JUNO experiment is developed using the SNiPER (Software for Non-collider Physics ExpeRiments) tool [25]. This simulation framework consists of different sub-module: physics generator, detector simulation, and electronics simulation modules.

The physics generator deals with generating the primary particles according to the correct physical processes while the detector simulation, which is based on Geant4, is responsible for the geometry description and the particle tracking. Physics generator interfaces, physics processes, and detector components are all configurable by using Python scripts. To be consistent and flexible, a detector element is proposed to represent one detector component, which is a high-level concept. For example, a central detector is a detector element, which contains only the LS, the container, and the buffer material and for example, PMTs are not placed in this detector element. Therefore different options for the central detector can be interchanged while keeping the arrangement of PMTs unchanged. Finally, the electronic simulation module converts the data generated by the detector simulation module into a digital waveform taking into account the trigger algorithm, the PMTs response, and the mixing of multiple events to reproduce a real-like event signal.

The sequence of the different operations can be synthesized as follow. The physics generator generates kinematic information of primary particles, which are saved into GenEvent objects. In the next step, the detector simulation algorithm accesses these GenEvent objects and starts tracking. Hits, which contain charge and time information, are generated in sensitive detectors and saved in SimEvent objects. After that, the electronics simulation algorithm reads these SimEvent objects and performs the digitization, which generates ElecEvent objects containing waveform information. These waveforms are processed by the PMT calibration algorithm and CalibEvent objects are saved. The event reconstruction algorithm performs the event reconstruction by reading CalibEvent objects and storing RecEvent objects. At last, the user can perform any physics analysis from RecEvent objects.

Details of the JUNO experimental setup as implemented in SNiPER are shown in Figure 2.7 on the facing page.

### 2.4.2 ARBY simulation code

ARBY is a general-purpose Monte Carlo simulation code — written by O. Cremonesi at INFN Milano-Bicocca — designed for low-energy particle physics applications. The ARBY software has been used for many years by the INFN Milano-Bicocca group for different

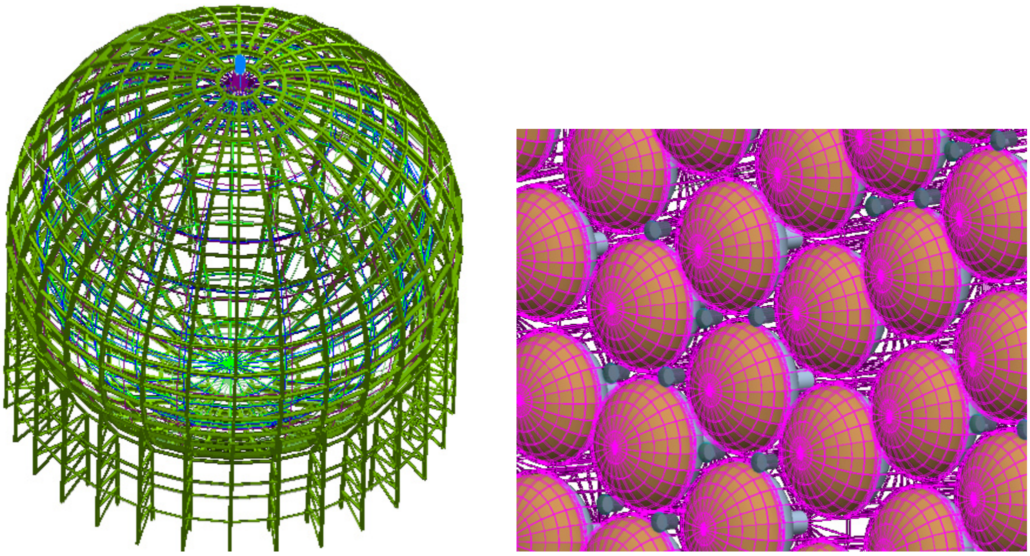

(a) Stainless steel truss

(b) Large and small PMTs

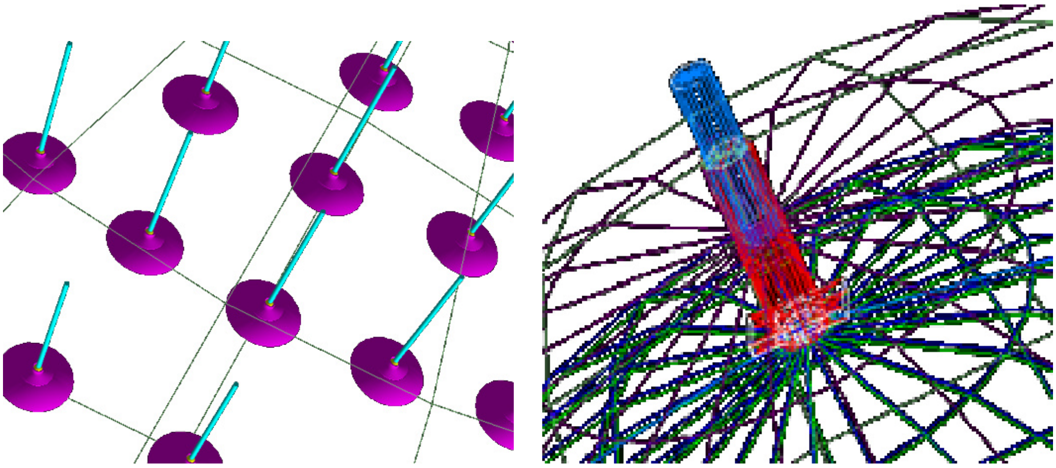

(c) Nodes and bars

(d) Chimney between the central detector and the calibration house

Figure 2.7: Some pictures of the JUNO geometry as implemented in SNiPER.

applications, like the efficiency evaluation in gamma spectroscopy with HPGE detectors and the development of accurate background models in rare-event experimental searches with bolometers [26, 27]. It is based on the Geant4 toolkit with a text-based interface for the description of the geometry. The Physics Lists used by ARBY can be chosen by the user to obtain better or fastest results. In particular, ARBY uses the G4RadioactiveDecay class of GEANT4 to manage the radioactive decays according to the ENSDF database [28]. When a daughter nucleus is itself unstable, like in the natural decay chains of $^{238}$U and $^{232}$Th, ARBY allows keeping track of the single steps in the chain — i.e. of each decay — while scoring the event information. In this way the peculiarities of subsequent decays, like time correlations, do not get lost and allow reconstructing particular effects which can manifest experimentally. Other information like the position of the event in the detector volume or the particle quenching in organic scintillators can be also saved for each event. The user needs just to describe the detector arrangement in the text-based configuration file, where details concerning the materials in use as well as the position of the radioactive sources are declared.

In the case of JUNO, a configuration file was built to reconstruct with ARBY the main detector components: the LS, the acrylic sphere, the SS truss, the large and small PMT systems together with their readout electronics, the calibration equipment, the water pool, and the veto system. The different contamination sources were then systematically positioned in each of these materials and the resulting experimental spectrum was evaluated with ARBY. Some details of the reconstructed geometries are shown in Figure 2.8 on page 39.

The work done with ARBY to implement the JUNO geometry, the performed tests and the comparison results will be discussed in the section 2.5.

### 2.4.3 G4-LA simulation code

The G4-LA simulation code has been developed at the Laboratoire de Physique des deux Infinis Bordeaux (LP2i Bordeaux) in France and it is based on the GEANT4 toolkit using the G4RadioactiveDecay class to generate the decays of all the radionuclides of interest. The relevant contaminants (mostly U and Th chains and $^{40}$K) are generated uniformly in the bulk materials. The subsequent particles are tracked and the deposited energy as well as the coordinates of the mean deposited energy in the LS are recorded, allowing energy and FV cuts. The quenching effect for alpha and electron particles has been taken into account as described in the paper. The detector geometry is simplified and includes the most critical materials of JUNO (LS, acrylic vessel, and inner water pool). This allows a precise crosscheck of the energy spectra and the derived singles rate for the LS and the acrylic vessel in order to validate the Monte Carlo electromagnetic simulation of SNiPER.

## 2.5 Monte Carlo results validation

In this section, firstly I'm going to discuss the work I've done with ARBY in order to implement the geometry of JUNO with a reasonable level of accuracy without affecting too much the speed of the simulations. Then, I'm going to describe the tests I've performed on different aspects of the simulation to understand their effect on the results and correct discrepancies or wrong behavior in our MC codes.

### 2.5.1 Implementation of the JUNO geometry in ARBY

The JUNO detector is a very complex system composed of many parts and materials and each of them can contribute to the background of the experiment. The materials and detector parts that have the most significant contribution can be classified into 13 components, based on the radiopurity requirements shown in Table 2.2, and each of these components have to be included in the simulation to study their contribution.

1. Liquid Scintillator
2. Acrylic
3. LPMT glass
4. LPMT acrylic cover
5. LPMT SS protection
6. LPMT potting
7. LPMT HV divider
8. SPMT glass
9. Truss
10. SS nodes and bars
11. Water shell
12. Rock
13. Calibration system

**Central detector** The liquid scintillator is modeled as a sphere of 34.5 m in diameter with a uniform composition of LAB, composed of hydrogen and carbon atoms in a 20:11 ratio and a density of $0.86\,\mathrm{g/cm^3}$. The acrylic vessel is a spherical shell with an inner diameter of 35.4 m and an outer of 35.64 m, composed of hydrogen, carbon, and oxygen in a 5:8:2 ratio and a density of $1.14\,\mathrm{g/cm^3}$.

**PMT** The large PMTs are modeled with more complex geometry to reproduce with higher accuracy the shape of the PMTs. Two pictures of the PMTs geometry are shown in Figure 2.8c on page 39 and 2.8d on page 39. The front bulb is a spherical shell made of glass (blue) covered with a semi-shell of acrylic (green) and stainless steel (gray) respectively on the front side and backside. The neck of the PMT is a cylinder of glass (white and yellow) with a cylindrical potting on the back (red). Inside the potting, a thin disc is placed to represent the HV divider.

The small PMTs are modeled in a similar way to the large ones, but with an ellipsoidal bulb and without the acrylic and SS covers.

A dedicated positioning algorithm was developed to compute the coordinate of each LPMT and SPMT around the central detector. The algorithm computes the Cartesian coordinates and the rotation matrices needed to correctly orientate the PMTs towards the center, which are saved in a file read by ARBY during the geometry construction.

**Truss** The complete structure of the truss has been implemented in a similar way, with a positioning algorithm to compute the correct coordinate and orientation of each element (see Figure 2.8a).

**Node and bar** The SS nodes and bars are the components that fix the acrylic sphere to the truss. The node (Figure 2.8e on page 39) is composed of two truncated cones made of acrylic (blue) and SS (white) while the bar is a simple SS cylinder (white).

**Water shell** The water shell is the part of the water pool between the acrylic sphere and PMTs and it is the main source of radon for the central detector because the product of decays that occurs in the outer region cannot reach the sensitive part of the detector.

**Rock** The rock surrounding the water pool was modeled as a cylindrical shell of 21.75 m of inner diameter, 43.5 m of height, and 20 cm of thickness, composed by silicon dioxide with a density of 2.8 g/cm$^3$. The width of the shell is a compromise between the necessity of a large path to simulate the interaction of gammas inside the rock before escaping and the efficiency of the simulation and, as a consequence, the CPU time. The most energetic gamma ray emitted by the natural nuclides is the 2615 keV emitted by $^{208}$Tl of the $^{232}$Th chain. In $SiO_2$ the absorption coefficient is $3.89 \cdot 10^{-2}$ cm$^2$/g, that for a density of 2.8 g/cm$^3$ it gives an half-thickness of 6.4 cm. The considered thickness of 20 cm corresponds to 3.3 half-thickness, with an interaction probability of about 90%.

**Calibration system** As introduced in 1.2.2.4, the calibration system of the JUNO detector is made of 4 different sub-systems. To simulate the contribution of these systems to the radioactive background, their geometry has been implemented in ARBY. The wire of the CLS is modeled with two parts: the cables and the anchors. The cables consist of a cylinder composed of a SS wire covered by Teflon and positioned in the LS where they will be placed during data taking that is from the chimney to the anchors (see Figure 1.7 on page 18, blue wire from the big blue points to the top chimney). The anchors are instead placed attached to the internal surface of the acrylic sphere. The GT system was modeled as a Teflon pipe around the external equator of the acrylic sphere with a SS wire inside and a SS cylinder to represent the sensor. Finally, the USS is composed of a Teflon pipe around the equator inside the LS with a copper wire inside and a Receiver attached to the internal surface of the acrylic sphere.

The complete geometry of the JUNO detector implemented in ARBY is shown in Figure 2.8a on the facing page. Since the complexity of this geometry, the time required to run a simulation is very long because Geant4 has to navigate in a very large number of elementary volumes. In order to reduce the CPU time, I implemented some simpler geometries without impacting the results of the simulations.

The first one is related to the PMTs (both large and small). In this case, instead of simulating contaminations in each of the more than 40000 PMTs, a sub-section composed of 37 LPMTs and 27 SPMTs has been created (Figure 2.8c on the next page). With this geometry, only the central LPMT and the six internal SPMTs are considered sources of radioactive nuclides. This allows having only a very small number of volumes (1 or 6) in which the simulator has to generate the uniform contamination and the surrounding volume acts only as passive material to simulate the potential interaction of a photon with an adjacent PMT. Since the complete geometry is symmetrical, this is a representative sub-unit and can be used to simulate the behavior of the whole structure with a huge time-saving.

Another simplification has been required by the truss. As in the case of PMTs, the truss is a symmetric structure composed of a very large number of identical elements and this allowed a simpler geometry to be created that could be representative of the complete one. This geometry is shown in Figure 2.8f on the facing page, where a cross, with the correct shape of the beams of the truss, is placed behind the PMTs sub-section. With this geometry, it is possible to simulate the effect of the presence of the PMTs and the auto absorption of the truss. Since the whole cross is used as a source, a small effect can be present at the edge of it but it is negligible.

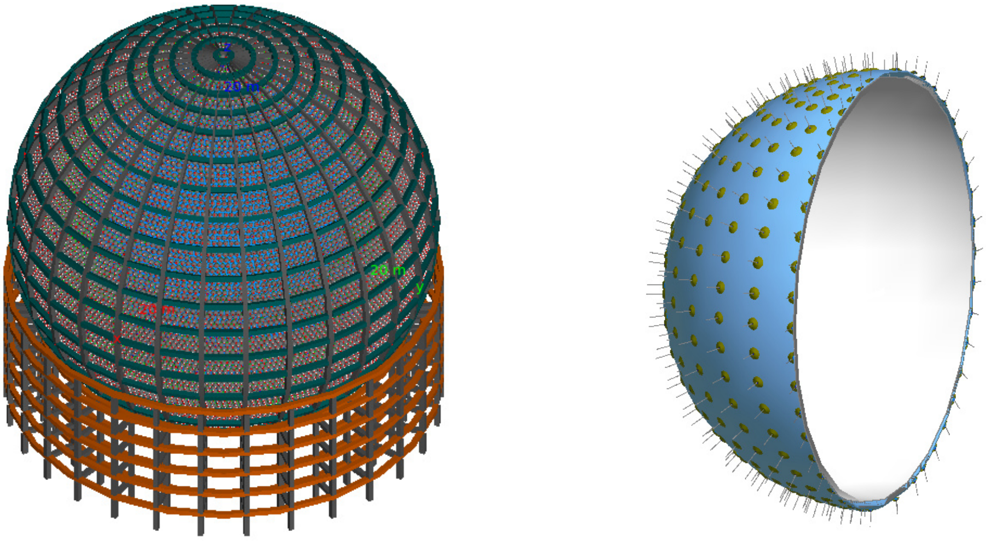

(a) Complete geometry (b) Central detector with nodes and bars

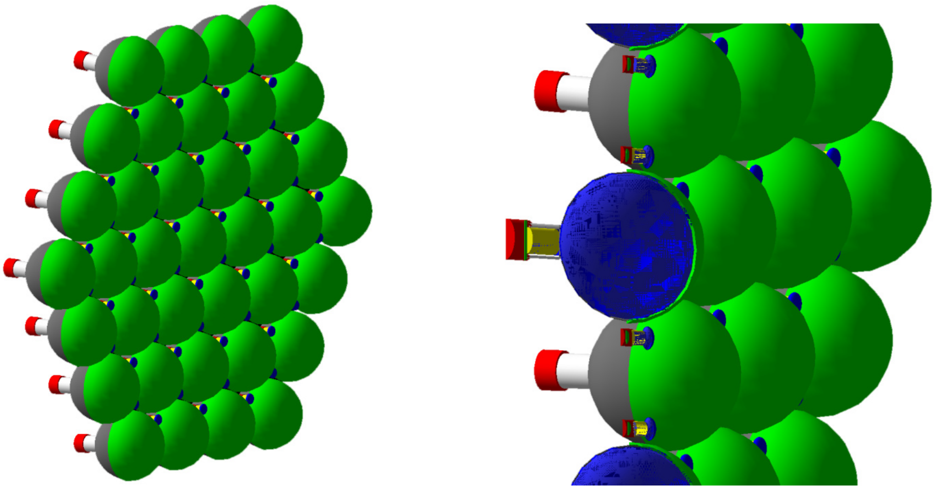

(c) Large and small PMTs (d) Large and small PMTs detail section

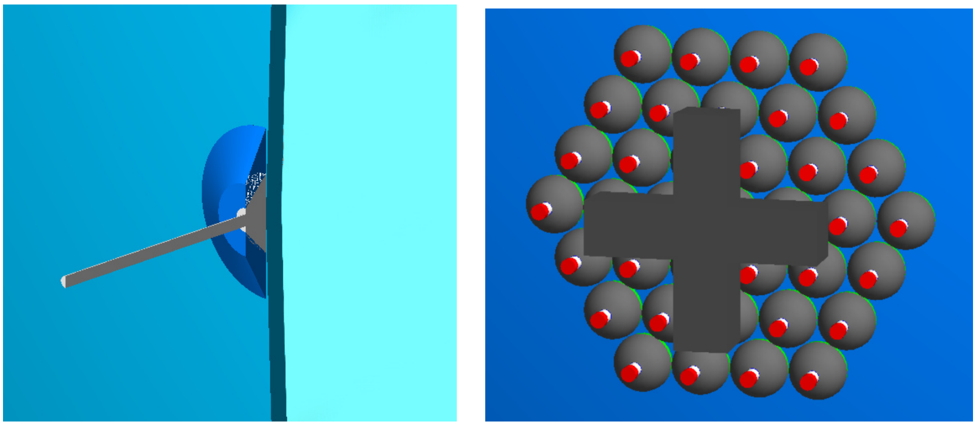

(e) Node and bar detail section (f) Simple truss behind PMTs

Figure 2.8: Some pictures of the JUNO geometry as implemented in ARBY.

As for the nodes and bars is concerned the simulations have been performed simulating the contamination in only one node and bar (Figure 2.8e on the previous page) because the distribution of them around the sphere is highly symmetric and the distance between them is so long to make negligible the cross talk.

## 2.6 Implementation of quenching in MC simulations

Geant4 is a powerful toolkit to simulate the interactions between particles and matter but, as introduced in Section 2.4, particular attention must be paid to the choice of the physics list and its parameters. The default ones are a good choice in a wide variety of situations providing accurate results but especially when the user introduces some non-standard features, some non-obvious behaviors can emerge. Some of the most significant for the simulations of the JUNO experiment are related to the application of the quenching factor.

When a charged particle interacts in a liquid scintillator only a small fraction of its lost kinetic energy is converted into light photons. The remainder is dissipated in non-radiative processes such as lattice vibration and heat. The fraction of the deposited energy that is converted into light depends on both the particle type and its energy and it is called scintillation efficiency. The response of organic scintillators to charged particles can be described by a relation between $dL/dx$, the fluorescent energy emitted per unit path length, and $dE/dx$, the specific energy loss for the charged particle. The widely used relation was suggested by Birks [29] and it is based on the assumption that a high ionization density along the track of the particles leads to quenching from damaged molecules and a consequent lowering of the scintillation efficiency. An extended version of the original Birks' formula was proposed by Craun and Smith [30] and can be expressed as follow:

$$\frac{dL}{dx} = \frac{S\frac{dE}{dx}}{1 + kB\frac{dE}{dx} + C\left(\frac{dE}{dx}\right)^2} \tag{2.1}$$

where S is the scintillation efficiency in absence of quenching, B is a proportionally constant between the specific energy loss and the resulting density of damaged molecules, k is the fraction of damaged molecules that lead to quenching and C is an empirical parameter. As a consequence, for low ionizing particles, such as electrons, the quenching effect is quite small but for highly ionizing particles, such as alphas, this effect is huge. The total amount of energy that is converted into light can then be computed using the following equation:

$$E_{scint} = S \cdot \int_0^E \frac{dE}{1 + kB\frac{dE}{dx} + C\left(\frac{dE}{dx}\right)^2} \tag{2.2}$$

In Geant4 the propagation of a particle is not continuous but performed in steps and the length of each step depends on the chosen interacting process and the physics list parameters. For example for alpha particles, the most probable interaction process is ionization and in each step, the particle lose an amount of kinetic energy that depends on the specific Bethe-Block $dE/dx$. In ARBY, as in SNiPER, the application of quenching is applied at each step and the resulting energy is then summed with the contributions of the following steps until the whole kinetic energy of the particle is deposited. If we consider a particle that loose and amount of energy $dE_i$ in the i-th step with a length $dx_i$, the energy that will be converted into light is computed with the following equation:

$$E_{scint} = S \cdot \sum_i \frac{dE_i}{1 + kB\frac{dE_i}{dx_i} + C\left(\frac{dE_i}{dx_i}\right)^2} \tag{2.3}$$

| Particle | a ($g/cm^2/MeV$) | b ($g/cm^2/MeV$) |
|---|---|---|
| Electrons, positrons | $6.5 \cdot 10^{-3}$ | $1.5 \cdot 10^{-6}$ |
| Protons | $6.5 \cdot 10^{-3}$ | $1.5 \cdot 10^{-6}$ |
| Alphas, ions | $3.705 \cdot 10^{-3}$ | $1.5 \cdot 10^{-6}$ |

Table 2.3: Values of the Birks' coefficients of Equation 2.3 used to compute the ionization quenching in JUNO simulations, based on the experience of the Daya Bay experiment.

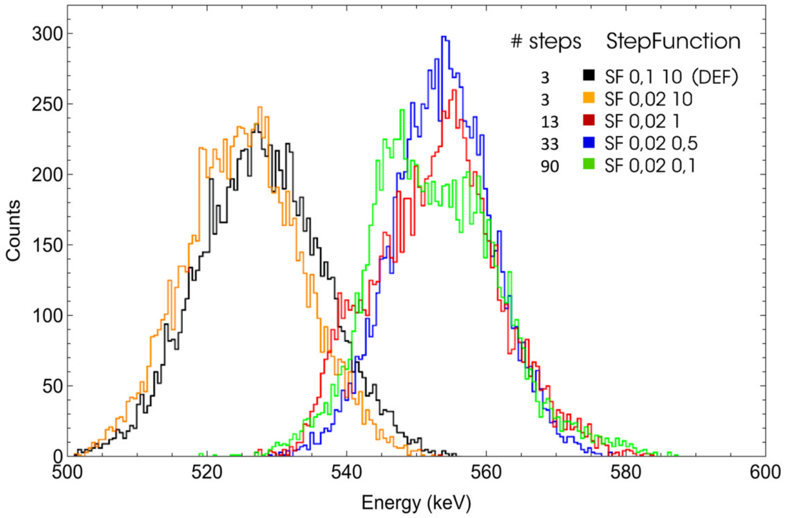

Figure 2.9: Spectra of the quenched deposited energy for different parameters of the step function for an alpha particle of 5.4 MeV

where the used Birks' coefficient values are reported in Table 2.3 and the S coefficient is fixed to 1 because it acts only as a normalization factor and is not relevant for the comparison of the simulations.

In the computation of the discrete quenching effect, the step length and number are crucial parameters because the $dE/dx$ is not a constant value but depends on the kinetic energy of the particles. In fact, the more steps there are, the more accurate the calculation will be because Equation 2.3 tends to Equation 2.2. Since it is possible in Geant4 to modify the computation of the step length, a study has been conducted in order to evaluate its effect on the resulting deposited energy. The chosen Geant4 physics list is the Livermore with the G4 version 10.04.p02. The step length can be controlled by using the *Step Function*, which is an internal algorithm of Geant4 used to compute the length of a step, based on the total range of the particle. This function depends on two parameters: $\alpha_R$ and $\rho_R$. The first one control the step size at high energy, and the step size tends to be $alpha_R \cdot$ Range. As the particle travels the maximum step size decreases gradually until the range becomes lower than the second parameter, $\rho_R$, and in this case, the step length tends to be equal to the total range. For example, the default parameters of the chosen physics list are 0.1 and 10 µm which results in the propagation of an alpha particle of 5.4 MeV in 3 steps. In Figure 2.9 is shown the effect of different choices of the step function parameters on the steps number and the resulting deposited energy for an alpha particle with an initial kinetic energy of 5.4 MeV. Looking at the plot starting from the black curve (default parameters of the Livermore physics list), if we change the first parameter from 0.1 to 0.02, the result

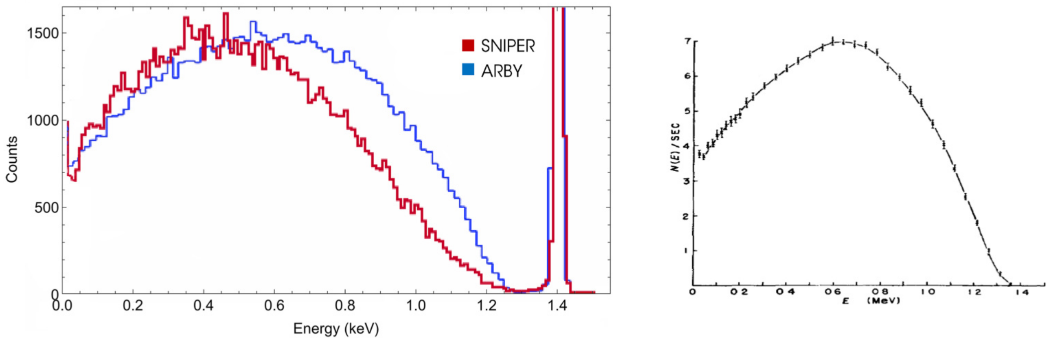

(a) ARBY/SNiPER $^{40}$K spectrum comparison (b) Kelly, Beard, Peters $^{40}$K spectrum

Figure 2.10: Spectra of $^{40}$K decays obtained by ARBY and SNiPER and the reference measured spectrum

is almost the same and the alpha particle is propagated always in three steps, in this case only the relative length of the steps is changed a little. This happens because the energy of the alpha particle is already low enough so that the step length is controlled almost by the second parameter. If we change the second parameter from 10 to 1, the alpha is propagated in 13 steps, and the resulting deposited energy increase by about 30 keV. If we now decrease again this value, the number of steps increases but the deposited energy is almost the same. This indicates that the computed quenched energy is converged to the correct value given by Equation 2.2 on page 40.

Another study has been conducted on the results associated with the propagation of electrons produced by gamma interactions or beta decays. The results obtained from pure electron simulation are in excellent agreement, while a very significant difference has been observed in the deposited energy spectrum associated with the decays of $^{40}$K. This nuclide can decay via $\beta^-$ or electron capture decays. In the first case, an electron with a maximum energy of 1311 keV is emitted, while in the second case is emitted a gamma photon of 1461 keV that transfer its energy to electrons when it interacts with matter. In Figure 2.10a is shown the spectrum of the deposited energy resulting from the simulation of the decay of $^{40}$K in the LS. Here can be seen that the gammas and electrons are propagated and quenched in the same way because the two peaks on the right overlap perfectly. On the contrary, the continuum produced by the beta electrons has clear different shapes. This effect is related to the use of an internal generator for the primary particle in SNiPER. This generator produces beta energy distribution only according to the allowed decay shape, but the $^{40}$K decay is four-forbidden so, the shape is quite different. Since ARBY uses the internal Geant4 generator it is able to better reproduce the experimental shape of the beta spectra as obtained by Kelly, Beard, and Peters [31], shown in Figure 2.10b. This wrong behavior has been corrected by using the Geant4 generator also in SNiPER.

## 2.7 Simulation results and comparison

### 2.7.1 Results of ARBY

For each component listed in 2.5.1 on page 37 three or four dedicated simulations have been performed, depending on the nuclides and chains to simulate. All components require the simulation of $^{238}$U, $^{232}$Th and $^{40}$K because these radionuclides are always present in all materials. Instead, only stainless steel-made components require the simulation of $^{60}$Co

| Component | LS | Acrylic | External | Rock |
|---|---|---|---|---|
| # of chains or events | $10^6$ | $10^7$ | $10^8$ | $2{\cdot}10^{10}$ |

Table 2.4: Number of events for the simulation of different components of the JUNO experiment

that can be found almost only in metal alloys.

The number of events for each simulation depends on the distance between the source and the detector (LS). The number of events is reported in Table 2.4. For the simulation of the rock, the source is so distant from the LS that the number of events required to obtain some signals in the detector is in the order of tens of billions. Since all alpha and beta decays cannot produce a signal in the detector, to drastically reduce the computation time required to simulate the complete chains, only gamma ray with the energy of 1460 keV and 2650 keV have been simulated. These two energies are representative of the most energetic gammas emitted in the $^{238}$U and $^{232}$Th chains and $^{40}$K. The results have been scaled to the whole chain based on the branching ratio of these radionuclides.

In Figure 2.11 on the following page and 2.12 on page 45 are shown the spectra obtained respectively from the simulation of $^{238}$U, $^{232}$Th and $^{40}$K in LAB and acrylic vessel. The first ones describe how the internal contaminations are seen by the detector together with the event reduction obtained by applying the default fiducial volume cut of 17.2 m. The second ones are instead representative of all external contamination, for which only gamma rays contribute to the events because alphas and betas are stopped before reaching the LS. In the plots are shown the spectra with and without the application of the default FV cut in red and blue respectively.

In the spectra of the LAB contamination, it is possible to distinguish two components: the beta and gamma decays. The energy of the beta electron and almost all the gamma ray emitted in the following nuclear deexcitation are summed to produce the continuum of the spectra, whose shape is given by the sum of the different energy distributions of all the decays in the chains. The only exception is the presence of the peaks associated with the gamma ray emitted in the electron capture decay of $^{40}$K. Since the energy released by the alpha particles is strongly quenched, the alpha peaks are present at lower energy with respect to the alpha initial energy. The effective energy that contributes to the emission of light in LS is in the order of 12% of the energy of the alpha particle. The width of the alpha peaks is not due to the application or simulation of the energy resolution of the detector but is related to the fluctuation in the energy loss of the alpha particle that fluctuates the total deposited energy. More detail about the value obtained for the quenching of the alpha particles will be provided in section 2.7.2. The application of the FV cut has a minimal effect on the shape of the spectra for LAB contamination because these are uniformly distributed, so the effect is only limited to a reduction of the global rate given by the ratio of the FV volume divided by the total detector volume $R = \left(\frac{17.2m}{17.7m}\right)^3 = 0.92$. Is it possible to see a small difference in the spectra shape in the region dominated by the sum of beta and gamma events because, if the FV cut is applied, there is the possibility that a gamma ray escapes from the FV and is not detected.

The application of the cut has a deep impact on both the shape and the global event rate for external contaminations (about 95% of the rate of events between 700 keV and 12 MeV). As for as the shape is concerned, the low energy component of the spectra is drastically reduced because it is not able to penetrate deeply into the LS volume, while the most energetic gamma rays present a lower reduction. The shielding effect of this external

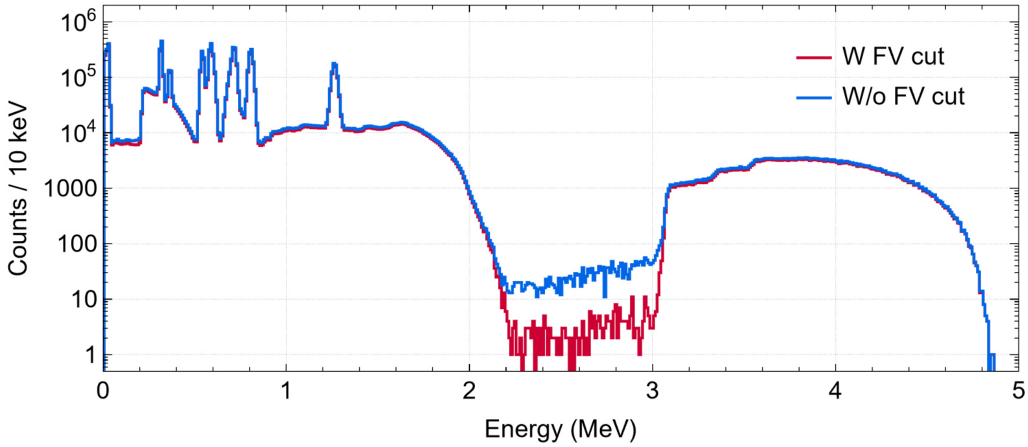

(a) $^{238}$U in LAB with and without FV cut

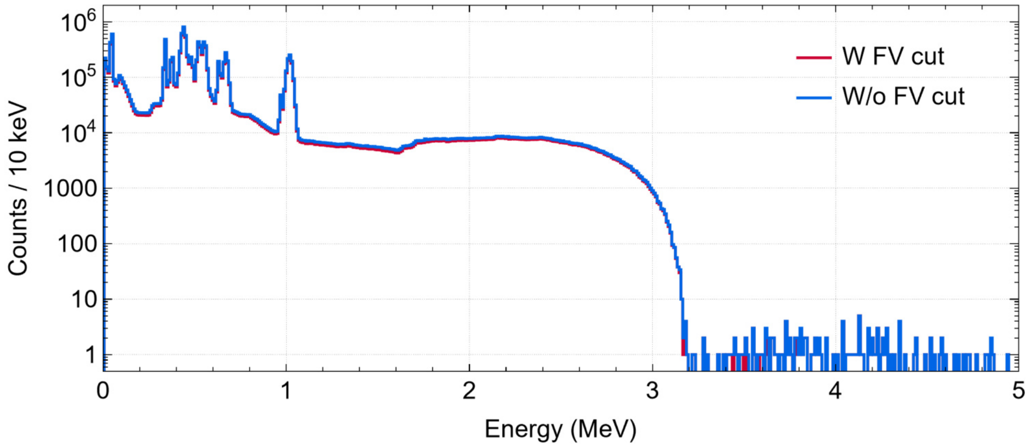

(b) $^{232}$Th in LAB with and without FV cut

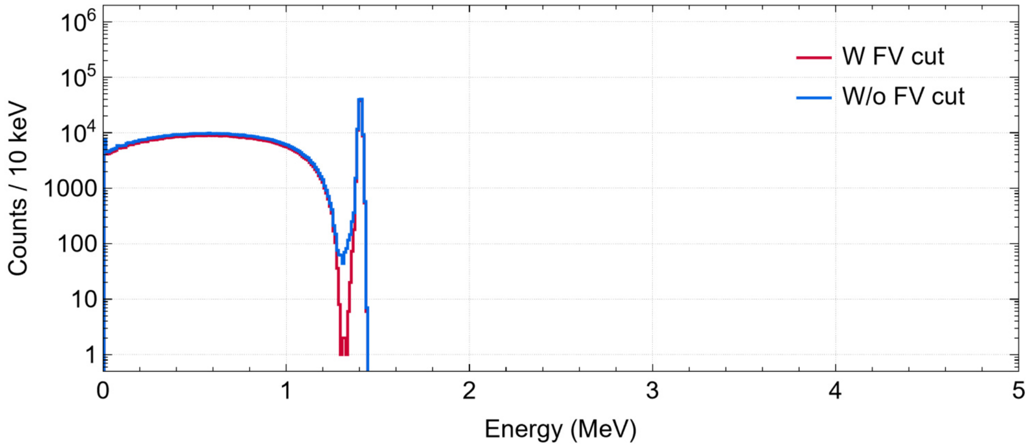

(c) $^{40}$K in LAB with and without FV cut

Figure 2.11: Spectra of the deposited energy in LS produced by uniform contamination of the LS with $^{238}$U, $^{232}$Th and $^{40}$K as computed by ARBY.

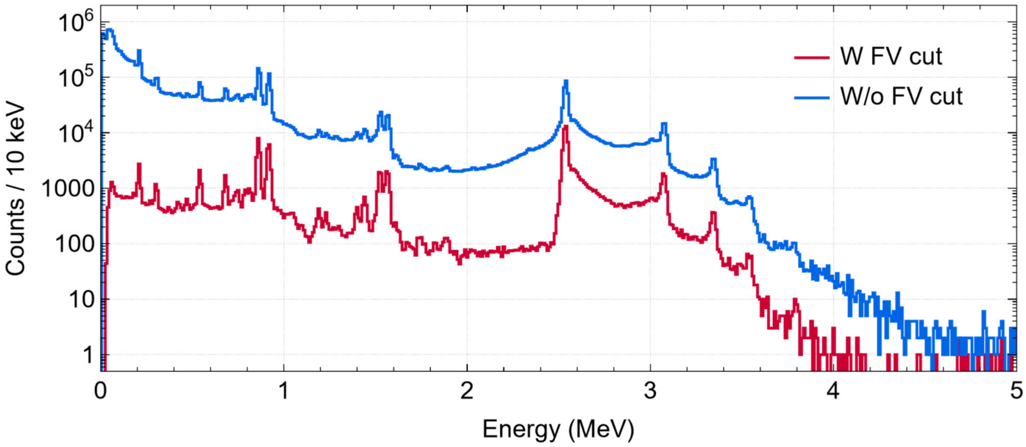

(a) $^{238}$U in acrylic with and without FV cut

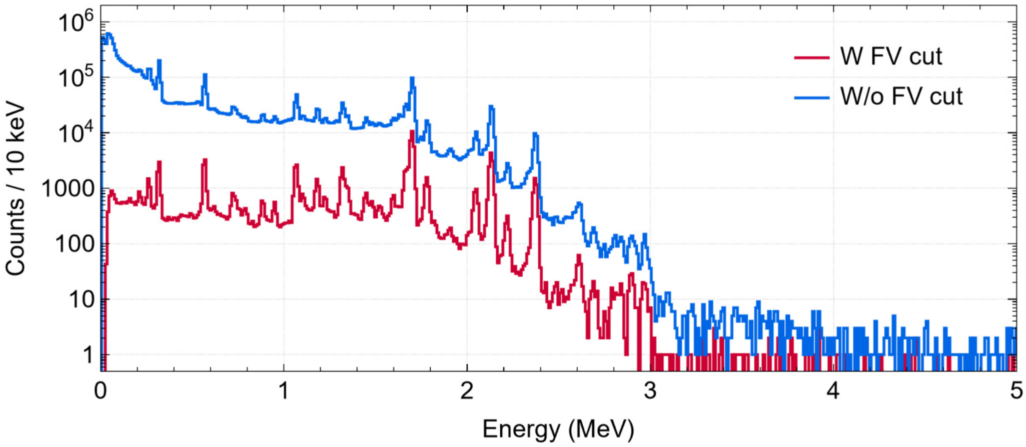

(b) $^{232}$Th in acrylic with and without FV cut

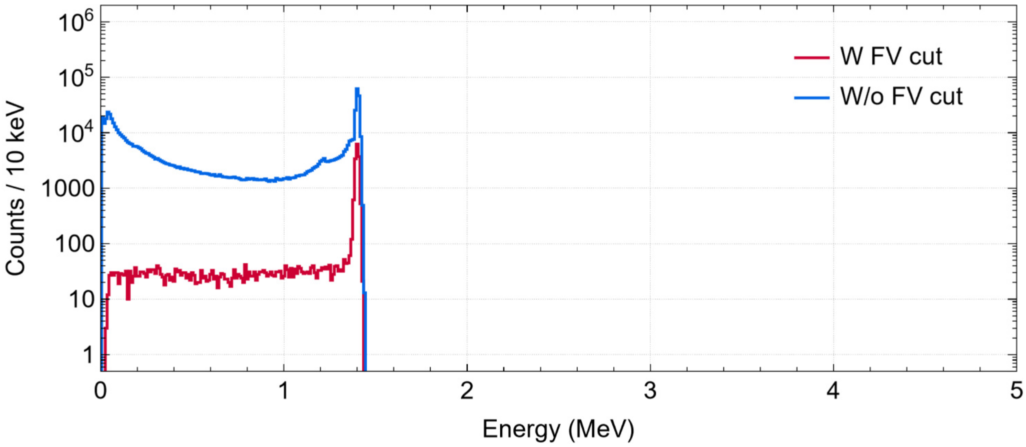

(c) $^{40}$K in acrylic with and without FV cut

Figure 2.12: Spectra of the deposited energy in LS produced by uniform contamination of the acrylic vessel with $^{238}$U, $^{232}$Th and $^{40}$K as computed by ARBY.

| Component | SNiPER | ARBY | G4-LA |
|---|---|---|---|
| LS | 🟩 | 🟩 | 🟩 |
| Acrylic | 🟩 | 🟩 | 🟩 |
| LPMT glass | 🟩 | 🟩 | 🟥 Not simulated |
| LPMT protection | 🟩 | 🟩 | 🟥 |
| LPMT electronics | 🟨 Scaled | 🟩 | 🟥 |
| SPMT glass | 🟨 Scaled | 🟩 | 🟥 |
| Nodes and bars | 🟩 | 🟨 Low detail | 🟥 |
| Truss | 🟨 Scaled | 🟨 Low detail | 🟥 |
| Calibration | 🟩 | 🟩 | 🟥 |
| Radon | 🟩 | 🟩 | 🟥 |
| Rock | 🟨 MC + analytic | 🟩 | 🟥 |

Table 2.5: Components simulated by each Monte Carlo software: in green are represented the components simulated with a high degree of accuracy, in orange are the components simulated with low detailed geometry or rescaling, and in red are those that were not simulated.

shell of the liquid scintillator plays an important role in the reduction of the background events due to the residual radioactive contaminations in all the external materials. To obtain a more effective reduction, the FV cut could be changed to increase the shielding width at the cost of a lower active mass. This approach will be widely used for the study of the solar neutrino, for which the background must be much lower than those required for reaction antineutrino measurement.

### 2.7.2 ARBY, SNiPER, G4-LA comparison

As introduced before, the simulations of the contribution of the different components and their contaminations have been performed with three different codes: SNiPER, ARBY, and G4-LA. Since SNiPER is the official tool for the JUNO experiment, the geometry is implemented with a very high degree of accuracy, but while we were doing the comparison work the development of the SNiPER code and the implementation of the geometry were in progress. As a consequence, not all the components have been simulated with the same level of detail and the contributions of some of them have been obtained by rescaling the contribution of similar components. With the ARBY software, all components have been simulated, but the degree of accuracy of some components is not very high, for example for the truss. The G4-LA code implements instead only the central detector geometry (LS and acrylic sphere), where the physics validation of three codes has been performed, but it didn't allow for evaluating the contribution of the external components. This is summarized in Table 2.5, where in green are represented the components simulated with a high degree of accuracy, in orange are the components simulated with low detailed geometry or rescaling, and in red are those that were not simulated.

A complete comparison of the results of the three codes has been performed for the LS and acrylic simulations. In particular, the resulting deposited energy spectra shape, the quenching computation, and the global event rate have been compared. The complete natural chains of $^{238}$U and $^{232}$Th, the sub-chain starting with $^{210}$Pb and the $^{40}$K are considered separately for the LS. The contribution of the $^{210}$Pb sub-chain is considered because it is produced by the $^{232}$Rn secular equilibrium breaking and could be in non-equilibrium with respect to the $^{238}$U chain. For the same reason, only the chains of $^{238}$U

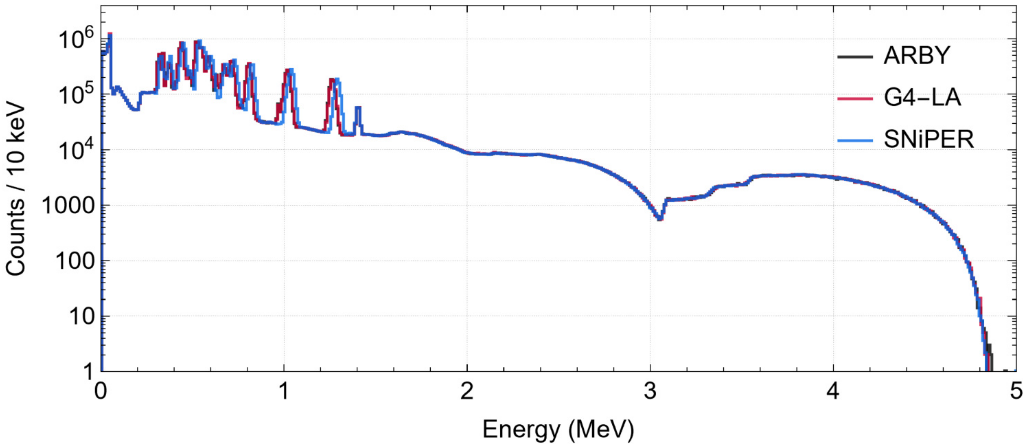

(a) LAB contaminations spectrum

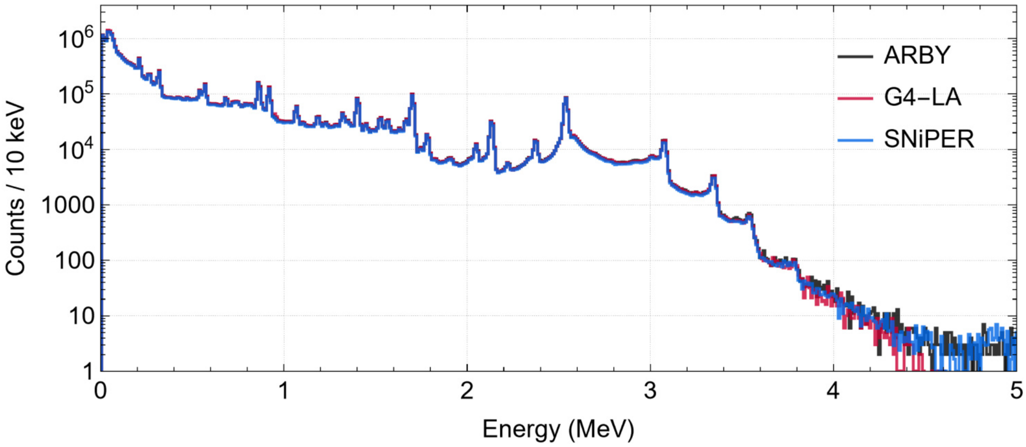

(b) Acrylic contaminations spectrum

Figure 2.13: Superposition of the sum spectra obtained by considering all energy depositions in the entire detector volume following $^{238}$U, $^{232}$Th, $^{40}$K, and $^{210}$Pb decays uniformly distributed within the LS and the acrylic vessel, as simulated by each of the three Monte Carlo codes.

and $^{232}$Th and the $^{40}$K have been simulated for the acrylic.

For each code, the contributions of the four contaminants are summed and the resulting spectra are superimposed in Figure 2.13. As one can see, the features of the spectra are in very good agreement and the residual differences are attributed to the implementation of the quenching factor calculation. In fact, the most relevant differences are related to the position of the peaks associated with the energy deposition by the alpha particles, while the beta and gamma continuum has an excellent agreement because in this case, the quenching effect is not so relevant.

In Figure 2.14a are shown the quenched energies of the alpha peaks as a function of the true alpha energies, while in Figure 2.14b are shown the differences (in keV) between the quenched energy computed by SNiPER and those computed by ARBY and G4-LA. The agreement between the three codes is good, in fact, the differences are within 25 keV for all the alphas. In Figure 2.14b is visible a systematic difference within the three codes, in particular between SNiPER and the other ones. In fact, except for one point (6288 keV) all the energies of the peaks computed by SNiPER are systematically higher. This is probably related to differences in the propagation of the alpha particles that result in a different

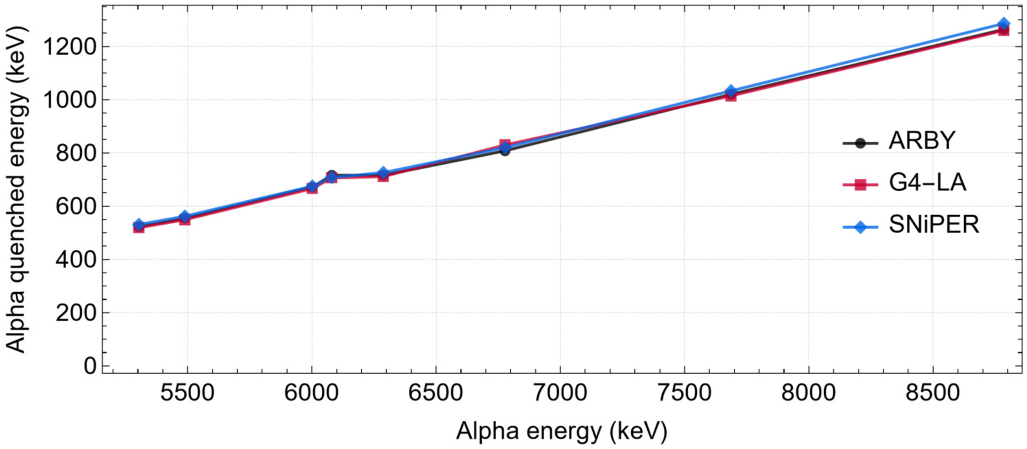

(a) Plot of the quenched energy of the alpha peaks as a function of the true alpha energy

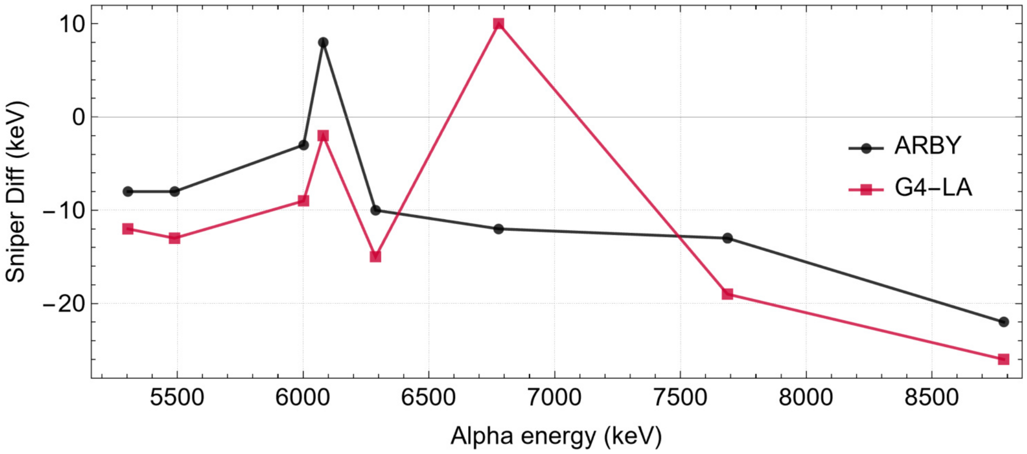

(b) Difference between the quenched energy computer by SNiPER and those computed by ARBY and G4-LA

Figure 2.14: Comparison of the energy of the quenched alpha peaks computed by SNiPER, ARBY, and G4-LA

application of the quenching faction because the value of the quenching factor depends on the energy of the alpha particle when it deposits its energy. This difference is however negligible for the scope of this analysis because it is not so relevant for the estimation of the total global rate of background events and the particular implementation of the quenching factor coefficient and propagation parameter will be adjusted to match with the experimental data when available.

The results of the simulation provide important information about the efficiency with which the detector can detect an event of radiogenic background in the materials. In particular, this efficiency can be computed by using the following equation:

$$\epsilon = \frac{\#\text{ of event in the spectra}}{\#\text{ of generated event/chains}} \tag{2.4}$$

where the number of events in the spectra is selected according to the different cuts that will be applied to the data, in particular the fiducial volume cut of 17.2 m and the lower energy cut of 0.7 MeV. Once the efficiency for every chain or nuclide and each component have been evaluated, it is possible to compute the expected background rate by using the information on the concentration of radioactive nuclides in the materials. The rate is

| Cut | Code | $^{238}$U (HZ) | $^{232}$Th (HZ) | $^{40}$K (HZ) | $^{210}$Pb (HZ) | Total (HZ) |
|---|---|---|---|---|---|---|
| R<17.7 m<br>E>0.7 keV | SNiPER | 0.70 | 0.37 | 0.23 | 0.69 | 1.99 |
| | ARBY | 0.67 | 0.35 | 0.23 | 0.70 | 1.95 |
| | G4-LA | 0.67 | 0.35 | 0.22 | 0.69 | 1.95 |
| R<17.2 m<br>E>0.7 keV | SNiPER | 0.64 | 0.34 | 0.21 | 0.63 | 1.83 |
| | ARBY | 0.61 | 0.32 | 0.21 | 0.64 | 1.78 |
| | G4-LA | 0.63 | 0.30 | 0.21 | 0.63 | 1.77 |

Table 2.6: Rate of background events expected for LS contaminations for the different radiogenic sources and with or without the application of the FV cut. The assumed mass of LS is 20000 tons. The computation is performed using the requirements indicated in Table 2.2 on page 32 as radionuclide concentration.

| Cut | Code | $^{238}$U (HZ) | $^{232}$Th (HZ) | $^{40}$K (HZ) | Total (HZ) |
|---|---|---|---|---|---|
| R<17.7 m<br>E>0.7 keV | SNiPER | 1.70 | 0.71 | 4.54 | 6.95 |
| | ARBY | 1.66 | 0.72 | 4.46 | 6.84 |
| | G4-LA | 1.72 | 0.71 | 4.49 | 6.92 |
| R<17.2 m<br>E>0.7 keV | SNiPER | 0.084 | 0.041 | 0.25 | 0.38 |
| | ARBY | 0.078 | 0.039 | 0.25 | 0.36 |
| | G4-LA | 0.080 | 0.039 | 0.25 | 0.37 |

Table 2.7: Rate of background events expected for acrylic contaminations for the different radiogenic sources and with or without the application of the FV cut. The assumed mass of acrylic is 566 tons. The computation is performed using the requirements indicated in Table 2.2 on page 32 as radionuclide concentration.

computed using the following equation:

$$R(Hz) = C(g/g) \cdot m(g) \cdot \epsilon \cdot SA(Bq/g) \tag{2.5}$$

where C is the concentration of the considered radionuclide (e.g. $^{238}$U, $^{232}$Th or $^{40}$K), m is the total mass of this material in the JUNO experiment and SA is the specific activity of the considered radionuclides.

The rates of expected background signals have been evaluated for each simulated component and a detailed comparison of the three codes results has been also performed on these results. In Table 2.6 and 2.7 are reported the results of this computation obtained for the liquid scintillator and acrylic contaminations by using the efficiency calculated with and without the application of the FV cut. The radionuclides concentrations are assumed to be equal to the requirements indicated in Table 2.2 on page 32. The results obtained are in very good agreement within the three codes indicating that the small differences observed in the spectra shape are negligible for this estimation. As deduced previously by the visual analysis of the spectra, the background rate produced by LS contamination is reduced by only a small amount, proportional to the considered fiducial volume. The background rate produced by acrylic contamination is instead very high, especially for $^{40}$K, if all the detector volume is considered. The application of the FV cut at 17.2 m drastically reduces the total rate (about a factor of 20), because these events are all associated with gamma rays absorbed in the outer shell of the liquid scintillator.

A similar analysis has been performed for the external component but, as introduced

| Component | Mass (t) | ARBY No-FV (Hz) | ARBY FV (Hz) | SNiPER No-FV (Hz) | SNiPER FV (Hz) |
|---|---|---|---|---|---|
| LPMT glass | 177 | 24.1 | 3.28 | 30.6 | 3.84 |
| LPMT protection | 260 | 0.068 | 0.0093 | 0.15 | 0.02 |
| LPMT electronics | 24.6 | 0.44 | 0.06 | - | - |
| SPMT glass | 3.1 | 0.91 | 0.23 | 1.3 | 0.14 |
| Nodes and bars (SS) | 65 | 29.9 | 2.4 | 26.1 | 2.2 |
| Truss | 1000 | 0.019 | 0.0017 | 0.3 | 0.03 |
| Calibration | - | - | 0.115 | - | 0.120 |
| Radon | 6000 | 16.2 | 1.3 | 16.2 | 1.3 |
| Rock | 4200 | - | <0.13 | 0.5 | 0.08 |

Table 2.8: Rate of background events expected for contaminations in external components for the different radiogenic sources and with or without the application of the FV cut. The computation is performed using the measured radionuclides concentrations, when available, or the requirements indicated in Table 2.2 on page 32.

before, only with SNiPER and ARBY. The total background rates have been computed by using the measured radionuclides concentrations, when available, or the requirements indicated in Table 2.2 on page 32. In Table 2.8 are reported the obtained results. As can be seen, in this case, there are some materials for which the differences within the two codes are significant, especially for the low-detail geometries or scaled results. The main external sources are the glass of large PMTs, the stainless steel of the nodes and bars, and the radon in water. These three sources completely dominate the total background of all the external components. Particular care has been applied during the mass production control of the radiopurity of these materials in order to guarantee the respect of this estimation.

## 2.8 Expected background count rate in JUNO

Although the ARBY code can simulate all the physics processes leading to the deposition of energy by the tracked particles, it is not able to simulate the emission of light photons by the liquid scintillator, propagate them in the materials and simulate their conversion into electrons by the PMTs of the JUNO detector. All these processes are important in the study of the impact of the radiogenic background on the global background event rate because they introduce additional energy spreading (detector resolution), inefficiencies in the detection, non-linearity in the detector response, and so on. To obtain a more realistic estimation of the background event rate produced by the radioactive contaminations in the materials, a full event simulation has been performed with the SNiPER framework. Here, the total number of photoelectrons (PEs) collected by the PMTs is evaluated for each event and converted into energy using a calibration obtained by simulating uniformly distributed 1 MeV gamma ray. This calibration allows taking into account the non-linearity of the detector response because it provides information on how the 1 MeV gamma rays are seen by the PMT as a function of their interaction radius in the detector. This response is shown in Figure 2.15. The number of emitted PEs is about 1400 at the center of the detector but there is a sharp decrease at large radii due to the energy leakage near the edge of the sphere (Compton scattering) and the total reflection of the optical photons at the interface between the acrylic and the water.

The simulations have been performed with the same statistics reported in Table 2.4 and

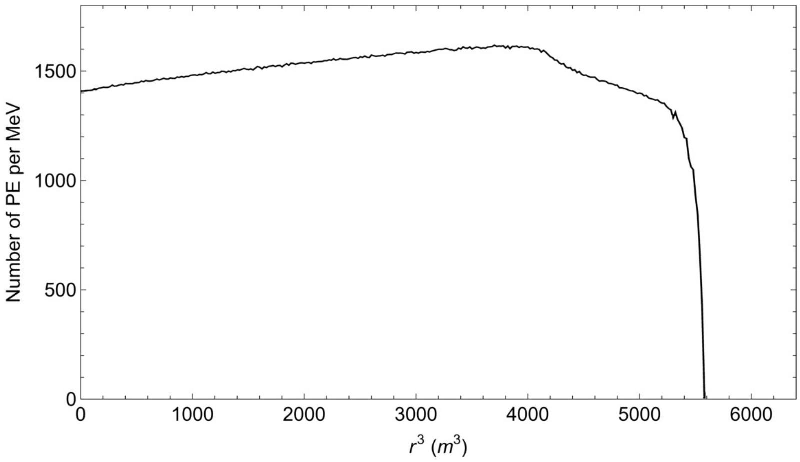

Figure 2.15: Total number of PEs collected by the PMTs as a function of volume for uniformly distributed 1 MeV gamma rays in the LS [23]

| Material | Mass (t) | Singles ALL (Hz) | Singles FV (Hz) |
|---|---|---|---|
| LS-reactor | 20000 | 2.5 | 2.2 |
| Acrylic | 610 | 8.4 | 0.4 |
| SS structure | 1065 | 15.9 | 1.1 |
| PMT glass | 136.6 | 26.2 | 2.8 |
| PMT readout | 141.3 | 3.4 | 0.3 |
| Other | | 2.5 | 0.3 |
| Sum | | 59 | 7.2 |

Table 2.9: Final background budget for the main materials used in the JUNO detector with reconstructed energy larger than0.7 MeV. The expected count rates are given both in the full detector volume (ALL, i.e. $r_{LS} = 17.7$m) and within the default FV ($r_{LS} = 17.2$m). The "Other" components include all materials that have a relatively smaller contribution to the background, such as the calibration parts, the LPMT cover, the rock, and the radon in water. These results include energy resolution, optical propagation, charge reconstruction, and non-uniformity corrections.

assuming the contaminations in Table 2.2. The resulting background count rates obtained for the dominant materials are reported in Table 2.9. As can be seen, the main contributions considering the FV are due to the glass of the PMTs, the stainless steel structure, and the liquid scintillator itself. The resulting background rate, taking into account the default energy and FV cut, is lower than the 10 Hz target for the IBD analysis channel, and further reduction can be obtained by increasing the FV cut for example for solar neutrino studies.

# Chapter 3

# Development of measurement techniques and detectors for ultra-trace elements analysis

## 3.1 Motivations and strategy

The liquid scintillator of the JUNO experiment is the component with the most stringent radiopurity requirements (see section 2.3). The organic nature of this substance makes it impossible to be directly measured by ICP-MS, so the only available technique able to measure directly the concentration of $^{238}$U, $^{232}$Th and $^{40}$K is the Neutron Activation Analysis (NAA). The typical sensitivities of this technique, combined with low background HPGe detector, are of the order of $10^{-12}/10^{-13}$ g/g, not enough to meet the requirements of JUNO.

In order to reach the required sensitivity, in my Ph.D. work, I continued the development of a new $\beta - \gamma$ coincidence detector, called GeSparK, started during my master's thesis, that exploits the coincidence between a liquid scintillator and an HPGe detector to reduce the intrinsic background of a typical HPGe spectrometer. Since the background reduction provided by the GeSparK detector is not enough, I worked on the development of measurement techniques based on radiochemical treatments on the samples. The radiochemical treatments allow to concentrate the nuclides of interest in the sample, making it possible to measure a higher mass and reduce the concentration of interfering nuclides produced by the neutron activation that reduces the sensitivity due to their contribution to the detector background. Moreover, a dedicated technique based on a new approach that exploits a delayed coincidence measurement has been developed to increase the sensitivity for $^{238}$U.

The combination of the GeSparK detector, the neutron activation, the application of radiochemical treatments, and the dedicated delayed coincidence technique should allow reaching the sensitivity required by JUNO for the concentration of $^{238}$U, $^{232}$Th and $^{40}$K in its liquid scintillator.

In this chapter, I will give a description of the NAA technique applied in particular to the LAB measurement and the HPGe gamma spectroscopy and then I will describe the GeSparK detector, its structure and operation, and the studies performed in order to develop a plastic scintillator system for cosmic muons veto. Finally, I will describe how the NAA technique is applied for the measurement of $^{238}$U, $^{232}$Th and $^{40}$K, describing, in particular, the measurement principle of the delayed coincidence techniques.

## 3.2 Measurement techniques

### 3.2.1 Neutron Activation analysis

#### 3.2.1.1 General description

The neutron activation technique makes it possible to carry out qualitative and quantitative measurements of trace elements by irradiating the sample with neutrons. This leads to the production of relatively short-lived radioactive nuclides from the long-lived or stable nuclides present in the sample. The nuclides produced can therefore be identified by the properties of the emitted radiation: type of particles, energy, intensity, and average life.

The neutron activation analysis method consists of the following five major steps:

1. Choice of the nuclear reaction of interest (if more than one is available)
2. Preparation of the sample
3. Irradiation of the sample
4. Measurement of the irradiated sample
5. Data analysis

The best nuclear reaction is chosen taking into account that it should have a high cross-section in order to obtain a high final activity with relatively short irradiation times, the nuclide produced must have a reasonable average life (not too short or too long), the radiation emitted in the decay of the activated nuclides must be easily detectable and the possible interferences produced by any competing reactions must be limited. Sometimes there is more than one reaction available for the same isotope and the optimum reaction depends also on the composition of the sample that is analyzed. The most used reactions are the (n,$\gamma$) type, which occurs with all the nuclides (with different cross sections), and in general, they have a higher cross section for thermal neutrons. Other neutron reactions are $(n, \alpha)$, $(n, p)$, $(n, 2n)$ but these have an energy threshold and therefore they can occur only for fast neutrons. For some particular nuclides, such as $^{238}$U, the neutron capture occurs at neutron energies above the thermal threshold, due to the presence of resonances in the cross-section. In Figure 3.1 is represented a scheme of the typical neutron activation process that can be divided into three phases:

1. The neutron is captured by a nucleus (A,Z) of the sample which is transformed into the excited nucleus (A+1,Z)*
2. The excited nucleus decays on the ground state with the emission of a prompt gamma ray, generating a radioactive nuclide (A+1,Z). This process is called prompt because it happens almost simultaneously with neutron capture.
3. The radioactive nuclide decays $\beta^-$, as a consequence of the excess of neutrons, with the emission of an electron and the following deexcitation gamma rays. This decays is called delayed because it occurs after a time related to the mean life of the radioactive nuclides.

The mass of the sample is determined by experimental aspects such as the maximum activity that can be handled in the laboratory, the size of the sample holder, the self-absorption of the radiation emitted by the reaction products, and the size of the detector with which the sample will be analyzed.

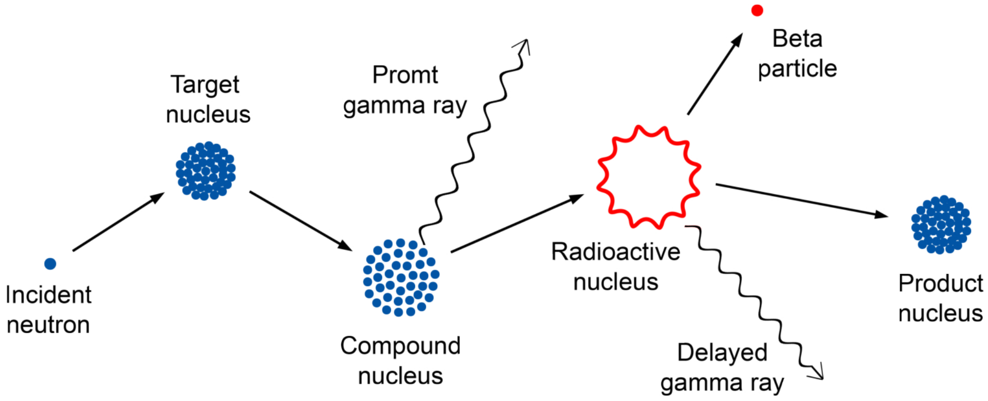

Figure 3.1: Scheme of the neutron activation process

The sample must be carefully prepared and placed inside a dedicated container. In particular, the preparation of the sample must be carried out with extreme cleanliness in order not to contaminate the sample, especially in the case of searching for trace elements, for which neutron activation is a highly sensitive technique. The materials used for the containers must be resistant to radiation and temperatures, must have a very low content of interfering elements that can be activated, and must be easy to handle.

The irradiation is performed by exposing the sample to a high neutron flux with the correct properties depending on the reaction of interest. The main source of neutrons for activation are research nuclear reactors, which are capable of providing very high thermal neutron fluxes (up to $\sim 10^{14}\ neutrons/cm^2$), although accelerators and isotopic sources are frequently used. More details are provided in Section 3.2.1.3.

At the end of the irradiation process, the sample is analyzed with a suitable detector according to the type of radiation to be identified and for what purpose. The typical case involves the detection of gamma or X-ray photons emitted by the activated nuclides using a germanium detector, which allows for a high energy resolution and sensitivity. In this case, the energy spectrum of the photons emitted by the activated sample can be analyzed qualitatively, determining which elements are present by recognizing the energies of the emitted photons, and quantitatively, determining the concentration of the nuclides.

The neutron activation technique has numerous advantages, such as the need for very small mass samples, the possibility of simultaneously detecting more than one nuclide, identifying different isotopes of a given element, and not depending on the chemical form of the element of interest. On the other hand, however, it is a technique that allows identifying only the progenitors of the natural radioactive chains, while it is not of great use to identify the other elements present in the chain and the eventual break of the secular equilibrium. Of particular interest in trace radioactive element determination is the fact that nuclides with a very long lifetime, such as $^{238}$U, $^{232}$Th, $^{40}$K, are transformed by neutron activation into nuclides with a much shorter half-life, typically days, and therefore, with the same concentration, much higher activity is obtained, allowing their detection with extremely high sensitivity and accuracy.

#### 3.2.1.2 NAA equation and sensitivity

Neutron activation is a complex process that involves at the same time many nuclides and different reactions. The sensitivity of this technique is related to many parameters associated with the sample, the activation facility, and the measurement system. In order to understand how these parameters affect the sensitivity and in order to compute the mass or the concentration of the nuclides of interest at the end of the analysis, the NAA equation is used. The following steps allow this equation to be derived.

For a specific nuclide of the sample, it is possible to describe the time evolution of the number of associated activated nuclides ($n$) with the following differential equation:

$$\frac{dn}{dt} = m\frac{N_A}{A}a_i\sigma\Phi_n - n\lambda \tag{3.1}$$

where $N_A$ is the Avogadro number, m is the mass of the element of interest, A is its atomic mass, $a_i$ its isotopic abundance, $\sigma$ is the cross-section of the neutron capture, $\Phi_n$ is the neutron flux and $\lambda$ is the decays constant of the activated nuclides. It is important to highlight that this equation is valid under the hypothesis of a uniform neutron flux, constancy of the number of target nuclei, and negligible cross-section for the reaction products. These assumptions are well verified in practical applications of this technique.

By integrating the equation 3.1 it is possible to compute the number of activated nuclides present in the sample after an irradiation time $t_i$ and the resulting activity:

$$n(t_i) = \frac{mN_Aa_i\sigma\Phi_n}{A\lambda}\left(1 - e^{-\lambda t_i}\right) \rightarrow A(t_i) = m\frac{N_A}{A}a_i\sigma\Phi_n\left(1 - e^{-\lambda t_i}\right) \tag{3.2}$$

This equation indicates that the number of activated nuclides saturates to the value $\frac{mN_Aa_i\sigma\Phi_n}{A\lambda}$ for $t_i >> \frac{1}{\lambda}$, while the activity saturates to the value $m\frac{N_A}{A}a_i\sigma\Phi_n$. This means that a longer irradiation time increases the sensitivity only if the mean life of the activated nuclides is longer than the irradiation time.

The quantitative analysis is conducted by inverting the previous equation in order to determine N by measuring the resulting activity after the irradiation. The activity is commonly measured by gamma spectroscopy, so it is required to know the detection efficiency ($\epsilon$) and the branching ratio (BR) of the observed gamma ray. Another important aspect to consider is that the gamma measurement is performed after a waiting period ($t_w$) at the end of the irradiation because the sample must be extracted from the reactor core and shipped to the measurement laboratory. The number of gamma rays detected can be computed by integrating over the measurement time the exponential law of radioactive decay to obtain the total number of decays and multiply this quantity by the branching ratio of the observed gamma ray and the absolute efficiency of the detector ($\epsilon$):

$$n_\gamma = \epsilon\, B\, R\, n(t_w)(1 - e^{-\lambda t_m}) \tag{3.3}$$

where $n_\gamma$ is the number of counts below the peak of interest (number of gamma rays detected), $\epsilon$ is the peak efficiency for the detector used, BR is the branching ratio of the used gamma transition, $n(t_w)$ is the number of activated nuclides present in the sample when the gamma measurement starts (after the waiting time) and $t_m$ is the duration of the measurement. In Figure 3.2 is represented the timeline of a neutron activation analysis with the meaning of the different times defined here.

Now we can substitute $n(t_w) = n(t_i)e^{\lambda t_a}$ and $n(t_i)$ with equation 3.2 to obtain the following complete relation:

$$n_\gamma = \epsilon B\, R\frac{N_A\sigma\phi_n m a_i}{n_\gamma A\lambda}(1 - e^{-\lambda t_i})e^{-\lambda t_w}(1 - e^{-\lambda t_m}) \tag{3.4}$$

The previous equation can be inverted in order to compute the mass of the nuclide of interest:

$$m = \frac{n_\gamma A\lambda}{\epsilon B\, Ra_iN_A\sigma\phi_n(1 - e^{-\lambda t_i})e^{-\lambda t_w}(1 - e^{-\lambda t_m})} \tag{3.5}$$

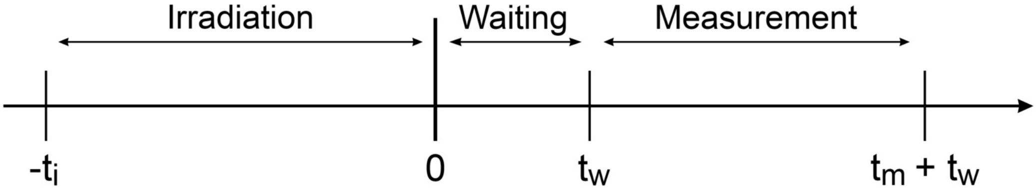

Figure 3.2: Timeline of a neutron activation analysis with the meaning of the different times: irradiation time, waiting time, and measurement time. The zero is the end of the irradiation.

This equation (3.5) allows understanding how the different parameters affect the sensitivity of NAA. As expected, the sensitivity increases if it is possible to choose a reaction that produces a radioactive nuclide with high BR gamma rays, the detector has a high efficiency and the neutron flux is high. The times should be optimized in order to reduce the waiting time, especially for short-lived nuclides, and to maximize the irradiation time and measurement time with respect to the mean life of the activated nuclide.

In order to use the equation 3.5 the neutron flux must be known with high accuracy and this is a very critical aspect in NAA because the neutron flux in a nuclear reactor is not constant neither over time nor in space, within different irradiation channels (see section 3.2.1.3 on the following page for more detail). If a sample of a known quantity of the nuclide of interest is irradiated at the same time as the unknown sample, the two are exposed to the same neutron flux so in this way the measurement of the sample can be carried out by comparison with the standard (relative method), eliminating the need to know precisely the neutron flux, the cross sections, the BR and in some specific conditions also the measurement efficiency, if this is the same for the standard and the sample. In this case, the mass of the searched element can be determined with the formula 3.6 (NAA equation), obtained by the ratio of two equations 3.5 computed for the sample (Sample) and the standard (STD):

$$C\left(\frac{g}{g}\right) = a_i \cdot \frac{m_{\text{STD}}}{m_{\text{Sample}}} \cdot \frac{n_{\text{Sample}}}{n_{\text{STD}}} \cdot \frac{\epsilon_{STD}}{\epsilon_{Sample}} \cdot \frac{e^{-\lambda \cdot t_{\text{w, STD}}}}{e^{-\lambda \cdot t_{\text{w, Sample}}}} \cdot \frac{1 - e^{-\lambda \cdot t_{\text{m, STD}}}}{1 - e^{-\lambda \cdot t_{\text{m, Sample}}}} \tag{3.6}$$

When in the germanium detector spectrum cannot be identified the peaks associated with the gamma rays emitted by the activated nuclides, because the intensities are too low with respect to the background fluctuation, the equation 3.6 can be still applied but the quantity $n_{\text{Sample}}$ represent the n-sigma fluctuation of the background in the region of interest (ROI). For example, if we are looking for a peak at 106 keV and there is no evidence, we consider a ROI equal to $1.2 \cdot \text{FWHM}$ centered at the energy of the peak (106 keV) and integrate the counts in that region. By computing the square root of the total counts in the ROI, we obtain the fluctuation at 1 sigma of the background, assuming a Poisson distribution of the background events. If we want a confidence level at, for example, 90% we can consider a factor of 1.64 in that value and use this quantity in the NAA equation. The result of the computation is an upper limit in the concentration of the nuclide of interest. The meaning of this value is that any concentration below that value cannot be observed as a consequence of the fluctuation of the background that can hide the presence of the signal.

The main consequence is that if the background of the HPGe spectrum is very high, the sensitivity of the analysis decrease if there is no evidence of the peak. This means that for ultra-trace analysis when the sensitivity is given by the background, it is very important to have it at a very low level in the detection system. The main source of background in NAA is the presence of other nuclides in the sample that are activated by the neutron flux and their decays are detected by the germanium detector. Unfortunately, there are many nuclides that can contribute to the background, for example, sodium, argon, bromine, chlorine, zinc, gold, and so on. For this reason, it is very important to guarantee a very high level of cleanliness in the preparation of the samples.

#### 3.2.1.3 Neutron sources and irradiation facility: TRIGA reactor at LENA

The NAA requires an intense source of thermal neutrons in order to achieve very high sensitivities. There are many sources of neutrons available with different characteristics in terms of neutron flux and neutron energy. These sources are:

- Spontaneous fission isotopes:

  Spontaneous fission (SF) involves the spontaneous splitting of the nucleus into two nuclides or fission fragments and the simultaneous emission of more than one neutron on average. The radionuclides $^{252}$Cf is a common commercially available source of this type. With a half-life of 2.65 years and a SF branching ratio of 3.1%, it produces an average number of 3.7 neutrons per fission with an average energy of 2.3 MeV. Typically, the intensity of these sources can reach $1{\cdot}10^{11}$ n/s isotropically emitted.

- Sources based on ($\alpha$,n) reaction:

  These sources are based on the reaction of alpha particles on low Z elements, typically beryllium. An alpha emitter, such as $^{241}$Am, is compressed with beryllium to create a compact neutron source. The neutrons emitted have energies over a broad spectrum from 0 to 10 MeV. The intensity can reach $1{\cdot}10^{8}$ n/s isotropically emitted.

- Accelerators:

  The accelerators generate a beam of charged particles such as electrons, protons, and deuterons into target materials. When the charged particles have enough kinetic energy to react with target nuclei, nuclear reactions occur. Electrons produce neutrons exploiting the ($\gamma$,n) reactions induced by the Bremsstrahlung photons produced in the interaction of the high-energy electrons in the material. Accelerated deuterons can be used to produce neutrons when deuterium or tritium are used as target materials according to the (d,n) reaction with an intensity up to $1{\cdot}10^{11}$ n/s. The acceleration of protons at high energy (GeV scale) against high Z materials will result in nuclear spallation reactions with the emission of 20-30 high-energy neutrons per proton. These sources can yield a neutron flux of up to $1{\cdot}10^{14}$ n/cm$^2$/s at the surface of the source.

- Nuclear fusion systems:

  The fusion reactions between deuterium and tritium (D-T) or deuterium and deuterium (D-D) emit one neutron per reaction with an energy of 14.06 MeV and 2.45 MeV respectively. Electrostatic fusion devices are available as sources of neutrons with a flux up to $1{\cdot}10^{10}$ n/s.

- Nuclear reactors:

  The production of neutrons by nuclear reactors is based on the induced fission on fissile nuclides such as $^{235}$U. When the $^{235}$U capture a thermal neutron has a high probability to split into two fragments with the release of energy and free neutrons

| Parameter | Value |
|---|---|
| Maximum thermal power | 250 kW |
| Maximum n flux (central channel) | $1.8{\cdot}10^{13}$ n/cm$^2$/s |
| Fuel | U-Zr ($^{235}$U 19.95 %) |
| Coolant | Light water |
| Moderator | HZr and H2O |
| Reflector | Graphite |

Table 3.1: Main technical data of the TRIGA MarK II reactor at LENA

(2.4 on average). The neutrons emitted vary in energy over the range from 0 to 10 MeV with an average value of 2 MeV. Because more than one neutron is released per fission, a self-sustaining chain reaction is possible with the release of considerable energy, forming the basis of the nuclear reactor as a principal source of neutrons and energy. Since for $^{235}$U slow neutrons are required for neutron capture, the nuclear reactor is equipped with a moderator in order to reduce the energies of the fast neutrons via elastic scattering with low atomic mass nuclei. Research nuclear reactors are the most intense source of fast and thermal neutrons, up to $1{\cdot}10^{14}$ n/cm$^2$/s. The TRIGA reactor is a particular type of research nuclear reactor that is able to produce neutron fluxes up to $1{\cdot}10^{16}$ n/cm$^2$/s for a very short period of time (milliseconds).

The analysis of radioactive contaminations in materials by NAA requires a high flux of thermal and epithermal neutrons because the nuclides of interest ($^{238}$U, $^{232}$Th and $^{40}$K) have the highest cross-section for neutron capture at these energies.

The best choice for our research is the TRIGA Mark II research reactor at the "Laboratorio di Energia Nucleare Applicata (LENA)" at the University of Pavia. This research facility is located at about 30 km from the University of Milano-Bicocca and this allows the waiting period to be minimized (when required) due to the transport from the irradiation facility to the radioactivity laboratory for the measurement of the samples. The main technical data of this reactor are provided in Table 3.1. The reactor is equipped with two irradiation channels in the core of the reactor for the irradiation of samples that require a high neutron flux with an equal fraction of fast and thermal neutrons, and a rotating rack around the core (called "Lazy Susan") that is equipped with 40 irradiation channels dominated by a thermal neutron component and other specific irradiation channels. The thermal neutron flux in the Lazy Susan channel is about $3{\cdot}10^{12}$ n/cm$^2$/s. In Figure 3.3 on the following page is shown a photo of the reactor operating at its maximum power of 250 kW with the emission of the characteristic Cherenkov light.

#### 3.2.1.4 Container for irradiation

The sample container for NAA must respect some requirements (see Section 3.2.1.1 on page 54) and the materials that are used most frequently are polyethylene (PE), silica, and aluminum. The silica and aluminum have the disadvantage that they became radioactive due to impurities in silica and activation of the aluminum. Another problem is that they are not very pure and could contaminate the sample in ultra-trace element analysis. The best solution for our research is PE which is a very cheap material, very clean, inert, and easy to handle. The only problem with polyethylene is that it is not very resistant to radiation and temperature because it becomes brittle after exposure to a fluence of $10^{17} - 10^{18} n/cm^2$. Since this quantity corresponds to about 10 irradiation campaigns at the TRIGA MARK II

Figure 3.3: Photo of the reactor operating at its maximum power of 250 kW with the emission of the characteristic Cherenkov light. The inner annular ring is the Lazy Susan channel with the sample loading pipe on the left (curved pipe).

reactor at LENA, this material is our choice. The Lazy Susan channels have a cylindrical shape with an inner diameter of about 32 mm and the standard container used at the LENA facility is a cylindrical container with an external diameter of 28 mm, an internal diameter of 23 mm, and a height of 94 mm plus 40 mm for the screw plug. In order to increase the volume available inside the containers (more volume, means more mass and more sensitivity) we decided to make our own containers with an optimized size to fit in the irradiation channel and to maximize the inner volume. The new container drawing is shown in Figure 3.4 on the facing page and they are made by machining a cylindrical rod of pure PE. The external diameters is 30 mm, the internal is 27 mm and the height is 135 mm plus 40 mm for the screw plug.

The sample to be irradiated is not placed directly inside this container because typically the samples are liquid and in order to avoid spills, a double container is required. Another reason is that the inner container can be cleaned in a deeper way and sealed in order to avoid contaminations during irradiation. The size of the irradiation container has been also optimized in order to contain our inner containers. The first ones are PE vials with different sizes and the biggest one has an external diameter of 25 mm and a height of 75 mm. This means we can put one and a half of these vials inside the irradiation container. The second type are PFA vials with a screw plug that are used for the cleanest procedure because the PFA is a very low contaminated material that can also be cleaned very well and have an external diameter of 25 mm and a height of about 90 mm. These vials are shown in Figure 3.5a and 3.5b on the next page.

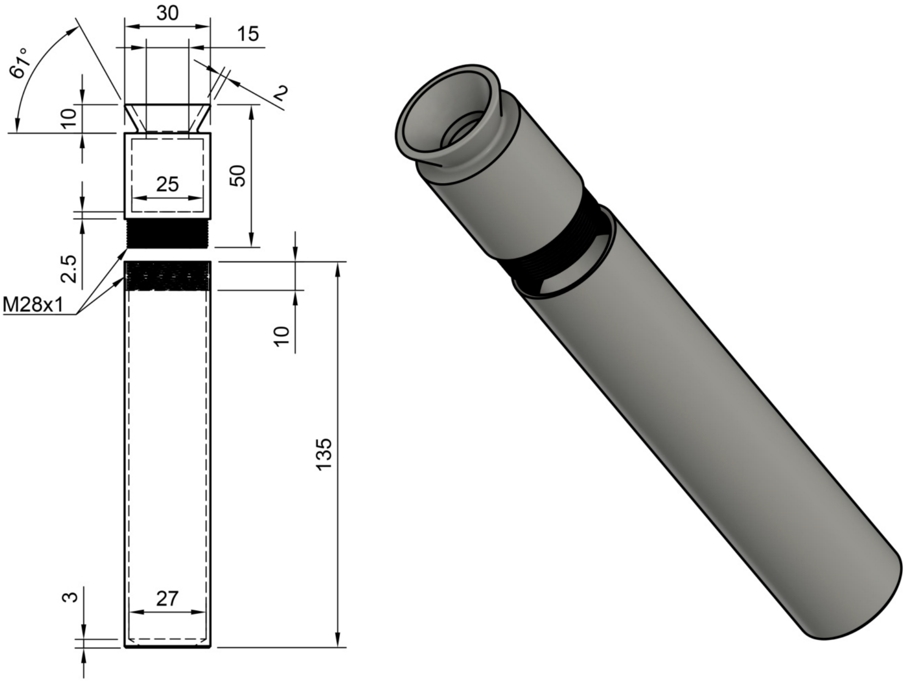

Figure 3.4: Technical drawing and picture of the new custom-made irradiation container

(a) PE vial

(b) PFA vial

Figure 3.5: PE and PFA vials used as inner containers for the irradiation of the sample.

### 3.2.2 HPGe gamma spectrometry

#### 3.2.2.1 General description

As a consequence of an alpha or more frequently beta decay, a nucleus can be produced in an excited state whose deexcitation generally occurs via the emission of one or more gamma ray photons. Since the energy of the emitted photons is related to the excitation energy of the nucleus, which is quantized, their energy is monochromatic and characteristic of the transition that produced them. By measuring the energy spectra of the photons emitted by an unknown source it is possible to perform both qualitative and quantitative analyses. In particular, it is possible to determine what radioactive nuclides are present in the sample, based on the energy of the gamma rays, and the activity (or concentration) of these nuclides by analyzing the rate of the emitted photons. This technique is called gamma spectrometry and can be performed with different types of detectors with different characteristics.

The most performing detectors are the High Purity Germanium Detector (HPGe) because they can reach the highest sensitivity both in qualitative and quantitative analysis. The HPGe is a type of semiconductor detector whose active volume consists of a high-purity germanium crystal. Through localized fusion techniques, developed in the mid-1970s, it is possible to create crystals of high purity with contaminations of the order of $10^9 - 10^{10}$atoms/cm$^3$ and with volumes up to a few hundreds of cubic centimeters. HPGe detectors are available in different geometries and the most common are planar and coaxial. The coaxial case has the advantage of being able to have a much greater detector thickness than the planar case, so as to have a high probability of interaction for high-energy gamma photons. The limit to the size of the crystals is given by the maximum distance at which the electrodes that create the electric field inside the crystal can be placed, necessary for the collection of the charges created by the interaction of a photon. Since the charge collection electrodes are placed on the external and internal surfaces of the cylinder, the coaxial crystal has the advantage that the distance between them does not change as the height of the cylinder increases, and therefore it is possible to make crystals whose length is much greater than the maximum distance of the electrodes.

The main feature of HPGe detectors is their excellent energy resolution. This is due to the fact that the energy gap between the valence band and the conduction band in germanium is only 0.7 eV, therefore, with the same deposited energy, more carriers (in this case electron-hole pairs) will be produced in a germanium detector than in detectors that require higher energies to produce single carriers. The improved energy resolution is a direct consequence of the reduction of the statistical fluctuations since they scale as $1/\sqrt{N}$, where N is the number of carriers generated per event. Figure 3.6 on the facing page shows spectra of environmental radioactivity obtained with different types of detectors, and the different energy resolution is clearly visible. The high energy resolution allows very close peaks to be resolved and lower activity sources to be detected when their signals are superimposed on a continuous background. Figure 3.7 shows an exploded view of an HPGe detector with the relative dewar containing the liquid nitrogen necessary to cool the crystal during operation. The need for cooling at cryogenic temperatures is due to the small energy gap (0.7 eV) between the valence and conduction bands of germanium, which makes it impossible to operate at room temperature due to the high thermal noise that would arise, as a consequence of the high conduction current generated by the charges released by thermal vibrations.

To perform spectroscopy measurements and obtain an energy spectrum, the HPGe detector must be equipped with an electronic chain for reading and processing the output

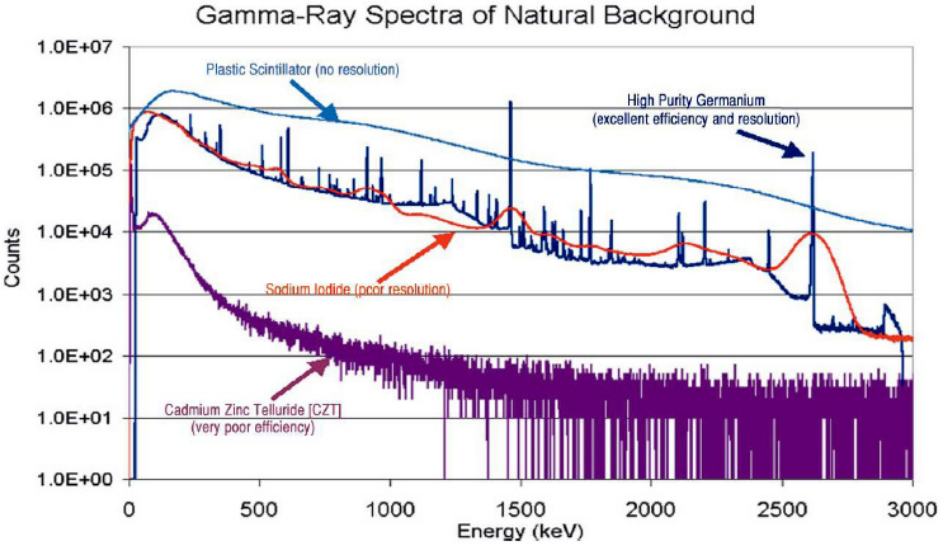

Figure 3.6: Background spectra acquired with different detectors where the different energy resolution is evident

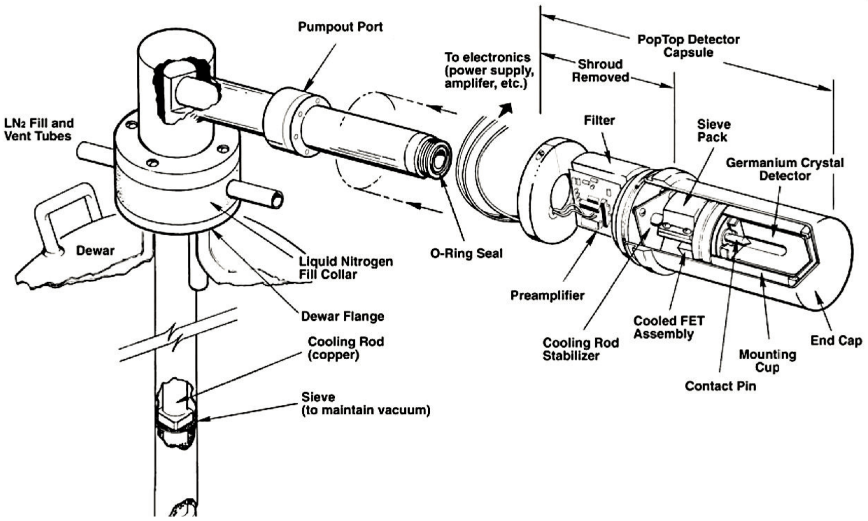

Figure 3.7: Exploded view of a PopTop HPGe detector with liquid nitrogen Dewar

Figure 3.8: Acquisition chain of an HPGe detector

signals and a storage system for the acquired data. The electronic chain of an HPGe detector is schematized in the diagram in Figure 3.8. The interaction of a photon with the germanium crystal produces electron-hole pairs that are collected by the electrodes through the electric field generated between them by the bias voltage. The charge produced is then converted into a current signal and sent to the preamplifier, which integrates it into a voltage signal whose amplitude is proportional to the energy of the incident photon. The pulse shape is optimized (semi-gaussian shaper) and its amplitude is increased by the amplifier. The signal coming from the amplifier is processed by a Multi-Channel Analyzer (MCA) which digitizes the amplitude of the analog signal and increases the counter of the channel corresponding to the amplitude of the measured signal by one unit. Each channel of the MCA then records the number of pulses that have a given amplitude/energy. The typical number of channels of an MCA for gamma spectroscopy with HPGe ranges from 4096 to 16384. In gamma spectrometry, the channel spectrum obtained through the MCA must be calibrated in energy in order to identify the energy associated with each peak. A source containing known nuclides that emit monochromatic gamma photons of known energy is used for the calibration. Since MCAs often do not exhibit perfect linearity over the entire measurement range, a multi-point calibration is performed in various regions of the energy spectrum.

A fundamental parameter that characterizes a germanium detector is the efficiency, which is necessary when it is required to determine the absolute activity of a sample. The absolute efficiency is defined as

$$\epsilon_{abs} = \frac{\#\text{ of event detected}}{\#\text{ of event emitted by source}} \tag{3.7}$$

From the definition it is clear that the absolute efficiency depends not only on the properties of the detector but also on the geometry of the detector-source system; in particular, it depends on the solid angle with which the source illuminates the detector, from the source materials and size, and from the dead layers present in the detector. The reconstruction of the efficiency is carried out by acquiring a spectrum of a source containing nuclides of known activity (standard source) and calculating the efficiency at each peak emitted by the source. Since the efficiency depends on the geometry of the detector-source system, as it varies, there is a variation in efficiency. An analytical procedure for calculating the efficiency can be poorly accurate, especially in the case of large sources, for which it is preferable to carry out an efficiency measurement with a standard source of known geometry (size of the source, distance from the detector, etc.). This measure is then used for comparison with the estimated efficiency through numerical simulators and, if the results provided are compatible, the numerical method itself is used for the efficiency calibration of any sample. The numerical methods normally used are based on Monte Carlo approaches. The typical systematic error obtained using this technique is less than 10 %.

#### 3.2.2.2 Low background facility at Milano-Bicocca

As introduced in Section 3.2.1 the NAA technique requires measuring the activated samples in order to determine the activity of the irradiated nuclides. This is generally performed with HPGe detectors. All the samples analyzed in this work are measured in the radioactivity laboratory at the University of Milano-Bicocca. This facility hosts four HPGe detectors with different characteristics, a low background HPGe detector and a $\gamma - \gamma$, and a $\beta - \gamma$ low background coincidence detector.

- GeSilena

This is a p-type coaxial HPGe detector produced by "Silena" with a relative efficiency of 30% and an energy resolution of 1.7 keV at 662 keV. A picture of the detector can be seen if Figure 3.9a

- GeGEM

  This is a p-type coaxial HPGe detector produced by "Ortec" with a relative efficiency of 30% and an energy resolution of 1.5 keV at 662 keV. A picture of the detector can be seen if Figure 3.9b

- GeKAN

  This is a p-type coaxial HPGe detector produced by "Canberra" with a relative efficiency of 70% and an energy resolution of 1.9 keV at 662 keV. A picture of the detector can be seen if Figure 3.9c

- GePozzetto

  This is a well-type HPGe detector produced by "Ortec" with a relative efficiency of 50% and an energy resolution of 1.9 keV at 662 keV. A picture of the detector can be seen if Figure 3.9d

- BeGe

  This is a planar-type broad energy HPGe detector produced by "Canberra" with a relative efficiency of 50% and an energy resolution of 1.2 keV at 662 keV. A picture of the detector can be seen if Figure 3.9e

- GMX

  This is a coincidence system based on two n-type GMX-type HPGe detectors produced by "Ortec" with a relative efficiency of 100% and an energy resolution of 1.7 keV at 662 keV. The system is equipped with a plastic scintillator detector for cosmic muon veto. A picture of the detector can be seen if Figure 3.9f

- GeSparK

  This is a $\beta - \gamma$ coincidence system based on a p-type coaxial HPGe detector produced by "Ortec" with a relative efficiency of 38% and an energetic resolution of 1.8 keV at 662 keV. The HPGE is coupled to a liquid scintillator detector in order to measure the beta events associated to the gamma photons. This system is described in detail in section 3.3.

### 3.2.3 Beta-gamma coincidence detector and radiochemical sample treatments

The typical sensitivities obtained with NAA and low background HPGe detector are of the order of $10^{-12}$ g/g to $10^{-13}$ g/g for $^{238}$U, $^{232}$Th and one order or magnitude lower for $^{40}$K. Since this is not enough for the requirements of the JUNO experiment we developed a new detector, called GeSparK [32] which allows obtaining a reduction of the background of a typical HPGe detector by exploiting the coincidence between the signal produced in a liquid scintillator detector by a beta (or alpha) particle and the coincidence signal produced in the HPGe detector by the deexcitation gamma photons. This is possible because the coincidence allows identifying with higher accuracy than the observed decay happened in the sample, and for example, it isn't due to environment radioactivity or cosmic muons,

(a) GeSilena (b) GeGEM

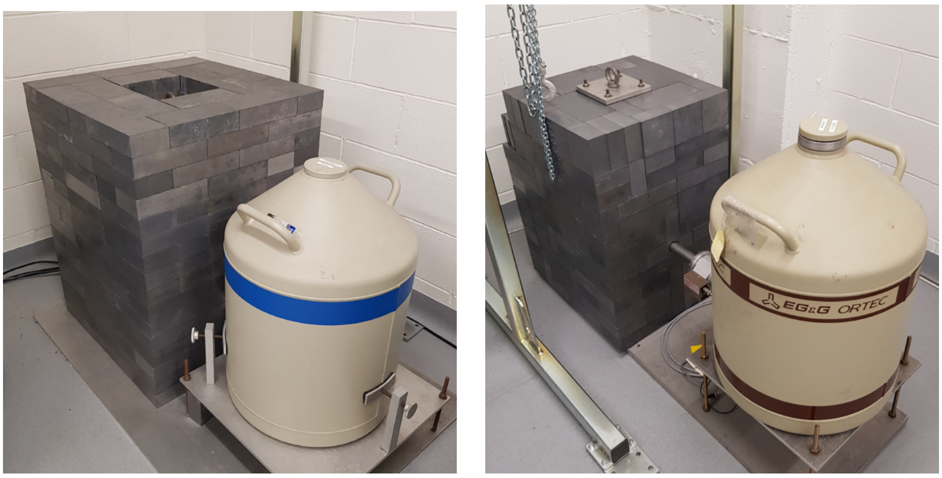

(c) GeKAN (d) GePozzetto

(e) BeGe (f) GMX

Figure 3.9: HPGe detectors at the radioactivity laboratory of the University of Milano-Bicocca

obtaining also more information about it, for example, the time distribution and the energy of both decays.

Most of the background of an HPGe detector is due to two components. The first is the gamma rays emitted in the decay of nuclides in the environment, in the detector shield, or in the material of the detector itself. The second component is due to the interaction of cosmic muons directly with the detector or more problematic are the interaction in the surrounding material and the production of electromagnetic showers that can be detected by the HPGe crystal. The use of coincidence detectors allows drastically reducing the first component because in order to accept a signal produced by the HPGe detector is required that a signal in the liquid scintillator detector is produced in coincidence. The only possibility for single gammas events to produce this type of event is to interact via the Compton effect in one detector and then be absorbed in the other. Another possibility is the simultaneous interaction of two uncorrelated gammas in the two detectors within the coincidence time window. These processes have a very low probability because the first is suppressed due to the interaction type probability and solid angle view of the two detectors, and the second contribution is negligible to due the very low background rate and short coincidence time window. As a consequence, the background of a coincidence detector is completely dominated by the cosmic muon interaction [32], because the electromagnetic showers can interact at the same time with both the detectors producing signal amplitudes in the regions of interest and there is no way to discriminate these events only using the information of the two detectors. The reduction of this component can be performed by using external plastic scintillators in order to detect the incoming muons (veto detectors). More details about the development of the GeSparK detector are provided in section 3.3 and the use of this detector for the measurement of activated samples for the JUNO experiment in section 3.4.

In parallel to the development of the GeSparK detector, we worked on chemical treatments to perform on the sample (LAB) in order to increase the measurement sensitivity. In particular, the main purposes of the chemical treatments are the removal of the interfering nuclides (as introduced at the end of the section 3.2.1.2) and the concentration of nuclides of interest in the sample. This topic is widely discussed in section 4.

## 3.3 The GeSparK detector

I started the development of the GeSparK detector during my master's thesis and during the Ph.D. the detector performances have been improved, both from the hardware and software point of view.

This detector was designed to allow measurements of the radioactivity content of a sample by exploiting the coincidence between beta or alpha decay and gamma photons to obtain a high reduction of the background. The main motivation was the measurement of the liquid scintillator of the JUNO experiment but this detector can also be used for different types of samples, such as materials screening of liquid samples or characterization of environmental samples. The sample to be analyzed is mixed with a liquid scintillator that emits light when it interacts with a charged particle. This mixture is optically coupled to a photomultiplier which generates an electrical signal that is used as a trigger for a decay (alpha or beta). This signal is digitized and memorized to allow studies on the shape and other features. The scintillation detector is positioned on top of a germanium detector for the detection of gamma photons emitted in coincidence with the beta or alpha decay, allowing an accurate spectroscopic analysis. The section of the structure of the GeSparK detector is shown in Figure 3.10. In the first part of this section the germanium

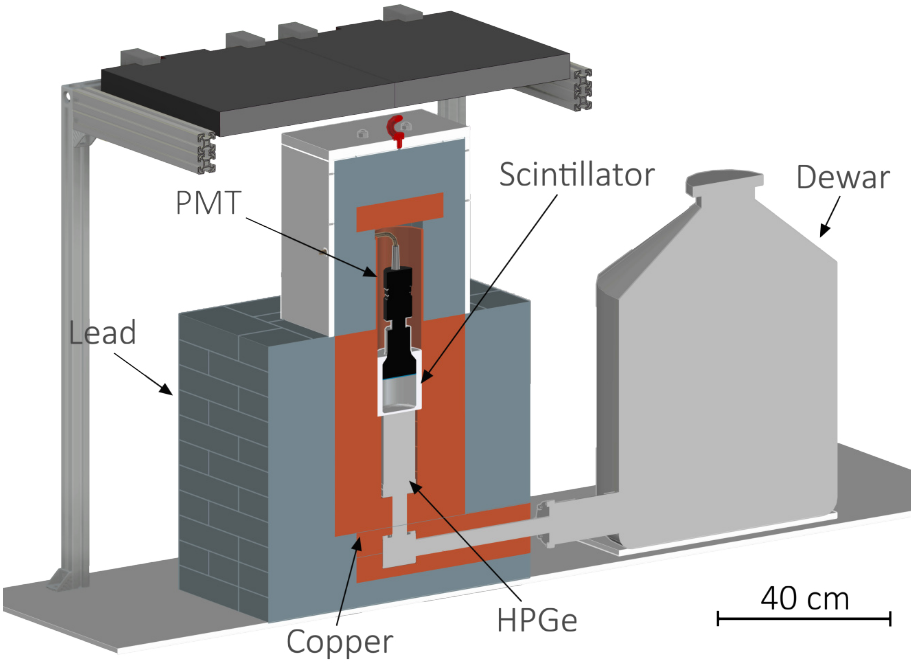

Figure 3.10: Section of the GeSparK detector with passive shielding and veto system

detector is described, in particular the characteristics of the instrument, the design, and the construction of the shielding. In the second part is described the liquid scintillation detector and, after a general introduction to liquid scintillators, its structure and operation.

Although the GeSparK detector is able to perform $\alpha/\beta$discrimination on the signal produced by the liquid scintillator [32], this feature will not be discussed here because it is not relevant for the measurement of activated samples. This is due to the fact that all the activated nuclides decay by beta decay since they have an excess of neutrons due to the neutron capture.

## 3.3.1 Detector structure

### 3.3.1.1 HPGe detector and passive shield

The germanium detector was chosen on the basis of the needs imposed by the system to be implemented. In particular, a first request is to have a low energy threshold, so as not to lose low-energy photons such as the X emission. For this purpose, a coaxial detector with 38% relative efficiency was chosen (900 g), which allows having good sensitivity at high energy and is equipped with a carbon window, which allows having a very low energy threshold. Another fundamental request is related to the geometrical structure required for the detector. Since we wanted to have the germanium detector facing upwards in a vertical position in order to facilitate the positioning of the scintillation detector and to optimize its geometrical efficiency, a dewar far from the detector was chosen, see Figure 3.10, so that it is possible to build the shield around it. The shield around the germanium detector consists of a 10 cm copper layer surrounded by a 15 cm lead layer. The copper and lead used for the shielding have been selected to minimize their radioactive contaminants: the copper is oxygen-free high thermal conductivity (OFHC) and the lead has an activity $<$135 Bq/kg for $^{210}$Pb. The upper shielding part is instead made up of a 3 mm layer of

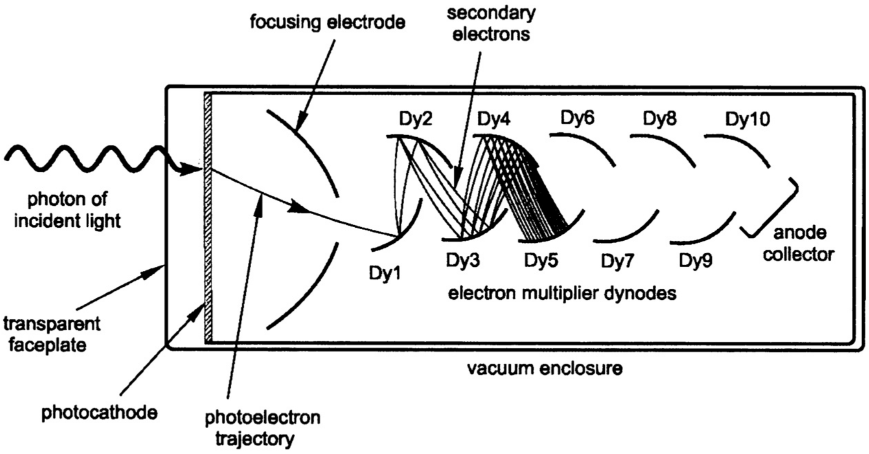

Figure 3.11: Scheme of a PMT and its operation.

copper and 5 cm of lead. The different size was chosen because in this section there are no detectors, but only the base of the photomultiplier and it was possible to lighten the structure. The upper part has a cap, a removable portion, consisting of 10 cm of lead and 5 cm of copper, for the insertion of the scintillator with the photomultiplier.

#### 3.3.1.2 Liquid scintillator

Liquid scintillation has been a quantitative detection and measurement technique of radioactivity since the early 1950s. It is widely used in many fields, ranging from monitoring environmental radioactivity to detecting rare events in particle physics. The widespread use of this technique is a consequence of its numerous advantages, such as the high detection efficiency, the possibility of automation, and spectroscopy on the acquired signals, allowing the analysis of several radionuclides simultaneously.

The liquid scintillation technique involves mixing the sample to be analyzed in a container with a particular scintillating mixture, containing fluorescent substances dissolved in a suitable solvent. The scintillating mixtures are typically made up of long-chain aromatic organic solvents, such as LAB (linear alkylbenzene), in which the actual scintillator is dissolved, i.e. a substance capable of emitting photons following the release of energy by charged particles.

Many scintillation cocktails are commercially available with varying scintillation capabilities and miscibility with other compounds. The best products, in addition to a high photon emission, have the characteristic of being able to accept both organic and aqueous samples and possibly acid solutions. Particular mixtures can be specially prepared for certain applications that require particular characteristics, such as those produced for rare event physics experiments like JUNO.

The scintillation process involves the conversion of the energy deposited by the interacting particle into light. To convert photons into an electrical signal, which can be processed by electronics, a photomultiplier tube (PMT) is generally used. This device converts the photons produced by the liquid scintillator into electrons when they interact with the photocathode positioned in the front face of the PMT, as shown in Figure 3.11. The photoelectrons produced at the photocathode are multiplied through a series of positively charged dynodes with increasing voltage. Since the amount of light produced by a scintillation event is

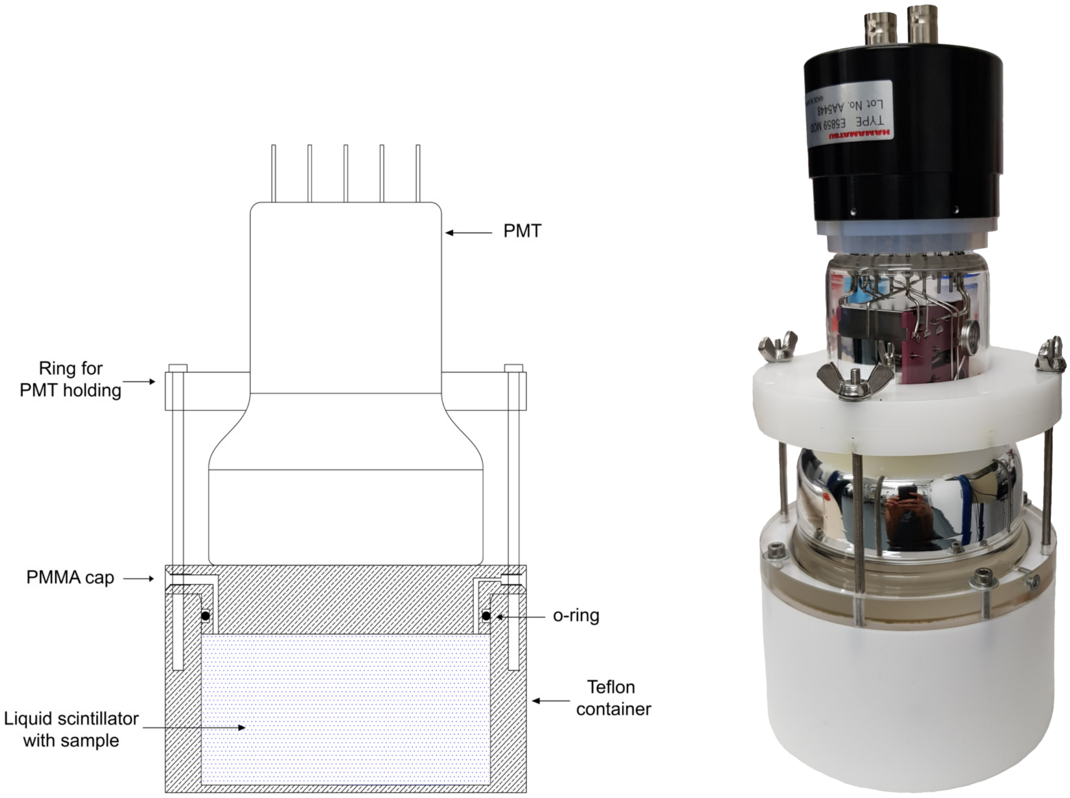

(a) (b)

Figure 3.12: Schematic representation and photograph of the liquid scintillation detector

normally very low ($\sim$ 10 photons per keV of absorbed energy), the PMT must be able to amplify the initial signal by a very large factor. PMTs used in liquid scintillation applications typically have a gain greater than $10^6$. The PMT is a fundamental component of the acquisition chain as it is the element that implements the light-to-current conversion and determines many of the characteristics of the final signal, such as the rise time and the signal/noise ratio.

The scintillation detector that has been developed for the GeSparK detector consists of a cylindrical container in Teflon with a thin bottom thickness (2 mm), in order to minimize the absorption of low-energy photons, and a cap of PMMA (polymethylmethacrylate) which, being transparent, allows coupling with the PMT, a low-background 3 inch Hamamatzu. The volume of the container is 200 mL, but it can eventually be modified according to the type of measurement; larger if you want a high mass, or smaller if the priority is the maximization of efficiency. The system is shown in Figure 3.12.

### 3.3.2 Introduction to cosmic muons veto

Passive shieldings consist of materials interposed between the detector and the source of the background in order to reduce its contribution to the detector signals. Active shieldings can also be added, where necessary, in order to provide a further reduction of the environmental and cosmic backgrounds. Active shieldings are all those techniques that are not based on the absorption of unwanted photons, but try to eliminate their causes or limit their effects. Anticoincidence techniques are usually used as shielding from cosmic muons. They are made by placing a plastic scintillator of suitable dimensions over the passive shielding. When a muon passes through the plastic scintillator, a signal is produced, which is used as a veto for the acquisition of the detector signals. In particular, when a coincidence is observed between the detector and the plastic scintillator within a certain time window, the detector signal is discarded as it is probably produced by the interaction of the muon.

During my Ph.D. I worked on the installation and optimization of a muon veto system for the GeSparK detector. As I will describe in detail in the dedicated section (3.4), the cosmic muons are the main background sources for the measurement of the content of $^{232}$Th by NAA. In this case, the implementation of a high-performance active muons veto system can increase the measurement sensitivity.

In this section firstly I'm going to give a general description of the use of plastic scintillators for the veto of cosmic muons and then I'm going to describe the preliminary measurement performed in order to verify the angular distribution of the muon flux in the radioactivity laboratory of the Milano-Bicocca University. After that, I'm going to provide a detailed description of the simulation of the plastic scintillator detectors for the GeSparK detector and their implementation.

#### 3.3.2.1 Plastic scintillator detectors for muon veto

As introduced before, a common method to implement the active shielding of the cosmic muons is based on plastic scintillator detectors. The plastic scintillators are produced by dissolving scintillator compounds in the plastic monomers before the polymerization process. With this technique, the resulting product exhibits highly uniform scintillation and optical properties. Scintillators are finally machined to final dimensions using diamond tools to provide optimum quality surfaces for total internal reflection. Based on the organic activator and the host material is it possible to produce a wide variety of plastic scintillators with different characteristics in terms of emission wavelength and decay time.

Typically, the scintillation emission of plastic scintillators has a maximum at around 425 nm and they are characterized by a relatively large light output, typically 25-30% of NaI(Tl) crystals, and a short decay time of around 2 ns. This makes the material suited for fast timing measurements, as required for veto applications. The plastic scintillators are optically coupled to a PMT in order to collect the emitted light and convert it into an electric signal that can be processed by electronics.

The scintillators are placed on the top and on the side of the detector to be shielded in order to intercept the incoming muons. When the muons pass through the scintillator they deposit a fraction of their kinetic energy. The amount of deposited energy is directly proportional to the width of the plastic scintillator detector. As described in the next section, the muon energies are in the GeV scale and at this energy, they are minimum ionizing particles. In these conditions, the energy loss of the muons is of the order of $2\,\mathrm{MeVcm^2/g}$. This value multiplied by the density of the plastic scintillator and its width provides the deposited energy in MeV. Assuming a width of 5 cm we get:

$$E(MeV) = 2\,\mathrm{MeVcm^2/g} \cdot 1\,\mathrm{g/cm^3} \cdot 5\,\mathrm{cm} = 10\,\mathrm{MeV} \tag{3.8}$$

This energy is then converted into light and electric signal that is used to register the passage of the muon in order to reject the detector signals in coincidence with the muon one. The coincidence is defined by a time window of suitable amplitude. If the time window is too large, erroneous coincidence events could be accepted and thus signals not produced

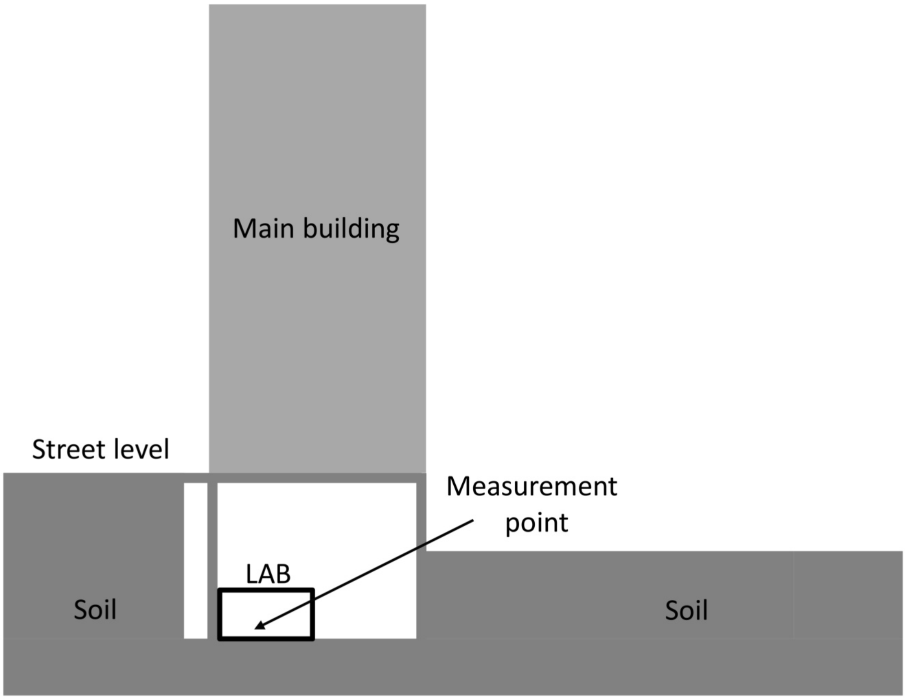

Figure 3.13: Section scheme of the physics building of the University of Milano-Bicocca and the location of the radioactivity laboratory, where the muon angular distribution was measured.

by muons could be discarded, and if it is too narrow there is the risk of not rejecting a muon signal due to the fluctuation of the arrival time of the detector and scintillator signals, which produces a non-coincidence event. The optimum value must be chosen according to the time specification of the detectors.

#### 3.3.2.2 Cosmic muons flux measurement

The overall angular distribution of muons measured at sea level follows with good approximation a $\cos^2$ distribution [33]: it is maximum at 0° on the vertical and goes to zero at 90°, parallel to the ground. The radioactivity laboratory of the physics department of the University of Milano-Bicocca is located on the -3 floor of the department building and this could modify the angular distribution of the muon flux due to different absorption at different angles as a consequence of the asymmetric structure of the building. A schematic section of the structure is shown in Figure 3.13.

In order to understand this effect, a dedicated measurement of the angular distribution has been performed. The experimental setup is composed of two plastic scintillators produced by Shonix, which have a size of $420\,\mathrm{mm} \times 300\,\mathrm{mm} \times 50\,\mathrm{mm}$, installed on a rotating support at a fixed distance of 30 cm. The two plastic scintillators are powered by a NIM high-voltage power supply at 800 V and the signals are processed by an analog NIM electronic chain composed of: a preamplifier, an amplifier with semi-gaussian shaper, a timing-SCA, a coincidence unit, and a counter. The NIM electronic chain is represented in Figure 3.14. The signal from the PMT is integrated by the preamplifier and then shaped into a semi-gaussian waveform with a short shaping time (0.5 µs) and amplified. These

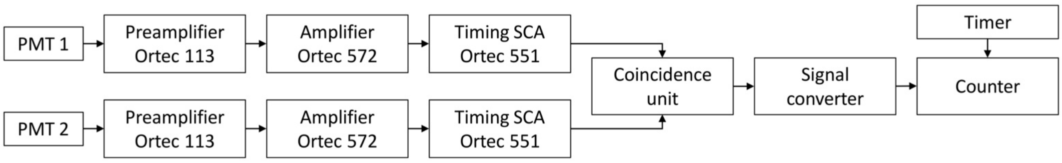

Figure 3.14: Block diagram of the electronic chain used to process the signal of the PMT for the measurement of the muon flux.

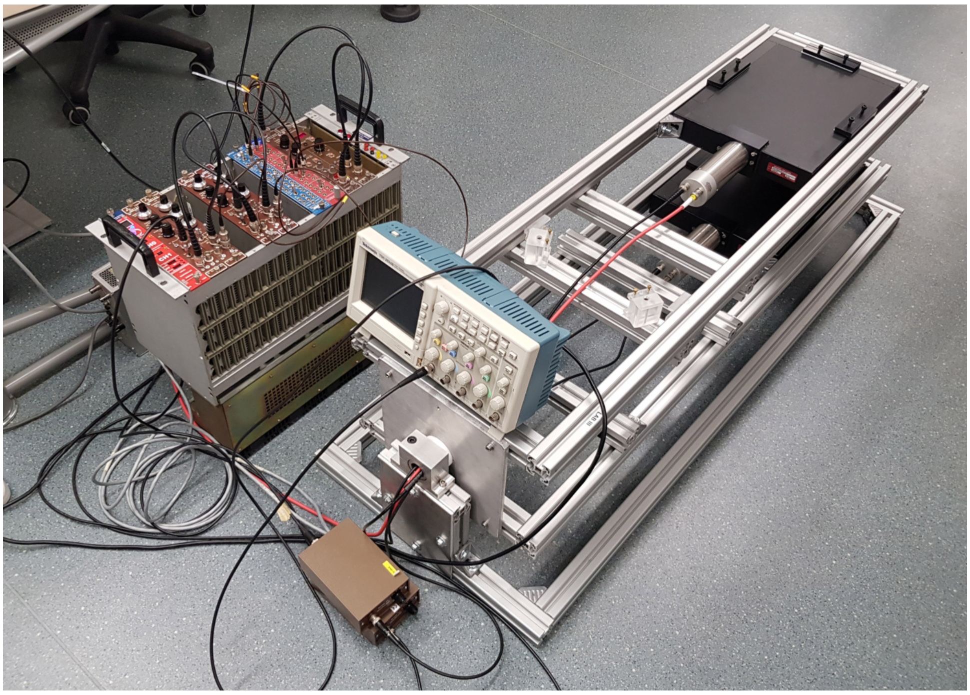

Figure 3.15: Experimental setup for the muon flux measurement.

signals are sent to the timing-SCA that allows generating a logic signal when the amplitude of the input signal is greater than a specific threshold. This is necessary because we want to select only the muons and not the environmental radioactivity signals. As calculated in equation 3.8 the deposited energy in these detectors by a muon is of the order of 10 MeV. Since the most energetic gamma ray produced by natural radioactive decays is the 2615 keV from $^{208}$Tl of the $^{232}$Th chain, it is possible to set the threshold of the timing-SCA around 5 MeV in order to select only the muon events. The logic signals of the timing-SCA are sent to the coincidence unit that generates another logic pulse only when the two input signals are overlapping (coincidence). The resulting coincidence signal is sent to a signal converter and then to the counter. A timer module is connected to the counter in order to set the measurement time. The complete setup is shown in Figure 3.15.

With this measurement system, two sets of measurements were performed. The rotation axis of the system was positioned parallel and transverse with respect to the main building. With reference to Figure 3.13 the rotation axis of the detectors was oriented perpendicular to the section in the picture for the "parallel" case (we call this $\phi = 0°$) and rotated by 90° for the transverse case (we call this $\phi = 90°$). For each of these two positions the measurement of the flux is performed every 10° from $-90°$ to $90°$, by counting the coincidence events for

8 minutes at each position. The results are shown in Figure 3.16

In order to interpret the experimental data, a simple model has been constructed. The experimental setup is not able to measure the exact angular distribution of muons because a muon that is able to induce a signal in both the detector can come from a range of angles. In other words, the detector integrates the muon angular distribution in an angular range given by the geometrical properties of the detectors. The integral goes from $\Theta - k$ to $\Theta + k$, where $\Theta$ is the angle formed by the axis perpendicular to the plastic scintillator with the vertical axis and k is the semi-range angle of the field of view of the system. Since the distance of the two plastic scintillators is about equal to the height, the k parameter is expected to be around $\pi/4$. The function that describes the data can be computed in the following way:

$$I(\theta) = a \cdot \frac{\int_{\Theta-k}^{\Theta+k} \cos^2(\theta) d\theta}{\int_{-k}^{k} \cos^2(\theta) d\theta} = a \cdot \frac{\cos(2\Theta)\sin(k)\cos(k) + k}{k + \sin(k)\cos(k)} \tag{3.9}$$

where "a" is a coefficient that represents the number of counts at $\theta = 0$ and the denominator is simply a normalization factor in order to obtain that the maximum of the function is equal to "a".

Although it would be possible to perform a fit of the data with the model function, the k coefficient is not a completely free parameter, because it is determined by geometric constraint and its best fit value would not be representative of its real value. This is because the deficit at high energy due to the absorption of the muons is strongly correlated with the k coefficient, so the fit can converge to a lower value of k in order to adapt the function to the lower data but this has no sense because the deficit is due to the absorption and not to a different field of view of the detection system. In order to have a more accurate estimation of the k value with respect to the simple consideration described before that can be used to describe the experimental data, a simulation was performed. The detector system response was reproduced with a Monte Carlo model using a simulation software based on Geant4 called "Genesis" that I developed during my master's and Ph.D. thesis (see Appendix B). The software allows describing the geometries with a text file and it is able to simulate a muon flux distributed with a $\cos^2$ around the experimental setup. More detail about these types of simulations will be provided in the next section when I describe the simulation of the GeSparK detector response. The simulations were performed for each angular position (every 10° from $-90°$ to $90°$) by simulating 100 000 muons for each position and counting the number of event that produces a coincidence signal in the two detectors. In Figure 3.17a and 3.17b are shown respectively the Monte Carlo model of the detectors and the resulting angular distribution. The best fit of the data with the equation 3.9 provided the best estimation for $k = Pi/4.11$ or 43.8°. This value is used to fix the k value for the function 3.9 used to describe the experimental data with "a" fixed to the data value at $\theta = 0°$. The resulting curves are also shown in Figure 3.16.

By observing the plot we can say that for the red data ($\phi = 0°$, rotating axis perpendicular to the building section) the flux is lower than the function for almost all the negative angles from about $-20°$ while for positive angles the deficit is visible only for very large angles, starting from 70°. This is due to the presence of the solid ground on the left (negative angles) of the building that reduces the muon flux starting from low angles while on the right the soil level is lower and the absorption is significant only at very high angles. For the blue data ($\phi = 90°$, rotating axis parallel to the building section) there is a very good agreement in almost all the ranges with only a small deficit at very high angles and a small asymmetry because at positive angles the deficit is higher than at negative angles. This can be explained considering that in this orientation the absorption is due only to the

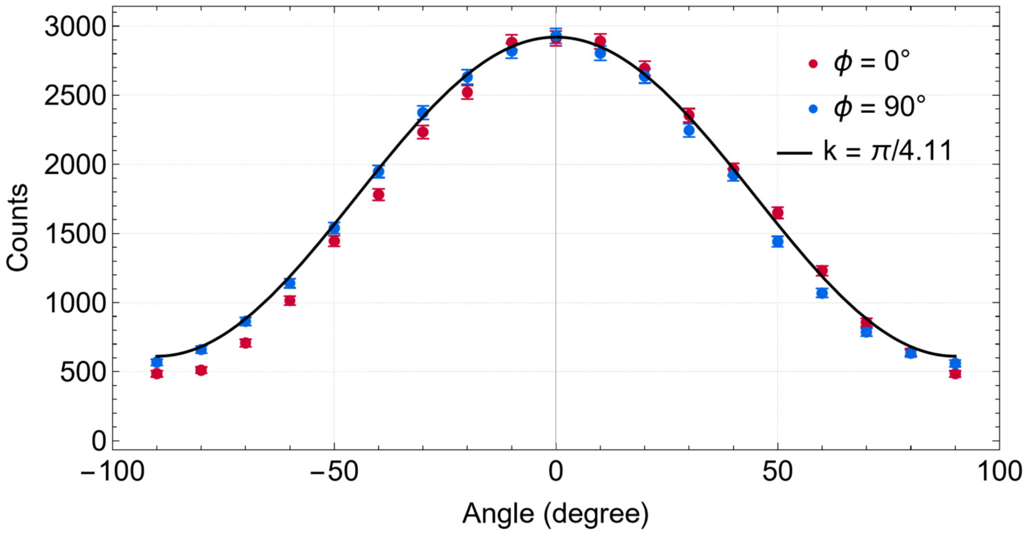

Figure 3.16: Muon angular distribution at the radioactivity laboratory. The $\phi = 0°$ is referred to the parallel configuration and the $\phi = 90°$ is referred to the transverse one. See the text for more detail about the orientations of the experimental setup.

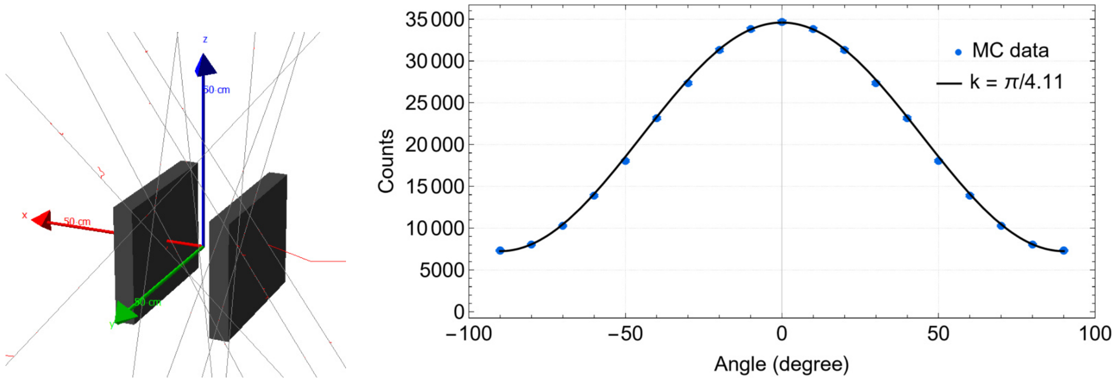

(a) (b)

Figure 3.17: Monte Carlo model of the detectors used to measure the muon flux angular distribution (3.17a) and the muon angular distribution obtained my MC simulation with the best fit (3.17b)

building that is mostly empty, but for high angles, its contribution can be significant and the asymmetry is due to the asymmetry of the building structure (is longer on one side that the other).

In conclusion, this measurement showed that the overall angular distribution of muons in the radioactivity laboratory follows with good agreement a $\cos^2$ distribution with small deviations due to the absorption in the soil and buildings. However, since these differences are quite small they will not be directly considered in the next considerations and in the simulations performed for the GeSparK detector.

#### 3.3.2.3 Monte Carlo reconstruction for veto system design

The information about the angular distribution of the muon flux in the radioactivity laboratory was used to implement a simulation of the whole structure of the GeSparK detector in order to determine the response of the plastic scintillator detectors and their veto efficiency.

As introduced in the previous section, these simulations were performed by using the Genesis Monte Carlo software, whose description is in Appendix B. To perform these simulations with the best accuracy the following information must be provided to Genesis:

- Geometric model of GeSparK detector with plastic scintillators
- Angular distribution of the muon flux
- Energy distribution of the muons

The geometric model of the GeSparK detector is constructed by combining the CAD model developed during the construction of the detector and a text-based description of the HPGe and scintillator detectors. The CAD model includes the geometry of the copper and lead shieldings, the liquid nitrogen Dewar and the cold finger of the HPGe. Using CAD have been also created the models of the support frame for the plastic scintillators and the plastic scintillators themselves. The text geometry is instead used for the description of the HPGe detector, comprising the germanium crystal, the holder, the end-cap, and the cold finger, and for the description of the LS detector, as described in Section 3.3.1.2.

The CAD models can be imported in Genesis by using the stl format and defining for each solid the material composition by using a dedicated interface while for the text geometry Genesis is currently used the TextGeom module of Geant4.

The proposed setup for the plastic scintillator detectors for the GeSparK detector is shown in Figure 3.18 on the next page. It is composed of six plastic scintillators: two on the top of the detector ($1000\,\mathrm{mm} \times 500\,\mathrm{mm} \times 50\,\mathrm{mm}$) and the other four around the liquid scintillator radiation shield ($420\,\mathrm{mm} \times 300\,\mathrm{mm} \times 50\,\mathrm{mm}$), in order to cover the sides of the detector.

The Genesis software utilizes the General Particle Source (GPS) class of Geant4 in order to generate the primary particles to propagate. This class is very versatile and allows defining a very wide range of sources. As many other G4 classes, the GPS can also be controlled by the G4 user interface (UI) with its dedicated commands and this allows modifying the properties of the generated particles during the execution of the program (but only between runs). In particular, the GPS allows the user to define the angular and energetic distributions of the primary particle, in this case muons, by providing a set of UI commands that define the histograms of the distributions.

As far as the angular distribution is concerned I used a $\cos^2$ distribution in $\theta$, based on the analysis described in section 3.3.2.2, and a uniform distribution in $\phi$. Since the GPS

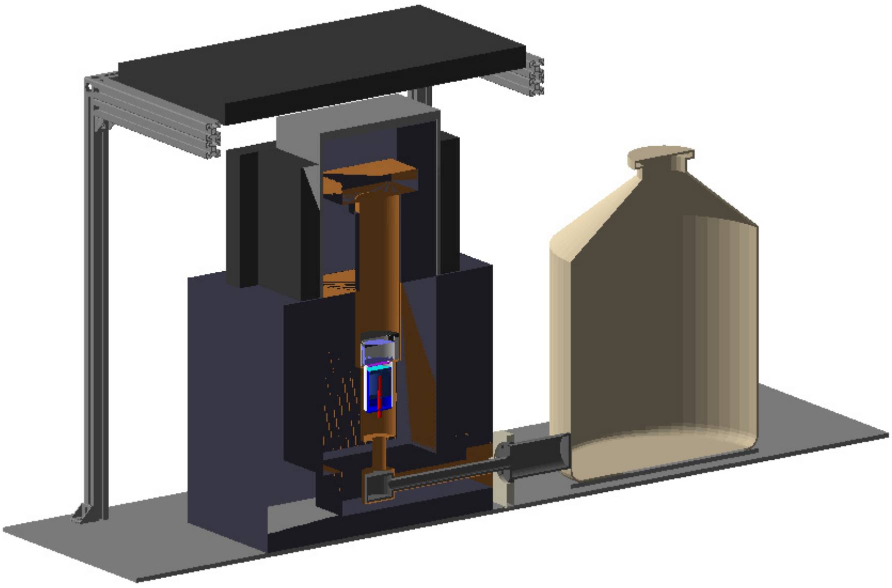

Figure 3.18: Complete Monte Carlo model of the GeSparK detector, including the HPGe and LS detectors, the passive shieldings, and the plastic scintillators for muons veto.

| Detectors | Efficiency |
|---|---|
| Top | 60% |
| 2 side | 33% |
| Top + 2 side | 75% |
| Top + 4 side | 87% |

Table 3.2: Plastic scintillators veto efficiency obtained by Monte Carlo simulation of the GeSparK detector by assuming a $\cos^2$ muon distribution.

samples the $\theta$ and $\phi$ coordinates independently, in order to allow the GPS to generate the desired distribution the provided histogram must include the $\sin(\theta)$ term of the differential in spherical coordinates system. In this case the resulting distribution is given by $\sin(\theta) \cdot \cos^2(\theta)$. A dedicated algorithm has been developed in Genesis in order to generate events distributed on a semi-spherical surface with a generic radius (1.5 m for these simulations) from the LS and HPGe detectors of GeSparK, with the angular distribution provided by the GPS class.

The energy distribution of the muons should not be a critical parameter of the simulation because the behavior of high-energy muons is not very different with respect to their energy due to the fact that they are concentrated in the minimum ionization region. In order to use a quite realistic distribution, instead of a monochromatic source, the energy histogram is obtained by approximating the distribution reported in [34] from the muons at 0° zenith angle at sea level from 1 GeV to 100 GeV. The histogram is shown in Figure 3.19.

A simulation of the experimental setup has been performed with 500 000 muons and from the resulting data, the veto efficiency for different combinations of plastic detectors has been evaluated. I considered the efficiency of the top detectors, two side detectors, the combination of the top and two sides, and the complete setup (top plus four sides). The obtained results are listed in Table 3.2. In the next section these results are discussed in relation to the experimental ones and the optimization of the modeling is described.

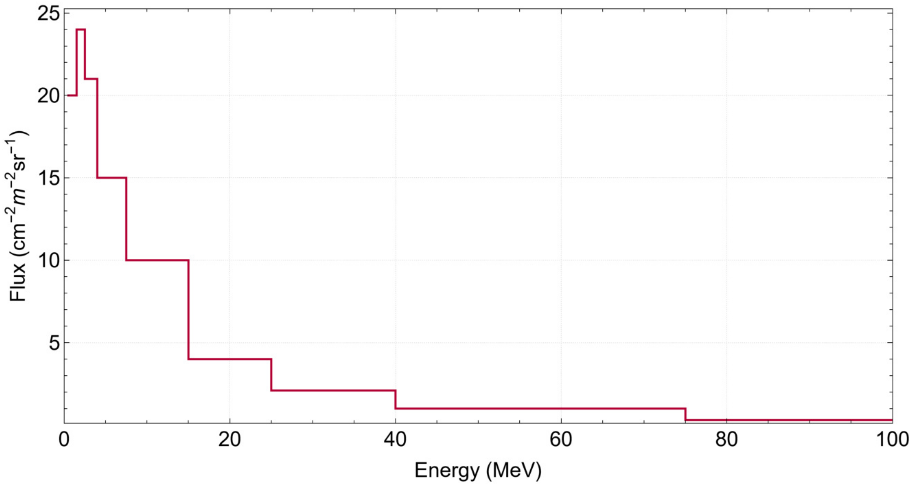

Figure 3.19: Energy distribution used in the Monte Carlo simulation of the GeSparK veto system for cosmic muons.

#### 3.3.2.4 GeSparK veto system and performances

Based on the encouraging results obtained from the simulations, the veto system has been implemented. Two plastic scintillators 1000 mm × 500 mm × 50 mm, produced by Nuvia, were placed on the top and four plastic scintillators 300 mm × 420 mm × 50 mm, produced by Scionix, were placed on the side. These detectors are equipped with a PMT in order to convert the light into an electric signal. The signals produced by the six detectors are summed with a summing amplifier and then sent to a NI oscilloscope for digitalization and the analysis of the veto signals is performed offline. The HV voltage for the PMTs is provided by a dual-channel HV power supply from CAEN. One channel provides the HV voltage to the two top detectors and the other channel to the four side detectors. More information about the signal processing of the GeSparK detector are provided in section 3.3.3.1. The resulting detector is shown in Figure 3.20.

With the complete system in operation, a set of background measurements were performed with the different combinations of anticoincidence detectors listed in 3.2 in order to compare the experimental value with the predicted ones by using the simulations. The four background measurements were performed by connecting to the summing amplifier only the relevant plastic scintillator detectors and acquiring the corresponding signal in coincidence to the LS and HPGe detectors. The resulting veto efficiencies are reported in Table 3.3 As can be seen from these results, the measured efficiencies are quite similar to the simulated ones but there are deviations. In particular, the effectiveness of the top plastic scintillator is overestimated by the MC (7%) while the effectiveness of the sides detectors is underestimated (3%), providing an overall overestimation for the complete set by 8%.

A possible explanation of these differences could be a non-exact estimation of the angular distribution of the muons, which could be quite different from the simple $\cos^2$ but not visible to the total flux measurement performed before. The angular distribution of atmospheric muons is not constant but depends on the energy of the muons considered [33]. At the sea level if we integrate all the energetic contributions we obtain the usual $\cos^2$ distribution which is characteristic of the muons of about 3 GeV of energy. At lower energy, the angular distribution becomes increasingly steep, while at higher energy it flattens,

Figure 3.20: Picture of the GeSparK detector with the complete muons veto plastic scintillator system.

| Detectors | Efficiency |
|---|---|
| Top | 53% |
| 2 side | 36% |
| Top + 2 side | 71% |
| Top + 4 side | 79% |

Table 3.3: Measurement results for the plastic scintillators veto efficiency.

approaching a $1/\cos$ distribution. At large angles low energy muons decay before reaching the surface and high-energy pions decay before they interact, thus the average muons energy increases. If we consider that the radioactivity laboratory is located on floor -3 of the Department building, we can assume that a fraction of the kinetic energy of the muons is lost in the passage through the walls of the building, losing an energy in the order of some GeV. In this hypothesis, the energetic distribution is simply shifted by some GeV to lower energies but also the angular distribution changes, because the original low-energy muons at ground level are stopped in walls and the more energetic muons became the new low-energy ones in the lab. In this case, we can think that the mean angular distribution is shifted to distributions associated with more highly energetic muons than 3 GeV (mean value at sea level).

In order to evaluate this effect, based on the data in reference [33], the angular distribution of muons at different energies has been reconstructed and used to generate the relative histogram distribution necessary for the Monte Carlo simulations. In Figure 3.21 are shown the reconstructed distribution for different energies, from 1 GeV up to 100 GeV, and are clearly visible the differences, in particular the increase of the contribution at large angles for high energy muons. The data at 1 GeV, 3 GeV, 10 GeV and 100 GeV are

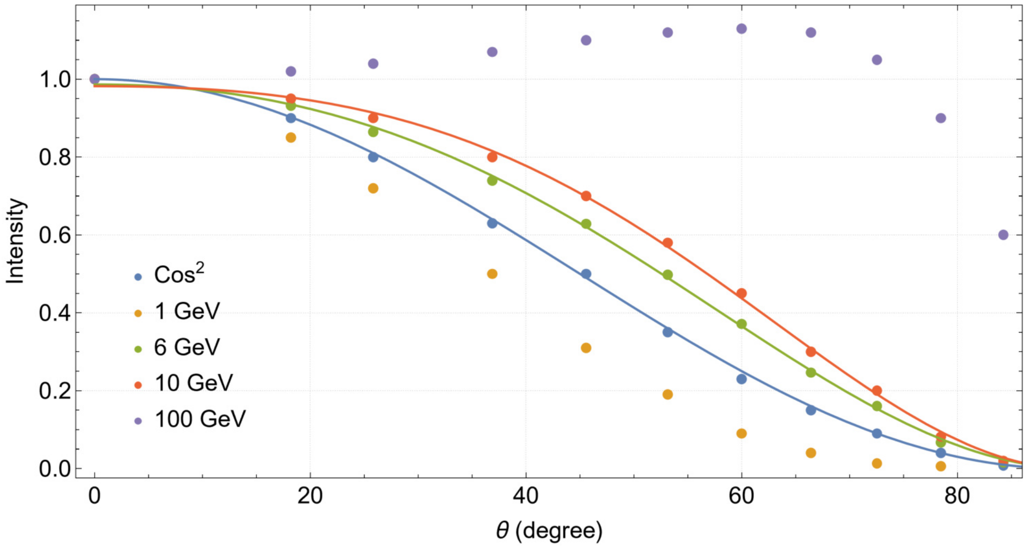

Figure 3.21: Reconstructed angular distribution for atmospheric muons at different energies from the data reported in [33] (1 GeV, 3 GeV, 10 GeV and 100 GeV). The data at 6 GeV are obtained by weighted mean of the data at 3 GeV and 10 GeV. The interpolations functions are: $0.9865 \cos^2\left(0.01151 \cdot x + 0.00006280 \cdot x^2\right)$ for the green line and $0.9820 \cos^2\left(0.007523 \cdot x + 0.0001081 \cdot x^2\right)$ for the red line.

| Detectors | Efficiencies | | | |
|---|---|---|---|---|
| | 3 GeV ($\cos^2$) | 6 GeV | 10 GeV | Measured |
| Top | 60% | 53% | 51% | 53% |
| 2 side | 33% | 33% | 34% | 36% |
| Top + 2 side | 75% | 69% | 68% | 71% |
| Top + 4 side | 87% | 83% | 82% | 79% |

Table 3.4: Monte Carlo estimations for the plastic scintillators veto efficiency for different assumed angular distribution compared to the experimental values.

obtained directly from the plot in the reference [33], while the distribution at 6 GeV has been estimated by using a weighted mean between the 3 GeV and 10 GeV data. The PDF of the distribution at 6 GeV and 10 GeV have been computed by fitting the data points with the parametric function $a \cdot \cos^2\left(b \cdot x + c \cdot x^2\right)$, where a, b and c are free parameters (green and red curve in Figure 3.21. These functions are then multiplied for $\sin(\theta)$ and normalized to obtain the PDFs. These PDFs are used to construct the histograms of the distributions required by Genesis. These histograms have been used to perform two other simulations and evaluate the new estimations of the veto efficiencies. The results are reported in Table 3.4, together with the efficiency computed assuming a $\cos^2$ distribution and the experimental values. The results at 6 GeV provide the most accurate estimation for the top detectors and a good agreement for the other configurations with an error much lower than the $\cos^2$ distribution. This corroborates the hypothesis that the angular distribution is distorted with respect to the $\cos^2$ distribution due to the muons kinetic energy loss and absorption in the materials. This condition can be used for further studies and improvement of the GeSparK veto system or other detectors in the radioactivity laboratory of the University of Milano-Bicocca.

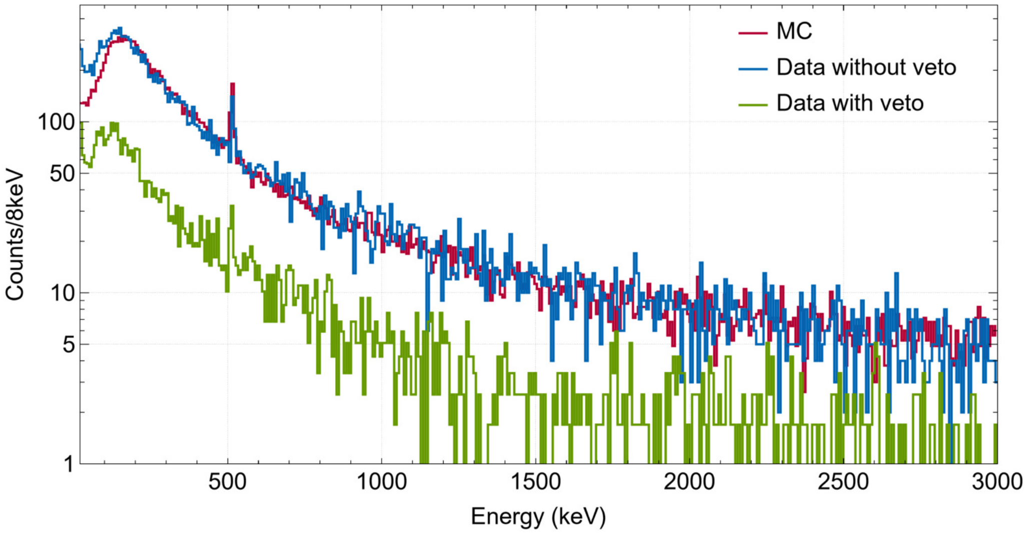

Figure 3.22: HPGe background spectra of the GeSparK detector with and without the application of the cosmic muon veto, obtained by measuring the coincidence events between LS and HPGe detector in absence of radioactive sources in the LS. In the plot is superimposed the simulated energy deposition in the HPGe detector produced by cosmic muons, normalized for the total number of events in the measured spectrum without veto.

The data produced by the simulation can also be compared to the residual background of the GeSparK detector after the application of the coincidence event selection. In this case, the detected events are associated only with signals that are produced in coincidence in both the LS and HPGe detectors. In Figure 3.22 are shown the spectra of the residual background of the GeSparK detector with and without the application of the cosmic muon veto, obtained by acquiring the coincidence events in absence of a sample in the LS detector. In the same plot is superimposed the distribution of the energy deposited in the HPGe detector obtained by the simulation and normalized for the number of events in the measured spectrum. The simulation reproduces with very good agreement the shape of the GeSparK background in the whole spectrum except for the very low energy region. This agreement and the absence of any particular peak in the background spectrum, except the 511 keV, which is produced by the annihilation of positrons produced by the muon showers, indicates that the background of the GeSparK detector is dominated by the contribution of the cosmic muon showers that can be produced when they interact with the passive shielding of the GeSparK system.

### 3.3.3 Data acquisition and analysis

#### 3.3.3.1 Signals processing and acquisition

As introduced in section 3.3.1, the GeSparK detector is composed of a liquid scintillator, an HPGe, and the muons veto plastic scintillator detectors. The signals produced by these detectors are acquired by a common acquisition system composed of two ADC boards, NI PXI 5122 and NI PXI 5153, produced by National Instrument (NI) that digitize the waveforms and store them for subsequent offline analysis. A block diagram of the signal processing electronic chain is shown in Figure 3.23.

The first is a 14-bit resolution ADC with a maximum sampling rate of 100 MHz and it

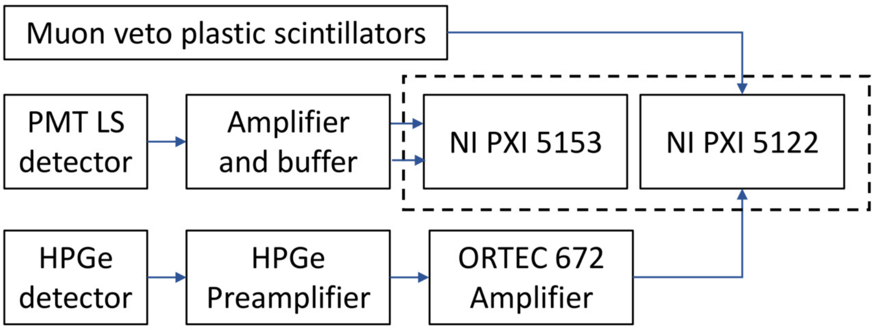

Figure 3.23: Block diagram of the electronic chain for the signals processing of the GeSparK detector

is used to acquire the germanium detector and muons veto signals. Thanks to the high resolution in bits, this card allows having a digitalization of the signals with a negligible discretization of the amplitudes compared to the intrinsic resolution of germanium (1-2 keV) and therefore not worsen it, allowing us to obtain spectra of the energy distribution of the detected events. The second board is an 8-bit resolution ADC with a maximum sampling rate of 2 GHz and it is used to acquire the liquid scintillator signals. Since the signals produced by an organic scintillator are characterized by extremely fast rise and decay times, $\sim$ 10 ns and less than 50 ns respectively, it is necessary to use a high-speed card to have a sufficient number of points both on the tail but also on the rise of the signal. The speed performance is at the expense of the resolution, limited to 8 bits, but this does not appear to be a problem because the intrinsic resolution of the scintillators is much lower (hundreds of keV) with respect to the germanium detector.

The anodic signal produced by the PMT coupled to the liquid scintillator is sent to an inverting amplifier that acts also as a buffer. This stage has a double function. The amplification allows increasing the amplitude of the signal in order to optimize the acquisition dynamics of the ADC and allows having a buffer with the correct impedance matching in order to avoid signal reflections in the transmission line, particularly critical because of the high speed of these signals and a quite long cable (about 2 m) required to conned the PMT to the acquisition board. Another important feature of this amplifier is that it allows the output signal to be split into two channels that are acquired by the NI PXI 5153 ADC with two different dynamics, in order to reduce the discretization of the signals at lower energies. With this technique we can exploit the 8-bit for two different amplitude ranges, from 0 V to 0.5 V for a higer range and from 0 V to 0.1 V for the lower range, improving the sensitivity to low energy signals but preserving the possibility to detect the high energy ones. The combination of the signals is then performed offline.

The signal produced by the HPGe crystal is firstly integrated by the dedicated charge preamplifier produced by the manufacturer of the detector and its output signal is sent to an Ortec amplifier mod. 672 in order to perform an optimization of the signal-to-noise ratio with a semi-gaussian shaping with a time constant of 6 µs and the amplification of the signal. The resulting signal is finally sent to the NI PXI 5122 ADC for digitalization.

As introduced before, the signal produced by the PMTs of the plastic scintillator detectors used for the cosmic muon veto are summed together with an operational amplifier and the resulting signal is digitized by the NI 5122 ADC.

The acquisition system has been structured in such a way as to be able to use a channel of the PXI 5122 (the fastest) as a trigger. When this board detects a signal that exceeds the set trigger threshold, it also sends the trigger command synchronously to the slow board (PXI 5153) to start the waveform acquisition. The control software of the cards was created in LabView and allows the acquisition parameters to be set for the two ADC, such as, for example, the channels to be acquired, the dynamics on the various channels, and the trigger settings and to monitor the progress of the measurement by displaying live the acquired waveforms, the number of recorded events, the relative rate, the dead time value and having rough spectra of the signals. The acquired waveforms are saved in binary format to disk for archiving and subsequent offline analysis.

In order to reduce memory usage and reduce the offline analysis time, the acquisition of the GeSparK detector is able to determine if the acquired event is a coincidence or a single LS event and store on disk only the coincidence ones. This allows drastically reducing the amount of data written on disk that would have been discarded anyway if only coincidence events are required, as in most cases.

#### 3.3.3.2 Offline data analysis

The acquired data are processed offline by using a dedicated software that has been created using the Wolfram Language with Mathematica. The software can read the binary file containing the waveforms and display the signals with an interactive view. The waveforms acquired at each trigger are analyzed by the software extracting the main signal features through the application of filtering algorithms in order to improve the signal-to-noise ratio. The lists of parameters characterizing each signal are then stored on disk in a file that can be successively inspected. The software also includes tools for the energy calibration of the germanium spectrum, the analysis of the germanium and scintillator energy spectra with functions dedicated to peak fitting and integral area calculation, and the creation of pulse shape scatter plot for alpha–beta discrimination. The software allows in particular coincidence events to be investigated. The first step consists in selecting the events where scintillator and HPGe signals are both present in the acquired time window. Among these, only the events presenting a relative time distance of less than 1.5 µs, are considered in coincidence and further analyzed. The second step allows events in coincidence with the muon veto to be rejected. In this case, only events presenting a time distance greater than 6 µs with respect to the signal from the veto monitor, are accepted. The events that satisfy these requirements are used to generate the gamma coincidence spectrum.

As mentioned before, the liquid scintillator detector signals are acquired with two different dynamic ranges of the ADC at the same time. The analysis algorithm verifies if the amplitude of the signal acquired with the smallest dynamic is lower than the maximum (the signal does not saturate the ADC) this signal is analyzed to extract the relevant parameters, otherwise (the signal is saturated) is analyzed the signal acquired by the other channel with the higher dynamic range.

A dedicated algorithm has been also developed to perform the delayed coincidence analysis for the determination of $^{239}$Np (the nuclide of interest for $^{238}$U determination by NAA). Detail about this technique and the relative algorithm are provided in the dedicated section 3.4.1.

## 3.4 Measurement of $^{238}$U, $^{232}$Th and $^{40}$K by neutron activation

The principal contribution to the radioactivity in materials coming from the natural fossil nuclides and their chains: $^{238}$U, $^{232}$Th and $^{40}$K. These nuclides are always present in all the materials in different concentrations and their quantitative determination is one of the main tasks of radiopurity material selection. As introduced in section 2.3.2, different techniques can be exploited to measure these nuclides based on the nature of the sample and its matrix. For quite large mass samples and up to concentrations in the order of 100 µBq/kg the gamma spectroscopy with HPGe detectors is the most sensitive technique and allows obtaining important information about secular equilibrium breaking. For lower concentrations, it is not easy or it is impossible to measure the concentration by gamma spectroscopy because the decay rate is too slow. In this case, the most sensitive technique is the ICP-MS, that measure directly the $^{238}$U, $^{232}$Th or $^{40}$K concentration, and not the decay of its daughters, or the neutron activation analysis that allow these nuclides to be transformed into newer nuclides with a much shorter half-life and making possible to measure them again with gamma spectroscopy.

The last technique is the one we choose for our analysis. In the following sections is described how the NAA technique is generally applied to measure $^{238}$U, $^{232}$Th and $^{40}$K and is discussed in detail the newer technique developed specifically for the $^{238}$U thanks to a peculiarity in the decays of its activated nuclide $^{239}$Np.

### 3.4.1 $^{238}$U measurement with delayed coincidence technique

When the $^{238}$U is exposed to a neutron flux it can capture a neutron and transform into $^{239}$U. This nuclide has a very short half-life (23 min) so it is completely decayed into its daughter $^{239}$Np during the irradiation period (several hours) that can be measured thanks to the half-life of 2.4 days. The complete activation reaction is shown in equation 3.10.

$$^{238}\mathrm{U} + n \rightarrow {}^{239}\mathrm{U} \xrightarrow{T_{1/2} 23min} {}^{239}\mathrm{Np} + e^- + \overline{\nu}_e \xrightarrow{T_{1/2} 2.4d} {}^{239}\mathrm{Np} + e^- + \overline{\nu}_e \tag{3.10}$$

The standard NAA technique for $^{238}$U determination exploits the 106 keV gamma ray emitted in the decay of the $^{239}$Np, that is the photon emitted with the highest branching ratio providing the best sensitivity, in order to measure its activity. The counts associated with this peak are determined for both the standard and the sample and the NAA equation is applied to determine the unknown concentration of $^{238}$U in the sample.

In order to maximize the sensitivity, the measurement should last as long as the signal contribution is greater than the background one. Although this depends on the background level of the detector, after about 3 half-lives about the 90% of the $^{239}$Np nuclides have been decayed and an increase in the measurement time is associated with a negligible increase of the signal events. For this reason our measurement time for $^{239}$Np determination is 1 week.

The factor that most limits the measurement sensitivity of $^{239}$Np produced by neutron activation is the presence of other activated nuclides that produce a background in the region of interest at 106 keV, whose fluctuations could not be removed. The most critical interference nuclides are $^{24}$Na and $^{82}$Br that are widely common nuclides in the environment (Na) and organic compounds (Br) because their half-lives are almost compatible with the $^{239}$Np one and their contribution cannot be reduced for example by waiting for its decay.

Based on the technique proposed in [35], a new improved technique has been developed in order to increase the measurement sensitivity thank to a strong reduction of the background produced by the interference nuclides and also the intrinsic background of the detector (cosmic muons). This technique, called "delayed coincidence technique", exploits a metastable level in the $^{239}$Pu nuclear structure in order to obtain a very strong marker of the $^{239}$Np decay. The $^{239}$Np decays with a 40.5% branching ratio on the metastable level at 391.6 keV with a $\beta^-$ transition which is followed by $\gamma$ or IC decay (Figure 3.24). $\gamma$s or IC

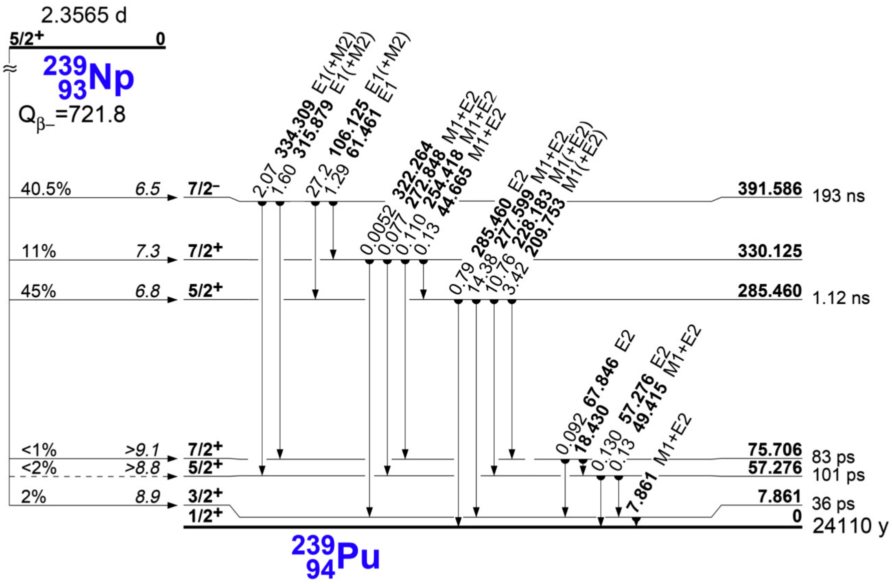

Figure 3.24: Simplified nuclear level scheme of $^{239}$Pu[36]. The main transitions related the metastable level deexcitation are shown.

electrons are emitted according to an exponential time distribution with a decay constant related to the half-life of the metastable level. The following de-excitation to the ground state can occur via subsequent $\gamma$ or IC transitions.

Thanks to the very high speed of its response, the liquid scintillator of the GeSparK detector allows measuring both the electron emitted by the beta decays and the delayed electrons emitted in the IC deexcitation transitions following the deexcitation of the metastable level (Figure 3.25). The GeSparK detector can also measure the time delay between the two events and thus provides very important information for the identification of this particular decay because the time distribution of these delays follows an exponential distribution with a decay constant that is characteristic of this particular level. Moreover, the GeSparK detector allows detecting the coincidence gamma ray emitted in the deexcitation of the metastable level providing a third marker for this particular transition.

The proposed event selection, based on three makers: one beta decay event followed by a delayed signal, with a specific time distribution, in coincidence with a defined gamma energy event in the HPGe detector, allows rejecting almost all the spurious coincidences due to interference nuclides and to drastically increase the measurement sensitivity. The proposed technique exploits the IC transitions and the capability of the LS detector to obtain the delay information with high time resolution with respect to the delayed coincidence based on the beta-gamma delay applied in [35].

A dedicated algorithm has been implemented in the analysis software of the GeSparK detector in order to select these events, with a quite simple principle. The algorithm determines if in the acquisition window of the LS is present more than one peak (Figure 3.25). If two peaks are present the time distance is evaluated by using a constant fraction algorithm in order to reduce the effect of the amplitude walk and improve the time resolution. The amplitudes of the two peaks are determined and are also analyzed in the HPGe channel, in order to determine the energy of the coincidence gamma ray, and the presence of a veto signal from the plastic scintillators. These and other minor information are stored for the next step of the analysis.

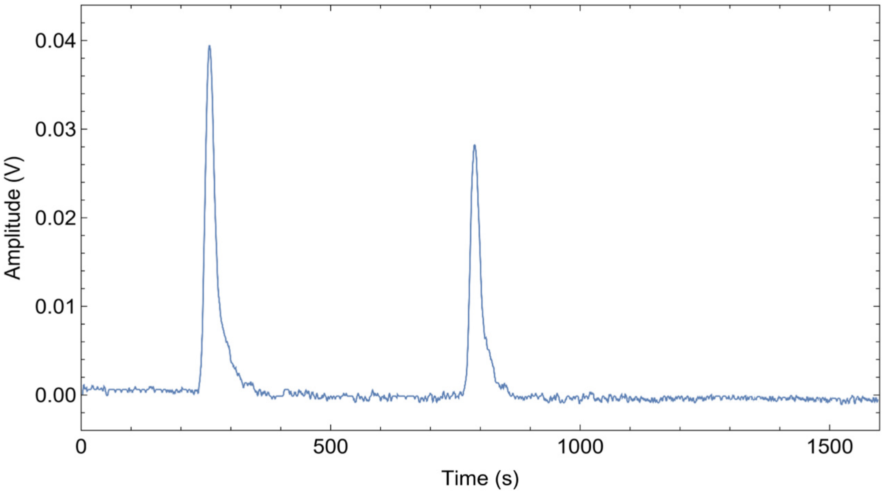

Figure 3.25: Example of delayed coincidence signals of $^{239}$Np decay as acquired by the GeSparK detector.

Once all the delayed coincidence events are determined and analyzed, a selection of these events is performed in order to reduce the residual background produced by random coincidence events. In particular, it is applied a cut relative to the time difference, which must be greater than a threshold set to a value equal to the length of the LS pulses, in order to eliminate false positives of the analysis due to a deformation of the LS pulses. A cut on the LS energy of the two pulses, in order to select the event with the correct energy, and a cut on the energy of the HPGe signal, that must be lower than about 300 keV because there are no gammas associated to the $^{239}$Pu deexcitation above this value.

After the selection of the events, the time distribution of the delays is plotted and fitted. The signal events, associated with the delay between the beta decay and the IC electron emitted in the deexcitation of the metastable state, follow an exponential distribution with a decay constant given by the reciprocal of the mean life of the metastable state: $\frac{1}{\tau}e^{-\frac{t}{\tau}}$. The potential background events are produced by random coincidence in the acquisition window and follow an exponential distribution with a decay constant given by the rate of singles background events: $R \cdot e^{-R \cdot t}$. If the exponent is $R \cdot t << 1$, low background rate compared to the reciprocal of the width of the acquisition window, the exponential distribution can be approximated with a uniform distribution $R \cdot e^{-R \cdot t} \sim R$. Since the detected events can be both signal and background, we can expect that the overall distribution is given by the sum of these two distributions with a weight given by the expected number of signal events with respect to the total ones (c parameter). The analytical expression of this distribution can be expressed as follows.

$$\mathcal{D} = c \cdot \frac{\frac{1}{\tau}e^{-\frac{t}{\tau}}}{\int_0^{\Delta t} \frac{1}{\tau}e^{-\frac{t}{\tau}} dt} + (1-c) \cdot \frac{1}{\Delta t} \tag{3.11}$$

In this equation has been included the fact that the exponential distribution is truncated after a time $\Delta t$ because of the finite acquisition window. This is included in the equation in two ways: the first one is the integral at the denominator of the exponential distribution in order to renormalize it and the second is the normalization of the uniform distribution between 0 and $\Delta t$. In this case, the c parameter represents exactly the ratio between the number of signal events and the total number of events observed.

The GeSparK detector is set in order to acquire the LS signal for 1600 ns for each trigger, with a pre-trigger of 250 ns. This means that there is a window of 1350 ns for the second pulse to be acquired. Moreover, as mentioned before, a threshold is applied in order to exclude pulses that are overlapped, excluding the firsts 120 ns. In conclusion, the available time window width for the events signals is 1230 ns. The resulting distribution is shown in equation 3.12

$$\mathcal{D} = c \cdot \frac{\frac{1}{\tau}e^{-\frac{t}{\tau}}}{\int_0^{1230} \frac{1}{\tau}e^{-\frac{t}{\tau}}dt} + (1-c) \cdot \frac{1}{1230} \tag{3.12}$$

By using this distribution, a Maximum Likelihood fit can be performed in order to estimate the value of the parameter c. Once this value is estimated, the number of signal events can be computed simply by multiplying c and the total number of observed events, following the definition of c. This analysis is performed for both the sample and the standard, with the application of the same analysis procedure and cuts. Based on the number of signal events associated with the sample and the standard, the usual comparative NAA analysis can be performed by using the equation 3.6. The only difference between the analysis applied for the sample and the standard is that for the standard the fit is performed with a chi-square minimization of the function $a \cdot \frac{1}{\tau}e^{-\frac{t}{\tau}} + c$ on binned data because the number of events does not allow a ML fit on the distribution to be performed.

During the development of this method, we realized that the GeSparK detector, used for the analysis of the activated samples with this technique, is not only able to detect the signals and measure the time difference between the prompt and delayed one in order to perform the event selection, but also to measure the delay distribution with very high accuracy. The accurate measurement of this distribution can be used to determine the half-life of the metastable level with higher accuracy with respect to the previous results. For this purpose, a dedicated measurement was performed, achieving a result for the half-life of the metastable state of (190.2±0.2) ns, that improve the error associated with the result of factor 20 with respect to the current reference result. In appendix A is described the complete analysis performed as described in the dedicated paper [37].

### 3.4.2 $^{232}$Th measurement

The determination of $^{232}$Th by NAA exploits the neutron capture reaction shown in equation 3.13. The $^{232}$Th captures a thermal neutron and transforms into $^{233}$Th that decays quickly of $^{233}$Pa. This nuclide has a quite long half-life, about 27 days, and decays $\beta^-$ on $^{233}$U. This decay is accompanied by the emission of a gamma ray of 312 keV with a branching ratio of 30% and it is used for the measurement of the $^{233}$Pa activity with HPGe gamma spectroscopy.

$$^{232}\mathrm{Th} + n \rightarrow {}^{233}\mathrm{Th} \xrightarrow{T_{1/2}22m} {}^{233}\mathrm{Pa} + e^- + \overline{\nu}_e \xrightarrow{T_{1/2}27d} {}^{233}\mathrm{U} + e^- + \overline{\nu}_e \tag{3.13}$$

In this case, in order to maximize the sensitivity, the measurement should last about 3 month (3 half-lives). Since the lifetime of $^{233}$Pa is much longer than almost all the interfering nuclides that can be commonly activated during the neutron activation, their contribution to the background of measurement can be reduced and almost completely eliminated by waiting before starting the gamma measurement, in order to wait for the almost complete decay of all the interfering nuclides. This is usually done by waiting one week from the end of the irradiation.

In this situation, the only source of background is the intrinsic one of the detector used. In particular, for the GeSparK detector this contribution is dominated by the cosmic muon showers (see section 3.3.2.4). The measurement of $^{233}$Pa will take the most advantages from the presence of the plastic scintillators veto, which allows this contribution to be reduced with very good efficiency.

### 3.4.3 $^{40}$K measurement

Potassium is a very common alkali metal that is present in nature in two stable nuclides: $^{39}$K and $^{41}$K, with an isotopic abundance of 93.26% and 6.73% respectively. When a sample of natural potassium is exposed to a thermal neutron flux, both the isotopes are activated, transforming respectively into $^{40}$K and $^{42}$K. Although the $^{39}$K has a much greater abundance and a higher cross section for neutron capture, the activated nuclide $^{40}$K has an extremely long half-life that makes it impossible to measure its activity by gamma spectroscopy due to the very low amount of activated nuclides produced during the irradiation. The $^{42}$K has instead a very short half-life, 12.4 h, which makes it possible to measure it with gamma spectroscopy. The $^{42}$K decays $\beta^-$ with the emission of a deexcitation photon of 1525 keV with a branching ratio of 18%, that is used to determine its activity. The activation reaction is shown in equation 3.14.

$$^{41}\mathrm{K} + n \rightarrow {}^{42}\mathrm{K} \xrightarrow{T_{1/2} 12h} {}^{42}\mathrm{Ca} + e^- + \overline{\nu}_e \tag{3.14}$$

The very short half-life makes it impossible to reduce the impact of interfering nuclides by waiting for their decay but, thanks to the high energy of the gamma ray, the region of interest is in a region of the spectrum where the background produced by the Compton interaction of the photons emitted by the other nuclides is much lower compared to the low energy regions of the gamma ray of $^{239}$Np and $^{233}$Pa. For these reasons the main, and almost the only, interfering nuclide is the $^{24}$Na that has very high energy gamma rays at 2754 keV and a comparable half-life.

### 3.4.4 Measurement of $^{238}$U and $^{232}$Th in LAB sample

The previously described techniques were applied to the measurement of a sample of LAB produced by the pilot plant for the production of the JUNO LAB. This sample was processed with the two purification steps foreseen for the JUNO LAB, the alumina column treatment and the distillation, as described in 1.2.2.1.

A sample of 22 g of LAB was irradiated at the TRIGA MK II research reactor at LENA for 6 hour together with a standard solution of 0.1 µg of $^{238}$U and 10 µg of $^{232}$Th. The following day, the sample was transferred to the radioactivity laboratory at the University of Milano-Bicocca and the measurement of the standards and the sample were performed. The measure of the sample lasted 1 week for the uranium determination and about 55 days for thorium. At the end of the respective measurement times, the data acquired by the GeSparK detector were analyzed by the dedicated analysis tool in order to extract the necessary information and select the signals of interest. the uranium standard was measured with GeSparK detector before measuring the sample while the thorium standard was measured by the GeGEM HPGe detector.

The determination of the uranium was performed using both the conventional analysis and the delayed coincidence technique in order to compare their performances. Two different analysis algorithms were applied to the standard and the sample data. For the standard analysis, the algorithm selects the signals in coincidence with the HPGe and LS detectors excluding saturated signals, and those in coincidence with the muons veto. The resulting data are used to compute the spectra of the HPGe detector and a fit of the 106 keV peak is

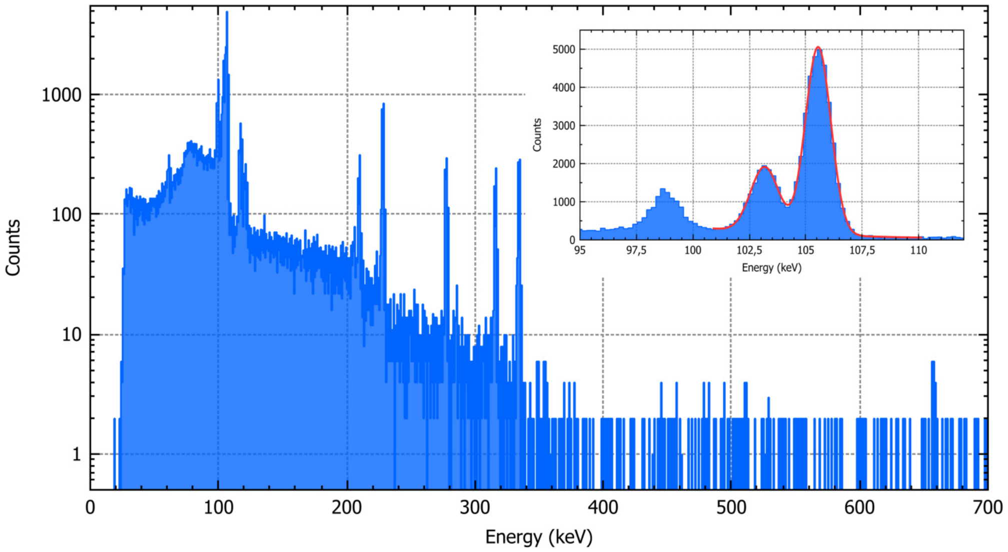

Figure 3.26: Spectrum of the HPGe detector signals of the selected events associated with the standard solution measurement. On the top-right a zoom around the 106 keV peak with the relative fit function.

performed if present, otherwise, the spectrum integral in the ROI is computed. For the delayed coincidence one the algorithm described in section 3.4.1 on page 84 have been applied in order to select the delayed events that respect the required temporal properties, in addition to the coincidence and anti-coincidence criteria described above.

In Figure 3.26 is shown the HPGe spectrum obtained with the conventional analysis applied to the data of the uranium standard solution. Here can be clearly seen the characteristic peaks of the $^{239}$Np and the fitted peak at 106 keV. An analogous spectrum was obtained for the delayed analysis, with the only difference in the total number of events due to the more stringent selection criteria.

The conventional analysis applied to the data acquired during the measurement of the sample provided the HPGe spectrum shown in red in Figure 3.27, where there is no evidence of a peak in the region of interest. In this case, the method for the evaluation of the limit on the $^{238}$U concentration was applied. The integral of the spectrum in the ROI is computed and the statistical fluctuation, based on Poisson statistics, computed as the square root of the number of events, is considered as the number of events used in the NAA equation. The Poisson error is multiplied by 1.64 in order to compute the limit at 90% of confidence level. The ROI is considered with a width of 1.2 FWHM centered at the energy of the expected peak. The number of background events in the ROI was 5673, so the number of events used in the NAA equation was $\sqrt{5673} \cdot 1.64 = 124$. The resulting limit on the uranium concentration is reported in Table 3.5.

As can be seen in the HPGe spectrum, this measurement is subjected to a very high background due to the presence of interfering nuclides that create a continuum background at low energies in the HPGe spectrum due to the Compton interaction of the photons in the detector. The main sources of this background are $^{82}$Br, which dominates the spectrum with its peaks, and the $^{24}$Na that has two peaks at 1369 keV and 2754 keV (out of the showed spectrum).

The delayed analysis applied to the same data allowed their contribution to be reduced

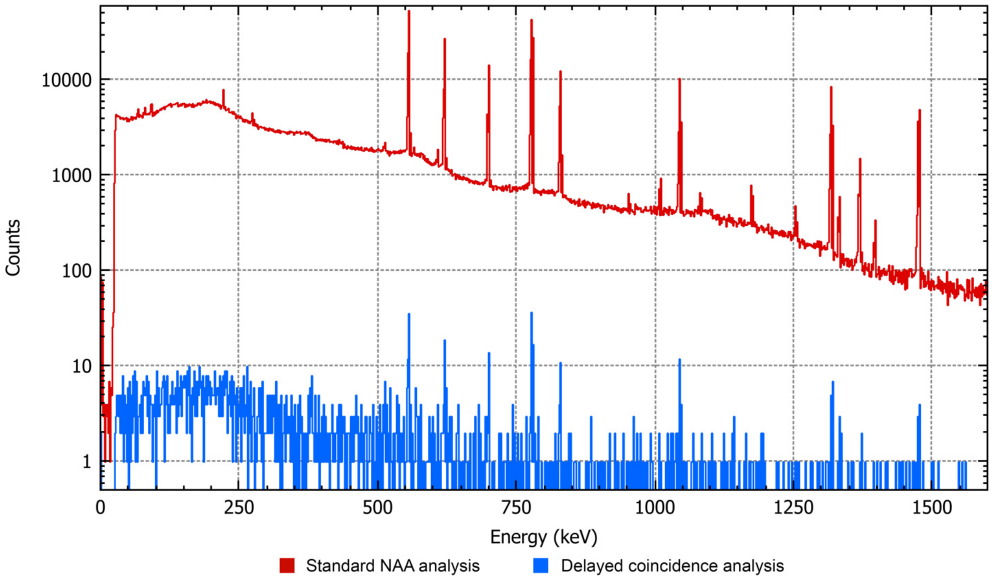

Figure 3.27: Spectrum of the HPGe detector signals of the events associated with the sample measurement and processed with the standard analysis (red) and delayed coincidence algorithm (blue).

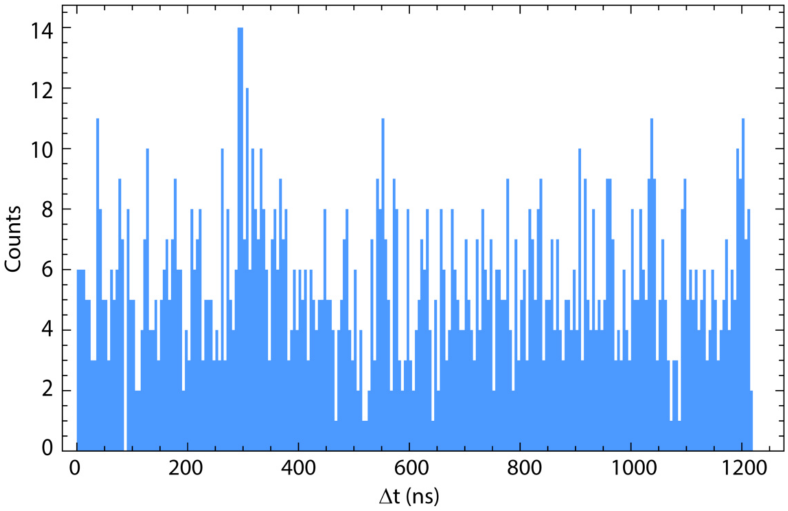

Figure 3.28: Distribution of the time difference between the two pulses in the LS detector in coincidence with the HPGe signals lower than 350 keV.

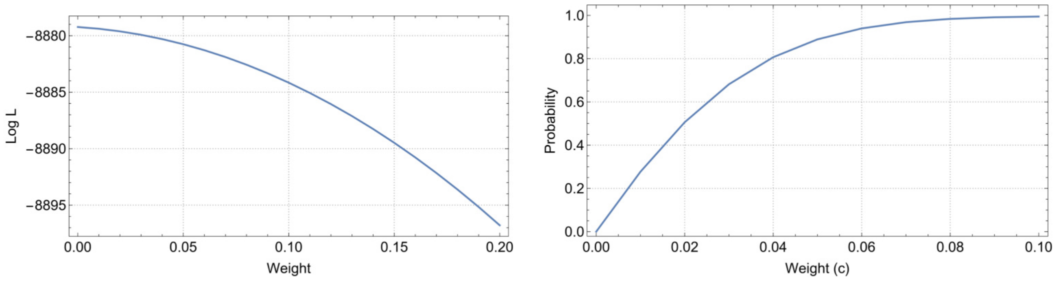

(a) Plot of the LogLikelihood profile as a function of the c parameter between 0 (maximum) and 0.2.

(b) Plot of the cumulative normalized LogLikelihood (cumulative probability) as a function of the upper integration limit, between 0 and 0.1. The 90% of probability is reached at c = 0.053.

Figure 3.29: LogLikelihood plots of the delayed coincidence analysis with the selection of the HPGe signal lower than 300 keV.

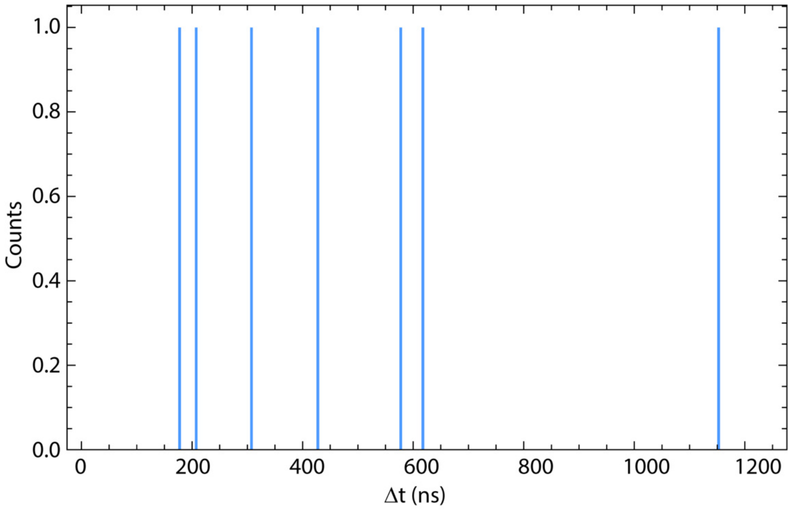

Figure 3.30: Distribution of the time difference between the signal in the LS detector in coincidence with the HPGe signal between 105 keV and 107 keV.

thanks to the stronger selection criteria based on the time properties of the signals. The HPGe spectrum of the events in the HPGe detector, in coincidence with delayed events in the LS detector is shown in blue in Figure 3.27 on the preceding page. Here is clearly visible the reduction in the number of background events.

The time distribution of the delays between the second and the first event in the LS detector is shown in Figure 3.28 on the facing page, with a total number of events of 1248. In general, the selected events can be both signal and background events. In order to determine the signal contribution, a fit using a maximum likelihood (ML) method is performed by using the distribution (equation 3.11 on page 86) reported in section 3.4.1. The maximum likelihood indicates that the best estimation for the c parameter (signal to total events ratio) is 0 (Figure 3.29a). This means that all the acquired events should be considered random background events. In this case, a limit on the uranium concentration is computed based on the number of events that can be considered signals with a confidence level of 90%. To compute this value the cumulative probability is computed by integrating the normalized likelihood function between 0 and a generic value of c, constructing the

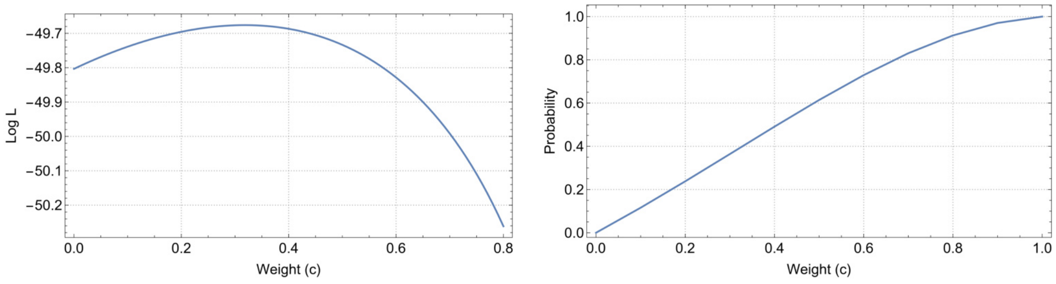

(a) Plot of the LogLikelihood profile as a function of the c parameter between 0 and 0.8.

(b) Plot of the cumulative normalized LogLikelihood (cumulative probability) as a function of the upper integration limit, between 0 and 1. The 90% of probability is reached at c = 0.78.

Figure 3.31: LogLikelihood plots of the delayed coincidence analysis with the selection of the HPGe signal between 105 keV and 107 keV.

| Measure | U ($10^{-13}$ g/g) | Th ($10^{-13}$ g/g) |
|---|---|---|
| Standard NAA analysis | <4.2 | <4.2 |
| Delayed analysis $E_{HPGe} < 300\,\mathrm{keV}$ | <2.0 | |
| Delayed analysis $105\,\mathrm{keV} < E_{HPGe} < 107\,\mathrm{keV}$ | <1.1 | |

Table 3.5: Concentration of $^{238}$U and $^{232}$Th obtained by the direct measurement of a LAB sample.

function shown in Figure 3.29b. The value of c associated with the 90% of probability is 0.053. Based on this value, the number of signal events considered for the following analysis is $N = 1248 \cdot 0.053 = 66$.

Since in this case there is no evidence of signal and we have a quite high residual background in the HPGe spectrum, it is possible to increase the sensitivity by selecting a narrower region of the HPGe spectrum around the main peak of the $^{239}$Np at 106 keV. With this selection criterion, the signal-to-background ratio is expected to increase because the ratio between the number of signal events and background events is much higher under a peak with respect to the continuum region. Applying a selection window of 2 keV between 105 keV and 107 keV for both the data associated with the standard solution and the sample, the time distribution showed in Figure 3.30 is obtained for the signal events of the sample, with a total number of 7 events. The same approach based on the ML fit is applied and the resulting ML plots are showed in Figure 3.31a and 3.31b. In this case, the LogLikelihood has a maximum around 0.3, indicating a probable contamination, but if we look at the error associated with this value by using the approximation of the $LogL - 1/2$ rule, we obtain very asymmetric errors that allow the value to be compatible with 0. For this reason and to be conservative, was decided to evaluate the cumulative distribution and set a limit as in the previous case. The cumulative probability reach the 90% value at $c = 0.78$, that corresponds to a number of signal events of $7 \cdot 0.78 = 5.5$. This value was used to compute the new limit on the concentration of uranium, which is reported in Table 3.5, together with the previous results.

From these results, it is evident the increase in the sensitivity obtained with the application of the delayed coincidence technique with respect to the conventional NAA one and the further increase achieved with the more stringent selection criterion of the HPGe detector signals.

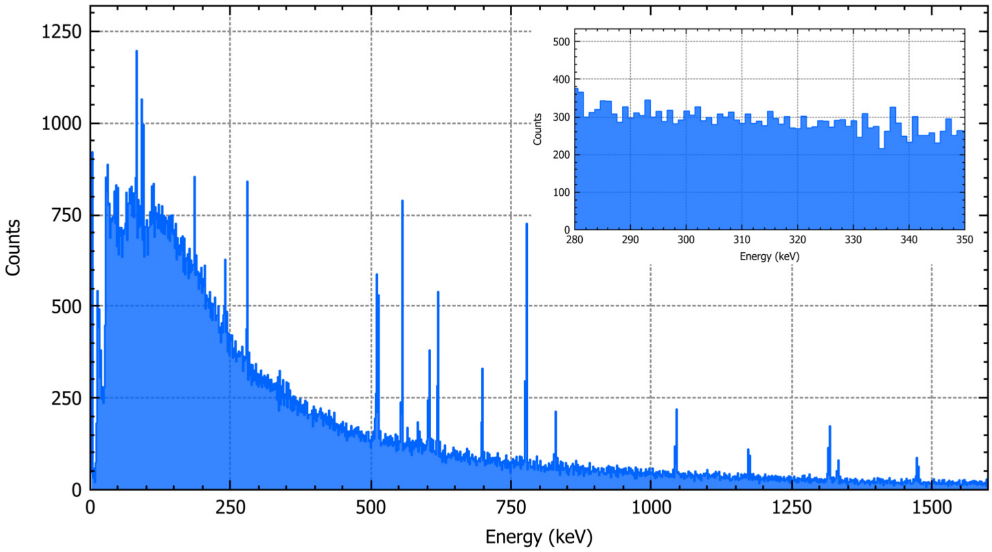

Figure 3.32: Spectrum of the HPGe detector signals of the events associated with the sample measurement for the determination of $^{232}$Th, with a waiting time of 10 days. On the top-right a zoom around the ROI between 280 keV and 350 keV.

The determination of the $^{232}$Th was performed by using the conventional NAA technique described in section 3.4.2. Since the measurement background is very high due to the presence of high activity of interfering nuclides (red spectrum in Figure 3.27 on page 90), the measurement period used for the thorium concentration determination was reduced by increasing the waiting time to 10 days in order to allow the interfering nuclides to decay. The reduction of the total background in the ROI largely compensates for the reduction in measurement time since the half-life of the $^{233}$Pa is very long compared to the waiting time considered. Since there is no evidence of a peak in the HPGe spectrum (Figure 3.32), the integral of the spectrum is computed in the ROI at 312 keV as described for the first uranium case. The number of background events in the ROI was 348 and the number of events used in the NAA equation was $\sqrt{348} \cdot 1.64 = 31$. The resulting limit on the thorium concentration is reported in Table 3.5 together with the uranium results.

Despite the high reduction obtained with the delayed coincidence technique, the achieved limits for both $^{238}$U and $^{232}$Th are about two orders of magnitude higher than the required sensitivities imposed for the JUNO LAB measurement. The main factors that limit the sensitivity are the residual background events produced by the interfering nuclides and cosmic muons and the limited mass of the sample. In order to solve both problems, the implementation of radiochemical treatments was evaluated.

### 3.4.5 Measurement of $^{40}$K in LAB sample

In a separate irradiation, a measurement of the concentration of $^{40}$K in LAB was performed. In this case, we irradiated a sample of 19 g of LAB and a standard solution of natural potassium of 10 µg. The conventional NAA analysis was applied as described in section 3.4.3.

The irradiation lasted for the usual 6 hours and the measurement of the sample with the HGPe detector started the same day because of the very short half-life of the $^{42}$K. The measure time is 44 hours and the acquired gamma spectrum is shown in Figure 3.33.

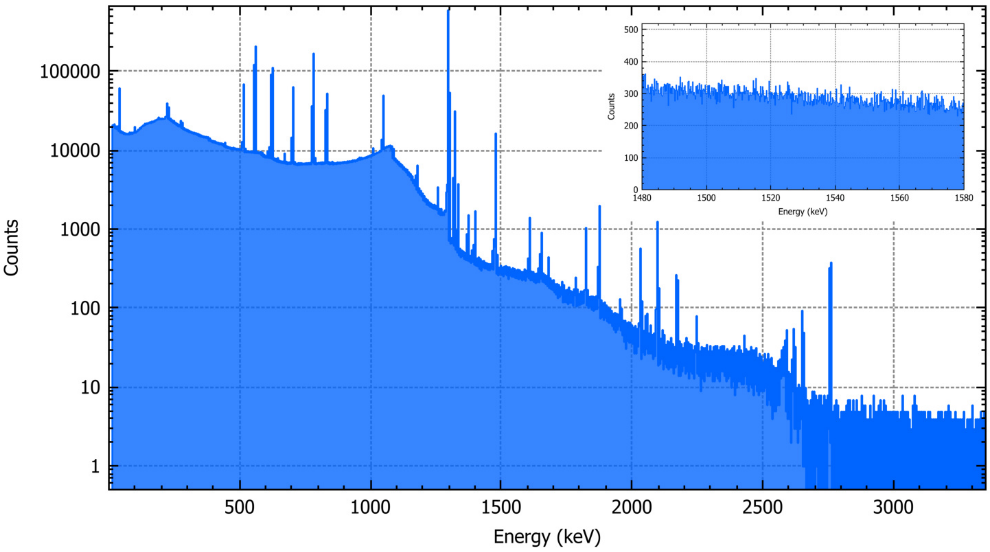

Figure 3.33: Spectrum of the HPGe detector signals of the events associated with the sample measurement for the determination of $^{40}$K. On the top-right a zoom around the ROI between 1480 keV and 1580 keV.

| K ($10^{-15}$ g/g) |
|---|
| <8.3 |

Table 3.6: Concentration of $^{40}$K obtained by the direct measurement of a 19 g LAB sample.

As can be seen in the figure there is no peak in the region of interest at 1525 keV, so a limit for the $^{40}$K concentration was computed by applying the usual procedure. The main sources of background in the spectra are the $^{82}$Br and the $^{41}$Ar but their characteristic peaks have energies below this value so they do not affect the measurement sensitivity. The only peaks above the ROI are those associated with some very low branching gammas of $^{82}$Br and the 2754 keV of the $^{24}$Na whose rate is not so high. The integral of the spectrum in the ROI was 2877 counts and the number of events used in the NAA equation was $\sqrt{2877} \cdot 1.64 = 88$. The resulting limit on the $^{40}$K concentration is reported in Table 3.6.

Although the limit on the $^{40}$K concentration achieved with a direct measure on a small LAB sample is very impressive, is not enough with respect to the requirements of the JUNO experiment. For this reason, a dedicated radiochemical procedure was developed in order to increase the sensitivity, by reducing the presence of interfering nuclides, increasing the mass sample and the efficiency of the measurement.

# Chapter 4

# Radiochemical treatments for activated samples

## 4.1 Introduction and strategy

### 4.1.1 Introduction

The combination of the GeSparK detector and the measurement techniques discussed in the previous chapter allows the measurement sensitivity to be increased but not enough to reach the requirements for the liquid scintillator of the JUNO experiment. The factors that limit the sensitivity are the presence of residual background, in particular for $^{232}$Th determination, and the limited mass of the sample. The latter is due to the maximum volume of the sample that can be introduced in the irradiation container (see section 3.2.1.4) and the maximum number of containers that can be irradiated simultaneously. In absence of correlated background produced by the sample itself, the sensitivity increase linearly with the mass, as can be seen from the NAA equation (equation 3.6 on page 57). On the contrary, a reduction of the intrinsic background of the detector brings to an increment in the sensitivity that grows as the square root of the background reduction factor, because it is related to the Poissonian fluctuation of events in the region of interest.

These considerations allowed us to conclude that the most effective approach that would allow reaching the required sensitivities in the mass increment at constant background. In order to reach this goal, radiochemical treatments of the LAB have been evaluated in order to concentrate the nuclides of interest contained in the LAB and reduce the concentration of interfering nuclides. The first objective is related to mass increase because it is possible to treat a very large mass of LAB and, after the radiochemical treatment, obtain a low-mass sample that can be irradiated in the nuclear reactor. The second objective is instead related to the constant background because if the nuclides of interest are concentrated by the radiochemical treatments, the interfering nuclides could be too. This would produce an increment of the background measurement, so it is mandatory to remove them. Dedicated radiochemical treatments must be applied in order to reduce the concentration of the undesired nuclides and preserve the concentration of the nuclides of interest.

In the following block diagram (Figure 4.1) is represented the conceptual sequence of the radiochemical procedures. In red are highlighted the pre and post-irradiation treatments.

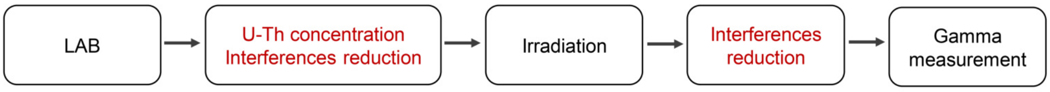

Figure 4.1: Block diagram of the radiochemical procedure.

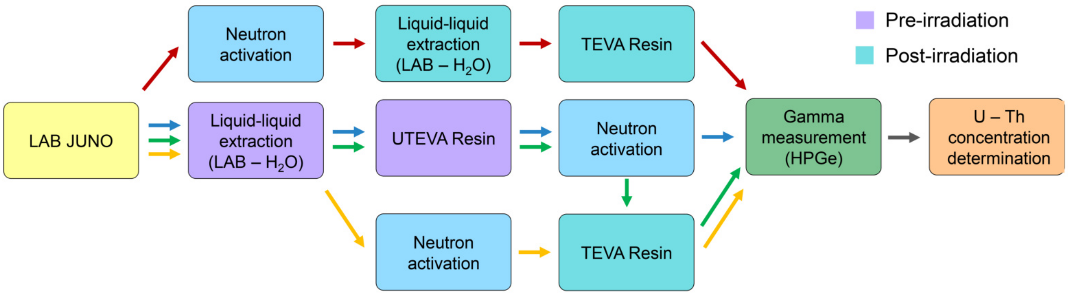

Figure 4.2: Different radiochemical sequences considered for the treatment of the liquid scintillator of JUNO. Each arrow color defines a different sequence.

Different options have been evaluated for the implementation of the specific treatments and for the whole procedure for $^{238}$U and $^{232}$Th that are described in the following section. The radiochemical treatment for the determination of $^{40}$K will be described in a dedicated section after the discussion about $^{238}$U and $^{232}$Th. Radiochemical treatments have been already applied for a similar measurement as reported in [38] where the authors applied an evaporation step on the analysed liquid scintillator, followed by acid digestion, neutron activation, and extraction chromatography steps. The resulting procedure allowed the authors to reach very high sensitivities but not enough for the JUNO requirements. For this reason, a different radiochemical approach has been evaluated.

### 4.1.2 Implementation strategy

The radiochemical treatments can be classified as pre-irradiation and post-irradiation based on when they are performed on the sample with respect to its irradiation.

The radiochemical treatments we used can be classified into the following categories:

**Liquid-liquid extraction** This is the step that allows the nuclides of interest to be extracted from the LAB and transferred to an acid aqueous solution. This procedure allows performing an initial concentration of the sample because the volume of the extracting solution is lower than the volume of the LAB, but it is also necessary in order to perform the other treatments based on extraction chromatography because these use resins that can accept only aqueous solution and not an organic compound.

**Extraction chromatography** Extraction chromatography is a technique that allows ions to be separated based on their affinity to an exchanger absorbed on an inert support (resin). With this technique, it is possible to collect the nuclides of interest present in the aqueous solution obtained in the extraction step and transfer them to another aqueous solution. The advantage is that during this transfer it is possible to remove all the other undesired nuclides and to perform another concentration of the sample because the final volume is much lower than the initial volume.

These techniques, discussed in detail in section 4.2, can be applied both in pre and post-irradiation, with pros and cons, and, for the extraction chromatography, multiple times. What treatments and when they are performed define the specific procedure and in Figure 4.2 are schematized those we studied.

One crucial aspect is that all the commonly used materials are orders of magnitude more contaminated than the levels required by the LAB of JUNO for the $^{238}$U, $^{232}$Th and

$^{40}$K. This means that every manipulation of the LAB performed before the irradiation can hopelessly contaminate the sample. The post-irradiation treatments instead are safe because the $^{239}$Np and $^{233}$Pa are not present in any non-irradiated material so there is no risk of contamination. This is one of the most critical differences between performing a treatment before or after the irradiation, but the use of pre-irradiation treatment allows a much greater sensitivity improvement to be obtained.

The first procedure (red sequence) is the safer one because no pre-irradiation treatments are performed, so the risk of contamination is minimized. This procedure has been the first considered but subsequently excluded because although the post-irradiation radiochemical treatments allow the interfering nuclides to be reduced, the mass of the sample is limited by the irradiation capability and without a high mass sample the required sensitivity cannot be reached.

All the other procedures involve a first step of liquid-liquid extraction in order to transfer the nuclides of interest from the LAB to the acid aqueous solution. At this point, we can irradiate this solution (yellow sequence) and then treat it with extraction chromatography, but again the mass sample is quite limited because although the extraction allows performing a concentration, the concentration factor cannot be arbitrarily high. This is because a minimum ratio between the extracting solution and LAB volumes is required to have good extraction efficiency. As a consequence, in this case, in order to have a high-mass sample, also the extracting solution volume is quite high and cannot be irradiated in our facility. The use of the extraction chromatography with TEVA resin produced by Triskem [39] in post-irradiation allows the concentration of interfering nuclides to be reduced by separating the $^{239}$Np and $^{233}$Pa from the irradiated solution and the overall risk of contamination is only due to the extraction process.

The next two procedures (blue and green sequences) exploit the extraction chromatography with the UTEVA resin produced by Triskem [39] in order to concentrate $^{238}$U and $^{232}$Th contained in the extracting solution and perform a first reduction of the interfering nuclides. The resulting solution is then irradiated and can be directly measured (blue) or previously treated with TEVA resin (green) in order to further reduce the interfering nuclides activated during the irradiation. These sequences, in particular the green one, allow obtaining the best concentration factor and the best reduction of the interfering nuclides. The cons of these procedures are the high risk of contamination due to the liquid-liquid extraction and extraction chromatography process before the irradiation.

## 4.2 Treatments description

### 4.2.1 Liquid-liquid extraction

The liquid-liquid extraction is a separation process consisting of the transfer of an analyte from one solvent to another immiscible one. The transfer of the analyte from one solvent to the other is due to the different affinity between the two solvents. Frequently, one of the solvents is water or an aqueous mixture and the other is an apolar organic liquid. As in all extraction processes, liquid-liquid extraction comprises a step of mixing, followed by a step of phase separation. In the mixing step, the two solvents are vigorously mixed together in order to allow intimate contact between them and when the transfer equilibrium is reached, the distribution coefficient of an analyte is defined as the ratio of its concentration in one phase (e.g. aqueous) to that in the other phase (e.g. organic). The larger the distribution ratio, the higher the recovery of the analyte.

In our case, the organic solvent is the LAB which is a complete apolar compound immiscible with water (polar) that represents the other solvent. The analytes of interest are the $^{238}$U, $^{232}$Th and $^{40}$K if the extraction process is performed before the irradiation, or $^{239}$Np, $^{233}$Pa and $^{42}$K if it is performed after the irradiation. Since all the interesting analytes are metallic ions they have a very high affinity with water, in particular at low pH (acid solution). For this reason, the extracting solution is composed of water and nitric acid which is a strong mineral acid whose salts are almost always soluble in water.

Since the distribution coefficient is constant for a particular combination of analytes, solvents, and experimental conditions (e.g. temperature, pH), in order to obtain a higher extraction efficiency it is better to repeat the extraction process more than one time with a low volume of fresh extracting solution than use a large volume only one time. Another important aspect is that the volume of the extracting solution cannot be too small in order to guarantee good contact between the organic and aqueous phases. Based on literature information and expects advice we choose the extracting conditions. We use a ratio between the total water and the LAB from 1:3 up to 1:5 in volume, based on the LAB volume, and the extraction process is repeated three times. The higher ratio is used with a higher quantity of LAB in order to reduce the amount of extracting solution that must be handled in the following operations and increase the concentration factor. This means that for 100 mL of LAB we use a total extracting volume of 30 mL divided into three extraction with 10 mL for each one. Each extraction step lasts 20 minutes under vigorous agitation on a magnetic stirrer in order to guarantee very good contact between LAB and water.

The complete extraction procedure is the following:

1. The extracting solution is prepared by diluting the nitric acid with water up to desired concentration: 5 M for pre-irradiation and 8 M for post-irradiation extraction.

2. The LAB and 1/3 of the extracting solution are mixed together and vigorously stirred by a magnetic stirrer for 20 minutes.

3. The mixture is transferred into a separatory funnel where the LAB and the water phases are separated thanks to their immiscibility and different density.

4. The mixing and separation processes are repeated two other times.

### 4.2.2 Extraction chromatography with UTEVA and TEVA resins

The extraction chromatography (EC) is a separation technique, in which the extractant is fixed on inert support by absorption way, and the aqueous sample with the analytes to extract flows through it. The extractant can be very selective towards the ions to extract and its affinity can be changed by modifying the pH or the composition of the solution to be extracted. This technique has the advantages of exploiting the good selectivity of extractants and easy operations and the multi-stage possibility of chromatography.

The extraction chromatography resin is composed of an inert substrate on which is absorbed the liquid stationary phase (extraction phase) that can be composed of one or multiple compounds. The mobile phase is usually a mineral acid solution, e.g. nitric or hydrochloric acid, although complexants, such as oxalic or hydrofluoric acids, are frequently used to enhance selectivities or the stripping power to strongly retained metal ions from the resin. In Figure 4.3 is shown a representation of the structure of an EC resin.

The distribution coefficient ($K_D$) in the two phases is defined as the ratio of the concentration of a solute in the stationary phase ($c_s$) to the concentration in the mobile phase ($c_m$):

$$K_D = \frac{c_s}{c_m} \tag{4.1}$$

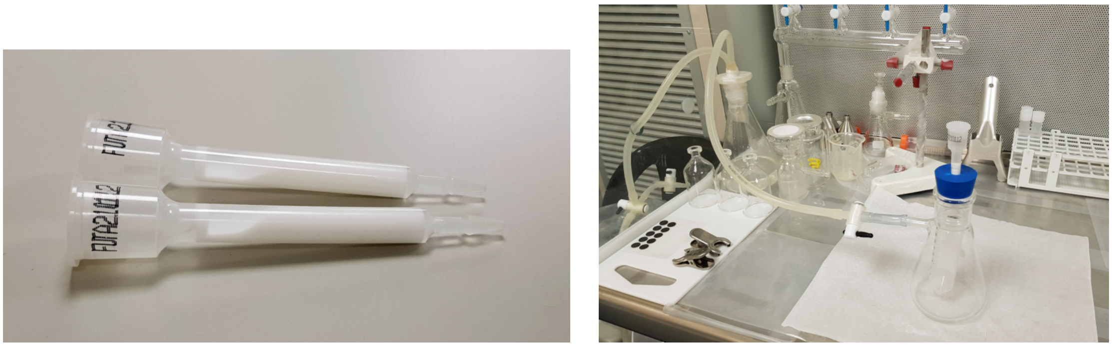

(a) (b)

Figure 4.4: Picture of 2 mL column for extraction chromatography on the left and of the vacuum system used for the extraction chromatography on the right

The retention factor, k, which is an important parameter in any chromatographic process, is defined as the ratio of the quantity of the solute in the stationary phase, $Q_x$, to the quantity in the mobile phase, $Q_m$:

$$k = \frac{Q_s}{Q_m} \tag{4.2}$$

The relationship between $K_D$ and $k$ is given by:

$$k = \frac{Q_s}{Q_m} = \frac{c_s \cdot V_s}{c_m \cdot V_m} = K_D \cdot \frac{V_s}{V_m} \tag{4.3}$$

where $V_s$ and $V_m$ are respectively the volume of the stationary and mobile phases.

From the definition of the retention factor, it is clear that the higher this parameter the higher the retention of the resin. Its values are provided by the manufacturer of the resins as a function of the composition and acid concentration of the mobile phase and can be used to determine the best operative condition.

The stationary phase is packed into columns (Figure 4.4a) of 2 mL volume that are equipped with a small funnel on the top to allow the charging of the solutions. A vacuum system is necessary in order to achieve the correct flow rate through the column because the EC columns require a flow in the range 0.6 mL/min to 0.8 mL/min. A picture of our system is shown in Figure 4.4b. The dry vacuum pump is connected to a flask with a faucet in order to regulate the vacuum level and compensate for its rapid variations, for example, due to the on-off of the pump or flow regulation. This flask is then connected to a filter flask on which the column is mounted.

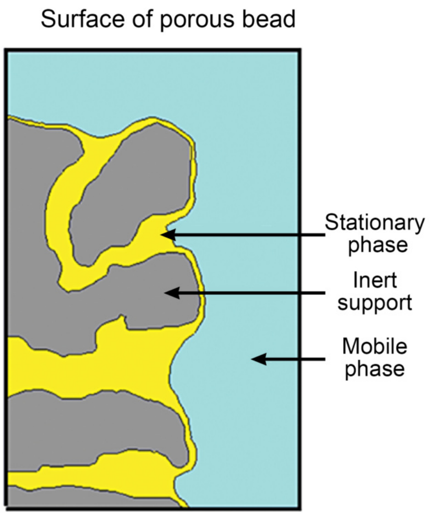

Figure 4.3: Representation of the structure of extraction chromatography resin [40].

The UTEVA resin (Uranium and TEtraValents Actinides) is widely used for the separation of uranium and tetravalent actinides like Th, Np, and Pu. The inert support is

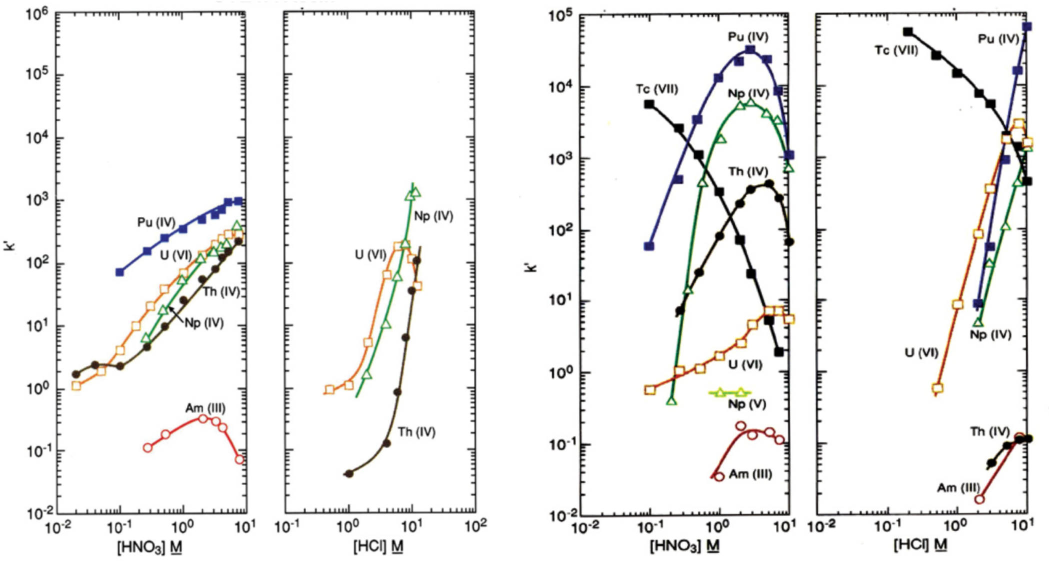

(a) (b)

Figure 4.5: k' values for different actinides on UTEVA resin on the left and on TEVA resin on the right as a function of the $HNO_3$ and HCl concentration in the solution.

Amberlite XAD-7 EC and the extractant is the Dipentyl pentylphosphonate (DPP[PP]). We choose this resin for pre-irradiation treatment because we have to extract the $^{238}$U and $^{232}$Th nuclides for which it shows very high efficiencies. In Figure 4.5a is shown the dependency of k' on the acid concentration for different actinides for the UTEVA resin. The uptake is very similar for each tetravalent actinides and uranium, with strong retention (k'$>$100) above 5 M nitric acid. These nuclides can be eluted from the resin with low concentration nitric acid, about 0.01 M.

The TEVA resin (TEtraValents Actinides) is mainly used for the separation of tetravalent actinides. The inert support is Amberchrom CG-71ms and the extractant is the Aliquat 336. We choose this resin for the post-irradiation treatments because in this case, we have to extract $^{239}$Np and $^{233}$Pa that are both tetravalent actinides, and this resin has higher retention factors for these nuclides with respect to the UTEVA. In Figure 4.5b is shown the dependency of k' on the acid concentration for different actinides for the TEVA resin. The uptake is very high for each tetravalent actinides and in particular for $^{239}$Np with a strong retention (k'$>$1000) at concentration greater than 1 M nitric acid. All the nuclides can be eluted from the resin with low-concentration nitric acid or hydrochloric acid.

The exchange chromatography with the EC columns consists of the following steps:

1. **Washing**: in this phase, the resin contained in the column is washed using an appropriate solution in order to remove the preservative liquid and any trace of the elements of interest that can be potentially present in the resin, especially when very low concentration are analyzed. This is generally done using a low-concentration acid solution in order to allow the resin to release the ions.

2. **Conditioning**: in this phase, the resin is prepared to accept the sample by flowing a solution with the same acid concentration as the sample.

3. **Charging**: in this phase, the sample is passed through the resin. In this process, the nuclides of interest are retained by the stationary phase of the resin while the others

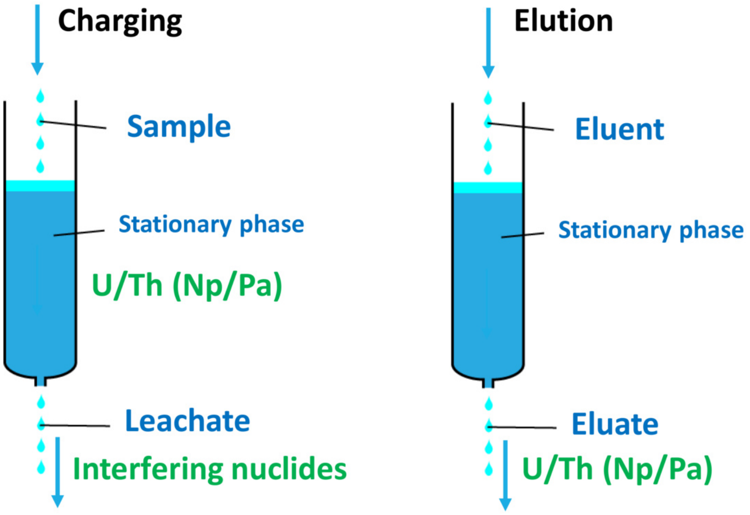

Figure 4.6: Changing and elution phases representation. In the charging phase, the nuclides of interest are retained by the stationary phase and the interfering nuclides are discarded in the leachate. In the elution phase, the nuclides of interest are released by the stationary phase and transferred to the eluate.

remain in the mobile phase that is called "leachate" when it comes out of the column.

4. **Washing**: in this phase, the resin is washed again with an acid solution at the same concentration of the sample in order to remove the sample solution that remained in the column but without removing the nuclides of interest from the stationary phase.
5. **Elution**: in this last phase, the elution solution flows through the column in order to release the nuclides of interest from the stationary phase of the resin. The resulting solution is called "eluate".

The main steps, charging and elution, are represented in Figure 4.6.

#### 4.2.2.1 UTEVA protocol

The best protocol for UTEVA treatment has been obtained starting from the manufacturer and literature information. The protocol has been tested during the efficiency studies (see section 4.4) and optimized in order to achieve the best results.

The final protocol is the following:

1. **Washing**: it is performed by using a solution 0.02 M of ultra-pure $HNO_3$. The volume is at least 50 mL in order to obtain a very deep cleaning of the resin.
2. **Conditioning**: it is performed by using 15 mL of 5 M ultrapure $HNO_3$. This allows ensuring that the resin has the correct pH to retain the $^{238}U$ and $^{232}Th$ of the sample.
3. **Charging**: the sample must have a concentration of 5 M of $HNO_3$.
4. **Washing**: this step is not performed in pre-irradiation because is not particularly crucial and to reduce the potential loss of analytes and the sample contamination.
5. **Elution**: it is performed by using 15 mL of 0.02 M ultra-pure $HNO_3$ to guarantee a complete release of the analytes of interest.

#### 4.2.2.2 TEVA protocol

Also for the TEVA resin, the best protocol has been obtained starting from the manufacturer and literature information. The protocol has been tested during the efficiency studies (see again section 4.4) and optimized in order to achieve the best results.

Unlike for $^{238}$U and $^{232}$Th with UTEVA resin, the $^{239}$Np and $^{233}$Pa can have different stable oxidation states and since the TEVA resin works only with tetravalent elements (Np(IV) and Pa(IV)) it is important to ensure that the elements are in correct oxidation state. This is done by adding to the sample a set of reagents in order to fix the redox potential of the solution and so fix the oxidation state to IV. The reagents are reported in the following final protocol:

1. **Correct oxidation state**: the $HNO_3$ concentration is corrected, if necessary, to 8 M and then the following reagents are added to the sample solution:

    - 25 µL sulfamic acid ($H_2NSO_3H$) 1.5 M
    - 2 µL $Fe(NO_3)_3$ 5 mg/mL in $HNO_3$ 1 M
    - 75 µL ascorbic acid ($C_6H_8O_6$) 1 M

    These quantities are calculated for 1 mL sample at the correct nitric acid concentration. The reagents volumes must be rescaled to the sample volume at the correct nitric acid concentration. Wait for at least 5 minute before charging the sample in the column.

2. **Washing**: this step is not performed since it is not necessary to clean the resin because $^{239}$Np and $^{233}$Pa cannot be present in the resin.

3. **Conditioning**: it is performed by using 15 mL of $HNO_3$ 8 M. This allows ensuring that the resin has the correct pH to retain the $^{239}$Np and $^{233}$Pa of the sample.

4. **Charging**: the sample must have a concentration of 8 M of nitric acid and the correct redox potential.

5. **Washing**: this step is performed with 15 mL of $HNO_3$ 8 M in order to remove the residual traces of interfering nuclides.

6. **Elution**: it is performed by using 15 mL of a solution composed by:

    - $HNO_3$ 2 M
    - Ammonium oxalate ($(NH_4)_2C_2O_4$) 0.5 M
    - Hydroxylamine hydrochloride ($NH_2OH \cdot HCl$) 0.01 M

## 4.3 Contaminations control

### 4.3.1 Importance of cleanliness

The uranium normally found in nature consists of four isotopes and $^{238}$U represents the 99.28%. Uranium is found in all rocks and soils with different concentrations depending on the rock type. Common rocks have concentration from 0.03 ppm to 3 ppm but can be as higher as 100 ppm in particular phosphate rock and bituminous shale [41]. Uranium occurs in traces also in many commercial products, such as steel, food, and human tissues, as a consequence of its presence in soil and phosphate fertilizers. For example the human skeleton is estimated to contain about 25 µg of uranium [41] which correspond to about 0.0025 ppm

Figure 4.7: Picture of the clean room class 10000 (ISO7) where the pre-irradiation treatments are performed.

or $2.5 \cdot 10^{-9}$ g/g. Uranium is also present in the air and correlated to the concentration of suspended particulates, most probably due to the airborne soil. A study in New York between the 60s and 70s [42] found concentration in the order of 1 ng/m$^3$.

Also thorium is widely present in the environment, as isotope $^{232}$Th. The thorium content of rocks ranges from 8 ppm to 33 ppm[41]. As for uranium, thorium is present in food (about 0.0002 ppm or $2 \cdot 10^{-10}$ g/g) and it is suspended in soil particles and this is the principal source of human exposure.

The concentration of $^{238}$U and $^{232}$Th in LAB required by JUNO is many orders of magnitude lower than the typical concentration in the environment. As a consequence, all the materials, air pollution, and the human body are an immense source of contaminations. For these reasons the cleanliness of the working area, the materials and consumables, and the purity of the reagents used in our treatments play a crucial role in the final sensitivity.

The definition of a cleaning protocol and operative procedures required a huge effort in order to determine the origin of the observed contaminations during the tests performed and to reduce their contribution. In the next sections will be described the working area and the cleaning protocols, the containers and consumables used, and the validation of the purity of the reagents.

### 4.3.2 Working area description and cleaning protocols

All the treatments performed in pre-irradiation must be conducted in a very clean environment with a very low concentration of suspended particulate. This is a clean room class 10000 (ISO7). This means that there are no more than 10 000 particles/ft$^3$ greater than 0.5 µm. The liquid-liquid extraction and the extraction chromatography are performed under a laminar flow hood that allows reducing the cleanliness class to 1000 (ISO6) around the operation area. A picture of the clean room is shown in Figure 4.7.

A clean room allows reducing the risk of contamination related to air particulate but another very important source is the contamination introduced by the instruments and consumables. As introduced before, all materials contain a small amount of uranium and


(a) PE vials with pressure cap.
(b) PFA vial with screw cap.

Figure 4.8: Pictures of the containers used for the irradiation of the samples

thorium and they can release these nuclides when getting in contact with the sample. For this reason, all the instruments and consumables are subjected to a deep cleaning process in order to reduce their release of uranium and thorium.

The developed cleaning protocol exploits the ability of an acid solution to bring into solution the nuclides on the surface of the materials, in a process similar to the extraction. All the consumables that will contain samples or extraction chromatography solutions, for example, vials, bottles, centrifuge tubes, and separatory funnels are immersed in a solution composed of ultra-pure water (Milli-Q) and ultra-pure nitric acid with a concentration of about 2% for some days in order to clean both the internal and the external surface. After this first cleaning step, they are filled with a fresh solution and maintained filled until they are used, but for at least one week. If not used, about every two weeks the acid solution is replaced with a fresh one. Other consumables that will not contain samples or solutions for a long time, for example, the micropipette tips, are immersed in the acid solution for one week and then dried in the clean room and conserved in sealed bags. Although the vacuum flask used in the extraction chromatography will not enter directly into contact with the samples, it is maintained filled with acid water when not in use.

### 4.3.3 Containers for samples and extraction solutions

All the solutions described in section 4.2.1 on page 97 and 4.2.2 on page 98 used in the liquid-liquid extraction and in the extraction chromatography have to be prepared in some containers. These containers should not contaminate the solutions and should prevent any contamination from external sources such as the environment or operators. During our studies and tests, we used different containers in order to determine the most performing ones. The preparation of the solutions has been conducted in the 50 mL centrifuge test tubes (produced by Falcon or Corning) made of polypropylene. These tubes have a screw cap that allows the inner content to be isolated from the outside in order to prevent contaminations and be easily filled with acid solution and sealed for long-term cleaning. Unfortunately, these tubes cannot be used for the samples because they cannot fit into the irradiation containers since the diameter is too large. For this reason, we used different containers and the first one was a polyethylene (PE) vial with a pressure cap (see Figure 4.8a). During the tests performed, we became aware of the presence of random contaminations and finally, we found that these vials are problematic for two reasons. The pressure cap requires that

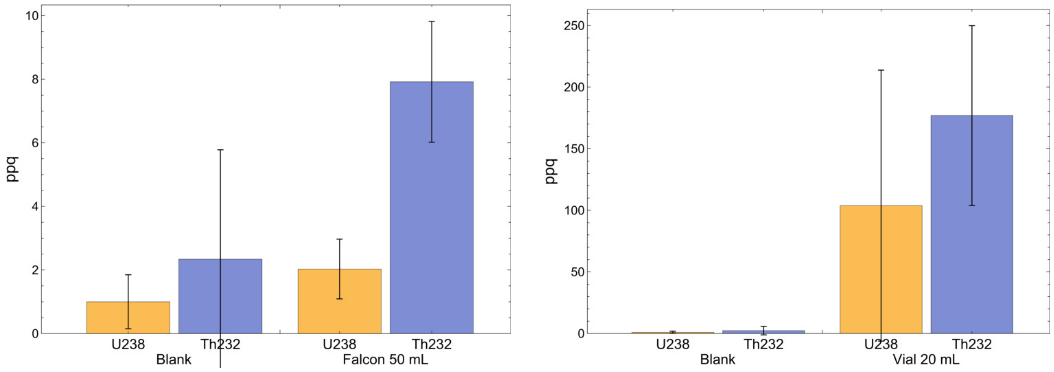

(a) (b)

Figure 4.9: In the plot on the left and right are shown the results of the measurement of the concentration of $^{238}$U and $^{232}$Th respectively in the cleaning solution of the Falcon tubes and in the 20 mL vials with pressure caps, after a cleaning period of one week. The results are the mean of six different samples and the error bars are the standard deviation of the measurements. The results marked as "Blank" are the control blanks of the ICP-MS system.

the operator, in order to close and open the tube, touches directly the edge of the cap and during this operation can contaminate its content. Another problem is that the intrinsic contaminations are higher than in other containers (for example the Falcon centrifuge test tube). This was established by measuring blank solutions by ICP-MS at the Gran Sasso national laboratory. A solution of about 2% of ultra-pure nitric acid has been introduced in the containers and after waiting for a week the cleaning solution has been measured in order to determine the concentration of $^{238}$U and $^{232}$Th. The tests have been performed on six vials for each type in order to study the fluctuation of the contaminations. The mean of the six results of the 20 mL vials (those used for the samples) and Falcon tubes are shown in the plots in Figure 4.9, together with the control blanks of the ICP-MS system. The error bars are computed as the standard deviation of the six results. It is evident that the 20 mL are subjected to much higher contaminations with very high fluctuations, while the falcon tubes are much cleaner and their cleanliness is well reproducible. The results of this test allowed us to conclude that the PE vials with pressure caps cannot be absolutely used for the preparation of the solutions for the radiochemical treatments and for the containment of the samples. For the radiochemical solutions, the falcon tube can be used because the contamination release is not so high to interfere with the sample since the dwell time in the tube is limited to some hours or less.

In order to resolve the problems related to the use of the pressure cap vials for the samples to irradiate we decided to try the PFA (Perfluoroalkoxy alkane) centrifuge vials produced by Nalgene (see Figure 4.8b). These tubes are produced in PFA, they have a screw cap and their size fits perfectly with the irradiation container size. The PFA material has similar chemical properties of PTFE (Teflon), such as complete chemical inertness and excellent resistance to strong acids and organic solvents, and has the advantage to be optically transparent and can be melt-processed. For these reasons is widely used in ultra-trace element analysis because it is a very clean material and can be very efficiently cleaned with acid solutions.

As will be discussed in the next chapter, the nitric acid used for extraction and chromatography is an ultra-pure acid that is sold in 500 mL PFA bottles. These bottles

|  | $^{238}$U$(g/g)$ | $^{232}$Th$(g/g)$ |
|---|---|---|
| $H_2O$ Milli-Q | $<0.7 \cdot 10^{-15}$ | $<0.8 \cdot 10^{-15}$ |
| $H_2O$ Milli-Q Element | $<0.7 \cdot 10^{-15}$ | $<0.8 \cdot 10^{-15}$ |
| Ultra-pure $NHO_3$ | $<3 \cdot 10^{-14}$ | $<3 \cdot 10^{-14}$ |

Table 4.1: Results of the measurement performed at LNGS for the validation of the purity of the reagents used in the pre-irradiation treatments.

are the perfect containers for the liquid-liquid extraction process and for the preparation of high-volume extracting solution because they contained ultra-pure highly-concentrated nitric acid for a long time making them the cleanest container available and, having a very high volume, allows high-volume samples and solutions to be processed.

### 4.3.4 Reagents validation

As introduced before, one of the most critical sources of contamination is the reagents used in the chemical processes performed in the pre-irradiation phases. In particular, there are two reagents used: water and nitric acid. The uranium and thorium nuclides present in these reagents cannot be removed and cannot be distinguished from those coming from the sample. Of course, it is possible to measure a blank sample and subtract the obtained concentration from the sample result, but this can be done only if the concentration in the blank is not much greater than in the sample. Since our goal is to reach a measured sensitivity of $10^{-15}$ g/g the concentration of uranium and thorium in the reagents should not be much greater than this value.

The water is purified by using the Milli-Q or Milli-Q Element ultra-pure water systems produced by Merk Millipore. These systems guarantee water with a conductivity of 18.2 MΩ cm and no particulates with >0.22 µm. The Milli-Q Element system is specific for trace-element analysis.

The nitric acid is the ultra-pure grade produced by Carlo Erba Reagenti, and it is guaranteed to contain less than 0.1 ppt ($1 \cdot 10^{-13}$ g/g) of uranium and thorium.

In order to determine the exact concentration of uranium and thorium in the produced water and certify their content in nitric acid with higher sensitivity, we asked for a dedicated measurement by ICP-MS at the Gran Sasso National Laboratory (LNGS). A set of PFA containers cleaned for a long time was shipped from LNGS to our laboratory. A sample of Milli-Q and Milli-Q Element water and ultra-pure nitric acid was introduced into these containers and shipped back to LNGS for the measurements.

The measurement results, shown in Table 4.1, confirm the quality of the Milli-Q water, obtaining a limit for uranium and thorium concentration lower than $10^{-15}$ g/g and no differences are present with the Milli-Q Element water from the uranium and thorium content point of view. Also the purity of the nitric acid was confirmed with a good improvement with respect to the certified value, but the obtained limit is a bit higher because the ICP-MS is able to measure solutions of nitric acid with a concentration lower than 10%, so it is required to dilute it in water and this operation reduces the sensitivity.

The fact that the limit obtained is one order of magnitude higher than our requirement is not a big problem because the amount of acid is only about 1/15 of the sample volume because there is a factor of 5 for the ratio of sample to extracting solution and another factor of 3 because the concentration of the nitric acid is 5 M, about 1/3 with respect to the concentrated one. This means that the contribution of eventually present contaminations is reduced by a factor of 15, allowing us to potentially achieve the required sensitivity.

Obviously, although it is not necessary because the limit is already lower than the required sensitivity, this consideration can be applied also to the water, lowering its potential contribution.

## 4.4 Treatments studies and efficiencies

All the radiochemical treatments described in the previous sections are affected by an efficiency, in principle lower than one. The knowledge of the efficiency is very important because it affects the final sensitivity of the measurements. In order to determine the best radiochemical sequence among those described in section 4.1.2 the efficiency of each treatment has been evaluated. In this section are described the most significant test and the obtained results.

During each irradiation together with the samples are irradiated the reference standards that are used to compute the nuclides concentration as described in section 3.2.1.2 with the equation 3.6 on page 57. In order to verify the dilution process are also irradiated what we call "dilutions" which are the samples of a known quantity of diluted standards in order to verify the concentration at dilution steps and the amount added during the contamination of the sample with a dilution sample containing the same amount of the samples. The efficiency of a process is evaluated as the ratio of the nuclide mass measured in a sample with the reference amount provided by the dilution sample.

### 4.4.1 Pre-irradiation

The pre-irradiation treatments are the most promising in therm of mass increasing because they allow the sample to be concentrated, but at the same time are the most dangerous for the contaminations they can introduce. Here will be discussed the preparation of the samples, the performed treatments, and the obtained efficiencies of these treatments while the potential contaminations are evaluated in the blank tests described in section 4.5.

#### 4.4.1.1 Sample preparation

In order to determine the efficiency of the processes it is necessary to contaminate with a known quantity of $^{238}$U and $^{232}$Th the LAB in order to compare it with the amount obtained at the end of the radiochemical processes. The contamination is performed by using standard solutions of $^{238}$U and $^{232}$Th in $HNO_3$ 1% with a certified concentration of 1000 ppm. As described in the introductory sections about NAA, the typical measurement sensitivity with standard low-background HPGe gamma spectroscopy on activated samples in the order of $10^{-12}$ g/g. The ultimate sensitivity is reached with long-term measurements (1 week for $^{238}$U and 1 month for $^{232}$Th) and relatively high mass samples (tens of grams). For these reasons the efficiency studies are performed by contaminating a LAB volume of 100 mL to $1{\cdot}10^{-11}$ g/g with $^{238}$U and $^{232}$Th, in order to have enough signal intensity to reduce the measurement time to about one day and accumulate enough statics to have a reasonable low statistical error.

The mass of nuclides associated with this concentration and sample volume can be easily computed by multiplying the mass of the sample and its concentration:

$$m = 100\,\mathrm{g} \cdot 1{\cdot}10^{-11}\,\mathrm{g/g} = 1{\cdot}10^{-9}\,\mathrm{g} = 1\,\mathrm{ng} \qquad (4.4)$$

The concentration of these standards is too high to be used directly because the required amount is contained in 1 nL of standard and it cannot be withdrawn directly. Another crucial problem is that they are not miscible with the LAB, since they consist of an aqueous solution. In order to solve these problems, a dedicated dilution protocol has been developed to reduce the concentration and create a standard solution miscible with the LAB.

The commercial standard solutions are diluted in multiple steps in acid water and the final one is performed in isopropyl alcohol. The final step in alcohol is required because it can be easily dissolved in LAB and allow the nuclides to be dispersed in the LAB matrix. The dilution steps are the following:

- Dilution 1:10 with $HNO_3$ 1% → standard 100 ppm
- Dilution 1:100 with $HNO_3$ 1% → standard 1 ppm
- Dilution 1:100 with isopropyl alcohol → standard 10 ppb

With the final concentration of 10 ppb, in order to have 1 ng of nuclides, it is required to use 0.1 mL of this solution that can be easily withdrawn with a micropipette.

The procedure to contaminate the LAB is the following:

1. Prepare the dilute standard in isopropyl alcohol.
2. 100 g of LAB are transferred in a beaker placed on a magnetic stirrer and maintained in strong agitation.
3. A volume of 0.1 mL of isopropyl alcohol standard is added to the LAB.
4. The agitation is maintained for some minutes in order to allow a uniform dispersion of the nuclides in the LAB matrix.

**Note**: In some tests, for example when multiple procedures are performed on the same sample and only a fraction of the total sample is measured for each treatment, the mass of contaminant is increased to 2 ng to have more signal. In this case, the procedure is the same with the only exception that the first dilution is performed 1:5 in order to double the concentration in the final standard solution to 20 ppb.

#### 4.4.1.2 Radiochemical treatments

The first pre-irradiation treatment is the liquid-liquid extraction that allows the transfer of $^{238}$U and $^{232}$Th from the LAB to an acid aqueous solution. This is also necessary for the possible subsequent extraction chromatography with UTEVA resin.

To evaluate their efficiency the contaminated LAB is extracted and a fraction of the obtained solution is measured with NAA, while the remaining amount is processed with the UTEVA resin.

The liquid-liquid extraction procedure is the following:

1. Add 10 mL of $HNO_3$ 5 M to the 100 g LAB sample.
2. Stir vigorously the mixture with the magnetic stirrer for 20 minutes.
3. Transfer the mixture to the separatory funnel and wait for the phase separation.
4. Spill the aqueous phase that is accumulated on the bottom (higher density).
5. Transfer the LAB to the original beaker.
6. Repeat step 1-5 for two more times.

At this point, the obtained solution has a volume of about 30 mL. 10 mL of this solution is conserved to be measured by NAA to determine the liquid-liquid extraction efficiency and the remaining 20 mL are treated with UTEVA resin according to the following procedure, that is simplified version of the procedure described in section 4.2.2.1 because less cleaning accuracy is required for contaminated samples.

1. The resin is washed with 15 mL of $HNO_3$ 0.02 M.
2. The resin is conditioned with 15 mL of $HNO_3$ 5 M.
3. The sample is charged into the column.
4. The nuclides are elated with 15 mL of $HNO_3$ 0.02 M.

The final sample (eluate) is then measured by NAA together with the previous sample.

#### 4.4.1.3 Efficiency results

The first efficiency of the extraction process has been obtained in test number 6, then repeated during test 17, and finally verified in a dedicated set of three measurements during test 21. All these efficiencies are computed on contamination of 1 ng in 100 mL of LAB except for test 17 in which the LAB was contaminated with 10 ng. The results are reported in Table 4.2 and in the plot in Figure 4.3 on the next page. The results show a very good recovery efficiency and good repeatability. This was quite expected because the affinity of $^{238}$U and $^{232}$Th is much higher with an aqueous acid solution with respect to a completely apolar organic compound.

From the efficiency point of view, the extraction process is very promising because allows quantitative recovery of the nuclides of interest. This process allows performing a first concentration of the sample thanks to the lower volume of the extracting solution with respect to the LAB volume.

Extraction chromatography is the other process that allows us to drastically concentrate the sample and in principle removes a large amount of interfering nuclides. Numerous dedicated tests have been performed in order to determine the best procedure and elution solutions. The efficiency of the final procedure are reported in Table 4.4 and in the plot in Figure 4.10 on page 111.

Also for the extraction chromatography the results show very good efficiencies both for $^{238}$U and $^{232}$Th. Based on the data provided by the manufacturer of the UTEVA resin, the stripping capability of $^{232}$Th could be better if HCl is used instead of $HNO_3$ or if ammonium oxalate is added to the elution solutions. The first option has been tested by performing an elution using HCl 1 M and shows a very high efficiency for both uranium and thorium, but the use of HCl is very problematic in NAA because the $^{35}$Cl, that is stable with an isotopic abundance of about 76%, is activated by the irradiation into $^{36}$Cl that having a half-life of $3 \cdot 10^5$ years cannot be eliminated and the bremsstrahlung radiation emitted by the beta electron increase the background of the measurement that is unacceptable for low concentration sample because of the reduction of the sensitivity. Despite the addition of ammonium oxalate produced an increase in the stripping efficiency, the risk of contamination due to the use of another reagent that is not available with an ultra-purity grade is not acceptable, because even though the efficiency obtained by using only $HNO_3$ is not as high for $^{232}$Th as for $^{238}$U, it is an excellent result.

Based on these results, also this process is very promising thanks to its very good efficiency and the possibility to obtain a very high concentration of the sample.

| Test number | U efficiency (%) | Th efficiency (%) |
|---|---|---|
| T6 | 107±8 | 102±8 |
| T17 | 99±8 | 95±19 |
| T21.1 | 86±11 | 111±16 |
| T21.2 | 69±7 | 88±16 |
| T21.3 | 93±9 | 67±12 |
| Mean | 91±14 | 93±17 |

Table 4.2: Results of the measurement of the liquid-liquid extraction efficiency for uranium and thorium in pre-irradiation

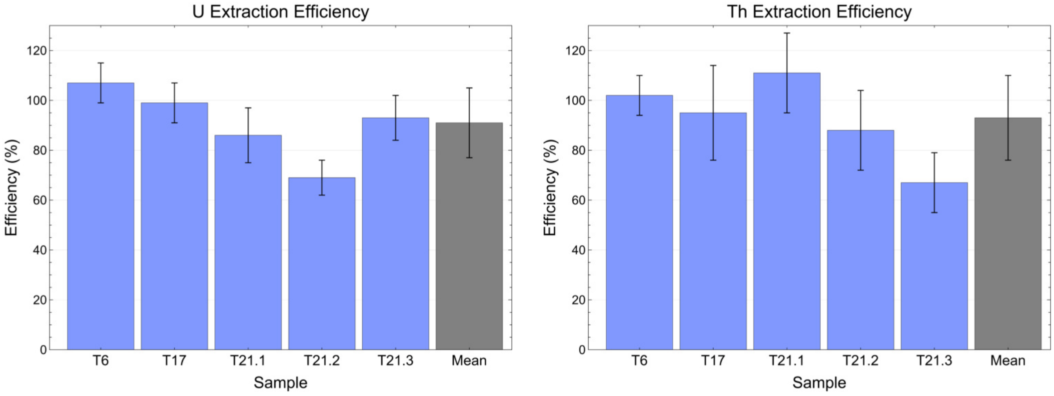

(a) (b)

Table 4.3: In the plot on the left and right are shown the results of the liquid-liquid extraction efficiency measurements respectively for uranium and thorium. The last column in each plot represents the mean of the five measurements and their error bar is computed as the standard deviation of the results.

| Test number | U efficiency (%) | Th efficiency (%) |
|---|---|---|
| T6 | 93±9 | 76±6 |
| T9 | 85±9 | 109±13 |
| T21.1 | 102±14 | 62±9 |
| T21.2 | 133±14 | 71±13 |
| T21.3 | 93±9 | 97±17 |
| Mean | 101±19 | 83±19 |

Table 4.4: Results of the measurement of the extraction chromatography efficiency for uranium and thorium in pre-irradiation

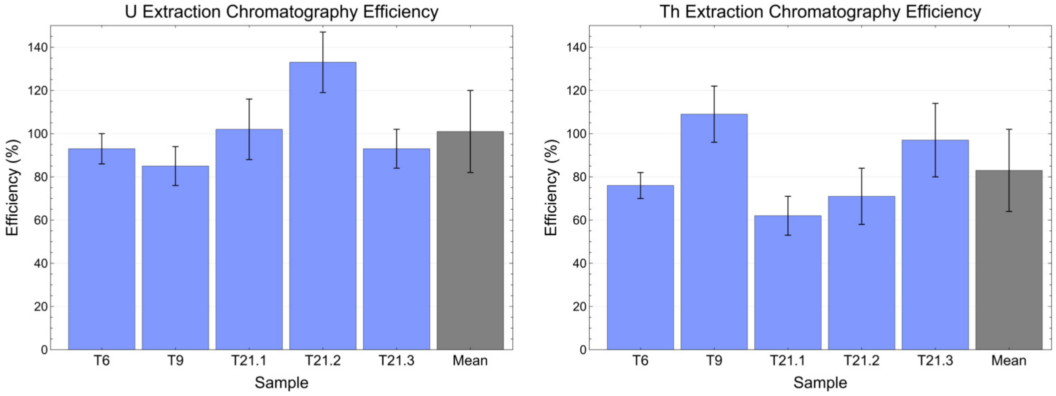

(a) (b)

Figure 4.10: In the plot on the left and right are shown the results of the extraction chromatography efficiency measurements respectively for uranium and thorium. The last column in each plot represents the mean of the five measurements and their error bar is computed as the standard deviation of the results.

| Test number | U efficiency (%) | Th efficiency (%) |
|---|---|---|
| T6 | 100±11 | 78±9 |
| T21.1 | 88±16 | 69±14 |
| T21.2 | 92±13 | 62±16 |
| T21.3 | 86±12 | 65±16 |
| T22.1 | 96±8 | 86±7 |
| T22.2 | 85±7 | 92±10 |
| T23.1 | 94±7 | 61±6 |
| T23.2 | 92±7 | 68±8 |
| Mean | 92±5 | 73±11 |

Table 4.5: Results of the measurement of the complete pre-irradiation procedure efficiency for uranium and thorium.

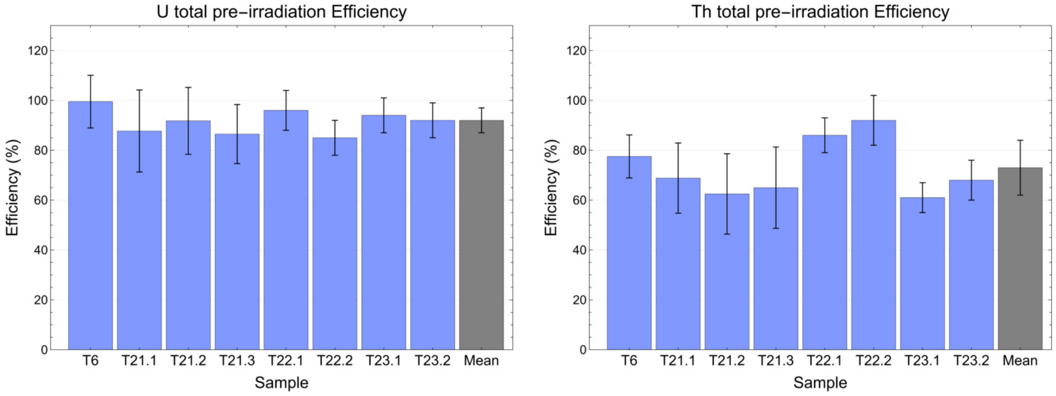

(a) (b)

Figure 4.11: In the plot on the left and right are shown the results of the complete pre-irradiation efficiency measurements respectively for uranium and thorium. The last column in each plot represents the mean of the measurements and their error bar is computed as the standard deviation of the results.

The efficiency of the complete pre-irradiation processes has been evaluated by combining the efficiencies of the single procedures (when available for the same test) and performing additional tests of the complete pre-irradiation procedure. The new tests 22 and 23 are performed by contaminating the LAB with 2 ng of $^{238}$U and $^{232}$Th and performing the liquid-liquid extraction and extraction chromatography on the whole sample, without splitting. The global efficiency has been computed as the ratio of the uranium and thorium mass recovered at the end of the extraction chromatography procedure and the expected value obtained by the dilution sample. The Final results are summarized in Table 4.5 and in the plot in Figure 4.11 on the previous page. The results of tests 22 and 23 are consistent with the ones obtained from the previous tests and provide a confirmation of the repeatability of the processes.

### 4.4.2 Post-irradiation

The post-irradiation treatments, in particular the extraction chromatography, allow us to reduce the concentration of interfering nuclides with no risk of contamination. It is important to remark that this treatment involves the nuclides $^{239}$Np and $^{233}$Pa because are performed after the irradiation. This implies that the concentration of the nuclides of interest is much lower with respect to the concentration of $^{238}$U and $^{232}$Th because not all the nuclides are activated during the irradiation. A simple calculation based on the experimental data of activation allows us to estimate that the ratio between the number of activated nuclides and the original one is about $3 \cdot 10^{-7}$. As a consequence, the procedure performed in post-irradiation in principle could be less efficient and reproducible. Here will be discussed the preparation of the samples, the performed treatments, and the obtained efficiencies of these treatments.

#### 4.4.2.1 Sample preparation

The preparation of the samples for the efficiency measurement of the post-irradiation treatments is different for the liquid-liquid extraction and for extraction chromatography.

For the liquid-liquid extraction, a sample of 30 g of LAB and separately a sample of standard solution are irradiated. After the irradiation, the LAB is contaminated and then extracted.

For extraction chromatography, the efficiency measurement has been performed in different ways. One option is to prepare a solution with a known quantity of irradiated standard and use this solution to charge the TEVA resins. This allows measuring the efficiency of the extraction chromatography process without any interference from the other processes. The second option is to use the resulting sample obtained by the liquid-liquid extraction in post-irradiation, in analogy to the pre-irradiation procedure. This allows measuring two efficiencies on the same sample, but it is required to split the extracted solution to measure the efficiency of the liquid-liquid extraction in order to know the starting point of the extraction chromatography.

The standard solution used to contaminate the LAB after the irradiation is prepared by diluting the usual 1000 ppm standard solution in acid water in order to reduce its concentration. The acid solution is irradiated and then diluted with the isopropyl alcohol in post-irradiation. The irradiation is performed before the alcohol dilution because the heating of the solutions during the irradiation can reduce the volume of the alcohol, concentrating the solution and changing its concentration. The dilution steps are the following:

- Dilution 1:10 with $HNO_3$ 1% → standard 100 ppm

- Dilution 1:100 with $HNO_3$ 1% → standard 1 ppm
- Irradiation of about 3 mL of 1 ppm solution.
- Dilution 1:100 with isopropyl alcohol → standard 10 ppb

As in the previous case, in order to have 1 ng of nuclides, it is required to use 0.1 mL of this solution. The procedure to contaminate the LAB is exactly the same as the pre-irradiation procedure (see 4.4.1.1 on page 107) with the exception that the mass of the LAB is lower because 100 g cannot be irradiated at the same time.

#### 4.4.2.2 Radiochemical treatments

The liquid-liquid extraction is performed in a similar way to the pre-irradiation case but since the LAB volume is lower, so it is the extracting solution, and the nitric acid concentration is different in order to adapt to the following extraction chromatography step. After the contamination of the LAB, the following liquid-liquid extraction procedure is applied:

1. Add 6 mL of $HNO_3$ 8 M to the 30 g LAB sample.
2. Stir vigorously the mixture with the magnetic stirrer for 20 minutes.
3. Transfer the mixture to the separatory funnel and wait for the phase separation.
4. Spill the aqueous phase that is accumulated on the bottom (higher density).
5. Transfer the LAB to the original beaker.
6. Repeat step 1-5 for two more times.

If only the extraction efficiency is required, the whole sample is measured. Otherwise, it is split to have a faction that can be treated with extraction chromatography.

The extraction chromatography with the TEVA resin is performed according to the procedure described in section 4.2.2.2 with the correct volume of reagents for the sample.

It is important to note that the application of post-irradiation treatments implies an increase in the waiting time, the time lapsed from the end of the irradiation and the beginning of the sample measurement, and the higher the waiting time, the lower the sensitivity. Since the time required to complete both the described post-irradiation treatments is in the order of some hours, the increase in the waiting time does not affect the sensitivity in a significant way, because the half-lives of $^{239}$Np and $^{233}$Pa are much longer, respectively 2.4 days and 27 days.

#### 4.4.2.3 Efficiency results

The liquid-liquid extraction process is involved only in the red sequence in Figure 4.2 on page 96 where the LAB is directly irradiated and then processed with liquid-liquid extraction and extraction chromatography with TEVA resin. Although this is the sequence with the least risk of contamination, it does not allow the sample to be concentrated before the irradiation. For this reason, this option has been excluded. Despite this, an evaluation of the extraction efficiency has been performed and the obtained result is reported in Table 4.6 on the following page. The efficiency is quite good but it is lower with respect to extraction efficiency obtained in pre-irradiation. This can be attributed to the fact the the extraction process is applied to $^{239}$Np and $^{233}$Pa nuclides that have different chemical

| Test number | U efficiency (%) | Th efficiency (%) |
|---|---|---|
| T14 | 93±9 | 76±6 |

Table 4.6: Results of the measurement of the efficiency of the liquid-liquid extraction post-irradiation treatment for uranium and thorium.

| Test number | U efficiency (%) | Th efficiency (%) |
|---|---|---|
| T22.1 | 94±11 | 97±11 |
| T22.2 | 106±12 | 82±12 |
| T23.1 | 112±12 | 85±12 |
| T23.2 | 108±12 | 63±10 |
| Mean | 105±8 | 82±14 |

Table 4.7: Results of the measurement of the efficiency for the extraction chromatography post-irradiation treatment for uranium and thorium.

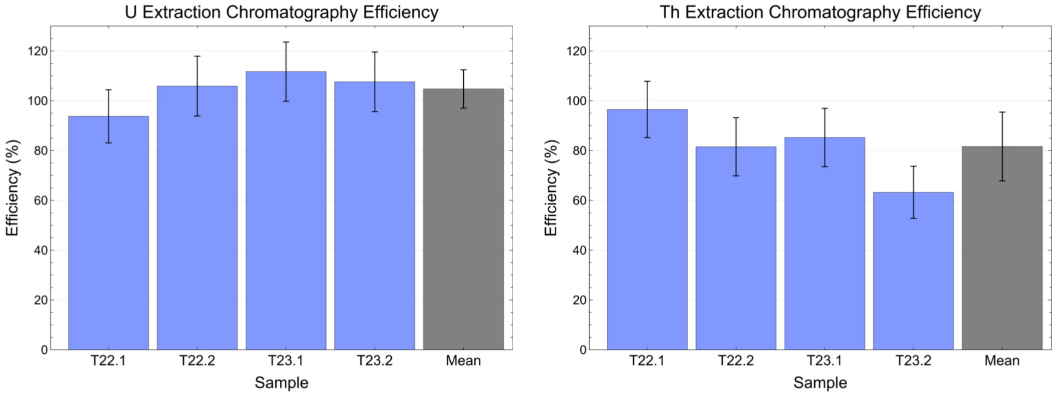

(a) (b)

Table 4.8: In the plot on the left and right are shown the results of the efficiency of the extraction chromatography post-irradiation measurements respectively for uranium and thorium. The last column in each plot represents the mean of the measurements and their error bar is computed as the standard deviation of the results.

behaviors than the precursor nuclides $^{238}$U and $^{232}$Th (see section 4.4.2 on page 112) and whose concentration is much lower.

The most useful post-irradiation treatment is extraction chromatography which allows removing all the interfering nuclides produced during the irradiation. The efficiency of this process has been evaluated in different tests in order to optimize the procedure and the solutions used for the treatments. In particular, the nitric acid concentration of the conditioning solution has been optimized, increasing it up to 8 M. At this concentration, we obtained the highest retention of $^{239}$Np and $^{233}$Pa by the TEVA resin. Other aspects that required optimization are the charging and elution times and the composition of the elution solution. The final procedure is the one described in section 4.2.2.2 on page 102, which provides the best recover efficiencies for both $^{239}$Np and $^{233}$Pa.

The results of the tests performed with the final procedure are shown in Table 4.7 and in Figure 4.8. The results show a very good recovery efficiency (almost unitary) for $^{239}$Np and $^{233}$Pa, even if in for this nuclide is a bit lower.

| Sample | $^{82}$Br (Bq/kg) Pre | $^{82}$Br (Bq/kg) Post |
|---|---|---|
| LAB | 232±2 | 97±3 |
| Extracted | 2.4±0.1 | 14.2±0.6 |
| Eluate | 0.96±0.03 | 0.040±0.002 |

Table 4.9: Specific activities of $^{82}$Br in the three samples used to evaluate the reduction efficiency of the liquid-liquid and extraction chromatography.

| Sample | Efficiency Pre | Efficiency Post |
|---|---|---|
| Liquid-liquid extraction | (98.97±0.04) % | (85.4±0.8) % |
| Extraction chromatography | (60±2) % | (99.72±0.02) % |
| Total reduction | (99.56±0.01) % | (99.959±0.002) % |

Table 4.10: Reduction efficiency of $^{82}$Br for the liquid-liquid and extraction chromatography. The last row reports the total reduction efficiency of the two processes. The reported errors are associated with the counting statistics.

### 4.4.3 Interfering nuclides reduction

As already introduced in the previous sections, one of the main purposes of the radiochemical treatment implementation is the reduction of the interfering nuclide concentration. The numerous test performed showed that both the liquid-liquid extraction and the extraction chromatography allow obtaining a very high reduction of the concentration of interfering nuclides. A quantitative estimation has been performed by exploiting the samples used to measure the efficiency of the treatments. One of the main interfering nuclides is the $^{82}$Br that is produced by the activation of the $^{81}$Br, a nuclide present in the LAB probably due to the production process of the LAB itself. The $^{82}$Br has a half-life of 35 h and its beta decays are followed by a cascade of numerous high-energy gamma rays. As a consequence, this nuclide can deeply impact the measurement sensitivity because it can increase the background in the region of interest and it has a half-life comparable to the $^{239}$Np one.

The reduction capability has been studied both in pre and post-irradiation. In both cases the evaluation has been performed by measuring the specific activity of $^{82}$Br in the samples with the following equation:

$$As\left(\frac{Bq}{g}\right) = \frac{N}{t \cdot \epsilon \cdot BR \cdot m} \tag{4.5}$$

where N is the number of events in the peak of interest, t is measurement time, $\epsilon$ is the detection efficiency at the energy of the peak, BR is the branching ratio of the observed gamma ray and m is the mass of the sample. The specific activity has been calculated as the mean of the specific activities obtained considering three main peaks of the $^{82}$Br: 554 keV, 619 keV and 777 keV.

The reduction efficiency associated with a treatment has been computed by using the following equation:

$$\epsilon_{red} = 1 - \frac{As_{After}}{As_{Before}} \tag{4.6}$$

The efficiency has been estimated for the liquid-liquid extraction and chromatography extraction for both the pre and post-irradiation phases by measuring the activity of the

| Test number | U efficiency (%) | Th efficiency (%) |
|---|---|---|
| T22.1 | 90±7 | 83±7 |
| T22.2 | 90±7 | 75±7 |
| T23.1 | 105±8 | 52±5 |
| T23.2 | 99±8 | 43±5 |
| Mean | 96±7 | 63±19 |

Table 4.11: Results of the measurement of the efficiency for the complete procedure for uranium and thorium performed on the same sample.

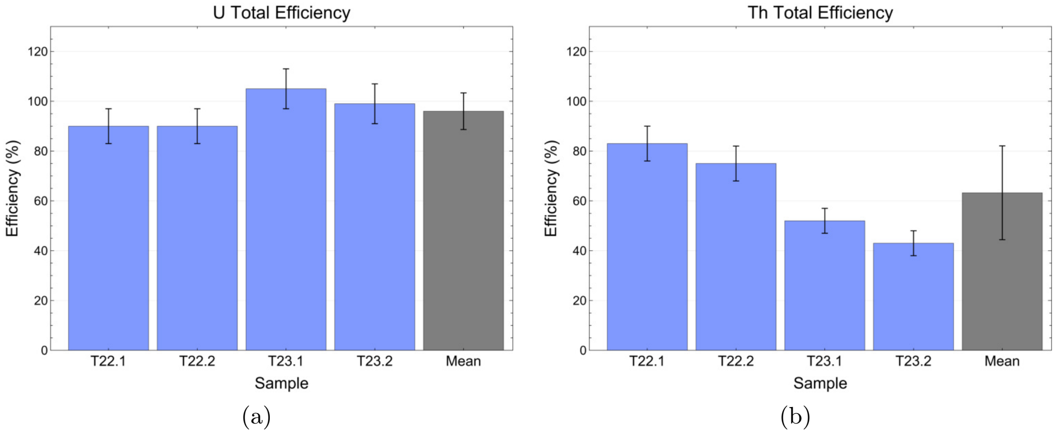

(a) (b)

Table 4.12: In the plot on the left and right are shown the results of the total efficiency of the pre- and post-irradiation treatments applied to the same sample respectively for uranium and thorium. The last column in each plot represents the mean of the measurements and their error bar is computed as the standard deviation of the results.

LAB, the extracted solution, and the eluate. The measured activities are reported in Table 4.9 and in Table 4.10 on the preceding page are reported the relative reduction efficiencies.

Although the major contribution to the total reduction is associated with the liquid-liquid extraction in pre-irradiation and to the extraction chromatography in post-irradiation, the reductions obtained by combining the two treatments are comparable, allowing us to obtain an almost quantitative reduction.

### 4.4.4 Final procedure

Based on the results obtained during the tests performed to estimate the efficiencies of the single procedures, the reagents validation, and interfering nuclides reduction the most suitable radiochemical procedure has been chosen. The pre-irradiation treatments showed very good recovery efficiency and the quality of the reagents and containers is adequate for the required sensitivities and also the post-irradiation treatment showed good efficiency. This made it possible to not exclude one of these treatments for low efficiencies or other problems. The application of the delayed coincidence for the analysis of the $^{239}$Np and the cosmic background reduction provided by plastic scintillator detectors does not allow reaching the sensitivity required by the JUNO experiment. In order to reach the objective we decided to implement the most promising procedure, the green one in Figure 4.2 on page 96, that implements both the liquid-liquid extraction and extraction chromatography in pre-irradiation and the extraction chromatography in post-irradiation. Although this is the most subject to contaminations, it is the most promising in therm of sensitivities because it allows obtaining the highest level of preconcentration. Since the efficiencies of the different processes are very good the use of all three is not deleterious and the sample mass increase and interfering nuclides reduction are much greater than the loss due to the lower efficiency.

The efficiency of the complete procedure can be computed as the product of the efficiencies of the pre-irradiation treatments and the extraction chromatography in post-irradiation as follows:

$$\epsilon_U = (92\pm5)\,\% \cdot (105\pm8)\,\% = (97\pm9)\,\% \tag{4.7}$$

$$\epsilon_{Th} = (73\pm11)\,\% \cdot (82\pm14)\,\% = (60\pm14)\,\% \tag{4.8}$$

These efficiencies are consistent with the ones determined by performing the complete pre- and post-irradiation procedure on the same sample. Tests 22 and 23 were performed in this way and a fraction of the whole sample is used to compute the partial efficiencies reported in the previous sections. The results obtained for the efficiency of the complete procedure in these two tests are reported in Table 4.11 and Figure 4.12 on the facing page.

The results obtained for the uranium show a very good efficiency of recovery with very high reproducibility, while the thorium results show a good efficiency but it is subjected to a higher fluctuation between different samples. This means that there is a random error associated not only with the measurement of the sample (counting statistics) but also with the chemical treatments and the latter is dominating the total error. For this reason, the errors associated with the efficiency are computed as the standard deviation of the single measurements.

## 4.5 Blank measurements and sensitivities

As pointed out many times in the previous sections, the most critical aspect of the complete procedure that involves the pre-irradiation treatments is the possibility of introducing contaminations of $^{238}$U or $^{232}$Th during the treatments themselves. In order to determine the quality of all cleaning processes and the entities of these potential contaminations, two blank tests have been performed.

A blank test is a measurement conducted on a fake sample that has the same mass (or volume) as the final one and it is subjected to the same procedures but it is neither contaminated with the standards nor entered in contact with the substance to measure.

In our case, the blank samples consist of 200 mL of 5 M ultra-pure nitric acid that is the volume of solution required for the liquid-liquid extraction of 1 kg of LAB. This solution is then racked into the extraction bottle and then, after a waiting time of 1 hour, into the separatory funnel, in order to simulate the contact with the bottle and the funnel for the same time as in a real extraction. The solution is then processed with the usual procedure of extraction chromatography with UTEVA resin as described in section 4.2.2.1 on page 101. The eluate is then irradiated and processed with the procedure of extraction chromatography with TEVA resin as described in section 4.2.2.2 on page 102. The resulting eluate is finally measured with the GeSparK detector in order to determine the concentration of $^{238}$U and $^{232}$Th.

### 4.5.1 Blank 1

The first blank test was performed during irradiation number 12518 on March 9, 2022 and the sample was irradiated for 6 hours. The next day we performed the post-irradiation

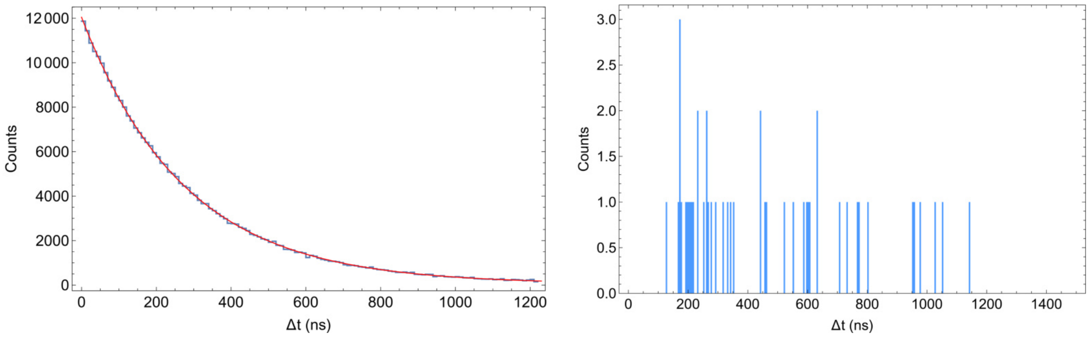

(a) (b)

Figure 4.12: Time distribution of the delayed events of the standard solution with the resulting best fit curve and the delayed events of the sample.

radiochemical treatments at the chemistry laboratory at LENA. The measure of the final sample began in the late afternoon of the same day and lasted 1 week for the uranium determination and about 1 month for thorium.

At the end of the respective measurement times, the data acquired by the GeSparK detector was analyzed by the dedicated analysis tool in order to extract the necessary information and select the signals of interest.

For the uranium determination, the developed delayed coincidence method was used. A standard solution containing about 0.1 µg of uranium and 2 µg thorium was measured as the reference standard for the NAA. As introduced during the description of the method, since the number of events associated with the standard is very large, a chi-square fit was performed in order to determine the number of signal events ($239\,300 \pm 700$). In Figure 4.12a is shown the time distribution of the delayed events and the resulting best fit curve.

The same selection criteria are applied to the sample data and the resulting time distribution is shown in Figure 4.12b, with a total number of events of 47.

In order to determine the signal contribution, a fit using a maximum likelihood (ML) method is performed by using the distribution (equation 3.11) reported in section 3.4.1 on page 84. The maximum likelihood indicates that the best estimation for the c parameter (signal to total events ratio) is 0.76. This means that only this fraction of the total events are "true" $^{239}$Np decay events, while the others are random background events. Based on this value, the number of signal events considered for the following analysis is $N = 47 \cdot 0.76 = 36$.

In order to verify the result obtained with this approach, an estimation of the number of background events was performed at the end of the long measurement performed for the $^{232}$Th determination. After a waiting time of about 1 month, almost all the potentially present $^{239}$Np nuclides have decayed and in this condition, a measurement of the rate of delayed events is a measure of the random coincidence rate, because there are no other sources of delayed events. By considering a time period of the same duration as the measurement, the number of delayed events detected was 15. With this estimation, the number of signal events is $N = 47 - 15 = 32$. This number is consistent with the number obtained with the maximum likelihood estimation based only on the first week's data. The advantage of the ML method is that it is based only on the data of the measurement and does not require waiting until the end of the long measurement to compute the final results for the $^{238}$U concentration. Moreover, if only the measurement of $^{238}$U must be performed, this method avoids to unnecessarily prolonging the measurement to compute the background events. An exception to this is that if the measurement event rate is dominated

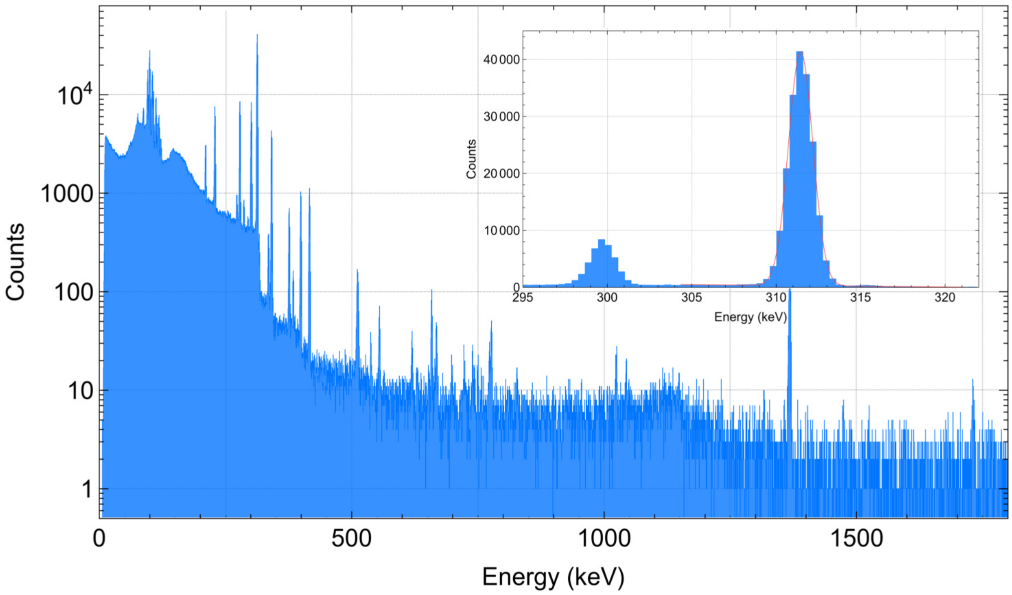

Figure 4.13: Spectrum of the events detected by the HPGe detector during the standard solution measurement. On the top-right a zoom near the 312 keV peak of $^{233}$Pa with the relative fit function.

by the background of the detector, the number of expected random coincidences is almost constant since it depends on constant parameters which are the measurement time and the total event rate, and in this case, it is not necessary to prolong the measure to estimate the background.

By using this information and the NAA equation, the concentration of $^{238}$U in the sample was computed and the results are shown in Table 4.13 on the following page.

The determination of the $^{232}$Th is performed by using the standard NAA technique described in section 3.4.2 on page 87. The spectrum of the measurement of the standard is shown in Figure 4.13, where are visible both the $^{239}$Np and $^{233}$Pa characteristic peaks. A simple fit of the 312 keV peak provided the number of events associated to the $^{232}$Th standard (189 100±500). The measurement of the sample lasted for exactly 2 664 000 s, during which the spectrum shown in Figure 4.14 on the following page was obtained. As can be seen, there is no evidence of a peak in the region of interest at 312 keV, so a limit is computed for the concentration of $^{232}$Th using the same approach described in section 3.4.4 on page 88

The integral of the spectrum in the ROI is computed and the statistical fluctuation is computed as the square root of the number of events multiplied by 1.64 in order to compute the limit at 90% of confidence level. The number of background events in the ROI was 131, so the number of events used in the NAA equation was $\sqrt{131} \cdot 1.64 = 19$.

By using this information and the NAA equation, the concentration of $^{232}$Th in the sample was computed and the results are shown in Table 4.13 on the following page.

For the $^{238}$U a value for the concentration was found indicating the presence of contamination in the $10^{-14}$ g/g scale, while for the $^{232}$Th a limit was obtained indicating the at the moment the measurement sensitivity is limited by the background of the detector and not by an internal contamination [43]. In order to verify this result and determine the possible sources of uranium contamination, another blank test was performed.

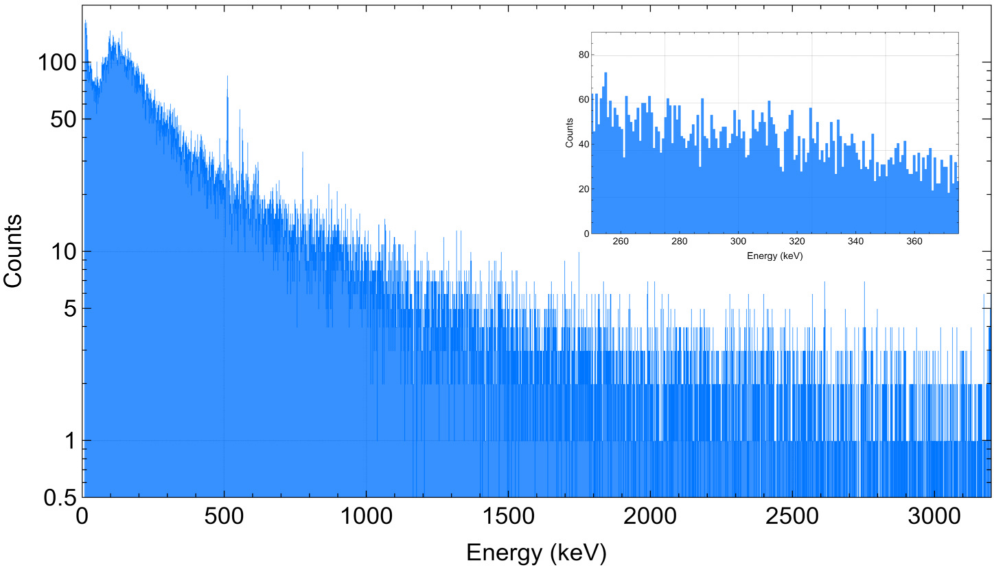

Figure 4.14: Spectrum of the events detected by the HPGe detector during the measurement of the sample. On the top-right a zoom around the ROI between 250 keV and 370 keV.

| U concentration ($10^{-15}$ g/g) | Th concentration ($10^{-15}$ g/g) |
|---|---|
| 7.9±1.4 | <44 |

Table 4.13: Concentration of $^{238}$U and $^{232}$Th obtained by the measurement of the first blank sample.

### 4.5.2 Blank 2

The second blank test was performed during irradiation number 12565 on July 25, 2022, and the sample was irradiated for 6 hours. The next day we performed the post-irradiation radiochemical treatments and the measure of the final sample began in the late afternoon of the same day and lasted 1 week for the uranium determination and about 1 month for thorium.

The mass and the composition are the same as the Blank 1 sample as well as the radiochemical treatments performed. The only difference, in this case, is a modification of the GeSparK detector configuration we tried to implement in order to verify a potential measurement sensitivity improvement.

The first modification is a reduction of the volume of the liquid scintillator detector. The original volume was 200 mL as described in the detector general description, but since the sample volume using the final radiochemical procedure is limited to 15 mL, that is the elution volume, the volume of the liquid scintillator detector can be reduced. The maximum allowed sample-to-LS ratio for the Ultima Gold AB is 1:1, but we decided to keep a conservative lower ratio (about 1:2) with a total volume of 50 mL. The smallest size of the LS detector, both in diameter and height, allow increasing the detection efficiency of the HPGe detector thank to the higher geometrical efficiency and lower absorption.

Another modification is the use of another HPGe detector. We tried to couple the LS detector to the HPGe of the GMX system, which has a crystal with a relative efficiency of 100%, with respect to the 38% of the GeSparK one, which would allow a further increase of

| Configuration | Efficiency $^{239}$Np | Efficiency $^{233}$Pa |
|---|---|---|
| 1 | 1.30% | 0.81% |
| 2 | 2.03% | 1.21% |
| 3 | 3.55% | 2.57% |

| Configuration | Efficiency gain $^{239}$Np | Efficiency gain $^{233}$Pa |
|---|---|---|
| 1→2 | 1.54 | 1.48 |
| 2→3 | 1.75 | 2.12 |
| 1→3 | 2.73 | 3.17 |

Table 4.14: Detection efficiencies for $^{239}$Np and $^{233}$Pa main peak for different detector configurations and the efficiency gain for the new configuration with respect the original GeSparK.

| U concentration ($10^{-15}$ g/g) | Th concentration ($10^{-15}$ g/g) |
|---|---|
| 9.5±1.0 | <24 |

Table 4.15: Concentration of $^{238}$U and $^{232}$Th obtained by the measurement of the second blank sample.

the total efficiency to be obtained. I'd like to point out that the efficiency gain is not equal to the ratio of the relative efficiencies because the $^{239}$Np and $^{233}$Pa gamma rays have low energies and in this case the sensitive part of the HPGe crystal in only the top part and not the entire volume. The efficiency increase is mostly due to the different diameters of the crystals.

In order to estimate the efficiency gain we could expect with these modifications, three Monte Carlo simulations have been performed in order to determine the efficiencies in the different configurations. The results are shown in Table 4.14.

1. Original GeSparK detector configuration: 200 mL container and 38% HPGe detector
2. New detector configuration: 50 mL container and 38% HPGe detector
3. New detector configuration: 50 mL container and 100% HPGe detector

As expected, it is possible to obtain a gain of factor 1.5 with the only reduction of the container size, while the use of the high-efficiency HPGE allows obtaining another factor $\sim 2$, higher for $^{233}$Pa than $^{239}$Np because of the higher energies of the associated gamma rays.

For this second blank test, we tried to implement the third option with both modifications and the analysis flow was the same described for Blank 1.

A net signal was found for the uranium contamination, with a number of signal events equal to 94 for $^{239}$Np and no evidence of signal for $^{233}$Pa with a ROI integral equal to 285 counts. These values, combined with the new measurement of a standard solution because of the changing of the experimental setup, allowed us to obtain the results shown in Table 4.15.

As can be seen, the concentration of uranium is compatible with the previous results, indicating that this contamination is intrinsic to the reagent and material used and most likely not due to accidental contaminations. The increase in the efficiency of the measurement system obviously had no effect on the final result, other than a reduction in the relative error. This is not the case of the $^{233}$Pa, because in absence of a signal the sensitivity takes advantage of the higher detection efficiency. In fact, the limit is reduced by a factor of 1.85 which is consistent with the square root of the efficiency gain ratio.

### 4.5.3 Final consideration on blank measurements and sensitivities

Based on the results obtained in the two blank tests, there is evidence of contamination of $^{238}$U at the level of about $1{\cdot}10^{-14}$ g/g considering the 200 mL of the extracting solution. The reproducibility of this result allows us to conclude that this contamination is not probably due to random effects associated with the procedures or the operators because in this we can expect a large fluctuation in the resulting concentration. The most probable source of this contamination is the nitric acid itself which has been validated at the level of $3{\cdot}10^{-14}$ g/g by ICP-MS and guaranteed at $1{\cdot}10^{-13}$ g/g by the manufacturer and also considering the dilution factor of 3 applied in the preparation of the extracting solution, the acid cannot be excluded by using these results.

In this case, we can expect that the amount of uranium introduce in the procedure is proportional to the quantity of extracting solution. With this assumption, the sensitivity of a measurement performed on 1 L of LAB can be estimated by rescaling the concentration of $^{238}$U in the extracting solution with the concentration factor of the liquid-liquid extraction, because the amount of $^{238}$U is the same, but the concentration is computed considering 1 kg of mass and not 228 g.

The resulting sensitivity is expected to be the following:

$$C\,(g/g) = 8.7{\cdot}10^{-15}\,\mathrm{g/g} \cdot \frac{228\,\mathrm{g}}{1000\,\mathrm{g}} = 2.0{\cdot}10^{-15}\,\mathrm{g/g} \tag{4.9}$$

The obtained uranium results represent an observed contamination and, for this reason, this value can also be subtracted from the value obtained in the measurement of a real sample. In this case, the sensitivity is increased because it is related not to the value of the observed contamination but to its fluctuation. Based on the results obtained by the two blank samples the fluctuation is much lower and this is very promising for the sensitivity. To apply this approach it is however necessary to measure more blanks in order to obtain a more robust estimation of the standard deviation. A further increase in sensitivity could also be obtained by increasing the mass of the processed LAB.

For the determination of $^{232}$Th, there is no evidence of contamination up to $2.4{\cdot}10^{-14}$ g/g. At the moment, the limitation to the sensitivity is not the intrinsic contamination of the reagent but the background of the detector.

With the same consideration exposed for the determination of $^{238}$U, the expected sensitivity for $^{232}$Th with the measurement condition used in the blank tests is the following:

$$C\,(g/g) = 2.4{\cdot}10^{-14}\,\mathrm{g/g} \cdot \frac{228\,\mathrm{g}}{1000\,\mathrm{g}} = 5.5{\cdot}10^{-15}\,\mathrm{g/g} \tag{4.10}$$

This value is higher than the required sensitivity for the JUNO LAB but there are margins for improvement. The sensitivity of NAA depends on many factors and it is possible to optimize each parameter in order to increase it. In particular, in the second bank test, we tried to increase the measurement efficiency that has a linear dependence on the sensitivity (with the assumption of constant background), but this parameter cannot be further increased. Another possibility is the reduction of the detector background which impacts the sensitivity with the square root. The new system that exploits the GMX HPGE with a relative efficiency of 100% has a much lower efficient cosmic veto system compared to the GeSparK detector one so it is currently on study and development an improvement of the veto system of the GeSparK detector in order to compensate for the lower efficiency of the HPGe detector and obtain an additional gain in the sensitivity thanks to an almost quantitative reduction of the cosmic background. Finally is possible to increase the mass of the LAB sample and eventually increase the irradiation time, eventually in multiple irradiation days thanks to the fact that the $^{233}$Pa has a very long half-life.

## 4.6 Radiochemical treatment for $^{40}$K measurement

The direct measurement approach by NAA on a LAB sample, described in section 3.4.5, allowed us to obtain a very good sensitivity on the $^{40}$K concentration, but it is not enough for the requirements of the JUNO experiment. In order to increase the sensitivity, a new dedicated measurement technique is under development.

The idea is to perform a radiochemical treatment on the sample to concentrate the content of potassium present in the LAB, obtaining an increase in the mass of the measured sample, as in the case of uranium and thorium. The chemical properties of uranium and thorium are very different from potassium, so it is not possible to use the same approach. In particular, there are no resins commercially available that are able to selectively separate the potassium from other elements, in particular sodium, which is its most important interfering nuclide. For this reason, a gravimetric approach is under study.

The proposed technique involves the selective precipitation of the potassium, the collection of the precipitate by filtration, and then the measurement of the filter, all performed post-irradiation in order to avoid contaminations from the environment. This is necessary because potassium is a more common element than uranium and thorium, playing also important biological roles.

The steps of the procedure are summarized as follows:

1. Irradiation
   The irradiation transforms the $^{41}$K into $^{42}$K.

2. LAB liquid-liquid extraction with $NaNO_3$ 0.1 M
   In this step the LAB is extracted with a solution of sodium nitrate ($NaNO_3$) 0.1 M in order to transfer the potassium from the LAB to an aqueous solution. This step is performed by repeating the extraction process three times with a fresh extracting solution.

3. Addition of 2 mg of non irradiated potassium as KCl
   A carrier of natural potassium (not irradiated) is added to the sample. The presence of the carrier is necessary to force the small amount of potassium extracted by the LAB to precipitate and for the following filtration step to work properly.

4. Addition of 1 mL of Na-TPB 0.1 M
   A solution of Sodium TetraphenylBorate (Na-TPB) is added to the sample. This reagent is able to precipitate selectively the potassium, because the K-TPB is an insoluble compound, while sodium and other elements remain in the solution.

5. Wait for the complete precipitation of K-TPB
   A waiting time of about 20-30 minutes is necessary to ensure the complete precipitation of the potassium.

| Sample | Carrier | Na-TPB | Efficiency (%) |
|---|---|---|---|
| 1 | $Tl^{2+}$5 mg | 2 mmol | 81±6 |
| 2 | $K^+$ 2 mg | 2 mmol | 78±6 |
| 3 | $Tl^{2+}$5 mg | 5 mmol | 84±7 |

Table 4.16: List of the three samples prepared for the test of the potassium procedure. For each sample are reported the type and mass of carrier, the amount of Na-TPB added for the precipitation of potassium, and the resulting efficiency of the precipitation procedure.

6. Filtration of the precipitate with a 0.45 µm glass fiber filter
   When the non-irradiated potassium precipitate as K-TPB, also the irradiated potassium precipitate, and the resulting crystals are filtered on a 0.45 µm glass fiber filter. The filter needs that the size of the precipitate crystals must be large enough (>0.45 µm) to be retained by the filter and the presence of the carrier allows obtaining a macroscopic quantity of precipitate with adequate particles size.

7. Washing of the filter with cold water saturated with K-TPB
   The precipitate is washed in order to remove the residual traces of activated sodium and other interfering nuclides present in the solution. Since the K-TPB has very little solubility (64 mg/L), in order to reduce the solubility of the precipitate, which would introduce a reduction in the recovery efficiency, we use cold water saturated with K-TPB. This is because the solubility of a salt decrease as the temperature of the water decrease and the presence of saturated K-TPB makes it impossible for other salts to pass into the solution.

8. Measurement of the filter with HPGe gamma spectrometry
   The small filter with the precipitate is finally measured with the well-type HPGe detector (GePozzetto) described in section 3.2.2.2 on page 64 in order to exploit its high measurement efficiency.

At the writing time, this procedure has been tested on a standard solution of potassium with a known quantity of potassium in order to verify the feasibility of the procedure and determine the efficiency of the precipitation process, and optimize the different steps.

The test has been performed with the goal of determining the best carrier and to have a first feedback on the efficiency of the procedure. In particular, in the literature, we found that in order to increase the precipitation of potassium with TPB it is possible to use both potassium and thallium as a carrier. In order to verify their effect on small concentrations of activated potassium and the use of different quantities of Na-TPB, we prepared a set of three identical solutions with the same amount of potassium (1 ng) and treated as described in the above procedure except for the LAB irradiation and extraction steps. In particular a standard solution of potassium was irradiated and then the desired quantity was dissolved in 45 mL of $NaNO_3$ 0.1 M, in order to reproduce the same conditions at the end of the extraction process. In Table 4.16 are reported the different conditions of each test, together with the resulting efficiencies for the precipitation procedure.

The efficiencies obtained are compatible with each other indicating the type of carrier and the amount of Na-TPB are not relevant parameters at the tested concentrations. Since thallium is a toxic compound and there is no benefit to using it, we decided to use potassium. The result is very promising because the resulting efficiencies of the precipitation process are very high and we expect the liquid-liquid extraction will have high efficiency because of the extremely high affinity of the alkali metal, like potassium, with water solutions.

In the next tests, we are going to test the possibility of reducing the mass of the carrier without a loss of efficiency in order to make for an easy and quick filtration process, which is a quite long procedure due to the tendency of the filter to clog up. In the following tests, we are going to test the complete procedure including the extraction process on LAB and finally test the procedure on a non-contaminated LAB sample.

# Chapter 5

# Conclusions

The work of my Ph.D. thesis has been dedicated to two main connected topics. The first one is the validation of the Monte Carlo simulations of the background of the JUNO detector with the verification of the correctness of the radiopurity requirements for its materials and the determination of the total background budget. The second topic is the development of a measurement system and technique able to measure the concentration of uranium, thorium, and potassium at the ppq level ($10^{-15}$ g/g), as required for the liquid scintillator of the JUNO detector.

A comparison of the simulation results with different Monte Carlo codes has been performed in order to cross-check the results in absence of experimental data. SNiPER, the official simulation software of the JUNO experiment has been compared with Arby, the Monte Carlo software developed at the University of Milano-Bicocca for the simulation of the efficiency of HPGe and bolometric detectors, and G4-LA, the software developed at PL2i in France. Different critical issues of the simulation of the JUNO response have been studied in particular how the quenching factor is implemented in SNiPER and the correctness of its implementation, the effect of the particle propagation parameters on the final quenched energy, and the correct parameterization of the $\beta$-decay spectral shape. These studies led also to the definition and standardization of the best parameters to be used in SNiPER before the data produced by JUNO will be available. The use of Arby allows access to its source code which has been critical for studying in detail these effects and the possibility of directly implementing the geometry of the JUNO detector allowed me to implement techniques to reduce its complexity in order to cut down the computation time. The bin-to-bin comparison of the spectra associated with liquid scintillator and acrylic sphere contaminations computed by the three independent Monte Carlo codes allowed verifying the correctness of the implementation of the particle transportation and the application of the quenching factor, especially for alpha particles, for which it is a very critical aspect due to the high intensity of the effect. Furthermore, thank the detection efficiency information obtained by the total number of events in the spectra associated with the contamination in the most critical components of the JUNO detector, I was able to compute the contribution of each component to the background rate of JUNO, providing its background budget, and to determine how the fiducial volume and energy cuts affect it. The resulting value for the total expected background event rate produced by natural radioactivity present in the detector materials and applying the default FV and energy cuts is 7.2 Hz that is safely lower than the limit of 10 Hz set to ensure the final sensitivity of the experiment.

In parallel to this activity, I worked on the development of a technique able to measure the concentration of the natural radioactive nuclide $^{238}$U, $^{232}$Th and $^{40}$K in the liquid scintillator of the JUNO detector (LAB) which is the material with the most stringent requirement since it is the active volume of the detector and it has a huge mass. To guarantee the radiopurity of the final liquid scintillator and during all steps of the purification process, a new technique has been developed. The proposed technique exploits the high sensitivity of the neutron activation analysis, which allow reaching sensitivity on $^{238}$U and $^{232}$Th in the order of $10^{-12}$ g/g when combined with standard HPGe gamma spectroscopy for the measurement of the activation products. To increase it, a $\beta - \gamma$ coincidence detector, the GeSparK, has been developed to allows reducing the background of a standard single HPGe configuration, and the development of a specific delayed coincidence techniques for the measurement of $^{238}$U and the implementation of radiochemical treatments on the sample have been performed. In order to reduce the contribution of the cosmic muons to the detector background, a dedicated muons veto system has been implemented by using plastic scintillator detectors. Before implementing it, the effectiveness of the veto system has been evaluated by using a dedicated Monte Carlo simulation. The simulation showed a very good reduction of the muons background and, based on that, the complete final setup was constructed. It is composed of two detectors on the top and four detectors on the sides of the GeSparK lead shield and makes it possible to obtain a reduction of about 80% of the cosmic muons signals, essential to increase in particular the sensitivity of thorium measurements. The speed of the signals produced by the liquid scintillator detector of the GeSparK system has been exploited to develop a new delayed coincidence technique that takes advantage of the nuclear structure of $^{239}$Np, the activation product of $^{238}$U, which has a metastable level, to obtain an extremely strong marker of this particular decay and significantly increase the measurement sensitivity compared to the traditional approach. This marker is extremely powerful at identifying the decay of $^{239}$Np because the beta and IC electrons that characterize it are produced with a delay related to the mean life of the metastable state of the $^{239}$Pu. The only residual background to this signal are random coincidences of right-energy events in a very short time and thus is extremely suppressed and, for this reason, this technique allowed increasing the sensitivity of the uranium measurement, gaining a factor of 4 on a measurement performed on a LAB sample directly irradiated. The development of this technique has also led to the measurement of the metastable level's lifetime itself with twenty times better accuracy than previous results.

Although the GeSparK detector and the delayed coincidence techniques make it possible to reach very high sensitivity, it was not enough for the JUNO liquid scintillator requirements. For this reason, a series of radiochemical treatments have been tested in order to increase the mass of the sample and reduce the background produced by the interfering nuclides activated during the irradiation process. For the determination of uranium and thorium a liquid-liquid extraction phase has been applied to transfer these elements from the LAB to an acid aqueous solution, which can be treated by extraction chromatography with UTEVA and TEVA resins respectively before and after irradiation to concentrate the radionuclides of interest and remove the interfering ones. At the required radiopurity level, the risk of contamination of the sample by the used materials and reagents is extremely high so the control of the contamination sources was a crucial aspect of this activity, making it necessary to validate each reagent and develop a dedicated cleaning protocol. In particular, the irradiation containers have been optimized to maximize their size, with custom-made ones, and the containers for the samples have been accurately chosen for the best radiopurity and cleanliness, using PFA vials for the sample manipulation and irradiation. Moreover, a dedicated cleaning protocol for these containers and all the other tools used for the radiochemical treatments has been implemented. The efficiency of each radiochemical process has been determined in order to evaluate the feasibility of each technique by using samples contaminated with a known amount of uranium and thorium. These results have led defining a radiochemical procedure that is composed of liquid-liquid extraction and extraction chromatography with UTEVA resin in pre-irradiation and an extraction chromatography with TEVA resin in post-irradiation to maximize the preconcentration of the sample and the interfering nuclides concentration reduction. The efficiency of this complete procedure has been estimated by the product of the pre- and post-irradiation steps and then directly measured by applying it to the sample tests, confirming the obtained values. The results show a high recovery efficiency for both $^{238}$U and $^{232}$Th, respectively of (97±9) % and (60±14) %. These values also demonstrate a very good reproducibility of the radiochemical processes for uranium and also quite good for thorium because in this case we observed a higher fluctuation most probably related to the different chemical behavior and affinity with the resin of the protoactinium. A dedicated measurement of the interfering nuclides reduction shows that the implemented procedure allows reducing its contribution almost quantitatively for both the $^{24}$Na and $^{82}$Br, the most important ones.

To demonstrate the sensitivity of the complete technique and verify the quality of the cleaning protocols, two measurements conducted on "blank samples" have been performed by combining the GeSparK detector, the delayed coincidence technique, and the radiochemical treatments. The results showed the presence of contaminations at the level of $9{\cdot}10^{-15}$ g/g for uranium and no contamination up to $2.4{\cdot}10^{-14}$ g/g. Since no LAB has been processed in these tests, the observed uranium contamination can only be associated with the solution or materials used in the radiochemical processes. One possible source that cannot be excluded is the ultra-pure nitric acid because it has been validated by ICP-MS measurement at the level of $3{\cdot}10^{-14}$ g/g and also taking into account that the acid is one-third of the total sample mass, for which its contribution must be lowered by a factor 3, the obtained limit on its uranium concentration is compatible with those obtained on the blank samples. The water can instead be excluded because it has been validated at a much lower level than the observed contamination. Other possible sources include the UTEVA resin and the containers, but in this case, the high reproducibility of their contribution is quite surprising, which is expected to be very random. The contamination source could be investigated by measuring a blank sample with a lower or higher mass of nitric acid solution. In these cases if the same value of uranium concentration will be obtained we could conclude that the contamination comes from the acid because the introduced amount of uranium is proportional to the acid mass, on the contrary, only other sources should be considered.

If the uranium contamination cannot be reduced, we have to consider this value as the background of the procedure and thus treat it in the proper way. An estimation of the sensitivity can be performed by considering that the acid solution used in the blank tests is representative of a LAB sample of 1 kg, so if the LAB is not contaminated, the obtained concentration can be rescaled by the mass to obtain the values to be associated with the LAB. These values are $2{\cdot}10^{-15}$ g/g and $5.5{\cdot}10^{-15}$ g/g for uranium and thorium respectively. The proposed technique allowed obtaining very high sensitivities for the JUNO LAB that are in the same order of magnitude as the requirements. Nevertheless, they are quite higher for the final measurement, there is a margin of improvement for both values. Since the uranium result represents an observed contamination, this value can also be subtracted from the value obtained in the measurement of a real sample and thus the sensitivity can be also greater because in this case it is related not to the value of the observed contamination but to its fluctuation. Based on the results obtained by the two blank samples the fluctuation is much lower and this is very promising for the sensitivity, despite this requires more blank tests to be performed in order to obtain a more robust estimation of the standard deviation. For the thorium measurement, an higher efficiency veto configuration is currently under study and development in order to obtain an almost quantitative reduction of the cosmic background and thus compensate for the lower HPGe efficiency of the GeSparK detector with respect to the GMX one and obtain a further increase on the final sensitivity. Another improvement can be obtained by extending the measurement and the irradiation times and evaluating the possibility of a further increase in the sample mass.

For the measurement of $^{40}$K, I started to develop a dedicated radiochemical procedure based on a gravimetric separation of the potassium from the other nuclides after a liquid-liquid extraction to transfer the potassium to an aqueous solution. This technique is currently under development and it is very promising thanks to the initial efficiency test performed.

The proposed methods for measuring uranium, thorium, and potassium are among the most sensitive in the world for directly measuring trace amounts of these elements in liquid scintillators.

# Appendices

# Appendix A

# High precision measurement of the half-life of the metastable level of Pu239

## A.1 Introduction

During my Ph.D. work, I worked on the development of a dedicated measurement technique to increase the sensitivity in the $^{238}$U determination on activation samples. As described in section 3.4.1 on page 84, this technique exploit the particular characteristics of the decay of the nuclide $^{239}$Np, produced in the activation of $^{238}$U, on $^{239}$Pu. In fact, the $^{239}$Pu is characterized by the presence of an excited metastable state at 391.6 keV that introduce a delay in the following deexcitation transitions that can be exploited in order to increase the capability of identifying the signal event with respect to the background ones and so increase the sensitivity.

During the development of this method, we realized that the GeSparK detector, used for the analysis of the activated samples with this technique, is not only able to detect the signals and measure the time difference between the prompt and delayed one in order to perform the event selection, but also to measure the delay distribution with very high accuracy. The accurate measurement of this distribution can be used to determine the half-life of the metastable level with higher accuracy than the previous results.

The nuclear structure of $^{239}$Pu has been studied extensively since the 1950s, leading to a well-known level scheme. In 1955 Engelkemeir and Magnusson performed the measurement of the half-life of the $^{239}$Pu(391.6 keV) level achieving a result of (193±4) ns by exploiting a coincidence circuit between anthracene and sodium iodide scintillation counter, a result confirmed by Patel et al. almost twenty years ago obtaining a value of (192±6) ns.

During our studies in the development of the measuring technique, we performed a dedicated measurement of a sample of $^{239}$Np in order to determine with higher accuracy the half-life of this level. This work has been concluded with the publication of a dedicated paper [37].

In this appendix, I will describe the measurement principle and how the measurement and analysis have been performed.

## A.2 Measurement principle

In figure A.1 is shown a simplified version of the decay scheme of $^{239}$Np on $^{239}$Pu. As can be seen, the beta decay of $^{239}$Np has a 40.5% of probability populating the metastable level at 391.6 keV. The deexcitation of this level can happen via $\gamma$ or internal conversion (IC) transitions. The $\gamma$-rays or IC electrons are emitted according to an exponential time distribution with a decay constant related to the half-life of the metastable level. The following deexcitations to the ground state can occur via subsequent $\gamma$ or IC transitions.

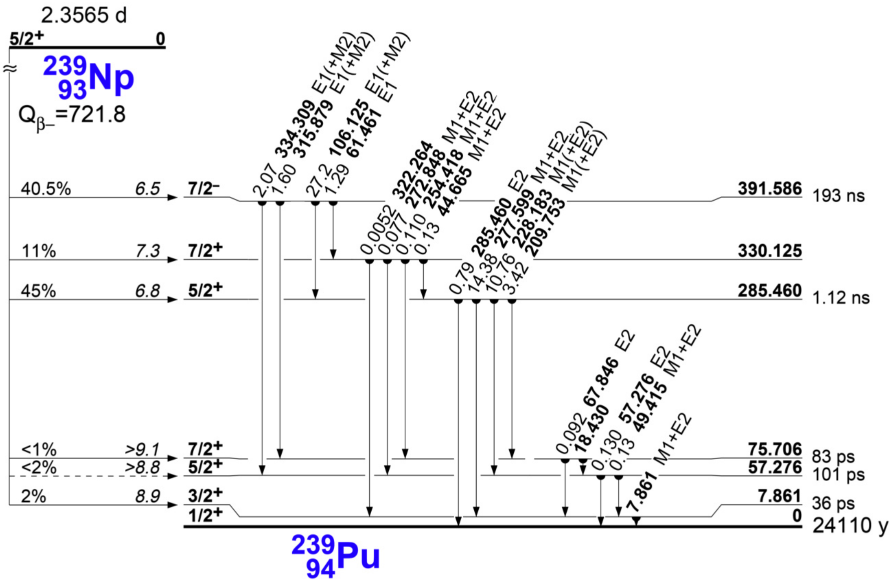

Figure A.1: Simplified nuclear level scheme of $^{239}$Pu[36]. The main transitions related the metastable level deexcitation are shown.

The LS detector of the GeSparK makes it possible to detect with high efficiency and good time resolution of both the $\beta^-$ and IC/$\gamma$ electrons, while the HPGe detector is useful to detect the $\gamma$ or X photons frequently emitted as a consequence of the IC transitions. The $\beta$-$\gamma$ coincidence capability of the GeSparK detector was exploited to select different decay channels in order to evaluate possible systematic uncertainties and to perform a reduction of the possible random coincidences. In Table A.1 the main observed signatures are reported. By measuring the delay between the two signals generated in the liquid scintillator from $\beta^-$ and IC/$\gamma$ electrons it is possible to construct the life distribution of the metastable levels that are populated by the observed beta decays. An exponential least squares fit on the obtained time difference distribution allows us to achieve an accurate evaluation of the half-life.

## A.3 Half-life measurement description

### A.3.1 Source preparation

As introduced before, a dedicated measurement was performed in order to estimate the half-life of the metastable level. A source of $^{239}$Np was produced by neutron activation at the research reactor TRIGA Mark II at LENA (PV), irradiating a sample of $^{238}$U certified standard solution. The total irradiated mass of $^{238}$U was about 0.5 $\mu$g diluted in 2.5 mL of water.

After six hours of irradiation in the Lazy Susan channel, the sample was dissolved in the liquid scintillator of GeSparK detector (Ultima Gold AB - Perkin Elmer) and sealed in its Teflon container in order to be measured.

| $\beta^-$ (keV) | IC (keV) | $\gamma$/X-ray (keV) |
|---|---|---|
| $\beta^-$ (330) | $e^-$ (278)<br>$e^-$ (228)<br>$e^-$ (210) | $\gamma$ (106) , $\gamma$ (106) + X-ray |
| $\beta^-$ (330) | $e^-$ (8)<br>$e^-$ (57)<br>$e^-$ (75) | $\gamma$ (278)<br>$\gamma$ (228)<br>$\gamma$ (210) |
| $\beta^-$ (330) | $e^-$ (106) | X-ray (99, 104, 116, 120)<br>$\gamma$ (278)<br>$\gamma$ (228)<br>$\gamma$ (210) |

Table A.1: Example of the main observed signatures. The first column is the $\beta^-$ transition to the metastable level. The next two columns on the right are the delayed transitions detectable by GeSparK detector. These transitions are the main de-excitation channels of the metastable level. Other transitions can also occur with lower probability, contributing to the total signal.

### A.3.2 Experimental measurement and data acquisition

The acquisition parameters of the GeSparK detector are the same described in section 3.4.1 on page 84. Figure A.2 shows an example of the LS acquired signals. The first pulse (trigger) is identified as the $\beta^-$ electron signal and the second one is the IC/$\gamma$ electron signal (delayed). In coincidence with the PMT pulse, is also digitized the HPGe signal in order to verify the presence of the coincident $\gamma$/X-ray emission. Figure A.3 shows the spectrum of the HPGe signals in coincidence with the LS pulses. Therefore, for each detected coincidence event the LS and HPGe detectors acquired data are stored. The measure of the activated sample lasted 284 hours with a coincidence rate, at the measurement start, of about 150 Hz and a $^{239}$Np source activity of 1050 Bq.

### A.3.3 Analysis and results

The algorithm to perform the automatic detection of the pulses and the calculation of the relative time distance in each LS acquired window is the same developed for the analysis of the LAB. Figure A.4 shows the resulting distribution of the time differences between the $\beta^-$ trigger events and the delayed IC/$\gamma$ electrons.

Since the number of acquired signal events was huge, the fit of the time distribution was performed with a function defined by a decreasing exponential plus a constant and a chi-square minimization. The analytical form of the fit function is the following:

$$f(t) = a \cdot e^{-\frac{ln2\cdot t}{T_{1/2}}} + c \tag{A.1}$$

where $a$ is the amplitude of the exponential term and $c$ is the flat component to account for random coincidences in the approximation $R\cdot\Delta t_w << 1$ (R is the source rate). To reduce the contribution of random events generated from interference nuclei, activated during the irradiation, only LS events in coincidence with a $\gamma$ ray below 300 keV were considered in the analysis. This was possible because beyond that energy value the contribution of $^{239}$Np signals events is negligible with respect to the background.

The distortion at the beginning of the distribution of Figure A.4 is due to the pile-up of the trigger event with the delayed one. This affects both the determination of the delays

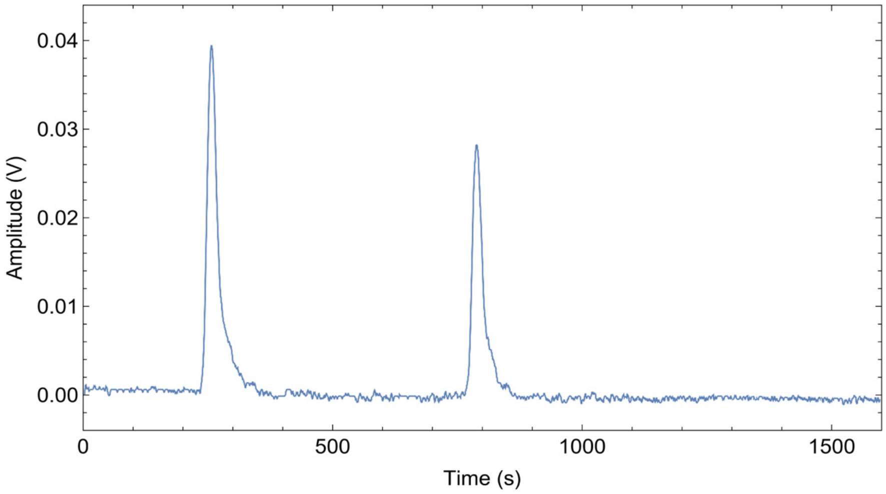

Figure A.2: Example of delayed coincidence signals of $^{239}$Np decay as acquired by the GeSparK detector.

and the evaluation of the pulse amplitudes.

In order to exclude the events that are affected by pileup, the lower limit of the fit was set at 150 ns, according to the timing features of the LS pulses (pulse width $\sim$ 100 ns). The upper limit of the adaptation has been set at 1280 ns in order to remove the signals acquired at the end of the time window since it is not sure to correctly measure their properties.

The best fit of the distribution and the fitting parameters are shown in Figure A.4. The goodness-of-fit is satisfactory and the pull distribution in the bottom panel shows a good agreement between data and model. The obtained $\chi^2$/ndf (0.928) and the corresponding probability (0.958) show a very good agreement between the data distribution and the fit function. The best estimation of the $^{239}$Pu half-life is (190.0±0.2) ns.

### A.3.4 Analysis of the systematic uncertainties

During the analysis process, some possible sources of systematic errors for the determination of the $T_{1/2}$ of the 391.6 keV metastable level were identified and their contribution was evaluated. These are:

- $T_{1/2}$[$^{239}$Pu(285.5 keV)]=1.12 ns
- ADC clock accuracy
- Histogram binning
- Fit threshold

The presence of the 285.5 keV level in the decay scheme of $^{239}$Pu could introduce a systematic error since this level, energetically below the 391.6 keV, is also a metastable state with a known half-life of 1.12 ns. Some events detected during the measurement are characterized by decay cascades that involve both these levels. In this case, the time delay from the trigger event ($\beta^-$) and IC/$\gamma$ electron are shifted by a quantity related to the $T_{1/2}$ of 285.5 keV) level. The resulting time delay distribution of these specific events is

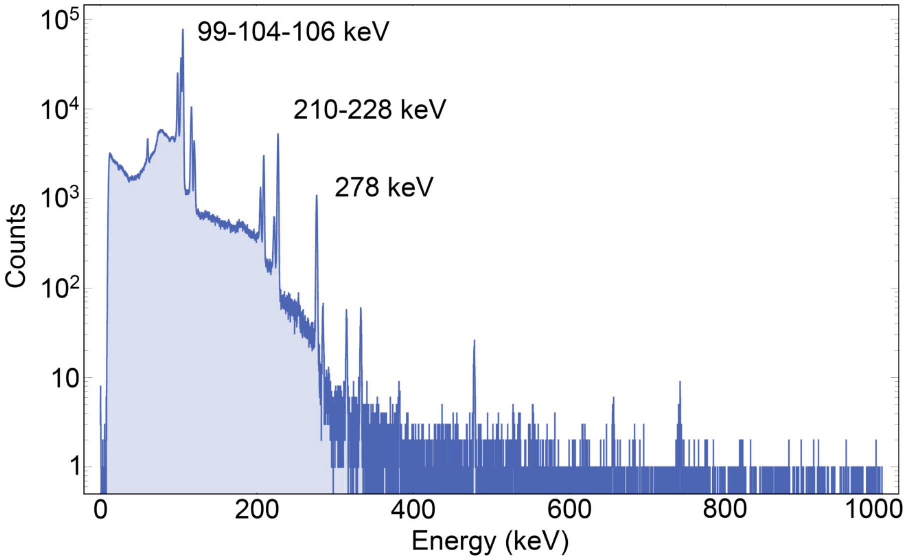

Figure A.3: HPGe energy spectrum of gammas in coincidence with delayed LS events. The main $\gamma$ lines of $^{239}$Pu are labeled in the plot.

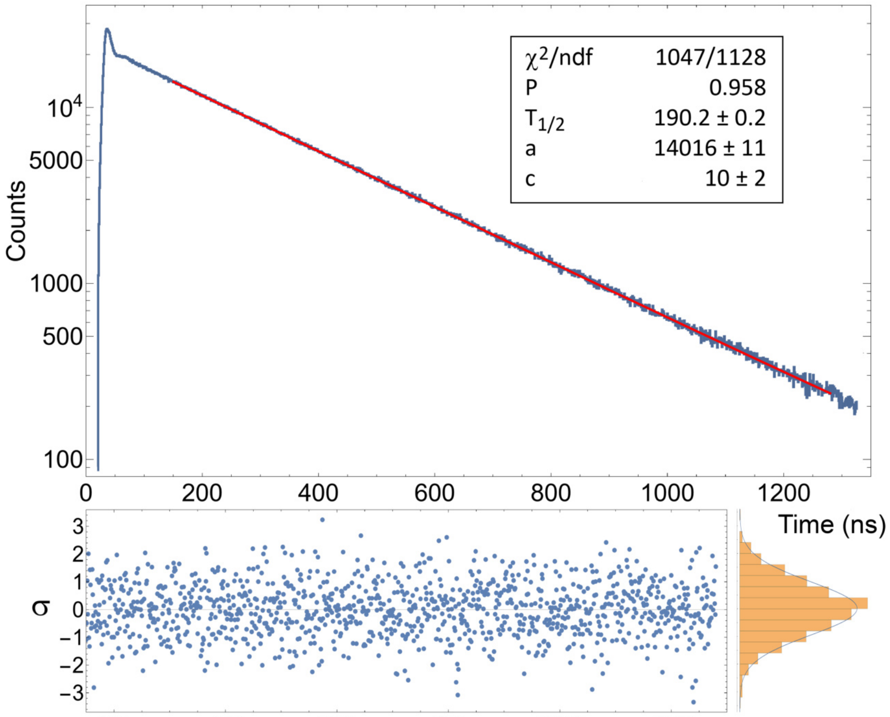

Figure A.4: Top panel: distribution of the time differences, between $\beta^-$(trigger event) and IC/$\gamma$ electron (delayed event). Red line shows the best fit in the range 150 ns - 1280 ns, with a bin width of 1 ns. Bottom panel: pull distribution.

described by the convolution of two exponential functions, whose decay constants are given

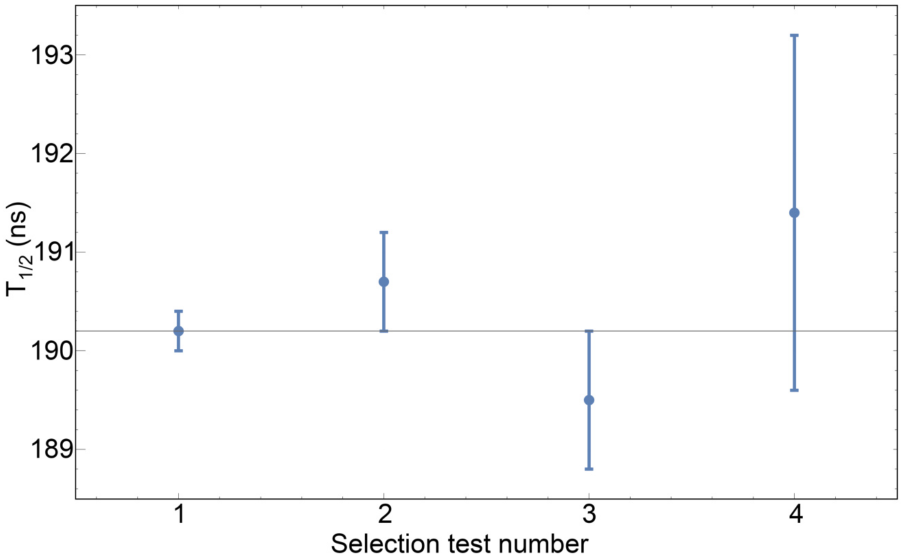

Figure A.5: Mean life obtained by fitting different time distributions constructed selecting a particular decay channel using the HPGe coincidence. Test 1 is obtained by selecting all the gammas below 300 keV. The test 2, 3 and 4 are performed selecting respectively the 106 keV, 104 keV and 228 keV peaks.

by the mean life of the two levels, as reported in the following equation:

$$\left(Exp(\tau_L) * Exp(\tau_S)\right)(t) = \frac{\tau_L \tau_S \left(e^{-\frac{t}{\tau_L}} - e^{-\frac{t}{\tau_S}}\right)}{\tau_L - \tau_S} \tag{A.2}$$

where $\tau_L$ (190/ ln(2) ns) and $\tau_S$ (1.12/ ln(2) ns) are the mean lives of the 391.6 keV and 285.5 keV metastable levels respectively. Since $\tau_L >> \tau_S$, for $t >> \tau_S$ the contribution of the fastest exponential term is negligible. This assumption is verified in the analysis since we set the lower limit of the fit interval at 150 ns, which is much higher than 1.12 ns. Another proof was obtained by a toy Monte Carlo simulation. In this case, the delays produced by the two metastable levels were simulated by generating a random number according to their exponential distribution. A fit of the resulting distribution was performed excluding the first 150 ns, obtaining a result perfectly compatible with the longer mean life.

A further source of systematic error could be the accuracy of the ADC clock. In accordance with the warranted specifications of the ADC (National Instrument mod. PXI-5153), this contribution was evaluated in tens of picoseconds, thus negligible.

Finally, the distribution of the time differences in Figure 4 was fitted for different choices of the binning in the histogram and fitting threshold between 150 ns and 650 ns. In both cases, the variations of the fit result are negligible with respect to the statistical error associated with the measurement. Thanks to these considerations it can be stated that statistics dominate the uncertainty of the final result. Moreover, this is also a test to study the presence of other radioactive contaminants that would produce different half-life estimations by changing the fit threshold.

In order to bring out other systematic errors not considered in the above list, a validation of the obtained result was performed. The presence of the HPGe detector in the experimental setup makes it possible to select with a good energy resolution gamma or X photons. By forcing an energy selection for $\gamma$/X-ray in the analysis of the acquired events, it is possible to identify specifically observed decay sequences. Figure A.5 shows the half-lives obtained from the different selections. The first point is the result achieved in the previously reported analysis selecting all the gammas with energy below 300 keV. The points 2, 3 and 4 were instead obtained by selecting respectively 106 keV, 104 keV and 228 keV energy emissions. The selections are representative of different types of transitions in the decay scheme. Since the results obtained from the fits are compatible within one standard deviation, it is possible to conclude that the effect of selecting a specific decay sequence is negligible (e.g. presence of 285.5 keV metastable level). This test also demonstrates the possibility of using all the gammas below 300 keV in order to increase the statistics of the measurement.

## A.4 Conclusions

The new measurement technique, which exploits the delayed coincidences generated between $\beta^-$ decay and IC/$\gamma$ electron emissions, allowed us to measure the half-life of the isomeric nuclear states with very high accuracy.

The dedicated analysis performed, allowed us to achieve the best results for $T_{1/2}$ of the 391.6 keV level: (190.2±0.2) ns. This value is statistically compatible with the best-known value obtained by Engelkemeir but with a factor of 20 smaller uncertainty and it represents an advancement in the knowledge of the $^{239}$Pu nuclear levels.

# Appendix B

# Genesis software for Monte Carlo simulations

## B.1 Introduction and motivations

Genesis (GEneral NuclidE Simulation Software) is an application based on the toolkit Geant4 [24] development for easy and customizable simulations of different types of detectors and experimental setups, mainly devoted to the radioactivity research field.

In particular, this project started during my master's degree with the main goal of developing a simulation software able to simulate the response of the GeSparK detector (see section 3.3 on page 67 and [32]). This detector is composed of two different detectors, a liquids scintillator, and an HPGe, that work in time coincidence and it can observe delayed decays in the liquid scintillator detector, as described in section 3.4.1 on page 84. These characteristics impose some requirements on the simulation software that must be able to simulate the decays of the nuclides following the deexcitation of metastable states up to the nanosecond scale.

During the following years, Genesis has been improved to increase its simulation capability and performance.

Since the beginning I have set some requirements for this software and, at the moment, they are the following:

- Provide a graphical user interface (GUI) to interact with the user to set the initial parameters and control the simulation
- Provide a set of commands that allow the user to modify the simulation parameters without restarting the application
- Run in multi-thread mode to speedup complex simulations
- Able to simulate decays of radioactive nuclides and their chains, separating the decay of each isotope and, when required, also the metastable states.
- Allow the user to simulate different sources most simply and completely and to distribute the primary particle uniformly inside a volume (radioactive contaminations)
- Implement a simple way to describe the experimental setup based on text files
- Support the import of stl files from CAD software for the definition of complex geometries

Geant4 is a toolkit written in C++ language that provides different classes, that allow the developer to create its own Monte Carlo application for the simulation of the passage of particles through matter, by defining some mandatory classes required by Geant4.

Furthermore, the developer can extend its own application as desired in order to include custom functionalities that are not present in the toolkit.

## B.2 Main features and general description

Geant4 implements different visualization libraries allow visualizing the geometry of the experimental setup and often the particle tracks and the developer/user can decide which one to use. For Genesis, I decided to use the Qt libraries because they offer the possibility to create a performant GUI that allows the user to interact with the software during a simulation and not only the possibility to visualize the geometry. The native GUI can be customized by dedicated Geant4 commands in order to add buttons, menus, and commands. Since this GUI cannot provide all the required functionalities to allow the user to set the simulation parameters before the start of the simulation, I have implemented a dedicated GUI (hereinafter called initialization window, Figure B.1), based on Qt, that is opened at the start of the software and allow the user to set all the relevant parameters for the simulation, such as geometry txt and stl files, physics lists parameters, output and information files, global setting and so on. This initialization window is opened when the program starts and only when it is closed, the Geant4 classes are created and the native GUI is started. With this solution, the user can start the program by a simple "double-click" on its icon and then set all the parameters for the simulation. At this point, it is possible to start Geant4 with the graphical interface and run the simulation from it or start the batch mode and run the simulations described in a macro file using the so-called "UI command" in Geant4. These commands allow the user to modify a lot of different aspects of the simulation without rerunning the application and the developer can add its own command to those natives of Geant4. In this way, the user can use the native GUI for example during the creation of the experimental setup visualizing the resulting geometry or simulate a small number of events in order to understand the behavior of the simulation and eventually correct it, while it is possible to run a complex simulation or multiple simulations with different options without opening the native GUI. For example, it is possible to create a macro file that set the starting nuclide and the output file name, for many nuclides, then by executing this macro file in batch mode, the software simulates each nuclide automatically without the necessity for the user to wait for the end of the simulation of a nuclide to start the next one.

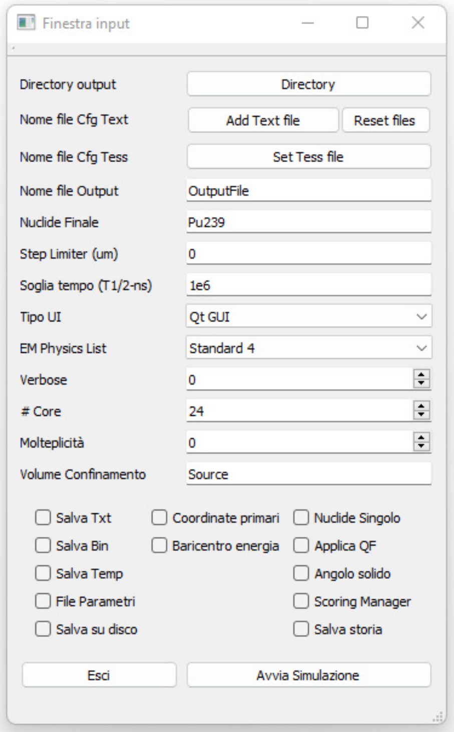

Nome file Output: OutputFile
Nuclide Finale: Pu239
Step Limiter (um): 0
Soglia tempo (T1/2-ns): 1e6
Tipo UI: Qt GUI
EM Physics List: Standard 4
Verbose: 0
# Core: 24
Molteplicità: 0
Volume Confinamento: Source

☐ Salva Txt
☐ Salva Bin
☐ Salva Temp
☐ File Parametri
☐ Salva su disco
☐ Coordinate primari
☐ Baricentro energia
☐ Nuclide Singolo
☐ Applica QF
☐ Angolo solido
☐ Scoring Manager
☐ Salva storia

Figure B.1: Picture of initialization window of Genesis.

The multi-thread mode is another requirement for Genesis because the Monte Carlo simulations generally require a lot of events to be simulated and this is very time-consuming. In order to speed up the simulations, Geant4 implement a simple way to parallelize the simulations by using multiple threads. The developers must initialize the dedicated classes and implement some methods in order to merge the output information of the simulated events from the different threads into the master one. This allows obtaining an improvement in the simulation time that is almost linear with the number of processor cores. Genesis allows the user to set the number of cores to be used in the simulation in the initialization window.

One peculiarity of Genesis is the algorithm that allows simulating the nuclides decay chains. When Geant4 simulates a particle it tracks it until it is stopped, decayed, or exits from the simulation volume (world). When a nucleus decays the first daughter particle that is tracked is the daughter nucleus and this creates a chain of decays until a stable nuclide is reached. At this point, Geant4 start to track all the other particles emitted in the decays (alphas, electron, neutrinos, etc.) making it impossible to separate the contribution of each decay. When the simulation of a radioactivity detector is performed the user wants to simulate the decay of each isotope of the chain separately without for example summing all the deposited energies of the chain because the decay of each nuclide contributes separately to the detector signal. Another similar problem is related to metastable states of excited nuclei. Also, in this case, the user may want to separate the contribution of particles emitted before and after the deexcitation of these states, because the detector could be able to observe them separately. In order to perform this task, a dedicated algorithm has been implemented in Genesis in order to separate the decays of each nuclide and the metastable states whose half-life is longer than a threshold defined by the user and eventually to interrupt the decay chain on a nuclide specified by the user. The particularity of this algorithm is to not interfere with the Geant4 simulation algorithm and event management. This is because, without going into detail, a Geant4 simulation is structured in Runs, Events, Tracks, and Steps and this structure should not be altered in order to obtain the best performances and use all the native functions of Geant4. For example, in the Geant4 logic, if the user wants to simulate 1 million decays of a nucleus, it should execute one run ("a simulation") composed of 1 million events and for each event, a number of particles is created (Traks), for example from the decays of the nucleus or due to secondary interactions, and tracked. The tracking of a particle is composed of many steps, and each of them is associated with a particular process and interaction type.

Genesis exploits the General Particle Source (GPS) class of Geant4 in order to help the user to define the generation of the primary particle of the simulation. The GPS allows the user to define the type and the properties of the primary particle by using the UI commands and provides a rich set of functions to define particular geometries and distributions. The GPS allows the user to set for example the type, energy, and direction of the particles and to define them as single values (constant) or to be distributions. The functionality of the GPS has been expanded in Genesis in order to allow the user to use specific setups. In particular, has been implemented a command that makes it possible for the user to generate the primary particles uniformly distributed inside a specific volume, which is a key feature for the simulation of radioactive contaminations in the samples. Another dedicated feature is the possibility to generate a flux of particles distributed on a semi-spherical surface with the momentum pointing to a specified point, region, or volume. This last feature was used for the simulation of the muon flux as described in section 3.3.2.3, while the uniform generation has been used for example for the simulation of uniformly distributed samples inside the LS detector of the GeSparK.

For the description of the geometry, Genesis exploits the text interface of Geant4 that allows the user to describe the geometry of the experimental setup by using one or more text files with simple commands that are used to define materials, solids, and their positions in the space. In addition to this interface, I added a dedicated system to easily import the stl file from CAD geometries. This allows the user to create its geometry by using CAD software and then save it in stl format file and import it in Genesis by assigning to each volume some properties, such as the material, color, and the possibility to be a detector. This functionality makes it possible to import in Geant4 very complex geometry, which can be extremely difficult or impossible to be described by using the text file. One example of the use of this functionality is the implementation of the GeSparK complete geometry (see Figure 3.18 on page 77).

# List of Figures

# List of Tables

# Bibliography

[1] Raymond Davis, Don S. Harmer, and Kenneth C. Hoffman. “Search for Neutrinos from the Sun”. In: *Phys. Rev. Lett.* 20 (21 1968), pp. 1205–1209. DOI: `10.1103/PhysRevLett.20.1205`. URL: `https://link.aps.org/doi/10.1103/PhysRevLett.20.1205`.

[2] John N. Bahcall, Neta A. Bahcall, and Giora Shaviv. “Present Status of the Theoretical Predictions for the $^{37}$Cl Solar-Neutrino Experiment”. In: *Phys. Rev. Lett.* 20 (21 1968), pp. 1209–1212. DOI: `10.1103/PhysRevLett.20.1209`. URL: `https://link.aps.org/doi/10.1103/PhysRevLett.20.1209`.

[3] John N. Bahcall et al. “Standard solar models and the uncertainties in predicted capture rates of solar neutrinos”. In: *Rev. Mod. Phys.* 54 (3 1982), pp. 767–799. DOI: `10.1103/RevModPhys.54.767`. URL: `https://link.aps.org/doi/10.1103/RevModPhys.54.767`.

[4] J. N. Abdurashitov et al. “Measurement of the solar neutrino capture rate with gallium metal”. In: *Phys. Rev. C* 60 (5 1999), p. 055801. DOI: `10.1103/PhysRevC.60.055801`. URL: `https://link.aps.org/doi/10.1103/PhysRevC.60.055801`.

[5] M. Altmann et al. “Complete results for five years of GNO solar neutrino observations”. In: *Physics Letters B* 616.3 (2005), pp. 174–190. ISSN: 0370-2693. DOI: `https://doi.org/10.1016/j.physletb.2005.04.068`. URL: `https://www.sciencedirect.com/science/article/pii/S0370269305005149`.

[6] S. Fukuda et al. “Constraints on Neutrino Oscillations Using 1258 Days of Super-Kamiokande Solar Neutrino Data”. In: *Phys. Rev. Lett.* 86 (25 2001), pp. 5656–5660. DOI: `10.1103/PhysRevLett.86.5656`. URL: `https://link.aps.org/doi/10.1103/PhysRevLett.86.5656`.

[7] J. Christensen-Dalsgaard et al. “The Current State of Solar Modeling”. In: *Science (New York, N.Y.)* 272 (June 1996), pp. 1286–92. DOI: `10.1126/science.272.5266.1286`.

[8] Y. Fukuda et al. “Evidence for Oscillation of Atmospheric Neutrinos”. In: *Phys. Rev. Lett.* 81 (8 1998), pp. 1562–1567. DOI: `10.1103/PhysRevLett.81.1562`. URL: `https://link.aps.org/doi/10.1103/PhysRevLett.81.1562`.

[9] Q. R. Ahmad et al. “Direct Evidence for Neutrino Flavor Transformation from Neutral-Current Interactions in the Sudbury Neutrino Observatory”. In: *Phys. Rev. Lett.* 89 (1 2002), p. 011301. DOI: `10.1103/PhysRevLett.89.011301`. URL: `https://link.aps.org/doi/10.1103/PhysRevLett.89.011301`.

[10] Planck Collaboration et al. “Planck 2018 results - VI. Cosmological parameters (Corrigendum)”. In: *A&A* 652 (2021), p. C4. DOI: `10.1051/0004-6361/201833910e`. URL: `https://doi.org/10.1051/0004-6361/201833910e`.

[11] Alessandro Strumia and Francesco Vissani. *Neutrino masses and mixings and...* 2006. DOI: `10.48550/ARXIV.HEP-PH/0606054`. URL: `https://arxiv.org/abs/hep-ph/0606054`.

[12] Pablo F. de Salas et al. “Neutrino Mass Ordering from Oscillations and Beyond: 2018 Status and Future Prospects”. In: *Frontiers in Astronomy and Space Sciences* 5 (2018). ISSN: 2296-987X. DOI: 10.3389/fspas.2018.00036. URL: https://www.frontiersin.org/articles/10.3389/fspas.2018.00036.

[13] Ivan Esteban et al. “The fate of hints: updated global analysis of three-flavor neutrino oscillations”. In: *Journal of High Energy Physics* 2020.9 (2020), p. 178. ISSN: 1029-8479. DOI: 10.1007/JHEP09(2020)178. URL: https://doi.org/10.1007/JHEP09(2020)178.

[14] Fengpeng An et al. “Neutrino physics with JUNO”. In: *Journal of Physics G: Nuclear and Particle Physics* 43.3 (2016), p. 030401. DOI: 10.1088/0954-3899/43/3/030401. URL: https://doi.org/10.1088/0954-3899/43/3/030401.

[15] M Koshiba. “Observational neutrino astrophysics”. In: *Physics Reports* 220.5 (1992), pp. 229–381. ISSN: 0370-1573. DOI: https://doi.org/10.1016/0370-1573(92)90083-C. URL: https://www.sciencedirect.com/science/article/pii/037015739290083C.

[16] Fengpeng An et al. “Neutrino physics with JUNO”. In: *Journal of Physics G: Nuclear and Particle Physics* 43.3 (2016), p. 030401. DOI: 10.1088/0954-3899/43/3/030401. URL: https://doi.org/10.1088/0954-3899/43/3/030401.

[17] Ran Han et al. “Potential of geo-neutrino measurements at JUNO”. In: *Chinese Physics C* 40.3 (2016), p. 033003. DOI: 10.1088/1674-1137/40/3/033003. URL: https://doi.org/10.1088/1674-1137/40/3/033003.

[18] Y. Zhang et al. “A complete optical model for liquid-scintillator detectors”. In: *Nuclear Instruments and Methods in Physics Research Section A: Accelerators, Spectrometers, Detectors and Associated Equipment* 967 (2020), p. 163860. ISSN: 0168-9002. DOI: https://doi.org/10.1016/j.nima.2020.163860. URL: https://www.sciencedirect.com/science/article/pii/S0168900220303648.

[19] A. Abusleme et al. “Optimization of the JUNO liquid scintillator composition using a Daya Bay antineutrino detector”. In: *Nuclear Instruments and Methods in Physics Research Section A: Accelerators, Spectrometers, Detectors and Associated Equipment* 988 (2021), p. 164823. ISSN: 0168-9002. DOI: https://doi.org/10.1016/j.nima.2020.164823. URL: https://www.sciencedirect.com/science/article/pii/S0168900220312201.

[20] P. Lombardi et al. “Distillation and stripping pilot plants for the JUNO neutrino detector: Design, operations and reliability”. In: *Nuclear Instruments and Methods in Physics Research Section A: Accelerators, Spectrometers, Detectors and Associated Equipment* 925 (2019), pp. 6–17. ISSN: 0168-9002. DOI: https://doi.org/10.1016/j.nima.2019.01.071. URL: https://www.sciencedirect.com/science/article/pii/S0168900219301299.

[21] H Wilkens, M Pohl, and Jan Kuijpers. “Experimental study of high energy muons from Extensive Air Showers in the energy range 100 TeV to 10 PeV”. In: (Jan. 2003).

[22] Tibor J. Dunai. *Cosmogenic Nuclides: Principles, Concepts and Applications in the Earth Surface Sciences*. Cambridge University Press, 2010. DOI: 10.1017/CBO9780511804519.

[23] Angel Abusleme et al. “Radioactivity control strategy for the JUNO detector”. In: *Journal of High Energy Physics* 2021.11 (2021), p. 102. ISSN: 1029-8479. DOI: 10.1007/JHEP11(2021)102. URL: https://doi.org/10.1007/JHEP11(2021)102.

[24] S. Agostinelli et al. "GEANT4–a simulation toolkit". In: *Nucl. Instrum. Meth. A* 506 (2003), pp. 250–303. DOI: 10.1016/S0168-9002(03)01368-8.

[25] Tao Lin et al. "The Application of SNiPER to the JUNO Simulation". In: *J. Phys. Conf. Ser.* 898.4 (2017). Ed. by Richard Mount and Craig Tull, p. 042029. DOI: 10.1088/1742-6596/898/4/042029. arXiv: 1702.05275 [physics.ins-det].

[26] C. Alduino et al. "Measurement of the two-neutrino double-beta decay half-life of 130Te with the CUORE-0 experiment". In: *The European Physical Journal C* 77.1 (2017), p. 13. ISSN: 1434-6052. DOI: 10.1140/epjc/s10052-016-4498-6. URL: https://doi.org/10.1140/epjc/s10052-016-4498-6.

[27] C. Alduino et al. "The projected background for the CUORE experiment". In: *The European Physical Journal C* 77.8 (2017), p. 543. ISSN: 1434-6052. DOI: 10.1140/epjc/s10052-017-5080-6. URL: https://doi.org/10.1140/epjc/s10052-017-5080-6.

[28] Jagdish Tuli. "Evaluated Nuclear Structure Data File and Related Products". In: *AIP Conference Proceedings* 769 (May 2005). DOI: 10.1063/1.1945002.

[29] J.B. Birks. *The Theory and Practice of Scintillation Counting*. International series of monographs on electronics and instrumentation. Pergamon Press, 1964. URL: https://books.google.it/books?id=-ayPjgEACAAJ.

[30] R.L. Craun and D.L. Smith. "Analysis of response data for several organic scintillators". In: *Nuclear Instruments and Methods* 80.2 (1970), pp. 239–244. ISSN: 0029-554X. DOI: https://doi.org/10.1016/0029-554X(70)90768-8. URL: https://www.sciencedirect.com/science/article/pii/0029554X70907688.

[31] W.H. Kelly, G.B. Beard, and R.A. Peters. "The beta decay of K40". In: *Nuclear Physics* 11 (1959), pp. 492–498. ISSN: 0029-5582. DOI: https://doi.org/10.1016/0029-5582(59)90292-5. URL: https://www.sciencedirect.com/science/article/pii/0029558259902925.

[32] G. Baccolo et al. "Development of a low background alpha–beta/gamma coincidence detector". In: *Nuclear Instruments and Methods in Physics Research Section A: Accelerators, Spectrometers, Detectors and Associated Equipment* 1003 (2021), p. 165290. ISSN: 0168-9002. DOI: https://doi.org/10.1016/j.nima.2021.165290. URL: https://www.sciencedirect.com/science/article/pii/S0168900221002746.

[33] S. Cecchini and M. Spurio. "Atmospheric muons: experimental aspects". In: *Geoscientific Instrumentation, Methods and Data Systems* 1.2 (2012), pp. 185–196. DOI: 10.5194/gi-1-185-2012. URL: https://gi.copernicus.org/articles/1/185/2012/.

[34] Prashant Shukla and Sundaresh Sankrith. "Energy and angular distributions of atmospheric muons at the Earth". In: *International Journal of Modern Physics A* 33 (Oct. 2018), p. 1850175. DOI: 10.1142/S0217751X18501750.

[35] T. Goldbrunner et al. "Neutron activation analysis of detector components for the solar neutrino experiment BOREXINO". In: *Journal of Radioanalytical and Nuclear Chemistry* 216.2 (1997), pp. 293–297. ISSN: 1588-2780. DOI: 10.1007/BF02033793. URL: https://doi.org/10.1007/BF02033793.

[36] R. B. Firestone and C. M. Baglin. *Table of isotopes*. Wiley, 1999.

[37] A. Barresi et al. "High precision measurement of the half-life of the 391.6 keV metastable level in $^{239}$Pu". In: *Phys. Rev. C* 105 (3 2022), p. 034346. DOI: 10.1103/PhysRevC.105.034346. URL: https://link.aps.org/doi/10.1103/PhysRevC.105.034346.

[38] Z. Djurcic et al. “Novel technique for ultra-sensitive determination of trace elements in organic scintillators”. In: *Nuclear Instruments and Methods in Physics Research Section A: Accelerators, Spectrometers, Detectors and Associated Equipment* 507.3 (2003), pp. 680–690. ISSN: 0168-9002. DOI: `https://doi.org/10.1016/S0168-9002(03)01362-7`. URL: `https://www.sciencedirect.com/science/article/pii/S0168900203013627`.

[39] *Triskem International.* `https://www.triskem-international.com/`.

[40] Triskem International. *Extraction Chromatography Technical Documentation.* `https://www.triskem-international.com/scripts/files/5addcf96423962.97324869/technical_doc_all-products_web-0.pdf`.

[41] M. Eisenbud. *Environmental radioactivity from natural, industrial, and military sources.* Academic Press, 1987.

[42] Peter McEachern, Willard G. Myers, and Frederick A. White. “Uranium concentrations in surface air at rural and urban localities within New York State”. In: *Environmental Science & Technology* 5.8 (1971), pp. 700–703. DOI: `10.1021/es60055a002`. eprint: `https://doi.org/10.1021/es60055a002`. URL: `https://doi.org/10.1021/es60055a002`.

[43] A. Barresi. *Ultra-sensitive measurements of* $^{238}U$ *through delayed coincidence analysis on activated liquid samples.* Talk at the conference ICRM-LLRMT 2022, Gran Sasso National Laboratory. 2022. URL: `https://icrm2022.lngs.infn.it/`.